OPTICAL SCIENCES

D. G. Rabus

Integrated Ring Resonators

The Compendium

Springer

Springer Series in
OPTICAL SCIENCES 127

founded by H.K.V. Lotsch

Editor-in-Chief: W. T. Rhodes, Atlanta

Editorial Board: A. Adibi, Atlanta
T. Asakura, Sapporo
T. W. Hänsch, Garching
T. Kamiya, Tokyo
F. Krausz, Garching
B. Monemar, Linköping
H. Venghaus, Berlin
H. Weber, Berlin
H. Weinfurter, München

Springer Series in

OPTICAL SCIENCES

The Springer Series in Optical Sciences, under the leadership of Editor-in-Chief *William T. Rhodes*, Georgia Institute of Technology, USA, provides an expanding selection of research monographs in all major areas of optics: lasers and quantum optics, ultrafast phenomena, optical spectroscopy techniques, optoelectronics, quantum information, information optics, applied laser technology, industrial applications, and other topics of contemporary interest.
With this broad coverage of topics, the series is of use to all research scientists and engineers who need up-to-date reference books.

The editors encourage prospective authors to correspond with them in advance of submitting a manuscript. Submission of manuscripts should be made to the Editor-in-Chief or one of the Editors. See also www.springeronline.com/series/624

Editor-in-Chief

William T. Rhodes
Georgia Institute of Technology
School of Electrical and Computer Engineering
Atlanta, GA 30332-0250, USA
E-mail: bill.rhodes@ece.gatech.edu

Editorial Board

Ali Adibi
Georgia Institute of Technology
School of Electrical and Computer Engineering
Atlanta, GA 30332-0250, USA
E-mail: adibi@ee.gatech.edu

Toshimitsu Asakura
Hokkai-Gakuen University
Faculty of Engineering
1-1, Minami-26, Nishi 11, Chuo-ku
Sapporo, Hokkaido 064-0926, Japan
E-mail: asakura@eli.hokkai-s-u.ac.jp

Theodor W. Hänsch
Max-Planck-Institut für Quantenoptik
Hans-Kopfermann-Straße 1
85748 Garching, Germany
E-mail: t.w.haensch@physik.uni-muenchen.de

Takeshi Kamiya
Ministry of Education, Culture, Sports
Science and Technology
National Institution for Academic Degrees
3-29-1 Otsuka, Bunkyo-ku
Tokyo 112-0012, Japan
E-mail: kamiyatk@niad.ac.jp

Ferenc Krausz
Ludwig-Maximilians-Universität München
Lehrstuhl für Experimentelle Physik
Am Coulombwall 1
85748 Garching, Germany
and
Max-Planck-Institut für Quantenoptik
Hans-Kopfermann-Straße 1
85748 Garching, Germany
E-mail: ferenc.krausz@mpq.mpg.de

Bo Monemar
Department of Physics
and Measurement Technology
Materials Science Division
Linköping University
58183 Linköping, Sweden
E-mail: bom@ifm.liu.se

Herbert Venghaus
Fraunhofer Institut für Nachrichtentechnik
Heinrich-Hertz-Institut
Einsteinufer 37
10587 Berlin, Germany
E-mail: venghaus@hhi.de

Horst Weber
Technische Universität Berlin
Optisches Institut
Straße des 17. Juni 135
10623 Berlin, Germany
E-mail: weber@physik.tu-berlin.de

Harald Weinfurter
Ludwig-Maximilians-Universität München
Sektion Physik
Schellingstraße 4/III
80799 München, Germany
E-mail: harald.weinfurter@physik.uni-muenchen.de

D.G. Rabus

Integrated Ring Resonators

The Compendium

With 243 Figures and 8 Tables

Springer

Dr. Dominik G. Rabus
Feodor-Lynen-Fellow
Baskin School of Engineering
University of California Santa Cruz
1156 High Street
Santa Cruz, CA 95064-1077, USA
E-mail: book@ringresonator.com
www.ringresonator.com

ISSN 0342-4111

ISBN-10 3-540-68786-6 Springer Berlin Heidelberg New York

ISBN-13 978-3-540-68786-3 Springer Berlin Heidelberg New York

Library of Congress Control Number: 2006940350

This work is subject to copyright. All rights are reserved, whether the whole or part of the material is concerned, specifically the rights of translation, reprinting, reuse of illustrations, recitation, broadcasting, reproduction on microfilm or in any other way, and storage in data banks. Duplication of this publication or parts thereof is permitted only under the provisions of the German Copyright Law of September 9, 1965, in its current version, and permission for use must always be obtained from Springer-Verlag. Violations are liable to prosecution under the German Copyright Law.

Springer is a part of Springer Science+Business Media.

springer.com

© Springer-Verlag Berlin Heidelberg 2007

The use of general descriptive names, registered names, trademarks, etc. in this publication does not imply, even in the absence of a specific statement, that such names are exempt from the relevant protective laws and regulations and therefore free for general use.

Typesetting by SPi using a Springer LaTeX macro package
Cover concept by eStudio Calamar Steinen using a background picture from The Optics Project. Courtesy of John T. Foley, Professor, Department of Physics and Astronomy, Mississippi State University, USA.
Cover design: WMX Design GmbH, Heidelberg

Printed on acid-free paper SPIN: 11600657 57/3100/SPi 5 4 3 2 1 0

Dedication

To my dad

If you want to build a ship, don't drum up people together to collect wood and don't assign them tasks and work, but rather teach them to long for the endless immensity of the sea.

Antoine-Marie-Roger de Saint-Exupéry

Foreword

This book is all about integrated ring resonators made out of optical waveguides in various materials for different applications. Integrated ring resonators are used to build optical filters, lasers, sensors, modulators, dispersion compensators, just to name a few. The book covers the range from simulation of various ring resonator configurations to the fabrication processes currently used, to the description of the application of integrated ring resonator in various fields. The book presents a summary of the activities in this field form the past to the current state of the art giving several examples. The book is written for students, graduates, professionals, academics and industry working in this exciting field.

The examples in literature used in this book have been collected over four years, categorizing the different examples into what are now the chapters of this book.

Integrated ring resonators have been and still are a fascinating class of devices and have interested me since the beginning of my PhD in 1999.

I am therefore grateful to the entire integrated ring resonator community for providing me with exciting and cutting edge research material which enabled me to write this book. Due to the enormous amount of publications in this attractive field, I hope, that I was able to refer to most of the work done so far and would be thankful if I was made aware of any "undiscovered" work.

As research on integrated ring resonators is ongoing, I would also be happy to receive material for my database which can then of course be included in further publications.

I would like to take this opportunity of expressing my sincere thanks to Dr. Venghaus, one of the editors of the Springer Series in Optical Sciences and Springer for making the publication of this book possible.

Furthermore, I would like to thank the Alexander von Humboldt foundation and the Baskin School of Engineering of the University of California, Santa Cruz, for supporting my research.

My special thanks go to my wife Regina and my two children, Anouk and Tizian, for giving me the freedom and time to write this book.

List of Abbreviations

ω	angular frequency
η	coupling efficiency to the fundamental waveguide mode
κ	coupling parameter
Γ	gain of the filter
Λ	length of waveguide segment
α	loss coefficient of the ring (zero loss: $\alpha = 1$)
α_n	absorption coefficient
θ	phase
β	propagation constant
λ	wavelength
γ_ϕ	complex angular propagation constant
$\Delta\lambda$	free spectral range (see also FSR)
$\Phi(\omega)$	phase shift
$\Delta\omega_n$	complex frequency deviation
λ_0	center wavelength of the passband
ε_0	permittivity of free space
α_coupling	fiber–chip coupling losses
λ_g	bandgap wavelength
$\alpha_\mathrm{insertion}$	insertion loss
ϕ_k	coupling angle
ψ_k	phase shift
$\alpha_\mathrm{propagation}$	intrinsic losses
$\omega_{\mathrm{R}n}$	resonant frequency of ring resonator n
φ_t	phase of the coupler
α_th	coefficient of thermal expansion
$1/\tau$	amplitude decay time-constant
$2\delta\lambda$	3 dB bandwidth
$A(z)$	polynomial
AFM	atomic force microscope

APF	all pass filter
ASE	amplified spontaneous emission
B	intensity enhancement or buildup factor
$B(z)$	polynomial
BCB	benzocyclobutene
BH	buried heterostructure
BHF	buffered hydrofluoric acid
BPF	bandpass filter
BW	modulation bandwidth
c	phase velocity of the ring mode ($c = c_0/n_{\mathrm{eff}}$)
c_0	vacuum speed of light
CAIBE	chemically assisted ion beam etching
$\mathrm{C_n}$	auger recombination coefficient
$\mathrm{C_p}$	auger recombination coefficient
CROW	coupled-resonator optical waveguides
CTE	coefficient of thermal expansion
CVD	chemical vapor deposition
cw	continuous wave
DEMUX	demultiplexer
DFB	distributed feedback
DGD	differential group delay
DI	deionized
$\mathrm{d_k}$	length of the ring waveguides
DR-RCL	double ring resonator coupled lasers
DTFT	discrete-time Fourier transform
DUT	device under test
E	complex mode amplitude
$e(t)$	energy amplitude
$E(t)$	time dependent mode amplitude
E-beam	electron beam
ECL	external cavity laser
ECR-CVD	electron cyclotron resonance chemical vapor deposition
EIM	effective index method
EO	electro-optic
F	finesse
FHD	flame hydrolysis deposition
FSK	frequency-shift keying
FSR	free spectral range
FWHM	full width at half maximum
FWM	four wave mixing
GRIN	gradient index
$h(n)$	impulse response of a filter
HEMT	high electron mobility transistors
I	intensity/current
ICP-RIE	inductively-coupled-plasma reactive ion etching
IPA	Iso-propanol or 2-propanol
K	contrast/confinement factor
k	vacuum wavenumber
L	circumference of the ring/optical output

L_{C}	lattice constant
l_{k}	length of the coupler (note: this is not the coupling length)
LPCVD	low-pressure chemical-vapor-deposition
m	integer
MBE	molecular beam epitaxy
MEMS	microelectro mechanical system
m_{h}	effective hole masses
m_{l}	effective electron masses
MIBK	methyl iso butyl ketone
m_{lp}	effective hole masses
MMI	multimode interference
m_{n}	mode number
m_{o}	mode order
MOVPE	metal organic vapor phase epitaxy
MQW	multiple quantum well
m_{t}	effective electron masses
MUX	multiplexer
MZI	Mach–Zehnder interferometer
n_{eff}	effective refractive index
n_{g}	group refractive index
NMP	n-methyl-2-pyrrolidone or C_5H_9NO
NSOM	near-field scanning optical microscopy
OEC	optimum end-fire coupling
OLCR	optical low-coherence reflectometry
OSA	optical spectrum analyzer
OSP	optical signal processing
P	transmission power
$P(t)$	time dependent power
$p(t)$	total energy stored in the ring
PBS	polarization beam splitter
PD	photo diode
PECVD	plasma enhanced chemical vapor deposition
PhC	photonic crystal
PIC	photonic integrated circuit
PLC	polarization controller
PMD	polarization mode dispersion
PMMA	polymethylmethacrylate
p_n	poles of $H(z)$
PRRM	pulse repetition rate multiplication
PSTM	photon scanning tunneling microscope
Q	quality factor
QC	quantum cascade
QCSE	quantum confined Stark effect
QW	quantum wells
R	effective radius of curvature/end-face reflectivity
r	radius
RF	radiofrequency
RIBE	reactive ion beam etching
RIE	reactive ion etching
RPM	rounds per minute

RTFT	real-time Fourier transformation
RW	ridge waveguide
RZ	return-to-zero
S	optical path length
SAMOVPE	selective area metal organic vapor phase epitaxy
SCCM	standard cubic centimeters per minute
SCISSORS	side-coupled, integrated, space sequence of resonators
SEBL	scanning-electron-beam lithography
SEM	scanning electron microscope
SMSR	side mode suppression ratio
SNOM	scanning near-field optical microscopy
SOA	semiconductor optical amplifier
SOG	spin on glass
SOI	silicon on insulator
SPM	scanning probe microscopy
STM	scanning tunneling microscopy
STP	standard temperature and pressure
T	characteristic matrix/temperature/tuning enhancement factor
t	coupling parameter/time
TE	transverse electric
T_g	glass transition temperature
TIR	total internal reflection
TM	transverse magnetic
$T_\mathrm{N}(x)$	Nth-order Chebyshev polynomial
TO	thermo-optic
U_Matrix	unit matrix
v_g	group velocity
w	width
WDM	wavelength division multiplexing
WGM	whispering gallery mode
x_0	3 dB cutoff frequency
x_C	center frequency
x_n	vector
x_P	changeover region on the passband
x_S	changeover region on the stopband
z_m	zeros of H(z)

Contents

1

Introduction

Integrated ring resonators have emerged in the last few years in integrated optics and have found their way into many applications. Integrated ring resonators do not require facets or gratings for optical feedback and are thus particularly suited for monolithic integration with other components. The response from coupled ring resonators can be custom designed by the use of different coupling configurations. In this way, the response from ring resonator filters can be designed to have a flat top and steep roll of. Other coupling configurations lead to a ring resonator reflector device, which can be used on one side or on both sides of an integrated semiconductor optical amplifier serving as a laser.

Ring resonators do not only find application in optical networks, they have recently been demonstrated to be used as sensors and biosensors.

Several PhD theses were and are still devoted to the study, fabrication and characterization of integrated ring resonators in several material systems. One of the first thesis on integrated ring and disk resonator filters is written by Rafizadeh (1997), where devices with diameters down to 10 µm in the material system AlGaAs/GaAs are fabricated and characterized. One of the first theoretical theses is written by Hagness (1998), which presents a finite difference time domain (FDTD) analysis of ring and disk resonators. A thesis which followed in 2000 based, on the material system AlGaAs/GaAs is written by Absil (2000), where vertical and lateral multiple coupled ring resonator configurations are fabricated and characterized. In this work, nonlinear effects are used in ring resonators to demonstrate four wave mixing.

These examples of fabricated ring resonators are all passive and do not contain any gain to modify the filter performance. Ring lasers have of course been realized consisting of all active material, but have not been used as optical filters. Gain is introduced into ring resonator filters in the theses of Djordjev (2002) and Rabus (2002) based on the InP material system. In Djordjev (2002) vertical coupled disk and ring resonator filters with a radius down to 10 µm are demonstrated which find application as modulators, routers, and switches. In Rabus (2002) lateral multiple coupled racetrack shaped ring resonators with

integrated semiconductor optical amplifiers (SOA) are presented, leading to modified filter functions. Ring resonators in InP with one of the smallest circumference of only 20 µm are fabricated and characterized in the thesis of Grover (2003). One of the first investigations of the nonlinear properties of InP-based ring resonator devices is presented in the thesis of Ibrahim (2003). These examples of ring resonator devices have all been realized in semiconductor material. Ring resonators in electro optic polymers used as modulators are fabricated in the thesis of Rabiei (2003). Polymer ring resonator modulators are also demonstrated in Leinse (2005). Ring resonator research at the University of Twente has recently led to a number of theses. Silicon oxynitride and silicon nitride based devices are fabricated and described in Tan (2004) and Geuzebroek (2005). Wafer bonding for fabricating ring resonator devices is described in detail in the thesis of Christiaens (2005). A coupled mode theory is used in Hiremath (2005) to analyze the filter characteristics of ring resonators.

These theses are examples of ongoing research on ring resonator devices, showing their potential and their diversity of application which are described in the following chapters of this book.

The book is organized as follows: Chap. 2 covers the main aspects of ring resonator theory. Chapter 3 gives an overview of the various fabrication methods and material systems. Chapter 4 serves as a brief introduction into the building blocks of ring resonator devices like couplers and bends. Chapter 5 describes the numerous applications of fabricated ring resonator devices. Chapter 6 provides a short introduction into whispering gallery mode resonators. The book ends with an outlook given in Chap. 7.

2

Ring Resonators: Theory and Modeling

One of the first papers dealing with the simulation of an integrated ring resonator for a bandpass filter has been published in 1969 by Marcatili. The layout of the channel dropping filter which he proposed is shown in Fig. 2.1. This can be regarded as the standard configuration for an integrated ring resonator channel dropping filter. Two straight waveguides also known as the bus or the port waveguides are coupled either by directional couplers through the evanescent field or by multimode interference (MMI) couplers to the ring resonator. A simpler configuration is obtained, when the second bus or port waveguide is removed. Then the filter is typically referred to as "notch" filter because of the unique filter characteristic. In the following chapter, the ring resonator simulation model is described beginning with the basic notch configuration and adding more bus waveguides and ring resonators to eventually build a multiple coupled ring resonator filter. Different types of ring resonator simulation models will be explained, so as to be able to chose from a range of models which best suit the need.

2.1 Single Ring Resonators

2.1.1 Ring Structure

The Basic Configuration

The basic configuration, which consists of unidirectional coupling between a ring resonator with radius r and a waveguide, is described in Fig. 2.2, based on Yariv (2002a, b). Defining that a single unidirectional mode of the resonator is excited, the coupling is lossless, single polarization is considered, none of the waveguide segments and coupler elements couple waves of different polarization, the various kinds of losses occurring along the propagation of

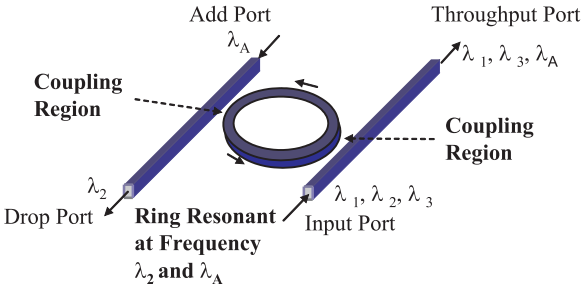

Fig. 2.1. Ring resonator channel dropping filter

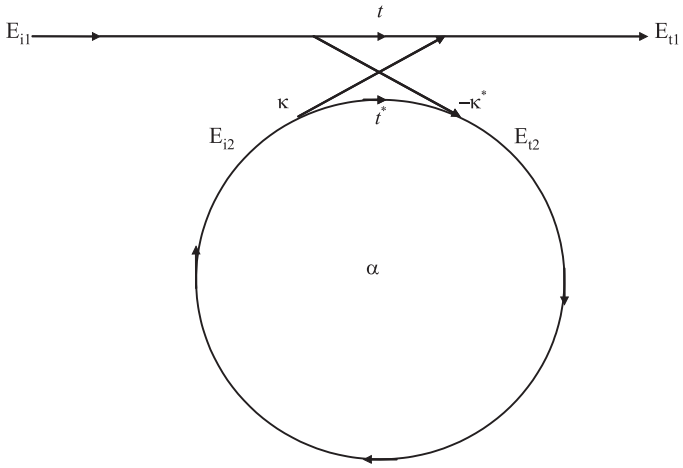

Fig. 2.2. Model of a single ring resonator with one waveguide

light in the ring resonator filter are incorporated in the attenuation constant, the interaction can be described by the matrix relation:

$$\begin{pmatrix} E_{t1} \\ E_{t2} \end{pmatrix} = \begin{pmatrix} t & \kappa \\ -\kappa^* & t^* \end{pmatrix} \begin{pmatrix} E_{i1} \\ E_{i2} \end{pmatrix}. \tag{2.1}$$

The complex mode amplitudes E are normalized, so that their squared magnitude corresponds to the modal power. The coupler parameters t and κ depend on the specific coupling mechanism used. The * denotes the conjugated complex value of t and κ, respectively.

The matrix is symmetric because the networks under consideration are reciprocal. Therefore

$$\left|\kappa^2\right| + \left|t^2\right| = 1. \tag{2.2}$$

In order to further simplify the model, E_{i1} is chosen to be equal to 1. Then the round trip in the ring is given by

$$E_{i2} = \alpha \cdot \mathrm{e}^{\mathrm{j}\theta} E_{t2}, \tag{2.3}$$

where α is the loss coefficient of the ring (zero loss: $\alpha = 1$) and $\theta = \omega L/c$, L being the circumference of the ring which is given by $L = 2\pi r$, r being the radius of the ring measured from the center of the ring to the center of the waveguide, c the phase velocity of the ring mode ($c = c_0/n_{\text{eff}}$) and the fixed angular frequency $\omega = kc_0$, c_0 refers to the vacuum speed of light. The vacuum wavenumber k is related to the wavelength λ through: $k = 2\pi/\lambda$. Using the vacuum wavenumber, the effective refractive index n_{eff} can be introduced easily into the ring coupling relations by

$$\beta = k \cdot n_{\text{eff}} = \frac{2\pi \cdot n_{\text{eff}}}{\lambda}, \tag{2.4}$$

where β is the propagation constant. This leads to

$$\theta = \frac{\omega L}{c} = \frac{kc_0 L}{c} = k \cdot n_{\text{eff}} \cdot 2\pi r = \frac{2\pi \cdot n_{\text{eff}} \cdot 2\pi r}{\lambda} = 4\pi^2 n_{\text{eff}} \frac{r}{\lambda}. \tag{2.5}$$

From (2.1) and (2.3) we obtain

$$E_{t1} = \frac{-\alpha + t \cdot \mathrm{e}^{-\mathrm{j}\theta}}{-\alpha t^* + \mathrm{e}^{-\mathrm{j}\theta}}, \tag{2.6}$$

$$E_{i2} = \frac{-\alpha\kappa^*}{-\alpha t^* + \mathrm{e}^{-\mathrm{j}\theta}}, \tag{2.7}$$

$$E_{t2} = \frac{-\kappa^*}{1 - \alpha t^* \mathrm{e}^{\mathrm{j}\theta}}. \tag{2.8}$$

This leads to the transmission power P_{t1} in the output waveguide, which is

$$P_{t1} = |E_{t1}|^2 = \frac{\alpha^2 + |t|^2 - 2\alpha\,|t| \cos(\theta + \varphi_{\text{t}})}{1 + \alpha^2\,|t|^2 - 2\alpha\,|t| \cos(\theta + \varphi_{\text{t}})}, \tag{2.9}$$

where $t = |t| \exp(\mathrm{j}\varphi_{\text{t}})$, $|t|$ representing the coupling losses and φ_t the phase of the coupler.

The circulating power P_{i2} in the ring is given by

$$P_{i2} = |E_{i2}|^2 = \frac{\alpha^2(1 - |t|^2)}{1 + \alpha^2\,|t|^2 - 2\alpha\,|t| \cos(\theta + \varphi_{\text{t}})}. \tag{2.10}$$

On resonance, $(\theta + \varphi_t) = 2\pi m$, where m is an integer, the following is obtained:

$$P_{t1} = |E_{t1}|^2 = \frac{(\alpha - |t|)^2}{(1 - \alpha\,|t|)^2} \tag{2.11}$$

and

$$P_{i2} = |E_{i2}|^2 = \frac{\alpha^2(1 - |t|^2)}{(1 - \alpha\,|t|)^2}. \tag{2.12}$$

A special case happens when $\alpha = |t|$ in (2.11), when the internal losses are equal to the coupling losses. The transmitted power becomes 0. This is known in literature as critical coupling, which is due to destructive interference.

In using the above equations, it is possible to get a good idea of the behavior of a simplified basic ring resonator filter configuration consisting of only one waveguide and one ring. The wavelength-dependent filter characteristic for a ring resonator configuration with a radius of $r = 148\,\mu\text{m}$ with matched coupling and loss coefficient, derived using (2.1)–(2.11), is shown in Fig. 2.3. This model can be extended to suit the requirement of various types of ring resonator configurations.

The next configuration which is discussed is the basic ring resonator add–drop configuration, consisting of one input, one output waveguide and the ring resonator. The four ports of the ring resonator are referred to in the following as input port, throughput port, drop port and add port (Fig. 2.4).

The ring resonator simulation model has been updated according to Fig. 2.4. For simplification E_{i1} is as defined before equal to 1. The throughput mode amplitude in the first waveguide is given by

$$E_{t1} = t_1 + \frac{-\kappa_1\kappa_1^* t_2^* \alpha_{1/2}^2 \mathrm{e}^{\mathrm{j}\theta|t_1|^2+|\kappa_1|^2=1}}{1 - t_1^* t_2^* \alpha_{1/2}^2 \mathrm{e}^{\mathrm{j}\theta}} = \frac{t_1 - t_2^* \alpha_{1/2}^2 \mathrm{e}^{\mathrm{j}\theta}}{1 - t_1^* t_2^* \alpha_{1/2}^2 \mathrm{e}^{\mathrm{j}\theta}} = \frac{t_1 - t_2^* \alpha \mathrm{e}^{\mathrm{j}\theta}}{1 - t_1^* t_2^* \alpha \mathrm{e}^{\mathrm{j}\theta}}. \tag{2.13}$$

In this calculation, $\alpha_{1/2}$ and $\theta_{1/2}$ are used which are the half round trip loss and phase, respectively. It is $\alpha = \alpha_{1/2}^2$ and $\theta = 2\theta_{1/2}$.

Now, the mode amplitude in the ring has to pass the second coupler as can be seen from the schematic to become the new dropped mode amplitude E_{t2}. The dropped mode amplitude in the second waveguide is then given by:

$$E_{t2} = \frac{-\kappa_1^* \kappa_2 \alpha_{1/2} \mathrm{e}^{\mathrm{j}\theta_{1/2}}}{1 - t_1^* t_2^* \alpha \mathrm{e}^{\mathrm{j}\theta}}. \tag{2.14}$$

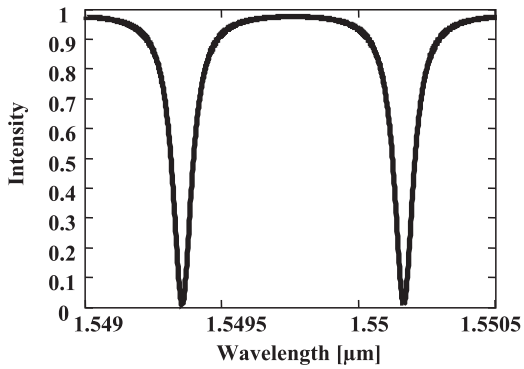

Fig. 2.3. Notch type ring resonator filter characteristic

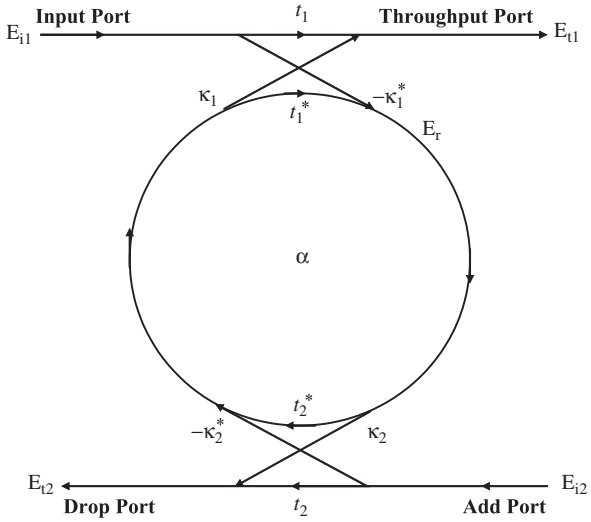

Fig. 2.4. Model of a basic add–drop single ring resonator filter

At resonance, the output power from the drop port is given by

$$P_{t2-\text{Resonance}} = |E_{t2-\text{Resonance}}|^2 = \frac{\left(1-|t_1|^2\right)\cdot\left(1-|t_2|^2\right)\cdot\alpha}{(1-\alpha\,|t_1 t_2|)^2} \tag{2.15}$$

The throughput port mode amplitude E_{t1} (2.13) will be zero at resonance for identical symmetrical couplers $t_1 = t_2$ if $\alpha = 1$, which indicates that the wavelength on resonance is fully extracted by the resonator. The value of $\alpha = 1$ can only be achieved by the implementation of gain incorporated in the ring resonator to compensate the waveguide losses. The value of the loss coefficient α is fixed in a purely passive ring resonator. A possibility of achieving minimum intensity ($P_{t1} = 0$) at resonance of the output transmission P_{t1} at the throughput port is to adjust the coupling parameters t_1, t_2 to the loss coefficient α. From (2.13) we obtain

$$\alpha = \left|\frac{t_1}{t_2}\right|. \tag{2.16}$$

If the ring resonator is lossless ($\alpha = 1$), then the couplers have to be symmetric in order to achieve minimum intensity. The transmission of a lossless ring resonator add drop filter with radius of $r = 148\,\mu\text{m}$ is shown in Fig. 2.5.

There are different kinds of requirements on the simulation of various kinds of ring resonator configurations. Starting of with the given equations satisfies most basic models. The ring model can for example be divided

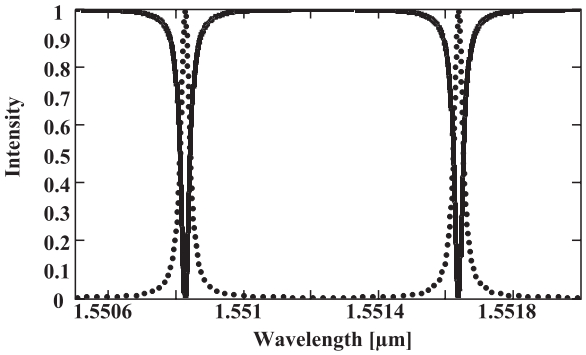

Fig. 2.5. Add–drop ring resonator filter characteristic

into more segments to account for different materials or modified waveguide paths. Examples of calculated models can be found in Rabus (2002) and Michelotti et al. (2004).

Ring Resonator Parameters

Ring resonator filters can be described by certain figures of merit which are also generally used to describe optical filters. One important figure is the distance between resonance peaks, which is called the free spectral range (FSR). A simple approximation can be obtained for the FSR by using the propagation constant from (2.4), neglecting the wavelength dependency of the effective refractive index

$$\frac{\partial\beta}{\partial\lambda} = -\frac{\beta}{\lambda} + k\frac{\partial n_{\text{eff}}}{\partial\lambda} \approx -\frac{\beta}{\lambda}. \tag{2.17}$$

This leads to the FSR $\Delta\lambda$, which is the difference between the vacuum wavelengths corresponding to two resonant conditions.

$$\text{FSR} = \Delta\lambda = -\frac{2\pi}{L}\left(\frac{\partial\beta}{\partial\lambda}\right)^{-1} \approx \frac{\lambda^2}{n_{\text{eff}}L}. \tag{2.18}$$

Note that (2.18) is for the resonant condition next to a resonance found for the used propagation constant.

If the wavelength dependence of the effective index can not be neglected, it can be incorporated in the following way to obtain a modified version of (2.17).

$$\frac{\partial\beta}{\partial\lambda} = -\frac{k}{\lambda}n_{\text{g}}, \tag{2.19}$$

where n_{g} is the group refractive index, which is defined as:

$$n_{\text{g}} = n_{\text{eff}} - \lambda\frac{\partial n_{\text{eff}}}{\partial\lambda}. \tag{2.20}$$

The group refractive index can be used instead of the effective index whenever appropriate avoiding the approximation and obtaining more accurate values.

The modified FSR $\Delta\lambda$ is then given by

$$\mathrm{FSR} = \Delta\lambda = \frac{\lambda^2}{n_\mathrm{g} L}. \tag{2.21}$$

The next parameter of importance is the resonance width which is defined as the full width at half maximum (FWHM) or 3 dB bandwidth $2\delta\lambda$ of the resonance lineshape. Using the expressions for the drop port (2.14) and (2.15)

$$\left| \frac{-\kappa_1^* \kappa_2 \alpha_{1/2} \mathrm{e}^{\mathrm{j}\theta_{1/2}}}{1 - t_1^* t_2^* \alpha \mathrm{e}^{\mathrm{j}\theta}} \right|^2 = \frac{1}{2} \frac{|\kappa_1|^2 |\kappa_2|^2 \alpha}{(1 - \alpha |t_1 t_2|)^2}. \tag{2.22}$$

Assuming that the coupling coefficients are real, lossless, and without a phase term, (2.22) can be written as

$$\frac{\left(\kappa_1 \kappa_2 \alpha_{1/2}\right)^2}{1 - 2t_1 t_2 \alpha \cos(\theta) + (t_1 t_2 \alpha)^2} = \frac{1}{2} \frac{\left(\kappa_1 \kappa_2 \alpha_{1/2}\right)^2}{(1 - t_1 t_2 \alpha)^2}. \tag{2.23}$$

Then

$$2(1 - t_1 t_2 \alpha)^2 = 1 - 2t_1 t_2 \alpha \cos(\theta) + (t_1 t_2 \alpha)^2. \tag{2.24}$$

For small θ, using the real part of the series expansion of the Euler formula

$$\cos(\theta) = 1 - \frac{\theta^2}{2}. \tag{2.25}$$

Therefore

$$\theta^2 = \frac{(1 - t_1 t_2 \alpha)^2}{t_1 t_2 \alpha}. \tag{2.26}$$

This equation can further be simplified if the loss in the ring is negligible and the coupling is symmetric ($t = t_1 = t_2$) to

$$\theta = \sqrt{\frac{(1 - t^2)^2}{t^2}} = \frac{1 - t^2}{t}. \tag{2.27}$$

Using (2.5) and (2.17) to translate into the wavelength domain

$$2\delta\lambda = \frac{\lambda^2}{\pi L n_\mathrm{eff}} \frac{1 - t^2}{t}. \tag{2.28}$$

The expression which is commonly used can be obtained by assuming weak coupling and $\lambda \gg \delta\lambda$

$$\mathrm{FWHM} = 2\delta\lambda = \frac{\kappa^2 \lambda^2}{\pi L n_\mathrm{eff}}. \tag{2.29}$$

Another parameter which can now be directly calculated from the parameters in the previous chapter is the finesse F of the ring resonator filter. It is defined as the ratio of the FSR and the width of a resonance for a specific wavelength (FWHM):

$$F = \frac{\mathrm{FSR}}{\mathrm{FWHM}} = \frac{\Delta\lambda}{2\delta\lambda} = \pi\frac{t}{1-t^2} \overset{\kappa\ll 1}{\approx} \frac{\pi}{\kappa^2}. \tag{2.30}$$

A parameter which is closely related to the finesse is the quality factor Q of a resonator, which is a measure of the sharpness of the resonance. It is defined as the ratio of the operation wavelength and the resonance width

$$Q = \frac{\lambda}{2\delta\lambda} = \pi\frac{n_{\mathrm{eff}}L}{\lambda}\frac{t}{1-t^2} = \frac{n_{\mathrm{eff}}L}{\lambda}F. \tag{2.31}$$

The quality factor can also be regarded as the stored energy divided by the power lost per optical cycle.

The intensity in the ring resonator can be much higher than that in the bus waveguides, as the traveling wave in the ring resonator interferes constructively at resonance with the input wave and thus the amplitude builds up. In addition to this intensity increase, the field also experiences a phase-shift of an integral multiple of 2π in one round trip. The intensity enhancement or buildup factor B is given by (for a configuration shown in Fig. 2.2)

$$B = \left|\frac{E_{i2}}{E_{i1}}\right|^2 = \left|\frac{-\alpha\kappa^*}{-\alpha t^* + \mathrm{e}^{-\mathrm{j}\theta}}\right|^2. \tag{2.32}$$

For a configuration like Fig. 2.4, the buildup factor is given by

$$B = \left|\frac{E_r}{E_{i1}}\right|^2 = \left|\frac{-\kappa_1^*}{1 - t_1^* t_2^* \alpha \mathrm{e}^{\mathrm{j}\theta}}\right|^2. \tag{2.33}$$

On resonance, the intensity enhancement factor is

$$B = \left|\frac{-\kappa_1^*}{1 - t_1^* t_2^* \alpha}\right|^2. \tag{2.34}$$

For a lossless resonator and setting $\kappa_1 = \kappa_2 = \kappa$ which is $\ll 1, B$ can be written as

$$B = \frac{1}{\kappa^2} \xrightarrow{(2.30)} \frac{F}{\pi}. \tag{2.35}$$

This equation directly relates the intensity enhancement factor B to the finesse F.

For the all-pass configuration and on resonance, the buildup factor is given by ($t_1 = t_2 = t$)

$$B = \frac{1+t}{1-t}. \tag{2.36}$$

Ring resonators can be used for nonlinear optical devices since the intensity in the resonator can be much higher than in the bus waveguide. Examples of devices utilizing nonlinearities in ring resonators are given in Sects. 5.7 and 5.8.

The Time-Dependent Relations

Before going on to extend the previous model incorporating additional ring resonators, the time-dependent relations are adapted from Little et al. (1997b) for the basic ring resonator add–drop configuration. Like in the previous model, it is assumed that the ring supports a traveling wave of amplitude $E(t)$, $P(t)$ represents the total power flowing through any cross section of the ring waveguide at time t. The ring is regarded as an oscillator of energy amplitude $e(t)$, normalized so that $p(t)$ represents the total energy stored in the ring. Energy and power in the ring are related through

$$p\left(t\right) = \left|e\left(t\right)\right|^2 = P\left(t\right)\frac{2\pi r}{v_{\mathrm{g}}}, \tag{2.37}$$

where v_{g} is the group velocity. The ring resonator has a resonant frequency of ω_{R} and amplitude decay time-constant of $1/\tau$. The decay rate and the power exciting the ring resonator are related to each other. The decay rate includes the power coupled to the transmitted wave $1/\tau_{\mathrm{tr}}$, the power lost due to intrinsic effects $1/\tau_{\mathrm{ie}}$, and power coupled to the output waveguide $1/\tau_{t2}$. This leads to

$$\frac{1}{\tau} = \frac{1}{\tau_{\mathrm{tr}}} + \frac{1}{\tau_{\mathrm{ie}}} + \frac{1}{\tau_{t2}}. \tag{2.38}$$

The time rate of change in ring energy can then be written as

$$\frac{\mathrm{d}}{\mathrm{d}t}e = \left(\mathrm{j}\omega_{\mathrm{R}} - \frac{1}{\tau}\right)e - \kappa^* \cdot E_{i1}. \tag{2.39}$$

The relation between the coupling parameter κ and the decay rates of the transmitted wave $1/\tau_{\mathrm{tr}}$ and the output waveguide $1/\tau_{t2}$, is determined by power conservation. The case is considered, when the ring resonator is excited to an energy of $|e_0|^2$, no output waveguide is present and no input wave E_{i1}. The ring energy, with no intrinsic loss, then decays as follow:

$$\left|e\left(t\right)\right|^2 = \left|e_0\right|^2 \exp\left(\frac{-2t}{\tau_{\mathrm{tr}}}\right). \tag{2.40}$$

From these set of eqs. (2.37–2.40), the power transfer characteristic for the drop port can be calculated with the input wave E_{i1} being proportional to $\exp(\mathrm{j}\omega t)$

$$e = \frac{-\mathrm{j}\sqrt{\dfrac{2}{\tau_{\mathrm{tr}}}}}{\mathrm{j}\left(\omega - \omega_{\mathrm{R}}\right) + \dfrac{1}{\tau}}E_{i1}. \tag{2.41}$$

From this equation, we can calculate the transmitted wave at the throughput port

$$E_{t1} = E_{i1} - \kappa^* e = \frac{\mathrm{j}\left(\omega - \omega_\mathrm{R}\right) + \dfrac{1}{\tau} + \mathrm{j}\kappa^* \sqrt{\dfrac{2}{\tau_\mathrm{tr}}}}{\mathrm{j}\left(\omega - \omega_\mathrm{R}\right) + \dfrac{1}{\tau}} E_{i1}. \tag{2.42}$$

Finally the drop port power transfer characteristic is obtained by using the equation for power conservation (note, $E_{i2} = 0$):

$$\left|E_{t2}\right|^2 = \left|E_{i1}\right|^2 - \left|E_{t1}\right|^2 = \frac{2}{\tau_{t2}} \left|e\right|^2 = \frac{\dfrac{4}{\tau_{t2}\tau_\mathrm{tr}}}{\left(\omega - \omega_\mathrm{R}\right)^2 + \dfrac{1}{\tau}} \left|E_{i1}\right|^2 \tag{2.43}$$

This equation can be simplified further if both waveguides couple equally to the ring, then $\tau_{t2} = \tau_\mathrm{tr}$.

The Z-Transform

Another approach to simulate ring resonator filters is by using the Z-transformation to describe the spectral and temporal response of ring resonator filters, described in detail in Madsen and Zhao (1999). Z-transform relationships for basic optical elements were first developed for fiber optic filters in Moslehi et al. (1984). This technique is used in pole-zero diagrams to design ring resonator filters in Kaalund and Peng (2004). In the following chapter, the Z-transform for the basic add–drop configuration (consisting of one ring resonator and two waveguides) is given which shall serve as a starting point for the calculation of more complex devices. Z-transforms are discussed extensively in the aforementioned literature on digital signal processing, therefore only a brief introduction is given here.

The Z-transform is an analytic extension of the discrete-time Fourier transform (DTFT) which converts a discrete time signal into a complex-variable frequency signal

$$H\left(z\right) = \sum_{n=-\infty}^{\infty} h\left(n\right) z^{-n}, \tag{2.44}$$

where z is a complex variable and $h(n)$ is the impulse response of a filter or the values of a discrete signal. Each term z^{-n} represents a delay. Of particular interest is when the absolute value of $|z| = 1$. This is called the unit circle in the complex plane where pole and zero locations of the function $H(z)$, which is evaluated along $z = exp(\mathrm{j}\omega)$, are plotted. In the case of ring resonator filters, $|z| = 1$ corresponds to resonant frequencies. A complete roundtrip of the unit circle corresponds to the FSR of the filter. Poles and zeros are related to the filter's frequency spectrum by their position on the complex plane. A zero positioned on the unit circle results in zero transmission at the frequency corresponding to the angle of this zero. A pole on the other hand on

the unit circle causes unity transmission at the corresponding frequency. As poles and zeros move away from the unit circle, their effect on the magnitude spectrum is reduced.

A linear discrete system with input signals x has the following output signal:

$$y(n) = b_0 x(n) + b_1 x(n-1) + \cdots + b_M x(n-M) - a_1 y(n-1), \\ - \cdots - a_N y(n-N). \tag{2.45}$$

The Z-transform for this type of filter is then given by

$$H(z) = \frac{\sum_{m=0}^{M} b_m z^{-m}}{1 + \sum_{n=1}^{N} a_n z^{-n}} = \frac{B(z)}{A(z)}. \tag{2.46}$$

$A(z)$ and $B(z)$ are Mth and Nth-order polynomials. The zeros z_m and poles p_n of $H(z)$ can be derived from the roots of the polynomials as follows:

$$H(z) = \frac{\Gamma z^{N-M} \sum_{m=1}^{M} (z - z_m)}{\sum_{n=1}^{N} (z - p_n)} = \frac{B(z)}{A(z)}, \tag{2.47}$$

where Γ is the gain of the filter. In passive filters, the transfer function can never be greater than 1, so Γ has a maximum value determined by $\max\{|\mathrm{H(z)}|_{\mathrm{z=exp(j\omega)}}\} = 1$ for these types of filters.

A ring resonator has a response which can be expressed in the form

$$H(z) = \sum_{n=0}^{\infty} a^n z^{-n} = \frac{1}{1 - az^{-1}}. \tag{2.48}$$

The basic configuration of an add–drop ring resonator filter (Fig. 2.4) is the simplest filter with a single pole response.

The sum of all optical paths for the drop port is given by

$$E_{t2}(z) = -\kappa_1 \kappa_2 \sqrt{\alpha z^{-1}} \left\{1 + t_1 t_2 \alpha z^{-1} + \cdots\right\} E_{i1}(z). \tag{2.49}$$

Using the Taylor series expansion, the equation can be simplified to give the drop port transfer function:

$$H_{21}(z) = \frac{E_{t2}(z)}{E_{i1}(z)} = \frac{-\kappa_1 \kappa_2 \sqrt{\alpha z^{-1}}}{1 - t_1 t_2 \alpha z^{-1}}. \tag{2.50}$$

There is a single pole at $t_1 t_2 \alpha$. As the matrix is symmetric, the transfer function $H_{21}(z)$ is equal to $H_{12}(z)$.

The sum of all optical paths for the throughput port resulting in its transfer function $H_{11}(z)$ is given by

$$\begin{aligned} E_{t1}(z) &= \left[t_1 - \kappa_1^2 t_2 \alpha z^{-1} \left\{1 + t_1 t_2 \alpha z^{-1} + \cdots\right\}\right] E_{i1}(z) \\ &= \left[t_1 - \frac{\kappa_1^2 t_2 \alpha z^{-1}}{1 - t_1 t_2 \alpha z^{-1}}\right] E_{i1}(z) \\ &= \left[\frac{t_1 - t_2 \alpha z^{-1}}{1 - t_1 t_2 \alpha z^{-1}}\right] E_{i1}(z), \\ \Rightarrow H_{11}(z) &= \frac{E_{t1}(z)}{E_{i1}(z)} = \frac{t_1 - t_2 \alpha z^{-1}}{1 - t_1 t_2 \alpha z^{-1}}. \end{aligned} \tag{2.51}$$

Similarly, the transfer function $H_{22}(z)$ can be derived to be

$$H_{22}(z) = \frac{E_{t2}(z)}{E_{i2}(z)} = \frac{t_2 - t_1 \alpha z^{-1}}{1 - t_1 t_2 \alpha z^{-1}}. \tag{2.52}$$

The obtained results for each transfer function can be expressed in two different matrix forms. The first form relates the input ports to the output ports and is called the scattering matrix (see also (2.1)) which is given by

$$\begin{pmatrix} E_{t1}(z) \\ E_{t2}(z) \end{pmatrix} = S_{\mathrm{RR}}(z) \begin{pmatrix} E_{i1}(z) \\ E_{i2}(z) \end{pmatrix}, \tag{2.53}$$

$$S_{\mathrm{RR}}(z) = \begin{pmatrix} \dfrac{t_1 - t_2 \alpha z^{-1}}{1 - t_1 t_2 \alpha z^{-1}} & \dfrac{-\kappa_1 \kappa_2 \sqrt{\alpha z^{-1}}}{1 - t_1 t_2 \alpha z^{-1}}, \\ \dfrac{-\kappa_1 \kappa_2 \sqrt{\alpha z^{-1}}}{1 - t_1 t_2 \alpha z^{-1}} & \dfrac{t_2 - t_1 \alpha z^{-1}}{1 - t_1 t_2 \alpha z^{-1}} \end{pmatrix}.$$

The second form relates the quantities in one plane to the ones in another plane as can be seen in Fig. 2.6. This type of matrix is called the transfer matrix which is given by

$$\begin{pmatrix} E_{i1}(z) \\ E_{t1}(z) \end{pmatrix} = \Phi_{\mathrm{RR}}(z) \begin{pmatrix} E_{i2}(z) \\ E_{t2}(z) \end{pmatrix}, \tag{2.54}$$

$$\Phi_{\mathrm{RR}}(z) = \frac{1}{-\kappa_1 \kappa_2 \sqrt{\alpha z^{-1}}} \begin{pmatrix} 1 - t_1 t_2 \alpha z^{-1} & -t_2 + t_1 \alpha z^{-1} \\ t_1 - t_2 \alpha z^{-1} & 1 + \kappa_1 \kappa_2 \alpha z^{-1} \end{pmatrix}.$$

The scattering matrix form is used to express the implication of power conservation and reciprocity. The transfer matrix form is used for describing multistage filters. It is therefore also referred to as the chain matrix. This type of transfer matrix is suitable to describe multiple serially coupled ring resonators. The transfer matrix to be used for describing multiple parallel coupled resonators has the form (Grover et al. 2002)

$$\begin{pmatrix} E_{i1}(z) \\ E_{t2}(z) \end{pmatrix} = \Phi'_{\mathrm{RR}}(z) \begin{pmatrix} E_{t1}(z) \\ E_{i2}(z) \end{pmatrix}, \tag{2.55}$$

$$\Phi'_{\mathrm{RR}}(z) = \frac{1}{t_1 - t_2 \alpha z^{-1}} \begin{pmatrix} 1 - t_1 t_2 \alpha z^{-1} & \kappa_1 \kappa_2 \sqrt{\alpha z^{-1}} \\ -\kappa_1 \kappa_2 \sqrt{\alpha z^{-1}} & t_1 t_2 - \alpha z^{-1} \end{pmatrix}.$$

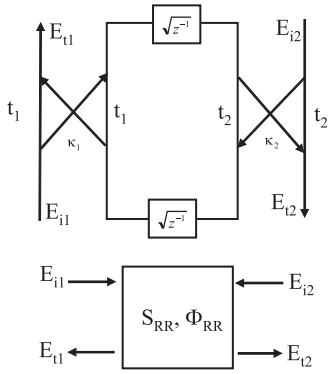

Fig. 2.6. Z-transform layout of an add–drop ring resonator filter

Using the different simulation techniques described in this chapter it is possible to build a simulation model for all relevant lateral and vertically coupled ring resonator filter configurations.

Incorporating Loss in Ring Resonator Filters

In the previous simulation models, loss is basically included by insertion of the parameter α in the formulas. Loss in ring resonator filters scales the spectral curves without changing them significantly if the loss is not too large. Different types of losses have been considered and described in literature to account for various fabrication methods and tolerances. A few examples will be given in the following paragraph to give a starting point for the calculation and simulation of losses in ring resonators.

A loss which is most obvious is the radiation loss which occurs in the curved section of ring resonators (Chin and Ho 1998). The radiation loss will become large for a large surface roughness. The surface roughness on the other hand can induce contradirectional coupling which can degrade the performance of a ring resonator filter and can even cause a splitting of the resonant peak (Little et al. 1997a). The calculation of the radiation and scattering losses in ring resonators is presented in detail in Rabiei (2005). Here a perturbative method for the calculation of losses due to an arbitrary variation in the refractive index of the core or due to an arbitrary variation in the shape of ring resonator is described.

Loss in ring resonator devices can also be used advantageously as was demonstrated using (2.16). An analysis of how loss and gain can be used to tune, trim, or compensate the wavelength response of ring resonator filters is described in Little and Chu (2000).

In the following chapter the basic model of a ring resonator is extended to analyze a racetrack shaped ring resonator.

2.1.2 Racetrack-Shaped Resonators

The equations in the previous chapter described the general behavior of a basic ring resonator filter. However to simulate certain ring resonator configurations, this set of equations has to be extended. In a waveguide-coupled ring resonator filter, the coupling gap size is determined by the amount of coupling required and the coupling length available. Using lateral coupling, a larger gap is desirable as it increases the fabrication tolerance. In this case, for a given coupling coefficient, the gap size can be enlarged if the coupling distance is increased to obtain a racetrack-shaped ring resonator (Fig. 2.7).

The coupling distance can be increased by using a lateral or vertical geometry (Chin and Ho 1998). In the case of the racetrack shaped ring resonator, the coupling distance is approximately the length of the straight sections (if no coupling occurs before the actual coupler region starts), which are tangential to the circular arcs at output and input ports. At the transitions between the curved and the straight sections, the mode will change adiabatically between the radial mode in a curved waveguide and the normal mode in a straight waveguide. As the straight sections are lengthened the radius of the curved sections must be reduced if the total cavity length is to remain constant. This cannot always be achieved in practical applications.

In the case of racetrack resonators, it is important to consider the variation of phase difference φ which occurs in the coupling region in both couplers between t and κ. The phase difference is length-dependent and affects the output characteristics, not only in the magnitude but also in the resonant conditions. This phase difference can be implemented in (2.13) and (2.14) using the method described in Lee et al. (2004).

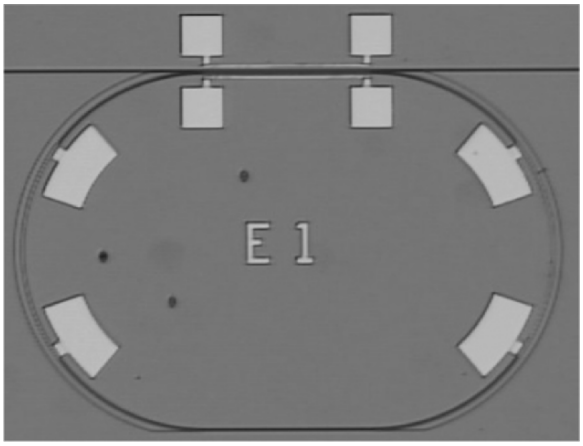

Fig. 2.7. A racetrack-shaped ring resonator filter with integrated platinum resistors on top of the curved sections and the coupler (contact pads visible)

For the throughput port:

$$E_{t1} = \frac{t_1 \mathrm{e}^{\mathrm{j}\varphi_{t1}} - t_2^* \alpha_{1/2}^2 \mathrm{e}^{\mathrm{j}\theta} \left(t_1 t_1^* \mathrm{e}^{\mathrm{j}2\varphi_{t1}} - \kappa_1 \kappa_1^* \mathrm{e}^{-\mathrm{j}2\varphi_{\kappa 2}} \right) \mathrm{e}^{\mathrm{j}\varphi_{t2}}}{1 - t_1^* t_2^* \alpha_{1/2}^2 \mathrm{e}^{\mathrm{j}\theta} \mathrm{e}^{\mathrm{j}\varphi_{t1}} \mathrm{e}^{\mathrm{j}\varphi_{t2}}}. \tag{2.56}$$

For the drop port

$$E_{t2} = \frac{-\kappa_1^* \kappa_2 \alpha_{1/2} \mathrm{e}^{\mathrm{j}\theta_{1/2}} \mathrm{e}^{-\mathrm{j}\varphi_{\kappa 1}} \mathrm{e}^{-\mathrm{j}\varphi_{\kappa 2}}}{1 - t_1^* t_2^* \alpha \mathrm{e}^{\mathrm{j}\theta} \mathrm{e}^{\mathrm{j}\varphi_{t1}} \mathrm{e}^{\mathrm{j}\varphi_{t2}}}. \tag{2.57}$$

The resonant condition $(\theta + \varphi_{t1} + \varphi_{t2}) = 2\pi m$ has changed slightly compared to (2.9). The output transmission at resonance is no longer independent of t and κ which can be seen comparing the relevant terms in (2.50) and (2.51). This leads to a significant performance change and confirms the importance of taking into account the phase difference when analyzing racetrack shaped ring resonator configurations. The phase difference is not only of importance in directional couplers, but also in MMI couplers. An analysis of a racetrack shaped ring resonator add–drop filter having two MMI couplers is given in Caruso and Montrosset (2003). The MMI length should be selected in order to satisfy the $\pi/2$ relation between the phases of the transmission and the coupling terms to obtain a symmetric transmission characteristic of the throughput and of the drop port. If the $\pi/2$ relation is not satisfied, a strong asymmetry in the transmission characteristic will be obtained.

A further description of the implementation of directional and MMI couplers in ring resonators is given in Sect. 4.1.

2.2 Double Ring Resonators

Double ring resonators offer the possibility of realizing a "box-like" filter characteristic which is favorably used in optical networks. This is not the only advantage, but also from the point of characterization, two rings if coupled in series have the drop port in the same direction as the input port, which is also convenient for interconnection of many 2×2 devices. Serially and parallel coupled ring resonator configurations have been described in detail in Chu et al. (1999a); Little et al. (1997b, 2000a); Melloni (2001) and Emelett and Soref (2005).

In the serially coupled configuration, each ring resonator is coupled to one another, and a signal that is to be dropped from the input port to the drop port must pass sequentially through each resonator. Because of this sequential power transfer, all resonators must be precisely resonant at a common wavelength. The resulting resonant line shape in the series configuration is determined physically by the separations between the ring resonators. In the parallel-coupled configuration, all resonators are coupled to both the input and drop port waveguides, but usually not directly to one another (the resonators can also be coupled to one another resulting in a wavelength selective

reflector as is described in Sects. 2.2.2 and 2.3.1). The resonators are instead indirectly coupled to each other by the optical path lengths along the input and output waveguides that interconnect them. These lengths determine the details of the resonant line shapes. An optical signal in the parallel configuration passes through all ring resonators simultaneously. This softens the requirement that the resonances of each ring have to be precisely identical. Nonaligned resonant frequencies instead lead to multiple peaks, or ripple in the lineshape.

The ready to use transfer functions of serially and parallel coupled double ring resonators will be described in the following sections.

2.2.1 Serially Coupled Double Ring Resonator

The schematic of a serially coupled double ring resonator is depicted in Fig. 2.8.

From this model and using the same procedure as in Sect. 2.1.1 the fields depicted in Fig. 2.8 can be calculated as follows:

$$E_{1a} = -\kappa_1^* E_{i1} + t_1^* \alpha_1 \mathrm{e}^{\mathrm{j}\frac{\theta_1}{2}} E_{1b}, \tag{2.58}$$

$$E_{1b} = t_2^* \alpha_1 \mathrm{e}^{\mathrm{j}\frac{\theta_1}{2}} E_{1a} - \kappa_2^* \alpha_2 \mathrm{e}^{\mathrm{j}\frac{\theta_1}{2}} E_{2b}, \tag{2.59}$$

$$E_{2a} = \kappa_2 \alpha_1 \mathrm{e}^{\mathrm{j}\frac{\theta_2}{2}} E_{1a} + t_2 \alpha_2 \mathrm{e}^{\mathrm{j}\frac{\theta_2}{2}} E_{2b}, \tag{2.60}$$

$$E_{2b} = -\kappa_3^* E_{i2} + t_3^* \alpha_2 \mathrm{e}^{\mathrm{j}\frac{\theta_2}{2}} E_{2a} \tag{2.61}$$

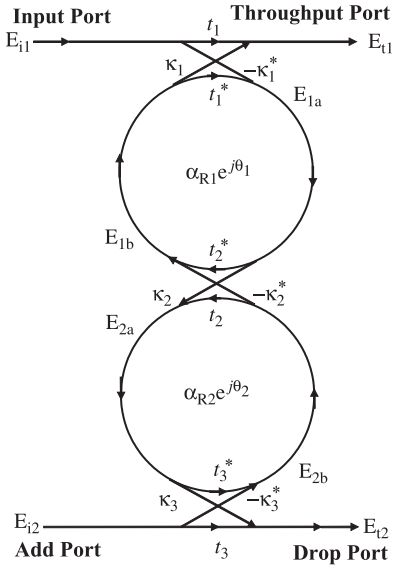

Fig. 2.8. Two ring resonators coupled in series

$$E_{t1} = t_1 E_{i1} + \kappa_1 \alpha_1 \mathrm{e}^{\mathrm{j}\frac{\theta_1}{2}} E_{1b}, \tag{2.62}$$

$$E_{t2} = t_3 E_{i2} + \kappa_3 \alpha_2 \mathrm{e}^{\mathrm{j}\frac{\theta_2}{2}} E_{2a}, \tag{2.63}$$

where $\alpha_{1,2} = \alpha_{\mathrm{R1}_{1/2},R2_{1/2}}$ represent the half round trip loss coefficients of ring resonator one and two respectively. From (2.58) to (2.63) the general expressions for the transfer functions for the throughput and the drop port can be derived. A simplified form can be obtained by assuming a coupler without losses and symmetric coupling behavior, setting $t = t^*$ and $\kappa = -\kappa^*$ (note that the phase factor $-\mathrm{j}$ has not been introduced into the assumption and can be added if required) which gives the ready to use amplitude forms for the throughput port ($E_{i2} = 0$)

$$\frac{E_{t1}}{E_{i1}} = \frac{-t_1 \kappa_1^2 \alpha_1 \mathrm{e}^{\mathrm{j}\theta_1} \left(t_3 \alpha_2 \mathrm{e}^{\mathrm{j}\theta_2} - t_2\right)}{1 - t_3 t_2 \alpha_2 \mathrm{e}^{\mathrm{j}\theta_2} - t_2 t_1 \alpha_1 \mathrm{e}^{\mathrm{j}\theta_1} + t_3 t_1 \alpha_1 \alpha_2 \mathrm{e}^{\mathrm{j}\theta_1} \mathrm{e}^{\mathrm{j}\theta_2}} \tag{2.64}$$

and for the drop port:

$$\frac{E_{t2}}{E_{i1}} = \frac{\kappa_3 \kappa_2 \kappa_1 \alpha_1 \alpha_2 \mathrm{e}^{\mathrm{j}\frac{\theta_1}{2}} \mathrm{e}^{\mathrm{j}\frac{\theta_2}{2}}}{1 - t_3 t_2 \alpha_2 \mathrm{e}^{\mathrm{j}\theta_2} - t_2 t_1 \alpha_1 \mathrm{e}^{\mathrm{j}\theta_1} + t_3 t_1 \alpha_1 \alpha_2 \mathrm{e}^{\mathrm{j}\theta_1} \mathrm{e}^{\mathrm{j}\theta_2}}. \tag{2.65}$$

For realizing a double ring resonator with maximally flat response, first the input/output waveguide ring coupling coefficient $\kappa_1(\kappa_3)$ has to be determined. To simplify the model further, it is defined that the input/output waveguide-ring coupling coefficients $\kappa_1 = \kappa_3$. The calculation of the coupling coefficients to obtain the appropriate coupling values between the two ring resonators in order to achieve maximally flat response can be made according to Emelett and Soref (2005), Little et al. (1997b) by using the geometry and index profile shown in Fig. 2.9, where two coupled waveguides of width $2w_p$ and $2w_q$ with indexes of n_p and n_q, surrounded by a cladding of n_0, at the plane of smallest separation $2s_0$, defined as the center to center gap are shown.

The approximate coupling coefficient is then given by

$$\kappa = \frac{\omega \varepsilon_0 \cos\left(k_{x_{p,q}} w_q\right)}{2\sqrt{P_p P_q}\left(k_{x_p}^2 + \alpha_q^2\right)} \left(n_p^2 - n_0^2\right) \sqrt{\frac{\pi R}{\alpha_q}} \mathrm{e}^{[\alpha_q (w_q - 2s_0)]} \times \left\{\alpha_q \cos\left(k_{x_p} w_p\right) \sinh\left(\alpha_q w_p\right) + k_{x_p} \sin\left(k_{x_p} w_p\right) \cosh\left(\alpha_q w_p\right)\right\}. \tag{2.66}$$

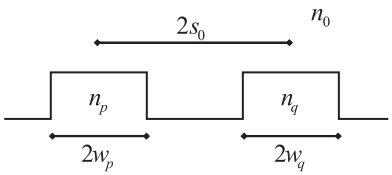

Fig. 2.9. Index profile and geometry of coupled waveguides

Using

$$P_{p,q} = \frac{\beta_{p,q}}{2\omega\mu_0}\left(w_{p,q} + \frac{1}{\alpha_{p,q}}\right), \tag{2.67}$$

$$k_{x_{p,q}} = \sqrt{n_{p,q}^2 k^2 - \beta_{p,q}^2}, \tag{2.68}$$

$$\alpha_{p,q} = \sqrt{\beta_{p,q}^2 - n_0^2 k^2}, \tag{2.69}$$

where $P_{p,q}$ is the mode power, $k_{x_{p,q}}$ is the transverse propagation constant of the core, and $\alpha_{p,q}$ is the decay constant in the cladding, $\beta_{p,q}$ is the propagation constant, ω is the circular frequency, ε_0 is the permittivity of free space, all within waveguide p or q. The refractive index n_0 of the surrounding media is set equal to 1 (air). The coefficient R is defined as the effective radius of curvature of the ring and is given by:

$$R = \frac{r_1 r_2}{r_1 + r_2}, \tag{2.70}$$

where $r_{1,2}$ represents the radius of ring one and two respectively. The radii of the rings are chosen to satisfy the 2π phase shift condition with the completion of one round trip in the ring resonator which is given by:

$$m\lambda_m = 2\pi r_{1,2} n_{\text{eff}}. \tag{2.71}$$

In order to realize a flat passband, the analysis of the power loss ratio, which is the ratio of total input power to power present at the detected port, is required. The power loss ratio in polynomial form is given by

$$P_{LR} = \left|\frac{E_i}{E_{t2}}\right|^2 = 1 + \frac{1}{\mu_1^4 \mu_2^4}\left[\Delta\omega^4 + \left(\frac{\mu_1^4}{2} - 2\mu_2^2\right)\Delta\omega^2 + \left(\mu_2^2 - \frac{\mu_1^4}{4}\right)^2\right], \tag{2.72}$$

where $\Delta\omega$ is the frequency deviation which is related to the resonant frequency ω_m by

$$\Delta\omega = \omega - \omega_m. \tag{2.73}$$

The coefficient μ is the fractional power coupled. It is given by

$$\mu_1^2 = \frac{\kappa_1^2 v_{g1}}{2\pi r_1} \text{ and } \mu_2^2 = \frac{\kappa_2^2 v_{g1} v_{g2}}{4\pi^2 r_1 r_2}. \tag{2.74}$$

The goal of realizing a maximally flat response is obtained when the power loss ratio is zero at the defined resonance. This is the case for

$$\mu_2^2 = 0.250\mu_1^4. \tag{2.75}$$

Assuming identical rings, this leads to the coupling coefficient

$$\kappa_2^2 = 0.250\kappa_1^4. \tag{2.76}$$

Using these equations, it is possible to design a double ring resonator filter with maximally flat response for the drop port.

A serially coupled double ring resonator opens up the possibility of expanding the FSR to the least common multiple of the FSR of individual ring resonators. This is done by choosing different radii in the double ring resonator. In the case of different radii, the light passing through the double ring resonator is launched from the drop port when the resonant conditions of both single ring resonators are satisfied. The FSR of the double ring resonator with two different radii is expressed by

$$\mathrm{FSR} = \mathrm{N} \cdot \mathrm{FSR}_1 = \mathrm{M} \cdot \mathrm{FSR}_2, \tag{2.77}$$

which leads to

$$\mathrm{FSR} = |\mathrm{M} - \mathrm{N}| \, \frac{\mathrm{FSR}_1 \cdot \mathrm{FSR}_2}{|\mathrm{FSR}_1 - \mathrm{FSR}_2|}, \tag{2.78}$$

where N and M are natural and coprime numbers.

The use of two ring resonators with different radii opens the possibility to realize a larger FSR than would be achieved using only a single ring resonator. The transmission characteristic of the throughput port has mainly a Lorentzian shape. A box-like filter response using two different radii can only be realized by using two parallel coupled double ring resonators ($R_1 \neq R_2$). The use of such configurations as optical filters is limited by unwanted additional resonant peaks. Investigations on these types of filters have been performed in Suzuki et al. (1995), Sorel et al. (1999). Different types of waveguide coupled ring resonator configurations to expand the free spectral range have been analyzed in Hidayat et al. (2003).

2.2.2 Parallel Coupled Double Ring Resonator

The schematic of a parallel coupled double ring resonator is shown in Fig. 2.10.

From this model, the fields in Fig. 2.10 can be calculated as follows:

$$E_{1a} = -\kappa_1^* E_{i1} + t_1^* \alpha_1 \mathrm{e}^{\mathrm{j}\frac{\theta_1}{2}} E_{1b}, \tag{2.79}$$

$$E_{1b} = t_2^* \alpha_1 \mathrm{e}^{\mathrm{j}\frac{\theta_1}{2}} E_{1a} - \kappa_2^* \mathrm{e}^{\mathrm{j}\theta_W} \left(\kappa_4 \alpha_2 \mathrm{e}^{\mathrm{j}\frac{\theta_2}{2}} E_{2a} - t_4 E_{i2} \right), \tag{2.80}$$

$$E_{2a} = -\kappa_3^* \mathrm{e}^{\mathrm{j}\theta_W} \left(t_1 E_{i1} + \kappa_1 \alpha_1 \mathrm{e}^{\mathrm{j}\frac{\theta_1}{2}} E_{1b} \right) + t_3^* \alpha_2 \mathrm{e}^{\mathrm{j}\frac{\theta_2}{2}} E_{2b}, \tag{2.81}$$

$$E_{2b} = -\kappa_4^* E_{i2} + t_4^* \alpha_2 \mathrm{e}^{\mathrm{j}\frac{\theta_2}{2}} E_{2a}, \tag{2.82}$$

$$E_{t1} = t_3 \mathrm{e}^{\mathrm{j}\theta_W} \left(t_1 E_{i1} + \kappa_1 \alpha_1 \mathrm{e}^{\mathrm{j}\frac{\theta_1}{2}} E_{1b} \right) + \kappa_3 \alpha_2 \mathrm{e}^{\mathrm{j}\frac{\theta_2}{2}} E_{2b}, \tag{2.83}$$

$$E_{t2} = t_2 \mathrm{e}^{\mathrm{j}\theta_W} \left(t_4 E_{i2} + \kappa_4 \alpha_2 \mathrm{e}^{\mathrm{j}\frac{\theta_2}{2}} E_{2a} \right) + \kappa_2 \alpha_1 \mathrm{e}^{\mathrm{j}\frac{\theta_1}{2}} E_{1a} \tag{2.84}$$

$$\theta_W = k_W \cdot n_{\mathrm{Weff}} \cdot \Lambda, \tag{2.85}$$

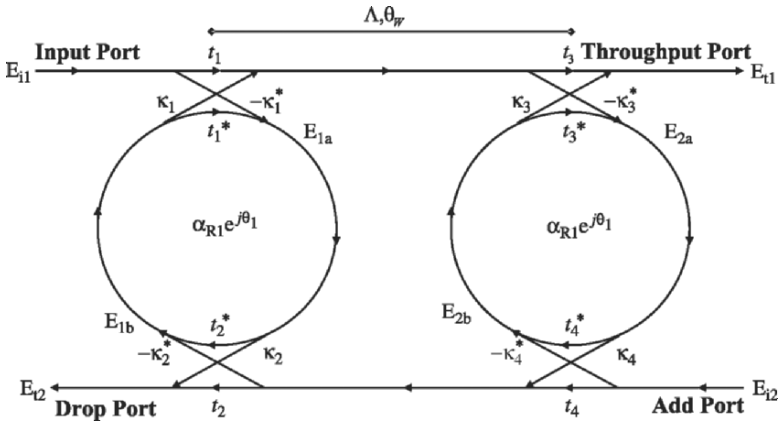

Fig. 2.10. Parallel coupled double ring resonator

where θ_{W} is the phase shift introduced by the segment of length Λ with effective refractive index n_{Weff} of the input waveguide joining both ring resonators.

From (2.79) to (2.85) the general expressions for the transfer functions for the throughput and the drop port can be derived. A simplified form can again be obtained by assuming couplers and bus waveguides without losses and symmetric coupling behavior, setting $t = t^*$ and $\kappa = -\kappa^*$ (note that the phase factor $-\mathrm{j}$ has not been introduced into the assumption and can be added if required) which gives the amplitude forms for the throughput port ($E_{i2} = 0$)

$$\frac{E_{t1}}{E_{i1}} = t_3 t_1 \mathrm{e}^{\mathrm{j}\theta_W} + t_3 \kappa_1 \alpha_1 \mathrm{e}^{\mathrm{j}\theta_W \frac{\theta_1}{2}} \left[h + \frac{f\,(a+bc)}{1-d} \right] + \kappa_3 t_4 \alpha_2^2 \mathrm{e}^{\mathrm{j}\theta_2} \frac{a+bc}{1-d}. \quad (2.86)$$

And for the drop port

$$\frac{E_{t2}}{E_{i1}} = \kappa_1 \kappa_2 \alpha_1 \mathrm{e}^{\mathrm{j}\frac{\theta_1}{2}} + \kappa_2 t_1 \alpha_1^2 \mathrm{e}^{\mathrm{j}\theta_1} \left[h + \frac{f\,(a+bc)}{1-d} \right] + t_2 \kappa_4 \alpha_2 \mathrm{e}^{\mathrm{j}\theta_W \frac{\theta_2}{2}} \frac{a+bc}{1-d}, \quad (2.87)$$

where

$$a = \frac{\kappa_3 t_1 \mathrm{e}^{\mathrm{j}\theta_W}}{1 - t_3 t_4 \alpha_2^2 \mathrm{e}^{\mathrm{j}\theta_2}}, \quad (2.88)$$

$$b = \frac{\kappa_1 \alpha_1 \mathrm{e}^{\mathrm{j}\frac{\theta_1}{2}}}{1 - t_3 t_4 \alpha_2^2 \mathrm{e}^{\mathrm{j}\theta_2}}, \quad (2.89)$$

$$c = \frac{\kappa_1 t_2 \alpha_1 \mathrm{e}^{\mathrm{j}\frac{\theta_1}{2}}}{1 - t_1 t_2 \alpha_1^2 \mathrm{e}^{\mathrm{j}\theta_1}} \quad (2.90)$$

$$f = \frac{\kappa_2 \kappa_4 \alpha_2 \mathrm{e}^{\mathrm{j}\theta_W \frac{\theta_2}{2}}}{1 - t_1 t_2 \alpha_1^2 \mathrm{e}^{\mathrm{j}\theta_1}}, \tag{2.91}$$

$$h = \frac{\kappa_1 t_2 \alpha_1 \mathrm{e}^{\mathrm{j}\frac{\theta_1}{2}}}{1 - t_1 t_2 \alpha_1^2 \mathrm{e}^{\mathrm{j}\theta_1}}. \tag{2.92}$$

$$d = b \cdot f \tag{2.93}$$

Similar to the serially coupled double ring resonator, it is possible to increase the overall FSR of this configuration by adjusting the length of the waveguide joining the two ring resonators.

The parallel configuration can be treated as a grating. Constructive interference of the reflected waves from each ring resonator is obtained by choosing Λ to be equal to an odd multiple of a quarter wavelength.

$$\Lambda = (2m + 1)\, \frac{\lambda_0}{4 n_{\mathrm{Weff}}}, \tag{2.94}$$

where λ_0 is the center wavelength of the passband.

If the length Λ is chosen such that the FSR of the ring resonators and the FSR of the "grating" obey the following condition:

$$\mathrm{FSR} = \mathrm{N_{Ring}} \cdot \mathrm{FSR_{Ring}} = \mathrm{M_{Grating}} \cdot \mathrm{FSR_{Grating}}. \tag{2.95}$$

The Vernier effect (Griffel 2000b) causes the transmission peaks of the ring resonators within the overall obtained FSR to be suppressed, which results in a larger FSR than would be achieved for a single ring resonator. The distance between the resonators can be calculated in this case using:

$$\Lambda = \frac{M_{grating} n_{\mathrm{eff}}}{N_{\mathrm{Ring}} n_{\mathrm{Weff}}} \pi r. \tag{2.96}$$

These set of equations can of course be transferred to multiple coupled parallel ring resonator configurations as will be shown in Sect. 2.3.

Parallel Coupled Double Ring Resonator with Coupling Between the Two Ring Resonators

A special double ring resonator configuration is obtained, when coupling between the two ring resonators is allowed (Fig. 2.11). The reflective properties of such a device have been analyzed in Chremmos and Uzunoglu (2005) and the following transfer functions are based on this reference. A similar wavelength reflective filter consisting of four interacting ring resonators has been presented in Poon, Scheuer, Yariv (2004e) which is going to be described in Sect. 2.3.1.

Using the fields and coupling coefficient in Fig. 2.11, it is possible to derive the general expressions for describing the transfer characteristics of this type of configuration.

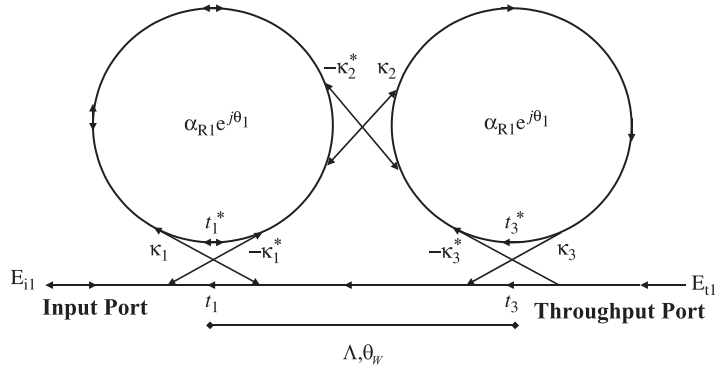

Fig. 2.11. Double ring resonator with inter ring coupling

A simplified expression for the reflectivity at port E_{i1} (denoted by the symbol $\leftarrow$ as the superscript) is obtained for the lossless case and symmetric coupling coefficients between the ring resonator and the bus waveguide ($\kappa = \kappa_1 = \kappa_3$):

$$\left|\overleftarrow{E}_{i1}\right|^2 = \frac{4\left(\frac{\kappa_2\kappa^2}{2t}\right)^2\left(\cos\theta - \frac{t_2\left(1+t^2\right)}{2t}\right)^2}{\left[\left(\cos\theta - \frac{t_2\left(1+t^2\right)}{2t}\right)^2 + \left(\frac{\kappa_2\kappa^2}{2t}\right)^2\right]^2}. \tag{2.97}$$

The phase factor for the distance Λ between the rings does not appear and therefore does not have an influence on the transfer characteristic. This is a special property of the double coupled configuration and does not apply for multiple serially coupled ring resonators. Different reflectivity profiles can be realized using appropriate coupling coefficients. Weakly coupled ring resonators lead to single reflection peaks in the reflectivity function where the height of the peak depend on the value of the coupling coefficients. In order to realize a maximally flat response with a single peak, the coupling coefficients have to obey the following equation:

$$\kappa_2 = \frac{\kappa^2}{\sqrt{2}\left(1+t^2+\sqrt{2}t\right)}. \tag{2.98}$$

The corresponding FWHM is given by

$$\mathrm{FWHM} = 4\sin^{-1}\left(\kappa\sqrt{\frac{\kappa_2}{2^{\frac{3}{2}}t}}\right). \tag{2.99}$$

The expression for the reflectivity at port E_{i1} incorporating loss parameter α is given by

$$\left|\overleftarrow{E}_{i1}\right|^2 = \frac{\left(\dfrac{\kappa_2\kappa^2\left(\alpha^2+1\right)}{2\alpha t}\right)^2}{\left[\left(\cos\theta - \dfrac{t_2\left(1+\alpha^2t^2\right)}{2\alpha t}\right)^2 + \left(\dfrac{\kappa_2\left(1-\alpha^2t^2\right)^2}{2\alpha t}\right)^2\right]^2} \times \left[\begin{array}{l}\left(\cos\theta - \dfrac{t_2\left(1+\alpha^2t^2\right)}{2\alpha t} + \dfrac{t_2}{2\alpha t}\dfrac{\left(1-\alpha^2\right)\left(1-\alpha^2t^2\right)}{1+\alpha^2}\right)^2 \\ + \left(\dfrac{1-\alpha^2}{1+\alpha^2}\right)\sin^2\theta\end{array}\right]. \tag{2.100}$$

So far ready to use transfer functions for single and double ring resonator configuration have been presented. In the following chapter, different calculation methods are presented to derive the transfer function of different types of multiple coupled ring resonators.

2.3 Multiple Coupled Resonators

The use of multiple vertical or lateral coupled ring resonator configurations opens up the possibility to realize custom designed transmission functions and thus is suitable for a wide variety of device implementations (Schwelb and Frigyes 2001). Vertical and lateral ring resonator architectures where the rings are either coupled in series or in parallel have been implemented in the past. A detailed theoretical analysis of a vertically stacked multiple coupled ring resonator, where the ring resonators are on top of each other is presented in Sumetsky (2005). The use of multiple coupled ring resonator configurations together with other photonic devices like grating couplers or Mach–Zehnder interferometers increases the functionality and transmission characteristic even further (Weiershausen and Zengerle 1996). One of the main targets of realizing optical filters is to tailor the passband shape. In analogy to electronic filter design, Butterworth (1930) and Chebyshev type of optical filters are preferred. Butterworth filters are maximally flat and do not have any ripples in the passband. The shape of the transfer function does not change for higher order filters except that the roll off becomes steeper as the order of the filter increases. Chebyshev filters have a steeper roll off than Butterworth type of filters and have ripples either in the passband or stopband which distinguishes Chebyshev type I and type II filters. The square magnitude response of a Butterworth filter has the form (Madsen and Zhao 1999)

$$\left|H_N\left(x\right)\right|^2 = \frac{1}{1+\left(\dfrac{x}{x_0}\right)^{2N}}, \tag{2.101}$$

where x_0 is the 3 dB cutoff frequency.

The response of Chebyshev type I and II filters have the form (Madsen and Zhao 1999)

$$\text{Type I}$$

$$|H_N(x)|^2 = \frac{1}{1 + y^2 T_N^2\left(\dfrac{x}{x_C}\right)} \tag{2.102}$$

$$T_N(x) = \begin{cases} \cos\left(N\cos^{-1}x\right) & \text{for} \quad |x| \le 1 \\ \cosh\left(N\cosh^{-1}x\right) & \text{for} \quad |x| > 1 \end{cases},$$

$$\text{Type II}$$

$$|H_N(x)|^2 = \frac{1}{1 + y^2\left[\dfrac{T_N^2\left(\dfrac{x_S}{x_P}\right)}{T_N^2\left(\dfrac{x_S}{x}\right)}\right]}, \tag{2.103}$$

where $T_N(x)$ is the Nth-order Chebyshev polynomial, y determines the passband ripples, x_C is the center frequency of the filter, x_P and x_S define the changeover region on the passband and stopband, respectively.

2.3.1 Serially Coupled Ring Resonators

One of the first papers to present a calculation method for serially coupled ring resonator synthesis is Orta et al. (1995). The method is based on the Z-transformation using the transfer matrix (see (2.54)). The Z-transformation has also been used in Madsen and Zhao (1996) to simulate and fabricate a serially coupled ring resonator filter. The transfer matrix method has also been used in Melloni and Martinelli (2002) and Poon et al. (2004c) for simulating and designing various serially coupled ring resonator configurations. Serially coupled ring resonators are also referred to as coupled-resonator optical waveguides (CROW) Poon et al. (2004d). A model for deriving the transfer functions of serially coupled ring resonators based on the time-dependent calculation as described in Sect. 2.1.1 is presented in Little et al. (1998b). Another method of simulating the transfer function of serially coupled ring resonators is by using a characteristic matrix approach presented in Chen et al. (2004a). These different methods for analyzing serially coupled ring resonators (Fig. 2.12) will be used in the following to derive the transfer functions.

The Z-transformation is used to start with in the beginning. In order to describe a serially coupled ring resonator, the filter can be broken down into two components, a symmetrical directional coupler and a pair of uncoupled guides as shown in Fig. 2.13 (Orta et al. 1995). Another way to describe the transfer function of a directional coupler is to use a chain matrix, which is given by

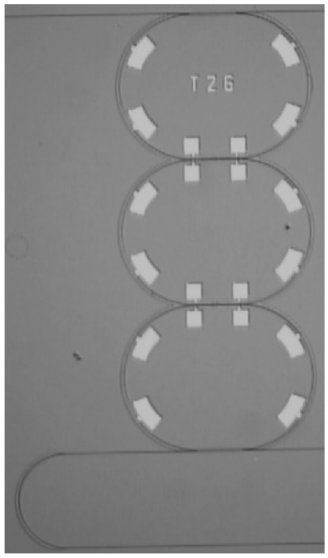

Fig. 2.12. Photograph of a serially coupled triple ring resonator

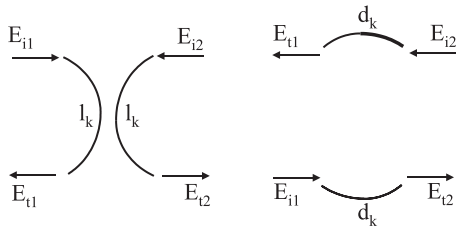

Fig. 2.13. Components of a serially coupled ring resonator filter

$$H_k^C = \mathrm{j}\mathrm{e}^{\mathrm{j}\beta l_k} \begin{bmatrix} \csc(\phi_k) & -\mathrm{e}^{-\mathrm{j}\beta l_k}\cot(\phi_k) \\ \mathrm{e}^{-\mathrm{j}\beta l_k}\cot(\phi_k) & -\mathrm{e}^{-2\mathrm{j}\beta l_k}\csc(\phi_k) \end{bmatrix}, \tag{2.104}$$

where ϕ_k is referred to as the coupling angle and l_k is the length of the coupler (note: this is not the coupling length). The chain matrix of the uncoupled guides is given by

$$H_k^R = \mathrm{e}^{\mathrm{j}\beta d_k} \begin{bmatrix} 1 & 0 \\ 0 & \mathrm{e}^{-2\mathrm{j}\beta d_k} \end{bmatrix}, \tag{2.105}$$

where d_k is the length of the ring waveguides. The chain matrix for the entire system is then expressed by

$$H = \prod_{k=N,1} \begin{bmatrix} \csc(\phi_k) & z^{-1}\mathrm{e}^{-\mathrm{j}\psi_k}\cot(\phi_k) \\ \cot(\phi_k) & z^{-1}\mathrm{e}^{-\mathrm{j}\psi_k}\csc(\phi_k) \end{bmatrix} \begin{bmatrix} \csc(\phi_0) & \cot(\phi_0) \\ \cot(\phi_0) & \csc(\phi_0) \end{bmatrix}, \tag{2.106}$$

where

$$z\mathrm{e}^{\mathrm{j}\psi_k} = -\mathrm{e}^{\mathrm{j}\beta(l_k+l_{k-1}+2d_k)}. \tag{2.107}$$

As previously described in Sect. 2.1.1 the elements of the matrix H are N degree polynomials. The chain matrix can also be compared to the chain matrix derived in (2.54). Of interest is again the transfer function for the throughput and the drop port, both related to the signal at the input port. The polynomials are given by

$$\frac{E_{t1}}{E_{i1}} = H_{11}(z) = \sum_{k=0}^{N} a_k z^{-k} \tag{2.108}$$

and

$$\frac{E_{t2}}{E_{i1}} = H_{21}(z) = \sum_{k=0}^{N} b_k z^{-k}. \tag{2.109}$$

The transfer functions of the filter are now based on the definition of these polynomials. Assuming, that the filter is lossless, the scattering matrix is unitary for $|z| = 1$. On $|z| = 1, z^* = z^{-1}$, then the relationship between (2.108) and (2.109) can be written as follows:

$$H_{11}(z)\, H_{11}^*\left(\frac{1}{z^*}\right) = 1 + H_{21}(z)\, H_{21}^*\left(\frac{1}{z^*}\right). \tag{2.110}$$

Using this equation, it is possible to calculate $H_{11}(z)$ for a given $H_{21}(z)$. The coupling angles $\phi_k\,(k = 0 \ldots N)$ and the phase shift $\psi_k\,(k = 1 \ldots N)$ are calculated as follows. First, a superscript is introduced which denotes elements belonging to the structure formed by the first $n+1$ coupler. Then the elements of the chain matrix relative to the first $(N-1)$ ring resonators, $H_{11}^{[N-1]}$ and $H_{21}^{[N-1]}$ are related to $H_{11}^{[N]}$ and $H_{21}^{[N]}$ through

$$\begin{bmatrix} \csc(\phi_N) & z^{-1}\mathrm{e}^{-\mathrm{j}\psi_N}\cot(\phi_N) \\ \cot(\phi_N) & z^{-1}\mathrm{e}^{-\mathrm{j}\psi_N}\csc(\phi_N) \end{bmatrix} \begin{bmatrix} H_{11}^{[N-1]} \\ H_{21}^{[N-1]} \end{bmatrix} = \begin{bmatrix} H_{11}^{[N]} \\ H_{21}^{[N]} \end{bmatrix}. \tag{2.111}$$

This leads to the equations for the coefficients of the polynomials (2.108) and (2.109), which are given by

$$a_k^{[N-1]} = a_k^{[N]} \csc(\phi_N) - b_k^{[N]} \cot(\phi_N) \tag{2.112}$$

and

$$b_k^{[N-1]} = \left[-a_{k+1}^{[N]} \cot(\phi_N) + b_{k+1}^{[N]} \csc(\phi_N)\right] \mathrm{e}^{\mathrm{j}\psi_N}, \tag{2.113}$$

where $k = 1 \ldots (N-1)$ and

$$a_N^{[N-1]} = b_{-1}^{[N-1]} = 0. \tag{2.114}$$

Then the coupling angle of the Nth coupler is given by

$$\cos(\phi_N) = \frac{b_0^{[N]}}{a_0^{[N]}} = \frac{a_N^{[N]}}{b_N^{[N]}}. \tag{2.115}$$

Equation (2.115) is satisfied if the ratio is real. Next step is to determine the phase shift ψ_k using (2.115) and (2.113). All other coefficients follow the same procedure.

In order to start this calculation method and derive a transfer filter characteristic, the polynomial $H_{21}^{[N]}$ has to be determined. As stated before in Sect. 2.3, a bandpass filter characteristic is preferred. When using the Z-transform, the resonant frequencies of the ring resonator filter are all placed on the circumference $|z| = 1$. For a Butterworth type filter, the "zeros" are located on $z = -1$. The zeros for a Chebyshev type of filter are given by

$$\begin{aligned} z_{0k} &= \mathrm{e}^{\left(2\mathrm{j}\arccos\left\{\sin\left(\frac{\mathrm{FWHM}}{4}\right)\cos\left(\frac{(2k-1)\pi}{2N}\right)\right\}\right)}, \\ k &= 1 \ldots N. \end{aligned} \tag{2.116}$$

This is an intuitive approach to design ring resonator filters, however it is challenging to extract the poles of the frequency response.

The time-dependent relations which have been presented for a single ring resonator can be extended to multiple serially coupled resonators. The response of the first ring (counted from the bottom of the ring filter) can be written as (Little et al. 1998b)

$$e_1 = \cfrac{-\kappa^* E_{i1}}{\mathrm{j}\Delta\omega_{\mathrm{R}1} + \cfrac{-\kappa_1^{*^2}}{\mathrm{j}\Delta\omega_{\mathrm{R}2} \ldots + \cfrac{-\kappa_{N-1}^{*^2}}{\mathrm{j}\Delta\omega_{\mathrm{R}N}}}}, \tag{2.117}$$

$$\Delta\omega_n = \left\{ \begin{array}{ll} \omega - \omega_{\mathrm{R}n} - \mathrm{j}\dfrac{1}{\tau_n}, & n \neq 1, N \\ \omega - \omega_{\mathrm{R}n} - \mathrm{j}\dfrac{1}{\tau_n} - \mathrm{j}\dfrac{1}{\tau_{\mathrm{tr}}}, & n = 1, N \\ \omega - \omega_{\mathrm{R}n} - \mathrm{j}\dfrac{1}{\tau_n} - \mathrm{j}\dfrac{2}{\tau_{\mathrm{tr}}}, & N = 1 \end{array} \right\},$$

where ω is the optical frequency of the input wave, $\omega_{\mathrm{R}n}$ is the resonant frequency of ring resonator n and $\Delta\omega_n$ is the complex frequency deviation. The energy decay rate of each ring is given by τ_n. The response of resonator N can be expressed by a product of continued fractions:

$$e_N = E_{i1} \prod_{n=1}^{N} T_n, \tag{2.118}$$

where

$$T_N = \cfrac{-\kappa_{n-1}^*}{\mathrm{j}\Delta\omega_n + \cfrac{-\kappa_{n-1}^{*^2}}{\mathrm{j}\Delta\omega_{n-1} + \cfrac{-\kappa_{n-2}^{*^2}}{\mathrm{j}\Delta\omega_{n-2}\ldots + \cfrac{-\kappa_1^{*^2}}{\mathrm{j}\Delta\omega_{\mathrm{R1}}}}}},$$

$$T_1 = \frac{-\kappa^*}{\mathrm{j}\Delta\omega_{\mathrm{R1}}}.$$

The coefficients for maximally flat and Chebyshev filter characteristics are given in the following table for two to six serially coupled ring resonators (Little et al. 1997b):

Table 2.1. Coefficients for maximally flat and Chebyshev filter characteristics

N	maximally flat	Chebyshev
2	$\kappa_1^{*^2} = 0.250\kappa^{*4}$	$\kappa_1^{*2} = 0.250\kappa^{*2}\,(1+2y)$
3	$\kappa_1^{*2} = \kappa_2^{*2} = 0.125\kappa^{*4}$	$\kappa_1^{*2} = \kappa_2^{*2} = 0.125\kappa^{*4}\left(1+1.5y^{\frac{2}{3}}\right)$
4	$\kappa_1^{*2} = \kappa_3^{*2} = 0.100\kappa^{*4}$ $\kappa_2^{*2} = 0.040\kappa^{*4}$	
5	$\kappa_1^{*2} = \kappa_4^{*2} = 0.0955\kappa^{*4}$ $\kappa_2^{*2} = \kappa_3^{*2} = 0.040\kappa^{*4}$	
6	$\kappa_1^{*2} = \kappa_5^{*2} = 0.0915\kappa^{*4}$ $\kappa_2^{*2} = \kappa_4^{*2} = 0.0245\kappa^{*4}$ $\kappa_3^{*2} = 0.0179\kappa^{*4}$	

y determines the passband ripples of the Chebyshev filter.

Another method of calculating the transfer functions of serially coupled ring resonator filters is by using a so called characteristic matrix approach, which has been presented in Chen et al. (2004a). The method is based on defining the optical paths which an optical signal travels form the input port to the drop port. There are several paths and the shortest path is called the common path or the zeroth-order path which is defined to be unity. Looking at a serially coupled triple ring resonator, the light using the first order paths for example has three choices, one additional ring resonator path and the common path. The mth order transfer function is related to the $m+1$th order transfer function by

$$\vec{H}_{m+1} = \begin{bmatrix} H_{1,m+1} \\ H_{2,m+1} \\ H_{3,m+1} \end{bmatrix} = \begin{bmatrix} T_{11} & T_{12} & T_{13} \\ T_{21} & T_{22} & T_{23} \\ T_{31} & T_{32} & T_{33} \end{bmatrix} \cdot \begin{bmatrix} H_{1,m} \\ H_{2,m} \\ H_{3,m} \end{bmatrix} = T \cdot \vec{H}_m, \tag{2.119}$$

t_{ij} are the transfer functions of the additional path in ring resonator i, with previous path ends in ring resonator j. T is called the characteristic matrix.

Using the coefficients for the ring resonators as described previously for symmetric coupling ($t = t^*$ and $\kappa = -\kappa^*$), T is given by

$$T_{\mathrm{DropPort}} = \begin{bmatrix} t_1 t_2 \alpha_1 \mathrm{e}^{\mathrm{j}\theta_1} \left(1 \ \frac{-\kappa_2^2}{t_2^2} \ 0\right) \\ t_2 t_3 \alpha_2 \mathrm{e}^{\mathrm{j}\theta_2} \left(1 \ 1 \ \frac{-\kappa_3^2}{t_3^2}\right) \\ t_3 t_4 \alpha_3 \mathrm{e}^{\mathrm{j}\theta_3} \left(1 \ 1 \ 1\right) \end{bmatrix}. \tag{2.120}$$

The general expression for the characteristic matrix for a filter consisting of n ring resonators is given by

$$T_{\mathrm{DropPort}} = \begin{bmatrix} t_1 t_2 \alpha_1 \mathrm{e}^{\mathrm{j}\theta_1} \left(1 \ \frac{-\kappa_2^2}{t_2^2} \ 0 \ldots 0\right) \\ t_2 t_3 \alpha_2 \mathrm{e}^{\mathrm{j}\theta_2} \left(1 \ 1 \ \frac{-\kappa_3^2}{t_3^2} \ 0 \ldots 0\right) \\ \ldots \left(1 \ldots 1 \ldots 0\right) \\ \ldots \left(1 \ldots \ldots 1 \ \frac{-\kappa_n^2}{t_n^2}\right) \\ t_n t_{n+1} \alpha_n \mathrm{e}^{\mathrm{j}\theta_n} \left(1 \ldots \ldots 1 \ 1\right) \end{bmatrix}. \tag{2.121}$$

The general expression for the transfer function for the drop port is then given by

$$H_{\mathrm{DropPort}} = \frac{\prod_k \kappa_k \sqrt{\prod_k \alpha_k} \mathrm{e}^{\ \mathrm{j}\sum_k \theta_k}}{|U_{Matrix} - T_{\mathrm{DropPort}}|}, \quad k = 1 \ldots n, \tag{2.122}$$

where U_{Matrix} is the unit matrix.

Filter synthesis using (2.121) and (2.122) can be done by solving a matrix eigenvalues equation. The poles of a filter function correspond to unity minus the eigenvalues of T_{DropPort}. The eigenvalues and power coupling ratios for a maximally flat transfer function are given in Table 2.2 assuming lossless devices.

Using the aforementioned techniques, it is possible to find the transfer functions for arbitrary serially coupled ring resonators. Each method has its pros and cons and therefore it is left to the designer to choose the right method which seems convenient to solve the problem. When designing ring resonator filters, it is appropriate to evaluate the technological feasibility of certain parameters like coupling coefficients and loss in order to easily transfer the design to fabrication.

A special serially coupled ring resonator design (Fig. 2.14) has been proposed and analyzed in Poon, Scheuer, Yariv (2004e). The following calculation method is based on this literature.

Table 2.2. Eigenvalues and power coupling ratios for a maximally flat transfer function

N	eigenvalues (= 1 – poles)	power coupling ratios
2	$0.63 + 0.32\mathrm{i};\ 0.63 - 0.32\mathrm{i}$	0.5; 0.2; 0.5
3	$0.73 + 0.42;\ 0.71;\ 0.73 - 0.42\mathrm{i}$	0.5; 0.14; 0.14; 0.5
4	$0.78 + 0.45\mathrm{i};\ 0.77 + 0.17\mathrm{i};\ 0.77 - 0.17\mathrm{i};$ $0.78 - 0.45\mathrm{i}$	0.5; 0.13; 0.09; 0.13; 0.5
5	$0.81 + 0.46\mathrm{i};\ 0.8 + 0.26\mathrm{i};\ 0.81;\ 0.8 -$ $0.26\mathrm{i};\ 0.81 - 0.46\mathrm{i}$	0.5; 0.13; 0.08; 0.08; 0.13; 0.5
10	$0.86 + 0.48\mathrm{i};\ 0.85 + 0.42\mathrm{i};\ 0.86 + 0.33\mathrm{i};$ $0.88 + 0.21\mathrm{i};\ 0.9 + 0.07\mathrm{i};\ 0.9 - 0.07\mathrm{i};$ $0.88 - 0.21\mathrm{i};\ 0.86 - 0.33\mathrm{i};\ 0.85 - 0.42\mathrm{i};$ $0.86 - 0.48\mathrm{i}$	0.5; 0.12; 0.07; 0.07; 0.07; 0.07; 0.07; 0.07; 0.07; 0.12; 0.5

(Chen et al. 2004a)

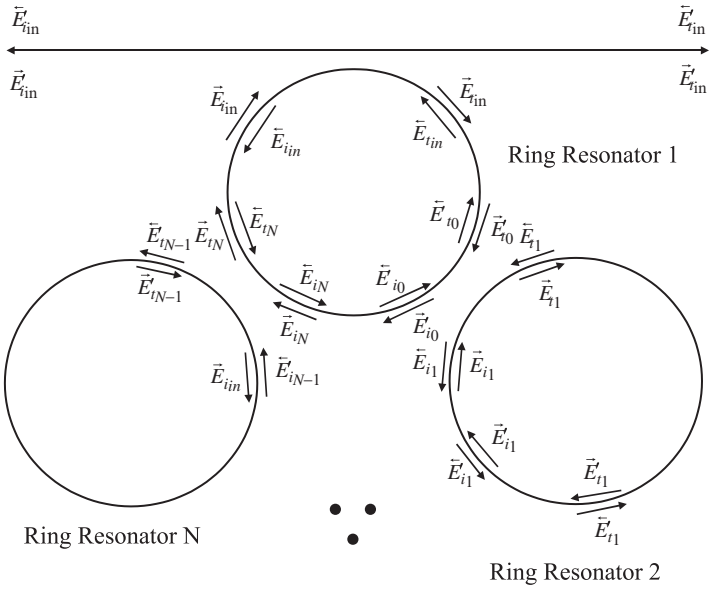

Fig. 2.14. Ring resonator configuration with interring coupling

Depending on the number of rings used the filter can either be reflecting or nonreflecting. The filter acts as a reflector for an odd number of rings (N $\geq$ 3), whereas a nonreflecting filter is obtained for an even number of rings (N $\geq$ 4). The transfer functions are derived by using a transfer matrix method, starting in defining a vector x_n, which represents the field component in ring resonator $n-1$:

$$x_n = \left[\overleftarrow{E}_\mathrm{t}\ \overleftarrow{E}_i\ \overrightarrow{E}_i\ \overrightarrow{E}_\mathrm{t}\right]_n^\mathrm{T} \tag{2.123}$$

The arrows used as superscripts are as described earlier for the double ring the direction of the propagating field, clockwise or anticlockwise without mixing of waves between the two directions. The coupling between the ring resonators can be represented by the following 4×4 matrix ($n \geq 0$):

$$x_{n+1} = \begin{bmatrix} \frac{-t}{\kappa} & \frac{1}{\kappa} & 0 & 0 \\ -\frac{1}{\kappa} & \frac{t^*}{\kappa} & 0 & 0 \\ 0 & 0 & \frac{-t}{\kappa} & \frac{1}{\kappa} \\ 0 & 0 & -\frac{1}{\kappa} & \frac{t^*}{\kappa} \end{bmatrix} \cdot x'_n = M_{\mathrm{P}} \cdot x'_n. \tag{2.124}$$

Assuming only the phase matched waves are being coupled ($L_{Coupler} \gg \lambda$).

The vector x'_n is related to x_n by the following propagation matrix:

$$x'_n = \begin{bmatrix} 0 & 0 & 0 & \mathrm{e}^{-\mathrm{j}\beta r\theta} \\ 0 & 0 & \mathrm{e}^{\mathrm{j}\beta r(2\pi-\theta)} & 0 \\ 0 & \mathrm{e}^{\mathrm{j}\beta r(2\pi-\theta)} & 0 & 0 \\ \mathrm{e}^{-\mathrm{j}\beta r\theta} & 0 & 0 & 0 \end{bmatrix} \cdot x_n = M_Q \cdot x_n, \tag{2.125}$$

$$\theta = 2\pi - \frac{\pi\,(N-2)}{N}.$$

Combining (2.124) and (2.125)

$$x_{n+1} = M_{\mathrm{P}} \cdot x'_n = M_{\mathrm{P}} \cdot M_{\mathrm{Q}} \cdot x_n = M_{\mathrm{T}} \cdot x_n. \tag{2.126}$$

For an N type ring resonator configuration with $N > 2$, (2.126) yields:

$$x_N = {M_{\mathrm{T}}}^{N-1} \cdot M_{\mathrm{P}} \cdot x'_0 = M_{\mathrm{A}} \cdot x'_0. \tag{2.127}$$

Only the components of vector x'_{in} hold the transfer functions, therefore the transfer functions of the ring resonator configuration are derived using the relation for the coupling to the external waveguide and the phase relations in the first resonator:

$$x_{\mathrm{in}} = M_{P_{\mathrm{in}}} \cdot x'_{\mathrm{in}}, \tag{2.128}$$

$$\begin{aligned} \overrightarrow{E}_{t0} &= \overrightarrow{E}_{t_{\mathrm{in}}} \mathrm{e}^{-\mathrm{j}\beta r\frac{\theta}{2}} & \overleftarrow{E'}_{t0} &= \overleftarrow{E}_{t_{\mathrm{in}}} \mathrm{e}^{\mathrm{j}\beta r\frac{\theta}{2}}, \\ \overrightarrow{E'}_{i0} &= \overrightarrow{E}_{iN} \mathrm{e}^{\mathrm{j}\beta r(2\pi-\theta)} & \overleftarrow{E'}_{i0} &= \overleftarrow{E}_{iN} \mathrm{e}^{-\mathrm{j}\beta r(2\pi-\theta)}, \\ \overleftarrow{E}_{tN} &= \overleftarrow{E}_{i_{\mathrm{in}}} \mathrm{e}^{-\mathrm{j}\beta r\frac{\theta}{2}} & \overrightarrow{E}_{tN} &= \overrightarrow{E}_{i_{\mathrm{in}}} \mathrm{e}^{\mathrm{j}\beta r\frac{\theta}{2}}. \end{aligned}$$

Using (2.127) and (2.128), x_N and x'_0 can be expressed by elements of x_{in}. Equation (2.127) can then be rewritten as

$$\begin{aligned} m M_{P_{\mathrm{in}}} x'_{\mathrm{in}} &= M_{\mathrm{T}}^{N-1} M_{\mathrm{P}} w M_{\mathrm{Pin}} x'_{\mathrm{in}} \\ \Rightarrow x'_{\mathrm{in}} &= M_{\mathrm{B}} x'_{\mathrm{in}}, \end{aligned} \tag{2.129}$$

where m and w represent matrices which express the terms $\overleftarrow{E}_{i_n}$, $\overrightarrow{E}_{i_n}$ and $\overrightarrow{E'_{i0}}$, $\overrightarrow{E'_{i0}}$, using components of vector x_{in} respectively. The matrix M_{B} can then be expressed by

$$M_{\mathrm{B}} = M_{\mathrm{Pin}}^{-1} m^{-1} M_{\mathrm{T}}^{N-1} M_{\mathrm{P}} w M_{\mathrm{Pin}}. \tag{2.130}$$

If only one input is considered as in the previous ring resonator examples, x'_{in} can be expressed by

$$x'_{\mathrm{in}} = \left[0 \ \overrightarrow{E'_{i_{\mathrm{in}}}} \ 1 \ \overleftarrow{E'_{t_{\mathrm{in}}}}\right]^{\mathrm{T}}. \tag{2.131}$$

The reflection and transmission function $\overrightarrow{E'_{i_{\mathrm{in}}}}$ and $\overrightarrow{E'_{t_{\mathrm{in}}}}$ can then be derived using elements of matrix M_{B} and solving the following matrix equation:

$$\begin{bmatrix} \dfrac{M_{B_{4,2}}}{1 - M_{\mathrm{B}_{4,4}}} & 1 \\ 1 & -\dfrac{M_{\mathrm{B}_{2,4}}}{1 - M_{\mathrm{B}_{2,2}}} \end{bmatrix} \begin{bmatrix} \overrightarrow{E'}_{i_{\mathrm{in}}} \\ \overleftarrow{E'}_{t_{\mathrm{in}}} \end{bmatrix} = \begin{bmatrix} \dfrac{M_{\mathrm{B}_{4,3}}}{1 - M_{\mathrm{B}_{4,4}}} \\ \dfrac{M_{\mathrm{B}_{2,3}}}{1 - M_{\mathrm{B}_{2,2}}} \end{bmatrix}. \tag{2.132}$$

The following equations are also valid for the solutions:

$$\begin{aligned} M_{\mathrm{B}_{3,2}} \overrightarrow{E'}_{i_{\mathrm{in}}} + M_{\mathrm{B}_{3,3}} + M_{\mathrm{B}_{3,4}} \overleftarrow{E'}_{t_{\mathrm{in}}} &= 1, \\ M_{\mathrm{B}_{1,2}} \overrightarrow{E'}_{i_{\mathrm{in}}} + M_{\mathrm{B}_{1,3}} + M_{\mathrm{B}_{1,4}} \overleftarrow{E'}_{t_{\mathrm{in}}} &= 0. \end{aligned} \tag{2.133}$$

In using the above equations, it is possible to calculate the reflectance and the transmittance spectra of this type of serially interring coupled ring resonator.

2.3.2 Parallel Coupled Ring Resonators

Parallel coupled ring resonators have been addressed in literature and the transfer functions have been derived by several methods. One of the advantages of parallel coupled ring resonators over serially coupled ring resonators is that their transfer functions are less sensitive to fabrication tolerances, as each ring resonator can compensate errors in any of the others. Two configurations are discussed, one where the ring resonators are coupled to two input/output waveguides and the other, where all share one input/output waveguide.

Coupled to Two Input/Output Waveguides

As can be seen from Fig. 2.15, parallel coupled ring resonators coupled to two waveguides share the same input, throughput, drop, and add port.

The synthesis of the transfer functions of parallel coupled ring resonators using a recursive algorithm is presented in Little et al. (2000a). A complex matrix formalism employing racetrack ring resonator filters is derived in Griffel (2000a). A technique using simple closed-form formulas to determine

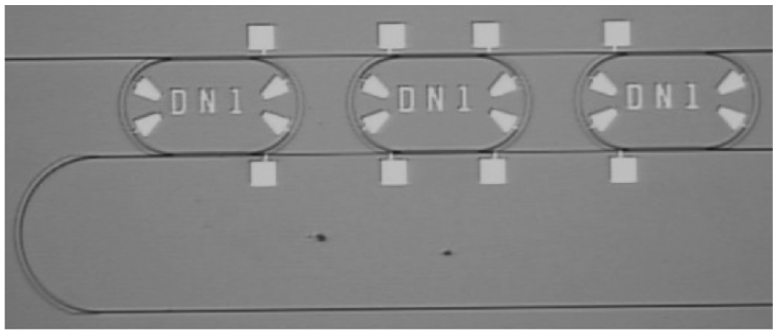

Fig. 2.15. Photograph of a parallel coupled triple ring resonator

the Q factor of each involved ring resonator which leads to the coupling coefficients is demonstrated in Melloni (2001). These different methods for analyzing the transfer functions will be used in the following.

The model which has been presented in Fig. 2.10 can be easily extended for multiple parallel coupled ring resonators. The distance between the uncoupled ring resonators Λ is chosen so that the transfer functions of each ring resonator add in phase. The transfer function derived by the recursive algorithm used in Little et al. (2000a) is given by

$$T_n = \frac{E_\mathrm{t}}{E_i} = R_n - \frac{E^i_{\mathrm{t}\,n} E^o_{\mathrm{t}\,n}}{R_n - T^{-1}_{n-1} \mathrm{e}^{\mathrm{j}2\theta_{\mathrm{W}\,n-1}}}, \tag{2.134}$$

$$R_n = -\frac{\mu^i_n \mu^o_n}{\mathrm{j}\Delta\omega + \frac{1}{2}\left(\mu^{i,o}_n\right)^2 + \frac{1}{2}\left(\mu^{i,o}_n\right)^2},$$

$$E^{i,o}_{\mathrm{t}\,n} = R_n - \frac{\left(\mu^{i,o}_n\right)^2}{\mathrm{j}\Delta\omega + \frac{1}{2}\left(\mu^{i,o}_n\right)^2 + \frac{1}{2}\left(\mu^{i,o}_n\right)^2},$$

where the indices i, o correspond to the through responses of each ring resonator n in the waveguides joining the ring resonators and $\Delta\omega$ is the frequency deviation away from resonance. The term μ is related to the coupling coefficient κ (2.74):

$$\mu^{i,o}_n = \kappa^{i,o}_n \sqrt{\frac{v_{\mathrm{g}\,n}}{2\pi r_n}}. \tag{2.135}$$

The recursion is started with $T_1 = R_1$. Loss can also be incorporated into this algorithm by substituting $\mathrm{j}\Delta\omega$ with $\mathrm{j}\Delta\omega + 1/\tau$.

In this type of synthesis, the transfer function is directly related to the coupling coefficient to obtain any desired filter shape. In the methods described earlier, the transfer functions are rational polynomials related to frequency, wavelength or z where the coefficients of the polynomials are adjusted for any specific filter function. In using the recursive algorithm, it is possible to

suppress unwanted sidelobes by apodization, which is realized by adjusting the coupling coefficients properly.

A straight forward method of designing parallel coupled ring resonator filters is presented in Melloni (2001). The filter shape can be calculated by using the given specifications for bandwidth, FSR, out of band rejection and selectivity. The formulas for a parallel N coupled ring resonator filter are as follows:

$$Q_n = \frac{\mathrm{FSR}}{g_n FWHM} \tag{2.136}$$
$$g_n = \sqrt{2}\sin\left(\frac{2n-1}{2N}\pi\right).$$

The coupling coefficients are given by

$$\kappa_n = \frac{\pi^2}{2{Q_n}^2}\left[\sqrt{1+\frac{4{Q_n}^2}{\pi^2}}-1\right]. \tag{2.137}$$

A specific filter characteristic can be derived by using this method and the relations described in Sect. 2.1.1.

For deriving the transfer functions for parallel coupled racetrack shaped ring resonators, the matrix formalism described in Griffel (2000a) is used. The parallel coupled filter can be broken down into two components, similar to the method shown for the serially coupled ring resonator filter, into a ring resonator coupled to two waveguides and into a pair of uncoupled guides as shown in Fig. 2.16.

The transfer matrix for the ring resonator coupled to two waveguides is given by

$$\begin{pmatrix} \overleftarrow{E}_i \\ \overrightarrow{E}_i \\ \overleftarrow{E}_t \\ \overrightarrow{E}_t \end{pmatrix}_n = \begin{pmatrix} \frac{a_{1_n}a_{2_n}-b_n^2}{a_{2_n}} & 0 & 0 & -\frac{b_n}{a_{2_n}} \\ 0 & \frac{1}{a_{1_n}} & \frac{b_n}{a_{1_n}} & 0 \\ 0 & -\frac{b_n}{a_{1_n}} & \frac{a_{1_n}a_{2_n}-b_n^2}{a_{1_n}} & 0 \\ \frac{b_n}{a_{2_n}} & 0 & 0 & \frac{1}{a_{2_n}} \end{pmatrix} \cdot \begin{pmatrix} \overleftarrow{E}_i \\ \overrightarrow{E}_i \\ \overleftarrow{E}_t \\ \overrightarrow{E}_t \end{pmatrix}_{n+1}. \tag{2.138}$$

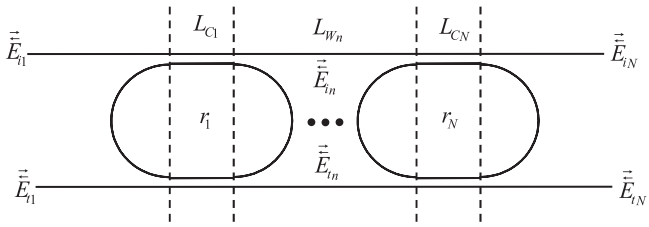

Fig. 2.16. Schematic of a parallel coupled ring resonator filter

The transfer matrix for the pair of uncoupled waveguides is given by

$$\begin{pmatrix} \overleftarrow{E}_i \\ \overrightarrow{E}_i \\ \overleftarrow{E}_t \\ \overrightarrow{E}_t \end{pmatrix}_n = \begin{pmatrix} \mathrm{e}^{\mathrm{j}\beta_W L_{\mathrm{W}n}} & 0 & 0 & 0 \\ 0 & \mathrm{e}^{-\mathrm{j}\beta_W L_{\mathrm{W}n}} & 0 & 0 \\ 0 & 0 & \mathrm{e}^{\mathrm{j}\beta_W L_{\mathrm{W}n}} & 0 \\ 0 & 0 & 0 & \mathrm{e}^{-\mathrm{j}\beta_W L_{\mathrm{W}n}} \end{pmatrix} \cdot \begin{pmatrix} \overleftarrow{E}_i \\ \overrightarrow{E}_i \\ \overleftarrow{E}_t \\ \overrightarrow{E}_t \end{pmatrix}_{n+1} . \tag{2.139}$$

The coefficients a_{1n}, a_{2n} and b_n are given by

$$\begin{aligned} b_n &= \frac{\kappa_{1_n}\kappa_{2_n}\mathrm{e}^{-\mathrm{j}(2\beta_W L_{\mathrm{C}n}+\beta_{\mathrm{R}}\pi r_n)}}{1-t_{1_n}t_{2_n}\mathrm{e}^{-2\mathrm{j}(\beta_W L_{C_n}+\beta_{\mathrm{R}}\pi r_n)}}, \\ a_{1_n} &= \frac{t_{2_n}\mathrm{e}^{-\mathrm{j}\beta_W L_{\mathrm{C}n}} - t_{1_n}\mathrm{e}^{-\mathrm{j}(3\beta_W L_{\mathrm{C}n}+2\beta_{\mathrm{R}}\pi r_n)}}{1-t_{1_n}t_{2_n}\mathrm{e}^{-2\mathrm{j}(\beta_W L_{\mathrm{C}n}+\beta_{\mathrm{R}}\pi r_n)}}, \\ a_{2_n} &= \frac{t_{1_n}\mathrm{e}^{-\mathrm{j}\beta_W L_{\mathrm{C}n}} - t_{2_n}\mathrm{e}^{-\mathrm{j}(3\beta_W L_{\mathrm{C}n}+2\beta_{\mathrm{R}}\pi r_n)}}{1-t_{1_n}t_{2_n}\mathrm{e}^{-2\mathrm{j}(\beta_W L_{\mathrm{C}n}+\beta_{\mathrm{R}}\pi r_n)}}. \end{aligned} \tag{2.140}$$

The arrows used as the superscripts indicate whether the field is propagating to the left or the right direction. Multiplying the transfer matrices in an alternating rhythm, the transfer functions for a parallel N coupled ring resonator filter can be derived. Note that in the calculation the propagation constant for the uncoupled waveguides and for the ring resonators is assumed to be the same for each one, respectively. The drop port $\overleftarrow{E}_{t1}$ and the throughput $\overrightarrow{E}_{iN}$ responses from the resulting matrix H, where h represent the elements of the matrix, are then given by (assuming only one input, $\overrightarrow{E}_{i1} = 1$):

$$\begin{aligned} &\overleftarrow{E}_{t1} = \frac{h_{3,2}}{h_{2,2}} \quad \overrightarrow{E}_{iN} = \frac{1}{h_{2,2}}, \\ &\text{where} \quad \overrightarrow{E}_{tN} = \overleftarrow{E}_{i1} = 0. \end{aligned} \tag{2.141}$$

As in the recursive algorithm mentioned earlier in this chapter, the coupling coefficients can also be varied to control the bandwidth of the filter and thus reducing the sidelobes by apodization.

Several configurations to obtain a box-like filter response using an array of parallel coupled ring resonators are presented in Ma et al. (2005). A special configuration consisting of a parallel coupled double ring resonator (with two waveguides), serially coupled with a single ring resonator has been analyzed in Okamoto et al. (2003).

Coupled to One Input/Output Waveguide

The basic ring resonator filter configuration consisting of a ring and a waveguide is used to realize a multiple parallel coupled filter. Another term for

parallel coupled ring resonators with only one input/output waveguides is side-coupled, integrated, space sequence of resonators (SCISSORS) (Heebner et al. 2002). The transfer functions of these types of filters can be derived using the methods and formulas described earlier in this chapter. In this chapter the focus lies on the optical properties of this kind of device which have been analyzed in detail in Heebner et al. (2002) and Pereira et al. (2002). The following expressions are based on this literature.

In order to describe linear propagation effects, a pulse is considered, which travels through a single ring resonator, obtaining a frequency-dependent phase shift that results in a delay or distorts the pulse shape (see also section "The Time-Dependent Relations"). The effective propagation constant for a resonator spacing of Λ is then given by

$$\beta_0(\omega) = \frac{n_{\text{eff}}\omega}{c_0} + \frac{\Phi(\omega)}{\Lambda}, \tag{2.142}$$

where $\Phi(\omega)$ is the phase shift which a field acquires when traversing a ring resonator. It is derived from the transfer function of a single ring resonator (Fig. 2.2) where the throughput field is related to the input field (2.9).

$$\begin{aligned} E_{t1}(\omega) &= \mathrm{e}^{\mathrm{j}\Phi(\omega)} E_{i1}(\omega), \\ \Phi(\omega) &= \pi + \theta(\omega) + 2\arctan\left(\frac{t\sin\theta(\omega)}{1 - t\cos\theta(\omega)}\right). \end{aligned} \tag{2.143}$$

The transfer function of a single ring resonator can be expanded into two terms using the Taylor series, representing the transmitted (expanded about the normalized detuning θ_0) and the exponential phase shift (expanded about the transmitted phase shift of the carrier Φ_0). The transfer function is given by

$$H(\omega) = \mathrm{e}^{\mathrm{j}\Phi} = \mathrm{e}^{\mathrm{j}\Phi_0}\left\{1 + \sum_{n=1}^{\infty}\frac{j^n}{n!}\left[\sum_{m=1}^{\infty}\frac{1}{m!}\left.\frac{\mathrm{d}^m\Phi}{\mathrm{d}\theta^m}\right|_{\theta_0} \times (\theta - \theta_0)^m\right]^n\right\}. \tag{2.144}$$

Using this equation, the field at some point z_{l+1} expressed by the field at another point z_l which is only a small distance δz away is given by (the transmitted phase shift induced by each ring resonator is assumed to be distributed over the separation Λ, leading to an effective propagation constant which is independent of propagation distance):

$$\begin{aligned} E_{l+1}(\omega) = \exp\left[\mathrm{j}\left(\frac{n_{\text{eff}}\omega_0}{c_0} + \frac{\Phi_0}{\Lambda}\right)\delta z\right] \\ \times\left\{1 + \sum_{n=1}^{\infty}\frac{j^n}{n!}\left[\frac{n_{\text{eff}}}{c_0}\Delta\omega\delta z + \sum_{m=1}^{\infty}\frac{1}{m!}\frac{\delta z}{\Lambda}\left.\frac{\mathrm{d}^m\Phi}{\mathrm{d}\theta^m}\right|_{\theta_0}(\theta - \theta_0)^m\right]^n\right\} E_l(\omega). \end{aligned} \tag{2.145}$$

The Fourier transform of (2.145) leads to a difference equation for the transfer function expanded to two Tailor series (transmitted and exponential phase shift)

$$A_{l+1}(t) = A_l(t) + \sum_{n=1}^{\infty} \frac{j^n}{n!} \left[\mathrm{j} \frac{n_{\mathrm{eff}}}{c_0} \delta z \frac{\partial}{\partial t} + \sum_{m=1}^{\infty} \frac{1}{m!} \frac{\delta z}{\Lambda} \frac{\mathrm{d}^m \Phi}{\mathrm{d}\omega^m}\bigg|_{\theta_0} \left(\frac{j}{\mathrm{FSR}} \frac{\partial}{\partial t} \right)^m \right]^n A_l(t) \tag{2.146}$$

For weak coupling, (2.146) can be rewritten using

$$\frac{A_{l+1}(t) - A_l(t)}{\delta z} \xrightarrow{\delta z \to 0} \frac{\mathrm{d}A}{\mathrm{d}z} \tag{2.147}$$

leading to

$$\frac{\mathrm{d}A}{\mathrm{d}z} = \left[-\frac{n_{\mathrm{eff}}}{c_0} \frac{\partial}{\partial t} + \mathrm{j} \sum_{m=1}^{\infty} \frac{1}{m!} \frac{1}{\Lambda} \frac{\mathrm{d}^m \Phi}{\omega^m}\bigg|_{\theta_0} \left(\frac{j}{\mathrm{FSR}} \frac{\partial}{\partial t} \right)^m \right] A. \tag{2.148}$$

This equation yields the group-velocity reduction and group-velocity dispersion including higher order dispersion. The group-velocity reduction, which is proportional to the inverse of the first frequency derivative of the propagation constant, is given by the term:

$$\beta'_{\mathrm{eff}} = \frac{\mathrm{d}\beta_{\mathrm{eff}}}{\mathrm{d}\omega} = \frac{n_{\mathrm{eff}}}{c_0} + \frac{1}{\Lambda} \frac{\mathrm{d}\Phi}{\mathrm{d}\omega} \xrightarrow{\theta_0 = 0, t \approx 1} \frac{n_{\mathrm{eff}}}{c_0} \left(1 + \frac{4r}{\Lambda} F \right), \tag{2.149}$$

where F is the finesse and r the radius of the ring resonator (see (2.30)). The group-velocity dispersion, which is proportional to the second frequency derivative of the effective propagation constant, is given by:

$$\beta''_{\mathrm{eff}} = \frac{\mathrm{d}\beta^2_{\mathrm{eff}}}{\mathrm{d}\omega^2} = \frac{1}{\Lambda} \frac{\mathrm{d}^2 \Phi}{\mathrm{d}\omega^2} \xrightarrow{\theta_0 = \pm \frac{\pi}{F\sqrt{3}}} \mp \frac{3\sqrt{3} F^2}{4\pi^2 \Lambda \mathrm{FSR}^2}. \tag{2.150}$$

The dispersion maxima are obtained at a detuning of $\theta_0 = \pm \frac{\pi}{F\sqrt{3}}$.

Higher-order dispersion is derived in a similar way as described before. The expression for the third-order dispersion is given by the term:

$$\beta'''_{\mathrm{eff}} = \frac{1}{\Lambda} \frac{\mathrm{d}^3 \Phi}{\mathrm{d}\omega^3}, \xrightarrow{\theta_0 = 0, t \approx 1} -\frac{4}{\pi^3} \frac{F^3}{\Lambda \mathrm{FSR}^3}. \tag{2.151}$$

All orders of dispersion have to be taken into account if the pulse bandwidth corresponds approximately to the resonance bandwidth given by the FWHM.

Ring resonators are versatile devices and do not only exhibit linear properties, but can also be used to realize nonlinear effects. This can be accomplished by using a material system like InGaAsP or GaAs for example. The effective nonlinear propagation constant is given by (assuming that the nonlinearity of the bus waveguide does not contribute significantly and can be neglected):

$$\beta^{nl}{}_{\mathrm{eff}} = \frac{1}{\Lambda} \frac{\mathrm{d}\Phi}{\mathrm{d}\left|E_{i1}\right|^2} = \frac{1}{\Lambda} \frac{\mathrm{d}\Phi}{\mathrm{d}\theta} \frac{\mathrm{d}\theta}{\mathrm{d}\left|E_{i2}\right|^2} \frac{\mathrm{d}\left|E_{i2}\right|^2}{\mathrm{d}\left|E_{i1}\right|^2} \xrightarrow{\theta_0 = 0, t \approx 1} \beta^{nl} \frac{8r}{\pi \Lambda} F^2. \tag{2.152}$$

The linear propagation (2.148) can then be modified to:

$$\frac{\mathrm{d}A}{\mathrm{d}z} = \left[-\frac{n_{\mathrm{eff}}}{c_0}\frac{\partial}{\partial t} + \mathrm{j}\sum_{m=1}^{\infty}\frac{1}{m!}\frac{1}{\Lambda}\frac{\mathrm{d}^m \Phi}{\omega^m}\bigg|_{\theta_0} \times \left(\beta^{nl} 2\pi r B\left|A\right|^2 + \frac{j}{FSR}\frac{\partial}{\partial t}\right)^m \right] A, \tag{2.153}$$

where B is the intensity enhancement or buildup factor (see (2.32)–(2.36)).

This configuration of side-coupled ring resonators exhibits strong dispersive and nonlinear properties and also supports solitons. As fabrication technologies mature, integration of these kinds of devices becomes feasible.

The following chapter highlights the realization and characterization of ring resonator devices in different material systems.

3

Materials, Fabrication, and Characterization Methods

Recently, advancing fabrication technologies enabled the realization of ring resonators in many material systems with excellent optical properties. In this chapter ring resonators made of different materials using corresponding manufacturing processes will be presented based on the current state-of-the-art in literature. Device performance details will be given in Chap. 5.

There are principally two configurations for the coupling between the ring or disk resonator and the bus waveguides, namely, a vertical coupling configuration, where the bus waveguides are either on top or beneath the ring or disk resonator and the lateral coupling configuration, where the bus waveguides and the ring or disk resonator are in the same plane.

The vertical coupling method allows the precise control of the coupling distance and thus the coupling coefficient by using epitaxial growth. In this configuration it is also possible to fabricate the ring and the bus waveguides out of separate materials which opens up the possibility of creating active ring or disk structures when using an appropriate material. Realizing vertically coupled ring or disk resonators increases the fabrication complexity because processes like wafer bonding, regrowth or re-deposition are required. The lateral coupling method is useful for realizing ring resonators with larger radius ($>100\,\mu m$) utilizing a weak guiding waveguide layout where, however, the confinement of the waveguide mode is still high enough to fabricate ring resonators with negligible bending loss. Ring resonators with small radii have also been fabricated utilizing the lateral coupling scheme as will be shown in Chap. 5. Choosing a suitable waveguide design reduces the tight requirements of fabricating a very small coupling gap which is usually much less than $1\,\mu m$ in the case of very strong guiding waveguides. The lateral coupling approach allows the use of multimode interference (MMI) couplers with higher processing tolerances with respect to the power coupling coefficient which eliminates the fabrication of small ($<1\,\mu m$) and deep coupling gaps. The incorporation of gain sections inside the ring resonator using a suitable material can be accomplished by selective area metal organic vapor phase epitaxy (SAMOVPE).

Both coupling schemes have advantages and disadvantages and it is up to the device designer to decide which one is more suitable. In the following chapters, dry etching and wafer bonding techniques for realizing laterally and vertically coupled ring resonator devices will be briefly explained.

3.1 Wafer Bonding

Wafer bonding is referred to a process in which two similar or dissimilar semiconductor wafers are bonded with various crystallographic orientations and lattice constants to form a single substrate which then features specific properties. The bonding process is activated by temperature, force, chemicals or plasma. An overview on wafer bonding can be found in Alexe and Gösele (2004). Wafer bonding techniques can be divided into two groups, one using an intermediate layer (e.g., adhesion bonding, eutectic bonding) and another without using an intermediate layer (e.g., fusion bonding, anodic bonding) to realize the bond. Wafer bonding allows using the advantages of different materials, while avoiding their disadvantages, allowing combinations of materials otherwise unachievable with other techniques. Wafer bonding is commonly applied to form silicon-on-insulator (SOI) substrates. Bonding of wafers of different materials has attracted great interest lately, e.g., GaAs on Si (Georgakilas et al. 2002), or SiC on Si (Kim and Carpenter 2003).

Different methods exist for bonding various materials and it is again up to the realized device which process is more suitable. In the following sections common wafer bonding methods are described.

3.1.1 Bonding with Intermediate Layer

Adhesion Bonding

Adhesive bonding uses photoresist, spin on glasses or polymers to deposit a planarizing material between two wafers. Such materials can be annealed at low temperature to provide a low-stress wafer stack. It is a relatively simple and inexpensive process. The use of polymers has the advantage of bonding samples which have been structured already which is the case for vertically coupled ring resonators, where the bus waveguides have been fabricated before the bonding takes place.

Eutectic Bonding

Eutectic bonding is a special kind of metal bonding, where the low melting temperature of the eutectic alloy is exploited to achieve low temperature bonding. Eutectic is a mixture of two or more elements and has a lower melting point than any of its constituents. Eutectic comes from the Greek word “eutektos” which means “easily melted.” Eutectic bonds are used when a

hermetic or vacuum seal is required. Eutectic alloys which are used for example are gold–silicon, gold–tin, or lead–silicon. The metal is usually deposited by plating, while the silicon source can be the wafer or chemical vapor deposition (CVD). Solid–liquid mixing occurs at temperatures slightly above the eutectic point and a high contact force (40 kN). A gold–silicon eutectic bond for example is realized by coating a silicon wafer with ∼500 nm gold. The Au–Si eutectic point is about 370°C. Au atoms diffuse into Si and the eutectic alloy is formed. The bonding temperature is higher than the eutectic point which is due to solid–liquid inter-diffusion at the interface.

3.1.2 Bonding Without Intermediate Layer

The requirements of the surface quality (cleanliness and roughness) and flatness of the used wafers are very tight when it comes to direct wafer bonding. There are basically three types of primary interactions which are responsible for forming a first bond, Van der Waals, electrostatic Columbic, and capillary forces.

Van der Waals forces are, however, quite small and decrease very rapidly as the distance between two molecules increases. Covalent bonds are established, when the wafers come into very close contact.

Electrostatic Columbic forces between two surfaces are usually stronger than the interaction between two contacted samples if one of the surfaces has been electrically charged by adsorbing or desorbing electrons or ions.

Capillary forces come into play when water is used in the bonding process. Water helps to activate the bonding process at room temperature. Due to the surface tension, the water between the two surfaces pulls the samples together and smoothens out any surface roughness present, thus increasing the contact area. During the following heating process, the water reacts with the surrounding oxide or diffuses away from the surface leading to the formation of covalent bonds. True crystal-to-crystal bonding is achieved by using hydrophobic bonding which requires a removal of the naturally formed oxide present at the surface of the samples.

Fusion Bonding

Fusion bonding uses applied temperature and pressure and is used for example to bond silicon to silicon without depositing an intermediate SiO_2 layer using the native oxide formation on the surface of the Si wafers. Fusion bonding is commonly used in mass production of bulk micromachined micro-electromechanical systems (MEMS) packaging. As the same materials are used in this bonding process, no thermal stress is induced, which results in a very strong bond strength. Initial bonding is performed in a temperature range between 300°C and 800°C, annealing is done between 800°C and 1,100°C which strengthens the bond. This high annealing temperature is also a key drawback to fusion bonding. Alternatively work is being

conducted by using plasma processing to reduce the annealing temperatures from ∼1,000°C to the range between 200°C and 300°C. Regardless of this plasma pretreatment, most of the work performed on direct bonding of III/V materials uses hydrophobic surfaces, where the oxide has been removed, to assure a true crystal-to-crystal bond and good electrical contacting through the bond.

Anodic Bonding

Anodic bonding or electrostatic bonding is performed by applying a high electric field across the two substrates. Temperatures used in this process are ∼400°C. An example of this type of bonding is the bonding of glass/Si. Here a voltage of ∼1.2 kV is applied. Silicon is attached to the positive, glass to the negative electrode. The positive ions in glass are attracted to the interface between Si/glass where a permanent chemical bond is formed. The used glass has to be of course electrically conductive.

The Si/Si anodic bonding process, is of course also used, when an intermediate glass layer (0.5–4 µm) is present. Sputtering or evaporation of for example Pyrex™ or spin on glass (SOG) is used in this bonding process. The advantage is the use of a low voltage which is between 30 and 60 V. The temperature is in the range of 350–450°C.

3.1.3 Benzocyclobutene Wafer Bonding

As described in the previous sections, several bonding techniques exist. Due to the fact that benzocyclobutene (BCB) wafer bonding is widely used to fabricate vertically coupled ring and disk resonators, the BCB wafer bonding process will be briefly explained in this section. BCB wafer bonding was first presented in Sakamoto et al. (1998) for realizing electro-optic modulators on GaAs.

A detailed description of a BCB bonding process for realizing vertically coupled ring resonators is presented in Christiaens et al. (2004), Christiaens (2005) which will be used in the following.

BCB is distributed by The Dow Chemical Company under the trade name Cyclotene*[1]. There are two varieties: the Cyclotene 3000 series resins (dry etch type) and the Cyclotene 4000 series resins (photosensitive type). Wafer bonding has so far been only demonstrated with the dry etch variety. The resins are derived from B-staged bisbenzocyclobutene-based (BCB) monomers. Typical properties of Cyclotene are: low curing temperature (∼250°C), excellent planarization properties, a dielectric constant between 2.65 and 2.5 (1 MHz–10 GHz) and low moisture uptake (<0.2%). One of the downsides of BCB is its

[1] ®™* Trademark of The Dow Chemical Company ("Dow") or an affiliated company of Dow

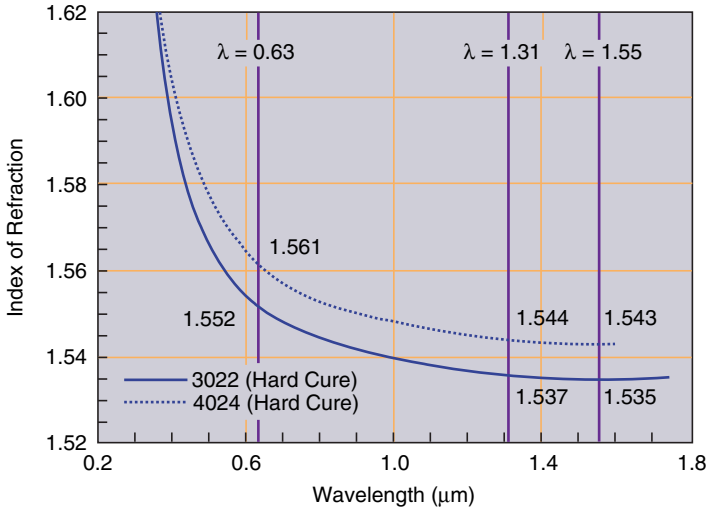

Fig. 3.1. Index of refraction as a function of wavelength for photo Cyclotene (4024–40) and nonphoto Cyclotene (3022–46) resins after curing at 250°C for 60 min[2]

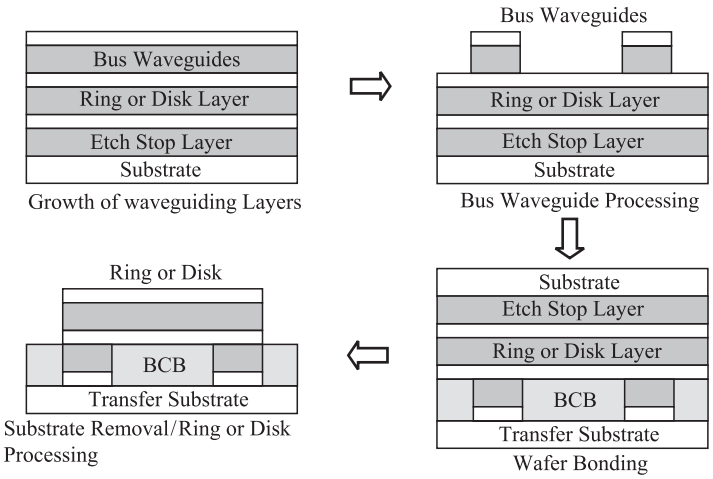

Fig. 3.2. BCB wafer bonding process

insulating nature like all common polymers and the low thermal conductivity, which is not suitable for realizing active devices. The refractive index of two types of resins is shown in Fig. 3.1.

A schematic of a BCB bonding process is presented in Fig. 3.2. Principally the process flow for realizing vertically coupled devices is started by growing the waveguiding layers on a suitable substrate (e.g., InP). An etch stop layer

[2] http://www.dow.com/cyclotene/solution/refwave.htm

is grown between the substrate and the waveguiding layers which is necessary for a later removal of the substrate after bonding. After the growth of the layers, the bus waveguides are defined using photolithographic techniques and etched using a suitable dry etching recipe. The sample is then spin coated with BCB using an adhesion promoter.

The BCB sample is then placed on a hotplate for outgassing which is followed by the bonding and a curing process in a nitrogen environment. As transfer substrate GaAs can be used for example which is chemically inert during the selective chemical etching if an InP substrate is being removed. The bonding process can also be performed in a vacuum chamber. The substrate is removed by a combination of mechanical polishing and selective chemical wet etching to the etch stop layer. Then the etch stop layer can be removed by using a selective chemical wet etching which does not etch the ring or disk layers. Finally the ring or disk resonator is fabricated using dry etching and the samples are cleaved. The samples can be antireflection (AR) coated in order to avoid Fabry–Perot resonances in the bus waveguides.

Several BCB bonded vertically coupled ring and disk resonators will be presented in Sect. 3.4.

3.2 Dry Etching

Dry etching is a technology widely used in semiconductor processing and has been developed in recent years to obtain reproducible etching results. In reactive ion etching systems, ions are accelerated towards the material to be etched, and the etching reaction is enhanced in the direction of travel of the ion. Different dry etching systems are available on the market with recipes for etching various material systems. Examples of systems are conventional reactive ion etching (RIE), inductively coupled-plasma reactive ion etching (ICP-RIE), reactive ion beam etching (RIBE), or chemically assisted ion beam etching (CAIBE). Gases which are commonly used (combining several) in dry etching processes are methane (CH_4), hydrogen (H_2), hydrogen bromide (HBr), nitrogen (N_2), chlorine (Cl_2), silicon tetrachloride ($SiCl_4$), argon (Ar), and xenon (Xe).

Despite the existence of numerous recipes, it is important to note that same conditions and used gases in etching processes can differ from machine to machine leading to different etching results. The reasons for this are multiple and can depend on the mixture and quality of gases and samples being etched regularly in the dry etching equipment which determine the chemical composition of the sidewalls in the reaction chamber. The wanted specific chemical deposition of the sidewalls is also referred to as conditioning or seasoning of the chamber and is usually done before etching of devices to obtain stable etch parameters. This conditioning affects the plasma in the etch chamber physically and/or chemically resulting in changes in the current and power density in the discharge and reaction rate.

Two ways of etching are distinguished, isotropic and anisotropic etching. RIE is an anisotropic etching technique. The etch rate which defines the rate of removal of the semiconductor material is the same in all directions in the case of isotropic etching. The etch rate is direction dependent in the case of anisotropic etching, which is important in the fabrication of ring resonators, where deeply etched waveguides are needed to obtain a strong mode confinement of the field which in turn results in a small radius of curvature with acceptable loss.

The pattern of a ring resonator layout is transferred to the material used by choosing the right masking technique. The unmasked regions like the coupling gap for example are "etched" away. There are three broad categories of masking materials: metals (nickel (Ni), chrome (Cr), nickel chrome (NiCr), titanium (Ti), aluminum (Al), wolfram (W), and platinum (Pt)), dielectrics (SiO_x, SiN_x) and polymers (Photoresist, E-beam resist). Metal masks are extremely etch resistant and good choices for deep etching, however, metal masks are difficult to remove and the metal grains result in transferred striations. Dielectric masks provide good etch resistance, and can be used to etch nanostructures. Dielectric masks are regarded as "soft" which results in very little transferred striations to the underlying material. Polymers are highly etch resistant when fully cured and can be used as masks for deep etching. However, polymers as etch resistance are not sufficient to etch the depths ($>1\,\mu m$) required for realizing waveguides used for ring resonator circuits and there is a risk of contaminating the etch chamber.

3.3 Si-Based Materials

Silicon-based devices in photonic integrated circuits are known for quite some time. Pure silicon has an absorption loss much smaller than $0.1\,dB\,cm^{-1}$ at the telecom wavelength of $1.55\,\mu m$ which makes this material interesting for telecommunication devices. The processing and fabrication technologies for this material system are mature also to the fact that the electronics industry is a driving force for these enabling technologies. Another advantage in using silicon is the possibility of combining photonic devices with electronic circuits, enabling pre- and postprocessing of optical/electrical signals.

A summary of the properties of silicon can be found in Table 3.1.

3.3.1 Ring Resonators Based on Si–SiO_2

One of the first and smallest ring resonators in the Si–SiO_2 material system which is also known as SOI has been presented in Little et al. (1998a) with radii of 3, 4, and $5\,\mu m$. The devices have quality factors up to 250, and an FSR of 20, 24, and 30 nm for a wavelength of 1,550 nm, respectively. The intensity difference between the on-resonance and the off-resonance state is measured to be more than 15 dB. The layout of a typical SOI waveguide is shown in

Table 3.1. Properties of silicon at 300 K

	symbol	
lattice constant		5.431 Å
density		2.329 g cm^{-3}
dielectric constant		11.7
auger recombination coefficient	C_n	$1.1 \cdot 10^{-30}\,cm^6\,s^{-1}$
auger recombination coefficient	C_p	$3 \cdot 10^{-31}\,cm^6\,s^{-1}$
Debye temperature		640 K
effective electron masses	m_l	$0.98\,m_o$
effective electron masses	m_t	$0.19\,m_o$
effective hole masses	m_h	$0.49\,m_o$
effective hole masses	m_{lp}	$0.16\,m_o$
electron affinity		4.05 eV
optical phonon energy		0.063 eV
infrared refractive index	$n(\lambda)$	3.42
		$3.38(1 + 3.9 \cdot 10^{-5} \cdot T)$
		$77\,K < T < 400\,K$
absorption coefficient	α_n	$10^{-18} \cdot n_o \cdot \lambda^2$
		$\lambda \geq 5\,\mu m$

http://www.ioffe.rssi.ru/SVA/NSM/Semicond/Si/basic.html

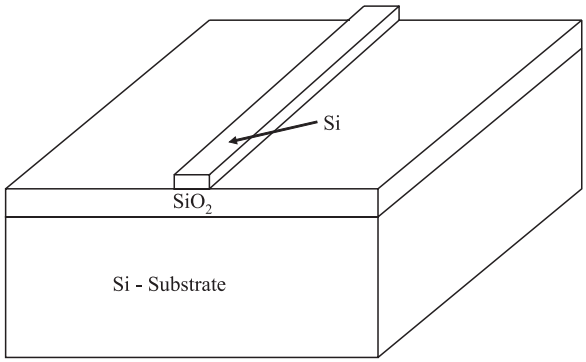

Fig. 3.3. Typical SOI waveguide layout

Fig. 3.3. The width of the waveguide should be less than 600 nm in order to achieve single mode operation.

The refractive index of SiO_2 plotted against the photon energy is shown in Fig. 3.4[3].

The fabrication process is made up of a deposition of a 1 µm thick buffer layer of SiO_2, followed by a deposition of a waveguiding core layer of amorphous Si at 560°C with a thickness of 0.2 µm. The amorphous Si was annealed

[3] http://www.ioffe.ru/SVA/NSM/nk/Oxides/Gif/sio2.gif

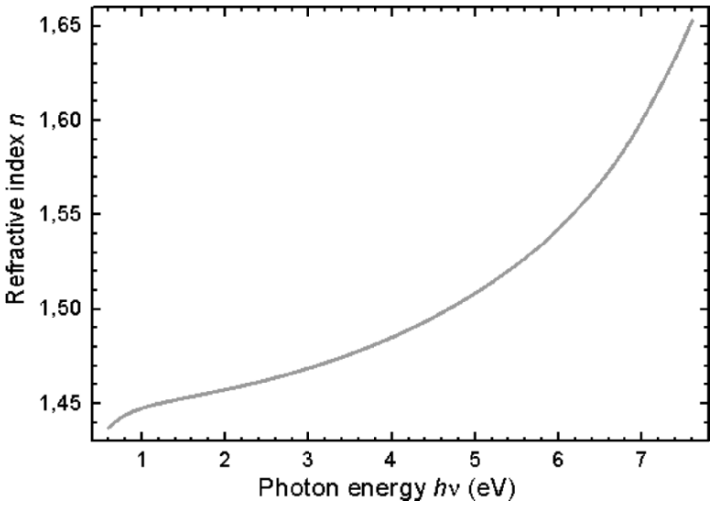

Fig. 3.4. Refractive index of SiO_2 vs. photon energy

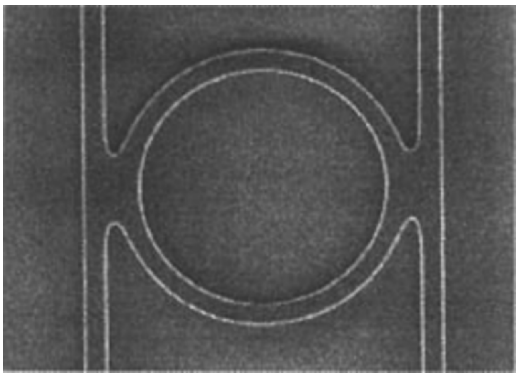

Fig. 3.5. SEM of a filter incorporating a 3 µm radius ring, with 0.5 µm wide by 0.2 µm-thick waveguides.

Reprinted with permission from IEEE Photonics Technology Letters, vol. 10, pp. 549–551 ©1998 IEEE

at 900°C for 2 h to convert it to polycrystalline silicon (polySi) out of which the ring and bus waveguides (width: 0.5 µm, height: 0.2 µm) were patterned using an HBr–Cl plasma etch process. In order to increase the fiber–chip coupling efficiency, the bus waveguides are flared to an 8 µm width. The achieved index contrast is either 3.5:1.5 or 3.5:1.0, depending on whether the material external to the Si waveguide is SiO_2 or air, respectively. An SEM photograph of a fabricated device is shown in Fig. 3.5.

Racetrack shaped ring resonators based on a similar fabrication process have been presented in Vörckel et al. (2003) where the radius is 3 µm and the length of the straight coupling region is 1 µm, obtaining an FSR of about

24 nm and a Q-factor of 1,800. The device exhibits asymmetrical coupling to achieve minimum intensity at the throughput port on resonance (see Sect. 2.1.1 (2.16)).

The thickness of the silicon layer and the buried oxide layer of the SOI substrate are 0.4 µm, respectively. The racetrack shaped ring resonators are defined by electron beam lithography. The waveguides are etched down to the buried oxide layer by an HBr inductive coupled plasma reactive ion etching process. The width of the waveguides is 0.4 µm. The bus waveguides are tapered to a 10 µm width to increase the fiber–chip coupling efficiency. Two types of coupling distance variations have been used. In the first one, the fixed coupling distance is 0.2 µm and the other coupling separation is varied between 0.1 and 0.2 µm. The second configuration used a fixed coupling distance of 0.25 µm and varying the other coupling separation between 0.125 and 0.25 µm. The throughput port minimum on resonance has been increased from −7.2 to −12.8 dB. Due to the unreproducibility of the waveguide loss and the coupling coefficients, an exact adjustment of the critical coupling cannot be possible.

Ring resonators with similar dimensions and figures of merit have been realized in Dumon et al. (2004) by deep UV lithography with an illumination wavelength of 248 nm. An SEM photograph of a fabricated racetrack shaped ring resonator is shown in Fig. 3.6.

Racetrack shaped ring resonators based on the design in Fig. 3.3 but having an SiO_2 cladding with radii down to 20 µm are presented in Kiyat et al. (2005).

A vertically coupled disk resonator fabrication process based on a separation by implantation of oxygen (SIMOX) has been presented in Koonath et al.

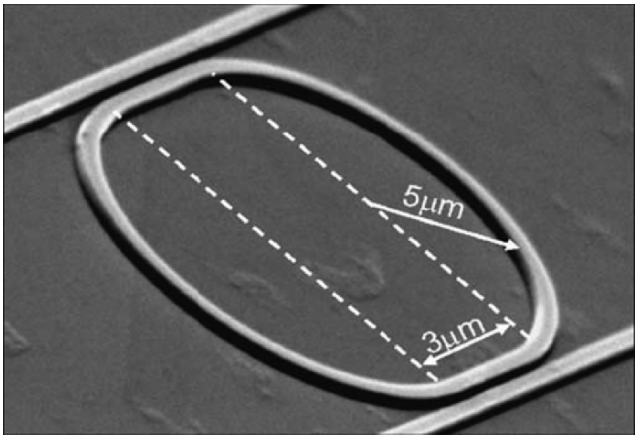

Fig. 3.6. Racetrack resonator in SOI. The isolated wire width is 500 nm, the gap width is 230 nm. Note that when the wires get closer together, the wire width decreases to 450 nm due to optical proximity effects during lithography.

Reprinted with permission from IEEE Photonics Technology Letters, vol. 16, pp. 1328–1330 ©2004 IEEE

(2003); Koonath et al. (2004, 2005). The SIMOX process involves the implantation of oxygen ions into a silicon substrate, followed by a high temperature (∼1,300°C) annealing of the substrate in order to cure the implantation damage and to effect SiO_2 formation. The thickness and the depth of the buried oxide layer are determined by the implantation dose and energy. The implantation dose should be in the range of 1×10^{17}–9×10^{17} ions per cm^2, with implantation energies in the range of 40–200 keV to keep the defect densities below $10^5\,cm^{-2}$. The implantation of oxygen ions is performed on an SOI substrate which is patterned with thermally grown oxide. The thickness of the oxide mask is chosen such that the oxygen ions that penetrate into the area underneath the mask are decelerated. After the high temperature annealing, angled side-walls of the buried rib waveguide are obtained due to the lateral spread out of the implanted oxygen ions. After annealing, rib waveguides can be defined on the top layer using a conventional lithography and etching process.

Disks with radii of 20, 20.5, and 21 µm have been fabricated. The free spectral rang of these devices is ∼5 nm. In order to fabricate the devices, an SOI wafer with 0.6 µm of silicon on top of a buried oxide layer of 0.4 µm thickness was oxidized and patterned using a reactive ion etching process to form oxide stripes of thickness 0.06 µm, with widths varying from 2 to 12 µm. The patterned wafer was then implanted with oxygen ions with a dose of 5×10^{17} ions cm^{-2}, at energy of 150 keV. The implanted wafers were then annealed at 1,320°C for 7.5 h in an ambient of argon, with 1% oxygen, to cure the implantation damage. To form the disks, a silicon nitride layer of thickness 0.1 µm was deposited on top, and patterned using standard lithography and reactive ion etching. The substrate was then oxidized to remove the silicon on the top layer, everywhere except underneath the disks, realizing vertical coupling to the buried bus waveguides. An SEM photograph of a vertically coupled disk is shown in Fig. 3.7.

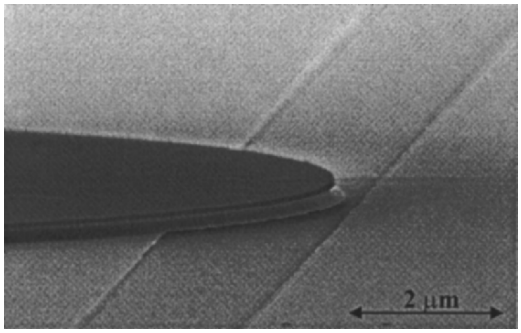

Fig. 3.7. SEM picture of the fabricated microdisk resonators on the top silicon layer with bus waveguides underneath.

Reused with permission from P. Koonath, Applied Physics Letters, 86, 091102 (2005)
©2005 American Institute of Physics

3.3.2 Ring Resonators Based on Ta_2O_5–SiO_2

The Ta_2O_5–SiO_2 material system has also been used very successfully to realize ring resonator devices. The advantage of using this material system is the ability to control the refractive index by adjusting the ratio of Ta_2O_5 to SiO_2. Vertically coupled ring resonators with a radius of 10 µm have been presented in Little et al. (1999). Here alternating layers of SiO_2 and Ta_2O_5–SiO_2 are deposited by radiofrequency (RF) sputtering. The waveguides for the ring and the bus are made using a composition of 30 mol.% of Ta_2O_5 and 70 mol.% of SiO_2 leading to a refractive index of 1.7825 at a wavelength of 1,550 nm. The bottom cladding layer is made up of 10 µm SiO_2. Then a 0.5 µm layer of Ta_2O_5–SiO_2 material is deposited on top. In order to fabricate the bus waveguides, a 150-nm-thick Cr mask was evaporated on to the sample and patterned by photolithography and dry etched to a depth of 0.5 µm. While the Cr on top of the bus waveguides remained intact, 0.5 µm of SiO_2 was sputtered onto the sample to fill in the amount of bus material etched away. In the Cr liftoff process, the sample was first soaked in buffered hydrofluoric acid (BHF) for 10 s to remove the SiO_2 deposited on the vertical walls of the Cr. This resulted in a liftoff, of both the Cr and the SiO_2 on top of it. For the vertical separation of the bus and ring waveguides, a layer of SiO_2 is sputtered onto the sample. The thickness of this layer defines the coupling coefficient between the ring and the bus waveguide. The ring resonator which is on top of the bus waveguide is made by deposition of a Ta_2O_5 layer with following Cr mask patterning process. The dimensions and the layer sequence of the device are sketched in Fig. 3.8.

A similar process realizing an eight channel add–drop filter is described in Chu et al. (1999c). Here the ring and bus waveguide cores are composed of Ta_2O_5–SiO_2 [17:83] mol% which gives a refractive index of 1.6532. SiO_2 is used for the cladding and the buffer layers. The bus waveguides has been slightly offset from the ring resonator waveguide. The dimensions and the waveguide layout are shown in Fig. 3.9.

The same waveguide and ring resonator layout has been used in Chu et al. (1999b) to realize a double ring resonator configuration. Here the composition

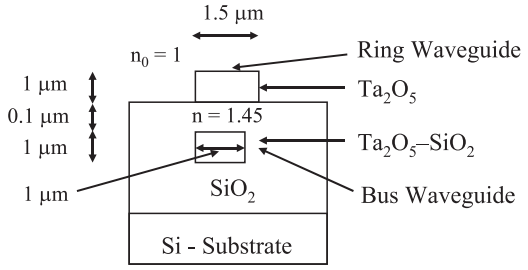

Fig. 3.8. Dimensions and layer sequence of a vertically coupled Ta_2O_5–SiO_2 ring resonator

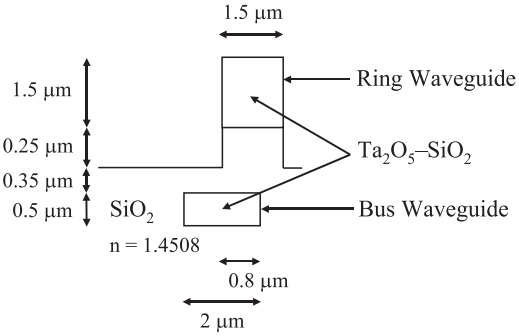

Fig. 3.9. Waveguide parameters of the eight channel add–drop filter

of Ta_2O_5–SiO_2 has been chosen to give a refractive index of 1.539. The ring and bus waveguide width are both 2 μm. The SiO_2 pedestal height for the ring waveguide is 0.5 μm. The bus waveguide are buried 0.5 μm below the surface with an offset of 0.8 μm.

A vertical coupled ring resonator configuration using the Ta_2O_5–SiO_2 compound has been presented in Hatakeyama et al. (2004) and Kokubun et al. (2005). The ring resonators are coupled to the bus waveguides using multilevel crossings which means that there is a lower and an upper bus waveguide. Single, double and quadruple coupled ring resonators have been demonstrated. The advantage of using a multilevel structure is to eliminate the scattering loss at bus waveguide crossings. The fabrication process is similar to the previously described methods, involving an RF sputtering and photolithography technique. The patterns of the waveguides are transferred using a Cr mask and a reactive ion etching (RIE) process with C_2F_6 gas. The waveguide core layers are made of Ta_2O_5–SiO_2 compound glass (Ta_2O_5 30 mol.%, n = 1.785 at the wavelength of 1,550 nm), and the cladding and separation layers are SiO_2 (n = 1.451 at the wavelength of 1,550 nm).

The fabrication of the vertically coupled ring resonator with multilevel bus waveguide crossing is started by patterning and RIE etching of the lower bus waveguide. Then the bus waveguide is covered by depositing SiO_2. The SiO_2 layer which has been deposited onto the lower bus waveguide is eliminated by a liftoff process through chemical etching of the Cr mask using a solution of Cerium (IV) diammondium nitrate 13.3 wt%, perchloric acid 70% and water. In order to realize a perfect planarized surface for the coupling to the ring resonator, SOG is used. SOG is spin coated and baked at 400°C for 40 min under N_2 gas, realizing a height of only 0.2 μm. SOG is made up of ethyl–silicate-polymer 9% (Si 5.9%), ethanol 73%, and methyl acetate 18%. The width and thickness of a ring waveguide is 1.2 and 0.7 μm, respectively. The thickness of the separation layer between the ring resonator and bus waveguides is 0.6 μm. The ring radius is 5 μm, obtaining a record 37 nm FSR. Other configurations with different dimensions have also been realized.

3.3.3 Ring Resonators Based on SiN, SiON, and Si_3N_4

Serially coupled triple ring resonators in SiN have been demonstrated in Barwicz et al. (2004). The ring and bus waveguides are made of a single layer of SiN. The high index contrast which is achieved by using this material combination induces strong polarization dependence. Therefore the device is optimized for transversal electric (TE) polarization operation. A photograph of a triple ring resonator is shown in Fig. 3.10.

The fabrication of the device is started by thermally oxidizing a silicon wafer to obtain a bottom SiO_2 layer. Then, a SiN layer is deposited by low-pressure chemical vapor deposition (LPCVD) in a vertical thermal reactor using a gas mixture of SiH_2Cl_2 and NH_3. Next, 200 nm of polymethylmethacrylate (PMMA) and 40 nm of Aquasave were spun on. PMMA is a positive E-beam resist while Aquasave is a watersoluble conductive polymer from Mitsubishi Rayon used to prevent charging during direct-write scanning-electron-beam lithography (SEBL). PMMA is exposed at 30 keV using a Raith 150 SEBL system. The Aquasave is removed, and the PMMA is developed. Next, 50 nm of Ni is evaporated on the structure, and a following liftoff is performed by removing the nonexposed PMMA. The waveguides are defined by conventional reactive ion etching (RIE) using Ni as a hardmask. A gas mixture of CHF_3–O_2 in a 16:3 flow-ratio was used during the dry etching process to obtain vertical and smooth sidewalls. The accuracy of the etch depth is monitored using several etch steps and is measured with a profilometer. Finally, the Ni is removed using a nitric-acid-based commercial wet Ni etchant.

The design and the dimensions of the used waveguide are shown in Fig. 3.11. The device is designed to have an FSR of 24 nm.

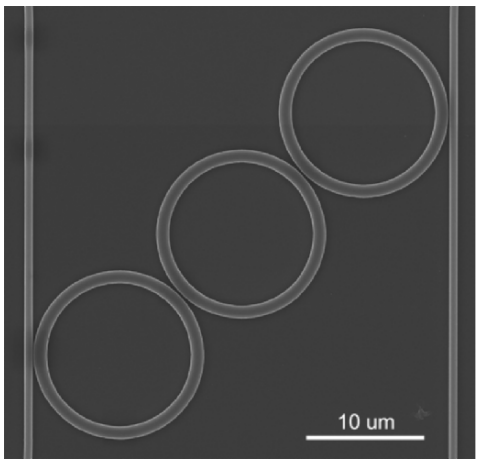

Fig. 3.10. Third-order add–drop filter based on series-coupled microring resonators. The rings' outer radius is 7.3 µm. The ring-to-bus gap is 60 nm and the ring-to-ring gap is 268 nm.

Reprinted with permission from T. Barwicz, Optics Express, vol. 12, no. 7, pp. 1437–1442 ©2004 Optical Society of America

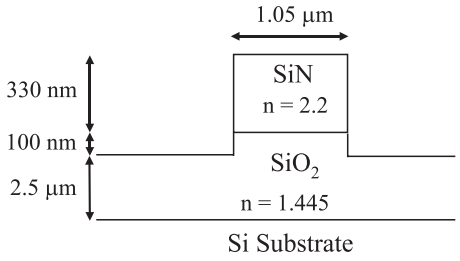

Fig. 3.11. Waveguide dimensions. The refractive index is given for $\lambda = 1{,}550\,\text{nm}$

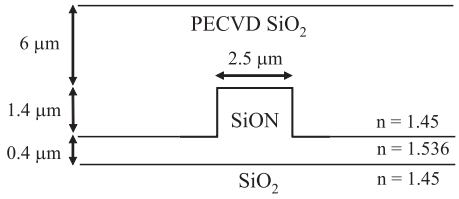

Fig. 3.12. Cross-section and layer sequence of SiON waveguide

A similar design is presented in Wang et al. (2005) with a radius of 25 µm resulting in an FSR of about 8 nm.

Ring resonators based on SiON are analyzed in Melloni et al. (2003a). The ring radius is 300 µm. The SiON waveguides are made by deposition using standard plasma-enhanced chemical vapor deposition (PECVD) techniques and dry etching. The cross-section and the dimensions of the used waveguides are sketched in Fig. 3.12.

Lateral and vertically coupled ring and disk resonators in Si_3N_4–SiO_2 and SiON are presented in Klunder et al. (2001) and Klunder et al. (2003b), respectively. The refractive index of Si_3N_4 plotted against the photon energy is shown in Fig. 3.13[4].

The dimensions and the layout of the lateral coupled configuration are shown in Fig. 3.14. Laterally coupled devices with a radius of 25 µm with and without a cladding of PMMA have been fabricated. The radius of the realized disk resonator is 15 µm.

The fabrication of the device is performed using standard lithography and reactive ion etching. Buffered hydrofluoric acid (BHF) etching is done after RIE to reduce the surface roughness and to obtain smoother sidewalls. The layer sequence of a vertically coupled ring resonator is shown in Fig. 3.15.

Here an additional SiO_2 layer is grown by PECVD which defines the coupling strength between the ring and the bus waveguides.

A high-index contrast silica on silicon technology with $\Delta n_{\text{eff}} = 0.02$ was developed at the IBM Zurich Research Lab[5] based on PECVD deposited

[4] http://www.ioffe.ru/SVA/NSM/nk/Nitrides/Gif/si3n4.gif
[5] www.ibm.zurich.com

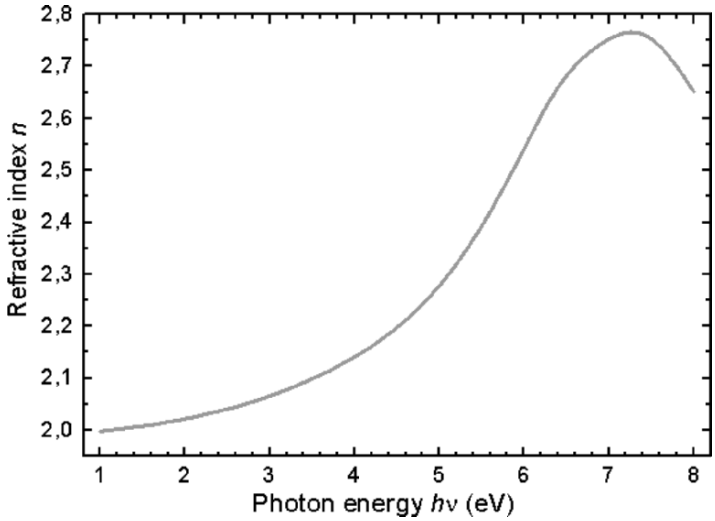

Fig. 3.13. Refractive index of Si_3N_4 vs. photon energy

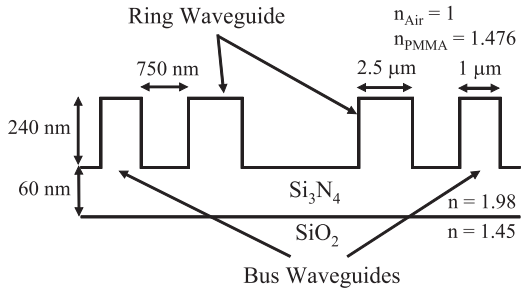

Fig. 3.14. Cross-section of a laterally coupled ring resonator

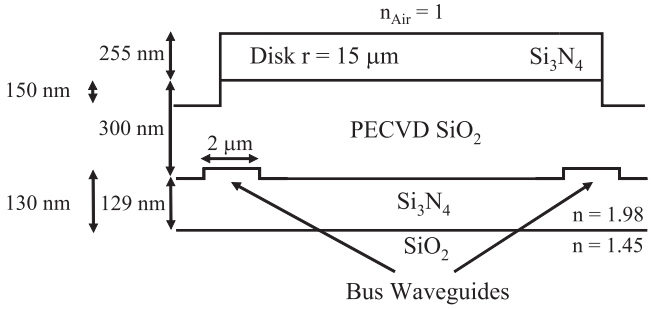

Fig. 3.15. Cross-section of a vertically coupled ring resonator

silicon oxynitride (SiON) films for realizing integrated ring resonators (Horst et al. 1998). The minimum bending radius is 1.5 mm. The waveguide layout is shown in Fig. 3.16.

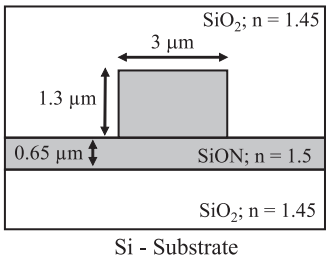

Fig. 3.16. Waveguide layout developed at IBM Zurich Research Lab

3.3.4 Ring Resonators Based on SiO_2–GeO_2

Ring resonators using GeO_2 doped silica waveguides and vertical coupling have been demonstrated in Suzuki et al. (1992). The GeO_2 doped silica waveguides are fabricated by a combination of flame hydrolysis deposition (FHD), electron cyclotron resonance CVD (ECR-CVD) with an applied RF bias (bias-CVD), and RIE. The waveguides for the ring resonator are realized in a first step unlike the configurations previously discussed, where the ring resonator is on top of the bus waveguides. The ring waveguides are made of GeO_2 doped silica with a 2% refractive index difference. The dimension of the ring waveguide etched into an under cladding layer of thickness 30 µm is 3.5 µm × 4 µm. The coupling distance is adjusted to a height of 2.5 µm between the ring and the bus waveguides by deposition. The dimension of the bus waveguides with a 0.75% refractive index difference is 5 µm × 6.5 µm. Finally the bus waveguides are covered by a cladding layer deposited again using FHD. The radius of the ring is 1.5 mm.

The advantage of using this kind of material is the low propagation loss which is smaller than 0.1 dB cm^{-1} at a wavelength of 1,550 nm. Several integrated devices based on this material are presented in Suzuki et al. (1994) using different refractive index differences for the employed waveguides. The idea which has been followed is the use of two types of waveguides, weak and strong guiding. Weak guiding waveguides are used for in and out coupling to reduce the fiber to chip coupling loss.

3.4 III–V Materials

In this chapter the most commonly used III–V material systems GaInAsP on InP and AlGaAs on GaAs are treated. Ring resonators both vertically and laterally coupled have been demonstrated in these material systems.

3.4.1 The Quaternary Semiconductor Compound GaInAsP

III/V semiconductors on the basis of InP with a direct bandgap are used for a variety of components in the all-optical network. The composition of

the quaternary (III–V) semiconductor compound GaInAsP lattice matched to InP, can be changed, so that the bandgap can be adjusted in the range between 0.97 and 1.65 µm. The choice of the appropriate bandgap, which is smaller than the signal wavelength, enables the fabrication of passive, transparent waveguides with low loss ($<1\,\mathrm{dB\,cm^{-1}}$). This material system is also used for the realization of lasers and optical amplifiers in the spectral window around 1.55 and 1.3 µm. A summary on optoelectronic and photonic integrated circuits on InP can be found in Kaiser and Heidrich (2002).

Electronic components can also be fabricated with this material system, by incorporating Si, Be, Zn, and realizing p- or n-doped areas. The properties of the semiconductor compound ($\mathrm{Ga}_x\mathrm{In}_{1-x}\mathrm{As}_y\mathrm{P}_{1-y}$) can be described by Vegard's law. Using this law and the known semiconductor compounds GaAs, GaP, InAs, and InP it is possible to determine the coefficients x and y (Fiedler and Schlachetzki 1987).

$$L_\mathrm{C}\left(Ga_xIn_{1-x}As_yP_{1-y}\right) = xyL_\mathrm{C}\left(\mathrm{GaAs}\right) + x\left(1-y\right)L_\mathrm{C}\left(\mathrm{GaP}\right) + y\left(1-x\right)L_\mathrm{C}\left(InAs\right) + \left(1-x\right)\left(1-y\right)L_\mathrm{C}\left(InP\right),$$

where L_C is the lattice constant. The composition of the semiconductor compound is displayed over the bandgap energy or the bandgap wavelength at room temperature in most diagrams and not x and y. The bandgap of common semiconductors is displayed in Fig. 3.17.

Physical properties of InP and of lattice matched $\mathrm{Ga}_x\mathrm{In}_{1-x}\mathrm{As}_y\mathrm{P}_{1-y}$ at room temperature (300 K) are presented in Table 3.2 (Fiedler and Schlachetzki 1987, Della Corte et al. 2000).

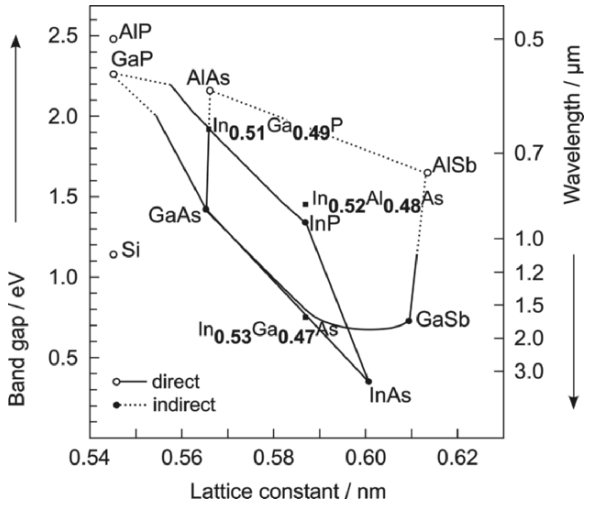

Fig. 3.17. Bandgap of III–V semiconductor compounds in eV and wavelength

Table 3.2. Physical properties of InP and of lattice matched $Ga_xIn_{1-x}As_yP_{1-y}$ at room temperature (300 K)

	symbol	unit	InP	$Ga_xIn_{1-x}As_yP_{1-y}$
lattice constant	L_C	nm	0.58688	
lattice match to InP				$y = 2.202x/(1 + 0.0659y)$
bandgap energy	W_g	eV	1.35	$1.35 - 0.72y + 0.12y^2$
electron mass/m_0	m_e/m_0		0.077	$0.07 - 0.0308y$
heavy hole mass/m_0	m_{hh}/m_0		0.6	$0.6 - 0.218y + 0.07y^2$
light hole mass/m_0	m_{lh}/m_0		0.12	$0.12 - 0.078y + 0.002y^2$
refractive index ($\lambda = 1.55\,\mu m$)	n_{eff}		3.169	
dielectric constant (static)	ε_s		12.35	$12.35 + 1.62y - 0.055y^2$
dielectric constant (high frequency)	ε_∞		9.52	$9.52 + 2.06y - 0.205y^2$
density	ρ	g cm^{-3}	4.81	$4.81 + 0.74y$
$\Delta W_g/\Delta T$		10^{-4} eV K^{-1}	-2.67	$-2.67 + 0.102y + 0.073y^2$
temperature dependence of the refractive index at 300 K	$\frac{dn}{dT}$	K^{-1}	2.01×10^{-5}	
temperature dependence of the refractive index ($\lambda = 1.523\,\mu m$)	$\frac{dn}{dT}$	K^{-1}	$-2.17\times10^{-10}\times T^2 + 3.5 \times 10^{-7} \times T + 1.15 \times 10^{-4}$	
length increase due to temperature	$\frac{1}{l} \cdot \frac{dl}{dT}$	K^{-1}	0.475×10^{-5}	

The refractive index of InP plotted against the photon energy is shown in Fig. 3.18[6].

3.4.2 The Semiconductor Compound AlGaAs

The AlGaAs material system is used in the same context as the GaInAsP material system and is a major optical material used for lasers and passive waveguide based devices. This material system is used as a barrier material in GaAs-based heterostructure devices. It is favorably used to fabricate field

[6] http://www.ioffe.ru/SVA/NSM/nk/A3B5/Gif/inp.gif

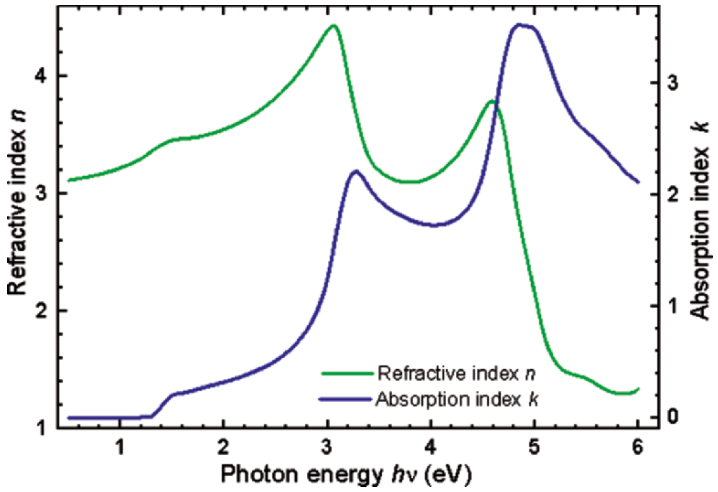

Fig. 3.18. Refractive index of InP vs. photon energy

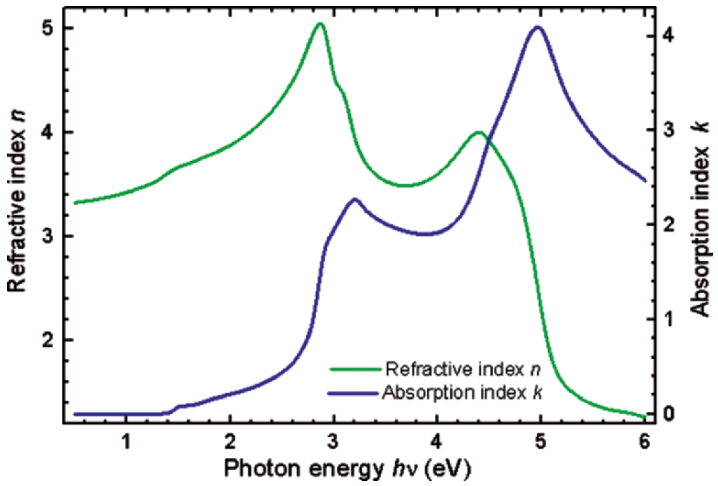

Fig. 3.19. Refractive index of GaAs versus photon energy

effect transistors like for example high electron mobility transistors (HEMTs). Some common physical properties of GaAs and AlGaAs are listed in Table 3.3.

The refractive index of GaAs plotted against the photon energy is shown in Fig. 3.19[7].

3.4.3 Lateral Coupling in GaInAsP/InP

One of the first passive ring resonator filters in this material system are presented in Vanderhagen et al. (1999). Racetrack shaped ring resonators with a

[7] http://www.ioffe.ru/SVA/NSM/nk/A3B5/Gif/gaas.gif

Table 3.3. Physical properties of GaAs and of $Al_xGa_{1-x}As$ at room temperature (300 K)

	symbol	unit	GaAs	$Al_xGa_{1-x}As$
lattice constant	L_C	nm	0.565325	$0.56533 + 0.00078x$
bandgap energy	W_g	eV	1.424	$x < 0.45$: $1.424+1.247x$ x > 0.45: $1.9+0.125x+0.143x^2$
electron mass/m_0	m_e/m_0		0.063	$0.063+0.083x$ (x < 0.45)
heavy hole mass/m_0	m_{hh}/m_0		0.51	$0.51 + 0.25x$
light hole mass/m_0	m_{lh}/m_0		0.082	$0.082+0.068x$
refractive index ($\lambda = 1.55\,\mu m$)	n_{eff}		3.3	$3.3 - 0.53x+0.09x^2$
dielectric constant (static)	ε_s		12.9	$12.90 - 2.84x$
dielectric constant (high frequency)	ε_∞		10.89	$10.89 - 2.73x$
density	ρ	g cm^{-3}	5.32	$5.32 - 1.56x$
temperature T dependence of the energy gap $E_g(0 < T < 10^3$ in K).		eV	$1.519 - 5.405 \cdot 10^{-4} \times T^2/(T + 204)$	
temperature dependence of the refractive index ($\lambda = 1.523\,\mu m$)	$\frac{dn}{dT}$	K^{-1}	$-1.86 \times 10^{-10} \times T^2 + 3.49 \times 10^{-7} \times T + 1.47 \times 10^{-4}$	

http://www.ioffe.rssi.ru/SVA/NSM/Semicond/GaAs/index.html
http://www.ioffe.rssi.ru/SVA/NSM/Semicond/AlGaAs/index.html
Della Corte et al. 2000

radius of 125 µm and coupler lengths of 80 µm are demonstrated. The layout and the layer sequence of the waveguide are shown in Fig. 3.20. The waveguide layers are grown by metal organic vapor phase epitaxy (MOVPE). A 100 nm thick SiN layer is used as the etching mask which is grown by PECVD. The waveguide patterns are transferred to the SiN layer by photolithography and a CHF_3 based RIE process. The waveguides are etched using a CH_4/H_2 and O_2 process.

A bi-level etching technique that permits the use of standard photolithography for lateral coupling to deeply etched racetrack shaped ring resonator structures is presented in Griffel et al. (2000), where a ring laser is fabricated and characterized. Here, deep etching is used to reduce the bending loss at the curved sections, but is avoided in the coupling region where the straight sections

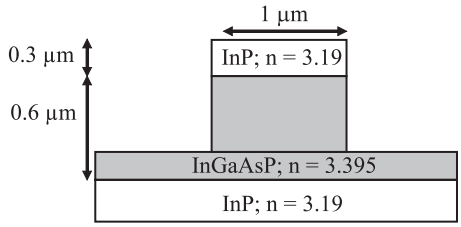

Fig. 3.20. Waveguide structure and composition

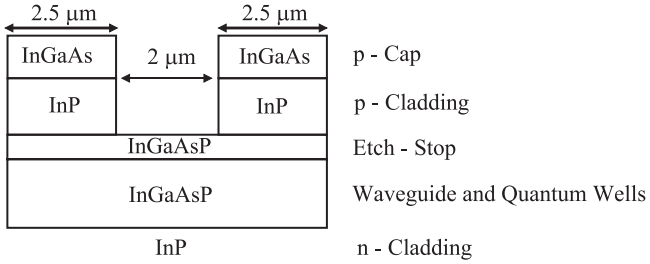

Fig. 3.21. Layer sequence of the waveguides in the coupling region

of the racetrack shaped ring resonator and the input/output waveguides form a gap whose distance defines the power coupling coefficient (Fig. 3.21). This is a way of eliminating the drawback of lateral coupling and realizing defined coupling parameters. A radius of curvature of 150 µm is combined with four different coupler lengths of 50 µm, 100 µm, 150 µm, and 200 µm, positioned at the center of the straight section of the racetrack, which is 50 µm longer. The width of the used ridge waveguides is 2.5 µm and the gap between resonator and coupling waveguides is 2 µm. The active waveguide consists of three compressively strained GaInAsP quantum wells imbedded in a 70 nm waveguide structure of two compositions with bandgap energy $E_g = 1.13$ and 1.00 eV. The layer sequence of the used waveguide is shown in Fig. 3.21.

A similar method is used in Rabus and Hamacher (2001) where a 3 dB MMI coupler of length 150 µm is used for coupling in and out of single and serially double coupled racetrack shaped ring resonators. Here the rings were deeply etched along the outer wall of their curved sections (Fig. 3.22) leading to a stronger optical confinement.

Passive single and double racetrack shaped ring resonator with a radius of 100 and 200 µm, respectively, are presented. The layer sequence of the used waveguide is shown in Fig. 3.23. The GaInAsP waveguide material used for the realization of the devices has a bandgap wavelength of $\lambda_g = 1.06$ µm at room temperature which can also be written as Q(1.06) referring to quaternary material.

The fabrication of the waveguides starts with depositing the silicon nitride (SiN_x) mask, realized by PECVD. It serves as the etching mask for the

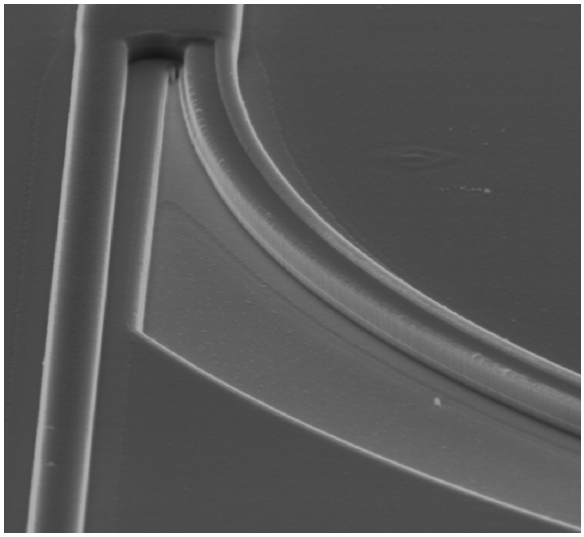

Fig. 3.22. Scanning electron microscope (SEM) photograph of the input region of an MMI coupler with deep etching along the outer walls of the curved sections

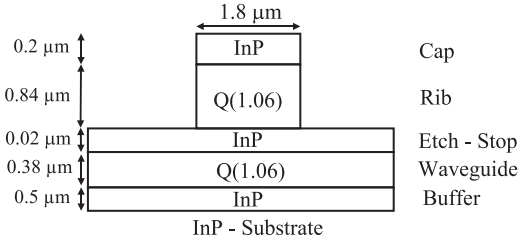

Fig. 3.23. Layer sequence of the waveguide

waveguides. The thickness of the SiN_x is ≈200 nm and is deposited at a temperature of 370°C. The structuring of the SiN_x layer is performed using standard photolithography. The photoresist used is AZ5214. An exposure dose of 12 mW cm^{-2} is used. The exposing time is 24 s and the developing time is between 40 and 50 s for a positive exposure. The developer used is MIF724. The developed photoresist serves as the etching mask for the following RIE process. The etching is done using the gases CHF_3 (22 sccm) and O_2 (2.2 sccm) at a pressure of 12 µbar and 50 W. The photoresist is removed after this RIE step and the structured SiN_x layer serves as the mask for the next RIE step. The gases now used for etching the waveguide are CH_4 and H_2 (6, 40 ml min^{-1}). In order to reduce the formation of polymers during dry etching and to minimize the sidewall roughness, a small fraction of O_2 (0.3 ml min^{-1}) is added. The power used is 150 W at a pressure of 0.02 mbar. The etching is controlled by an ellipsometer and a mass spectrometer. The etching is stopped

when the InP etch stop layer is detected. The next dry etching step is the realization of the deeply etched section on the outer wall of the waveguides in the curvatures. The SiN_x layer from the previous step serves as the etching mask which is structured again with standard lithography to open an etching window for this process. The photoresist which is used to structure the SiN_x layer therefore covers only a part of the waveguide, ideally only half of it. This self aligning process assures that the width of the waveguide is not changed by this processing step. The etching is again performed using RIE, but this time without the portion of oxygen which could partly remove the photoresist mask and cause etching errors. The photoresist is removed after dry etching by the use of an oxygen plasma (15 min, power = 500 W, $T \leq 200°C$). An SEM photograph of a waveguide in the curvature is shown in Fig. 3.24. The samples are AR coated to avoid Fabry–Perot resonances in the bus waveguides.

In Rommel et al. (2002) a $Cl_2/Ar/H_2$ chemistry is used to etch InP-based racetrack ring resonators using inductively coupled plasma reactive ion etching. An SEM photograph of a fabricated racetrack shaped ring resonator notch filter is shown in Fig. 3.25.

The composition of $Cl_2/Ar/H_2$ has a strong influence on the degree of undercut in the profile. A nearly perfect anisotropic profile is achieved for ratios between 2/3/1 and 2/3/2. Waveguide losses of 2 dB cm^{-1} are obtained. The straight length of the coupling region is 90 µm. The ridge width is 0.9 µm, and the coupling gap has a width of 275 nm. A radius of 15 µm is used in the curved regions. The etching depth is 4 µm. Three distinct etching profiles are obtained by adding H_2. For the Cl_2 dominated region ($Cl_2/Ar/H_2$ ratios between 2/3/0 and 2/3/1.5), high etch rates: 1.8 µm/min and large undercuts of InP and GaInAsP layers are reported. The second region ($Cl_2/Ar/H_2$ ratios between 2/3/1.5 and 2/3/2.5) has balanced chemistry yielding low but uniform etch rates between 0.5 and 0.6 µm min^{-1} and

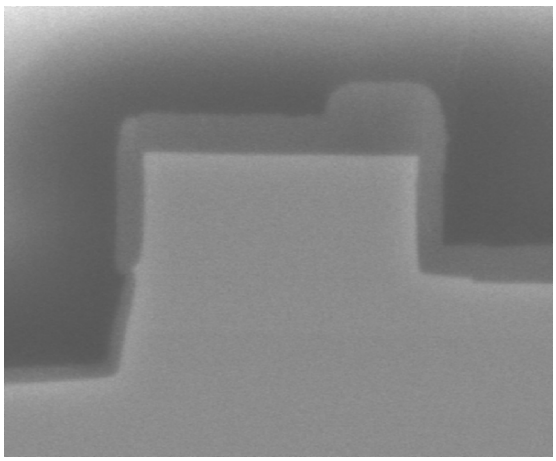

Fig. 3.24. SEM photograph of a waveguide in the curvature

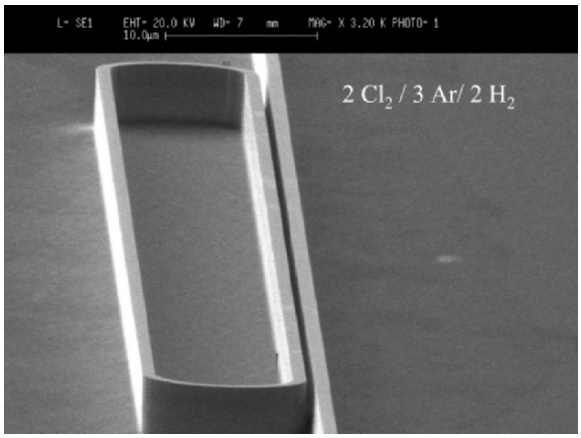

Fig. 3.25. The ridge is etched to a depth of 5 µm, and has a width of 0.9 µm and gap of 275 nm.

Reused with permission from S.L. Rommel, Journal of Vacuum Science and Technology B, 20, 1327 (2002) ©2002 AVS The Science and Technology Society

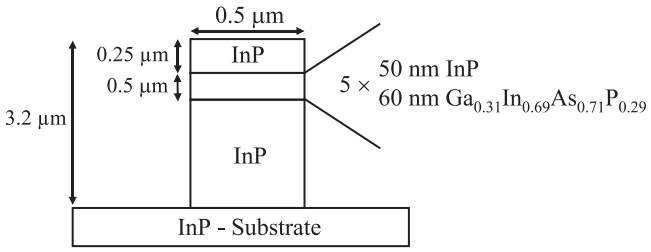

Fig. 3.26. Layer structure of laterally coupled ring resonator in InP

highly anisotropic InP/GaInAsP profiles. A H_2 dominated region is reported for $Cl_2/Ar/H_2$ ratios above 2/3/2.5. In this region, InP layers exhibit large undercuts, whereas GaInAsP layers showed little lateral etching. The authors suggest that the selectivity of GaInAsP layers relative to InP may be increased by increasing the As concentration.

One of the smallest racetrack shaped ring resonators in InP with a radius in the curved sections of 2.25 µm is presented in Grover et al. (2003) where an FSR of 19 nm near 1,550 nm, with an extinction of more than 25 dB is reported. The length of the straight sections is 10 µm and the coupling gap is only 200 nm. The bus waveguide is tapered to a width of 3 µm away from the coupling region to improve the fiber to chip coupling. The layer sequence of the device is shown in Fig. 3.26.

The refractive index of the used $Ga_{0.31}In_{0.69}As_{0.71}P_{0.29}$ compound is 3.39. The fabrication details are taken from Grover (2003). The process is started by depositing a wafer with 900 nm of silicon dioxide by PECVD. A Leica VB6

e-beam lithography machine is used to pattern a bilayer film of polymethylmethacrylate (PMMA). The patterning is started by spinning on 100 K MW 5% PMMA in Anisole at 4,000 rounds per minute (RPM) for 60 s, which gives a 113 nm thick film. A bake follows for 15 min at 170°C. Next 495 K MW PMMA A4 in Anisole is spin-coated at 2,000 RPM for 60 s, which leads to a 204 nm thick film. This is followed by a bake for 15 min. at 170°C. Finally the pattern is written using a dosage of $736\,\mu C/cm^2$ for waveguides and ring resonators, and $610\,\mu C\,cm^{-2}$ for device labels. The PMMA-based resist is developed with 2-methyl-2-pentanone (methyl isobutyl ketone or MIBK) diluted with 2-propanol as 1:3 for 2 min 30 s. In a final step the wafer is rinsed with 2-propanol and nitrogen is used to blow-dry.

The reason for choosing two layers of PMMA is to have the lower resolution PMMA on the bottom and the higher resolution PMMA on top, so that there is an overhang of the higher resolution PMMA where the pattern is written. This also enables a better liftoff in the following process. Next, a 50 nm thick layer of chromium is deposited and patterned by liftoff in warm 1-methyl-2-pyrrolidone (C_5H_9NO) also referred to as NMP. The pattern is transferred to the underlying silicon dioxide by dry etching in trifluoromethane oxygen plasma. Then the InP and quaternary layers are etched by a methane hydrogen plasma to a depth of 3.2 µm using a Cr–SiO_2 mask. The methane based dry etching process evaluating several mask (Ni, NiCr, Ti, SiO_2, and Ti–SiO_2) is presented in Grover et al. (2001c). Then in a final step, the mask is stripped with buffered hydrofluoric acid.

InP based devices are usually thinned to a thickness between 100 and 200 µm by a bromine methanol based lapping process. This ensures a better cleavage of the samples and reduces the contact resistance if active devices with top side p and backside n contact are realized.

Buried heterostructure ring resonators are presented in Choi et al. (2004b). Ring resonators with a radius of 200 µm are fabricated by first growing a 0.4 µm thick GaInAsP ($\lambda_g = 1.25\,\mu m$) waveguide layer on a (001) oriented InP substrate by metal organic chemical vapor deposition (MOCVD). The waveguide layer is then covered by a SiN_x layer which serves as the mask for the following CH_4 based dry etching process. The bus waveguides are aligned parallel to the [110] direction in the crystal lattice. The width of the buried waveguides is between 0.8 and 0.9 µm. The polymers generated on the sidewalls during the dry etching process are removed by an oxygen plasma treatment and the SiN_x mask is removed by a buffered oxide etchant. The waveguides are covered by a 1.5 µm thick InP layer. Finally the sample is thinned, cleaved, and AR coated. The waveguide loss of the straight bus sections is measured to be between 0.2 and $0.3\,cm^{-1}$. The dimensions and layout of the buried waveguide are shown in Fig. 3.27.

SEM photographs of a waveguide section and a cross-section of a buried waveguide are shown in Fig. 3.28.

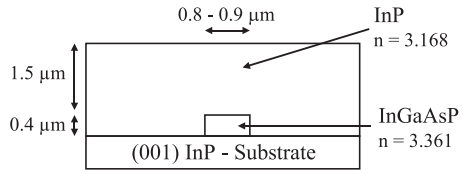

Fig. 3.27. Dimensions and layout of the buried waveguide

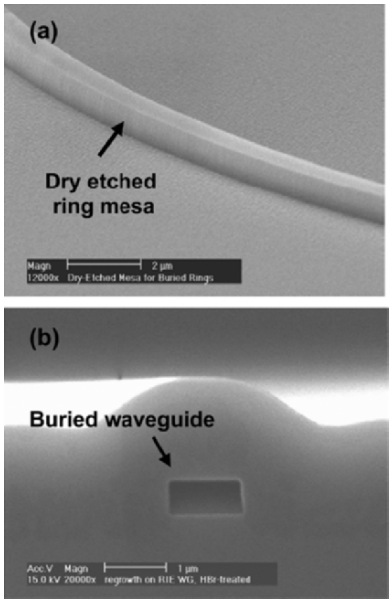

Fig. 3.28. (**a**) SEM image of a dry-etched ring resonator mesa. (**b**) SEM cross-sectional view of a buried waveguide.

Reprinted with permission from IEEE Photonics Technology Letters, vol. 16, pp. 2266–2268 ©2004 IEEE

3.4.4 Vertical Coupling in GaInAsP/InP

One of the first vertically coupled disk resonators with a diameter of 44 µm, both in the GaAs and InP materials systems, fabricated by wafer bonding is presented in Tishinin et al. (1999). The device design in both material systems incorporates an etch-stop layer (0.2 µm thick layer of InGaAs/InP and $Al_{0.95}Ga_{0.05}As$/GaAs) and two waveguiding layers (waveguide layers 0.5 µm thick and disk layers 0.3 µm thick) with low index material layer (thickness 0.5 µm) in between. In the GaAs sample, Al_xO is used for lateral

confinement of the light in the disk structure. The bus waveguides and disk are fabricated by standard optical lithography and chlorine based ECR-RIE. First, the waveguides are etched down through both the top cladding layer and the waveguiding layer and etching is stopped within the separation layer. The bus waveguides are multimode and have a width of 2 µm. After etching the bus waveguides, this processed side is wafer bonded to another substrate and the original substrate is removed after it has been lapped down to a thickness of 100–150 µm by selective chemical wet etching. GaAs samples are bonded to GaAs and InP samples to InP substrates. A bonding temperature for GaAs wafers of 750°C and of 400°C for InP-based materials is used. It is important to mention that the transfer substrate need not be the same material. After the removal of the original substrate, the disk is fabricated by back side alignment optical lithography and ECR-RIE.

A vertically coupled GaInAsP thin film disk resonator with a diameter of 10 µm resulting in an FSR of 20 nm using polymer wafer bonding with benzocyclobutene (BCB) is presented in Ma et al. (2000c). The wafer structure with a 0.4 µm thick GaInAsP ($\lambda_g = 1.2\,\mu m$) guiding layer is grown on an InP substrate by molecular beam epitaxy (MBE). A 400 nm thick SiO_2 layer is used as a hard mask and is deposited by PECVD. The wafer is patterned using electron beam lithography with a 180 nm thick 2% polymethylmethacrylate (PMMA) resist. The structured PMMA resist is transferred to the underlying SiO_2 layer using RIE. Inductively coupled plasma (ICP) RIE with a gas mixture of Cl:Ar (2:3) is used to transfer the pattern onto the epitaxy wafer through the SiO_2 hard mask at a temperature of 250°C. The waveguides are etched to a depth of about 1.3 µm. The SiO_2 hard mask is removed after RIE using buffered HF. The BCB bonding process is started by spin coating BCB onto both the patterned wafer and the transfer wafer (here GaAs is used). Then the wafers are brought into contact with their BCB side facing each other using an appropriate weight. The wafer stack is put into a nitrogen filled furnace at 250°C for 1 h. BCB becomes fully cured and the two wafers are glued together. The overall thickness of BCB is 3 µm. The InP substrate is removed after bonding using selective wet etching ($HCl : H_3PO_4 = 2 : 3$). The input and output waveguides are 2 µm wide and are tapered down (taper length = 500 µm) to 0.4 µm in the disk region. The bus waveguides and the disk are separated by a gap of approximately 180 nm.

Vertically coupled single mode ring resonators also using BCB wafer bonding with a radius of 5 and 10 µm are presented in Grover et al. (2001a) and Grover (2003). The layer sequence of the used device is shown in Fig. 3.29.

The patterns are transferred by photolithography to a 400 nm thick SiO_2 layer using a 10× i-line stepper and a CHF_3/O_2 plasma RIE process. The waveguides and ring resonator in GaInAsP–InP are etched using SiO_2 as the mask in a reactive ion etching system with a $CH_4/H_2/Ar$ plasma.

The fabrication process starts with etching of alignment keys to a depth of 2 µm down to the GaInAs layer. The use of Alignment keys eliminates the use of infrared (IR) backside alignment for processing the other side. Then

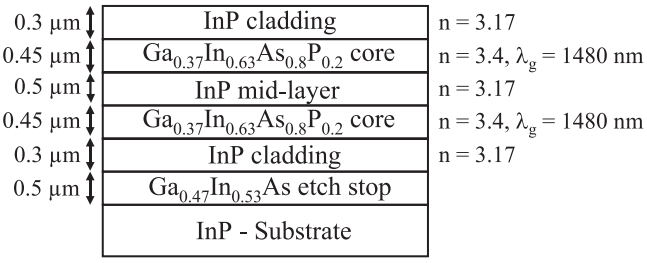

Fig. 3.29. Layer structure used for BCB bonded vertically coupled ring resonators

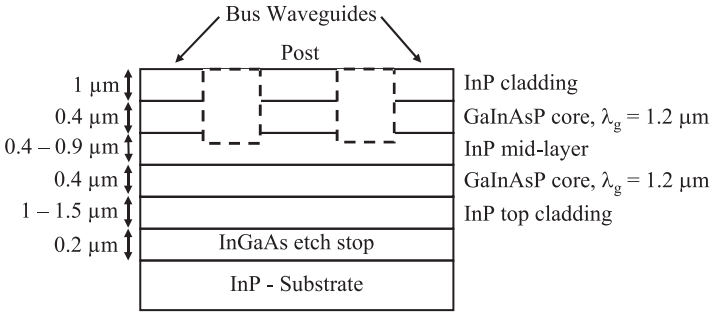

Fig. 3.30. Design of vertically coupled disk resonator

the waveguide layer is etched to a depth of 0.9 µm. Benzocyclobutene (BCB; n = 1.5) is used for bonding to a GaAs transfer substrate. A thickness of 1–2 µm is chosen for the BCB layer. The growth substrate is thinned to a height of about 100 µm by chemo-mechanical polishing. The remaining growth substrate is selectively etched and removed using H_3PO_4:HCl (1:1) which stops at the GaInAs etch stop layer. This etch stop layer is then selectively etched using H_2O_2:H_2SO_4:H_2O (1:1:10) which stops at the InP layer opening the second GaInAsP–InP layers for fabricating the ring resonator. The top layer is etched to a depth of 0.9 µm, leaving a gap of 200 nm to decrease losses caused by leakage to the substrate. Finally the whole device is encapsulated with BCB.

This fabrication process uses the advantages of both materials combining GaInAsP and GaAs. As appropriate, either layers of GaInAsP or GaAs are removed leading to a vertically coupled device.

A thermal wafer bonding process is used in Djordjev et al. (2002c) to realize vertically coupled disk resonators with radii of 4, 6, 8, 10, 12 µm. The layer sequence and design are shown in Fig. 3.30.

A novel feature which is incorporated in the design of the disk resonator is a circular post below the resonator. It improves the mechanical stability of the structure, improves current/field uniformity in active devices and suppresses higher order modes improving the transmission characteristics. A disk supports whispering gallery modes, which propagate by means of total internal

reflection from the disk/air interface (see Chap. 6). The first order mode has the smallest volume and occupies the outmost region of the disk in the radial direction. All of the higher order modes have larger volume and are therefore closer to the center of the disk which results in a leakage into the post. The post and the waveguides are separated by 1.2 µm which is large enough to prevent coupling between them.

The fabrication process is described using (Djordjev 2002). The layers are grown by low pressure MOCVD on a (001) InP substrate at 655°C. A 100 nm thick SiN_x is used as a hard mask for the bus waveguide and disk etching process which is deposited at 275°C with a power of 30 W using a pressure of 450 mTorr[8] and the gases $SiH_4/NH_3/N_2$ at a ratio of 40/20/60. This silicon nitride layer is structured using Shipley S1813 photoresist and a low pressure (10 mTorr) ECR-RIE CF_4 (30 sccm) plasma at 20°C, 500 W for 300 s. Before spin coating the photoresist, Silicon Resources AP405 is used to increase the adhesion of the photoresist on the silicon nitride. The photoresist is developed using Microposit MF321 developer. The bus waveguides are etched using a $CH_4/H_2/Ar$ RIE process. The process used is described in detail in Choi et al. (2002b). The width of the waveguides is between 0.7 and 0.9 µm. The waveguide width is tapered adiabatically to 2.5 µm to the edge of the chip to enhance fiber chip coupling. After the etching of the bus waveguides, the sample, which is usually 1 cm^2, is bonded to a transfer substrate of the same size. The cleanliness of the surface of the samples is vital for the following bonding process and many cleaning steps are performed (deionized (DI) water, trichloroethylene (TCE), acetone, methanol). After a final DI water rinse, both samples are brought into contact under water and are "wet bonded." This prevents oxidation and contamination of the surfaces. The samples are then loaded into a chamber which is evacuated and heated to 100°C for 10 min. Then H_2 is led into the chamber and the samples are heated to a bonding temperature of 505°C for 30 min. In a final bonding step, the samples are cooled down to room temperature in 15 min. The fabrication of the disk starts by removing the InP substrate which is done using mechanical polishing and a selective chemical wet etch (HCL:H_2O – 3:1). The etching is automatically stopped, when the InGaAs layer is reached. The etch stop layer is then removed using H_2SO_4:H_2O_2:H_2O (1:1:3) which opens the waveguide layers of the disk. In order to align the bus and the disk waveguides, the sample is etched down to the waveguide pattern on the edge in a small area making the alignment marks visible which have been patterned together with the bus waveguides. The disk is etched after the opening of the alignment marks using the same processing steps as for etching the bus waveguides.

One of the first ring resonators coupled to buried heterostructure (BH) bus waveguides in GaInAsP are presented in Choi et al. (2004a). A two step regrowth process is used in fabricating the devices. The radius of the ring resonators is 10 µm. The buried bus waveguides are made by growing a 0.4 µm

[8] 760 Torr = 1 atm = 101, 325 kPa = 1013, 25 hPa = 1, 01325 bar

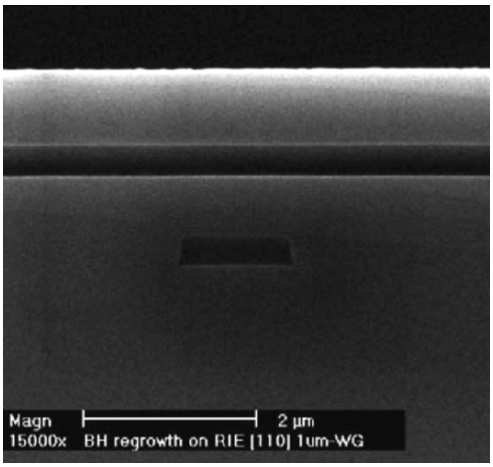

Fig. 3.31. Cross-section of a planar vertically stacked waveguide produced on BH mesas.

Reprinted with permission from IEEE Photonics Technology Letters, vol. 16, pp. 828–830 ©2004 IEEE

thick layer of GaInAsP with a bandgap wavelength of 1.1 µm on to an InP substrate followed by an SiN_x masking and etching step. The width of the bus waveguides is 1 µm. The area between the bus waveguides is filled with epitaxially grown InP. The silicon nitride masking layer is removed and the second growth step is initiated leading to the ring resonator. The material for the waveguide layer which has a thickness of 0.4 µm is GaInAsP with a bandgap wavelength of 1.4 µm. The ring waveguide and the bus waveguides are separated by a 0.8 µm thick InP buffer layer. The InP cladding layer for the ring waveguides has a thickness of 1 µm. An SEM photograph of a cross section of the ring resonator device showing the buried bus waveguides and the layer for fabricating the ring resonator is shown in Fig. 3.31. The fabricated ring resonator is shown in Fig. 3.32. The bus waveguides are AR coated to avoid Fabry–Perot resonances.

3.4.5 Lateral Coupling in AlGaAs/GaAs

One of the first ring and disk resonators based on this material system are presented in Rafizadeh et al. (1997b). Ring and disk resonators with diameters of 10.5 µm and 20.5 µm have been fabricated and characterized. The layer sequence of the used device is shown in Fig. 3.33.

The layers are grown by MBE. The coupling gap used is only 100 nm wide. A waveguide loss of 3.2 cm^{-1} is measured for TM polarized light at a wavelength of 1.55 µm. The devices are created by writing patterns upon a PMMA resist layer by electron-beam lithography (JEOL JBX 5DII). The AlGaAs/GaAs is etched using chemically assisted ion-beam etching (CAIBE).

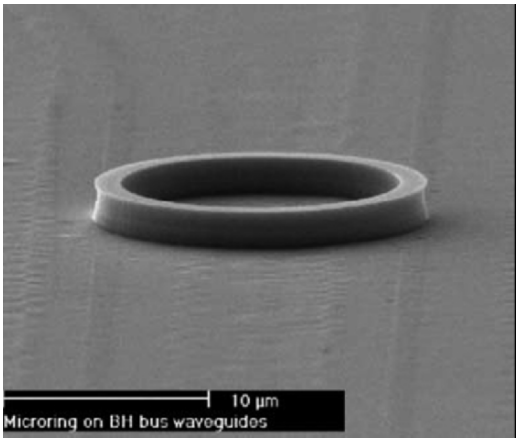

Fig. 3.32. Ring resonator coupled to buried heterostructure bus waveguides. Reprinted with permission from IEEE Photonics Technology Letters, vol. 16, pp. 828–830 ©2004 IEEE

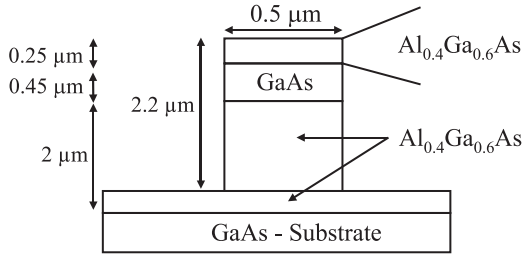

Fig. 3.33. Layer structure of AlGaAs/GaAs based ring and disk resonator

The electron-beam lithography exposure conditions are a 300 pA probe current, a 50 eV acceleration potential, an 80 µm × 80 µm field, and an 11 mm working distance. The PMMA mask is transferred to an underlying SiO_2 layer by RIE which provides a robust mask capable of withstanding the CAIBE process. The CAIBE parameters used, are a beam voltage of 500 V, a beam current density of 0.14 mA cm^{-2}, a chlorine flow rate of 15 standard cubic centimeters per minute (SCCM) at STP[9], an argon flow rate of 2 SCCM, and an elevated substrate temperature of 100°C. The SiO_2 mask is removed after the CAIBE process. The etch rate achieved is 0.1 µm min^{-1}. The sidewall roughness (vertical striations) observed under the SEM is 10–20 nm.

A similar layer sequence with waveguide parameters in the same range is presented in Absil (2000) where racetrack shaped ring resonators with radii between 1.2 and 10 µm have been realized. The layer sequence and dimensions of the used waveguide is shown in Fig. 3.34.

[9] Standard temperature and pressure. The volume measurement is made at or adjusted to a temperature of 0°C and a pressure of 1 atmosphere, or 101.325 kPa

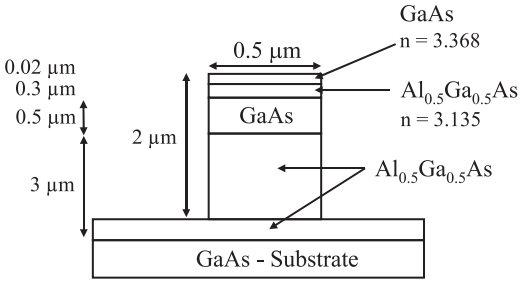

Fig. 3.34. Layer sequence and dimensions of AlGaAs/GaAs waveguide

A coupling gap between 0.1 and 0.3 µm is envisaged. The fabrication of the laterally coupled ring resonator devices starts by depositing a 420 nm thick SiO_2 layer with a nominal deposition rate of 13.6 nm min^{-1} by PECVD at 300°C which serves as the mask for the CAIBE process. Before deposition of the SiO_2 layer, the sample is rinsed in acetone, methanol and isopropanol followed by a 20 min soak in OPD 4262 (a photoresist developer) to increase oxide adhesion on the surface of the wafer. After deposition of the oxide mask layer, the sample is solvent cleaned and dried in a vacuum oven at 120°C for 1 h. This step is used to increase the adhesion of the electron beam PMMA resist on the oxide. The PMMA resist is spin coated onto the sample leading to a thickness of 500 nm. The resist is cured on a hotplate at 195°C for 150 s. A Leica Cambridge EBMF 10.5 is used at 50 keV to transfer the ring resonator patterns to the resist. The sample is developed using a solution of MIBK:IPA (1:3) at 25°C for 150 s and rinsing with isopropanol. The patterns are transferred from the PMMA to the underlying oxide mask layer by RIE using CHF_3 and O_2 (18:2) with a pressure of 40 mT and an RF power of 175 W. The etch rate of the oxide is 32.5 nm min^{-1}. The waveguides are etched using a CAIBE process in an ultrahigh vacuum system with 200 eV argon ions and chlorine gas. The etch rate for GaAs is 0.08 µm min^{-1}. The etching process is performed in three etching runs in order for the sample to cool down. After etching, the oxide mask is removed in an HF dip. Then the sample is spin coated with a 4 µm thick layer of cyclotene or BCB which serves as a protection and planarization layer. The polymer is cured at 200°C for 2 hours. The chip is thinned down in a final step to a thickness of 100 µm which is similar to the InP based devices, also using a bromine/methanol chemo-mechanical process. In order to avoid Fabry–Perot resonances in the bus waveguides, the facets are AR coated using a 250 nm Al_2O_3 layer which has a refractive index of n = 1.62.

3.4.6 Vertical Coupling in AlGaAs/GaAs

One of the first BCB bonded vertically coupled ring resonators in this material system is presented in Absil et al. (2001), Grover et al. (2001b). Here a single

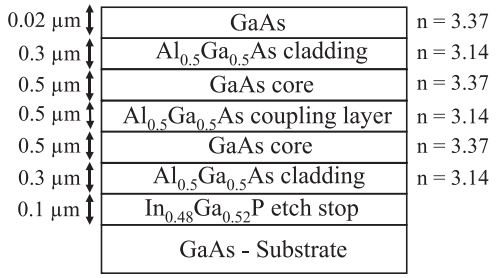

Fig. 3.35. Layer sequence of vertically coupled GaAs–AlGaAs ring resonators

ring resonator channel dropping filter and a 1×4 multiplexer/demultiplexer (MUX/DEMUX) crossbar array with double ring resonator filters is demonstrated. The radius of the fabricated ring resonators is 2.5 µm, 5 µm, and 10 µm. The waveguide width is 0.7 µm. The waveguides are tapered to 2.5 µm towards the facet of the chip to improve the fiber to chip coupling efficiency. The layer sequence of the used device is shown in Fig. 3.35. The layers are grown by MBE. A 10× i-line stepper is used for transferring the patterns by photolithography. ICP etching is used for fabricating the bus and ring waveguides. BCB with a thickness between 1 and 2 µm is used to bond the sample to a GaAs transfer substrate and cured at 200° C. After removing the original substrate, alignment of the ring resonator layer and etching the same, the sample is encapsulated with BCB. This ensures a refractive index symmetry profile, which is also necessary when identical ring resonator structures are realized on both layers for multiring resonators. In order to reduce the effect of layer misalignment a thin layer (∼0.2 µm) of AlGaAs is being unetched.

3.4.7 Implementation of Gain in Ring Resonators

Introducing gain inside the ring resonator adds additional functionality and device features. One of the first ring resonators with integrated semiconductor optical amplifiers (SOA) in the GaInAsP material system is demonstrated in Rabus et al. (2002b). Single, double and triple parallel and serially coupled ring resonators are presented in Rabus (2002). A photograph of a ring resonator with integrated SOA is shown in Fig. 3.36.

The SOA integration is based on a selective area MOVPE process which has also been used in Hamacher et al. (2000) to integrate lasers, photodiodes, waveguides, and spot size converters. The cross section of the used ridge waveguide (RW) semiconductor optical amplifier (SOA) structure is shown in Fig. 3.37. The dimensions are given in Fig. 3.38.

The layer sequence is given in Table 3.4. The layer sequence and composition of the used SOA is as follows (from bottom to top).

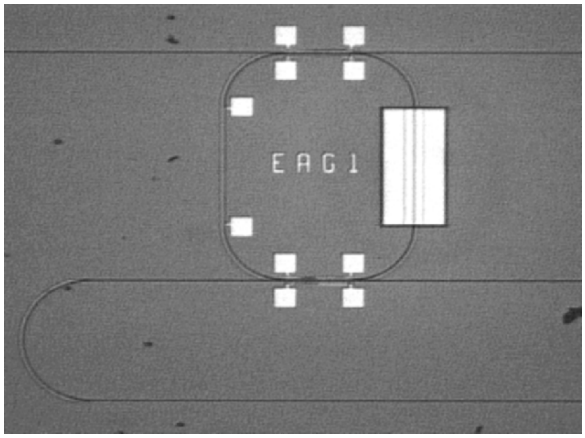

Fig. 3.36. Photograph of a ring resonator with integrated SOA

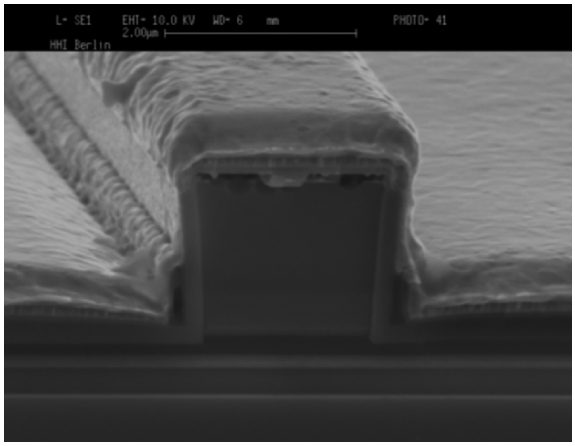

Fig. 3.37. SEM of cross-section of ridge waveguide SOA, covered with metal contact layer

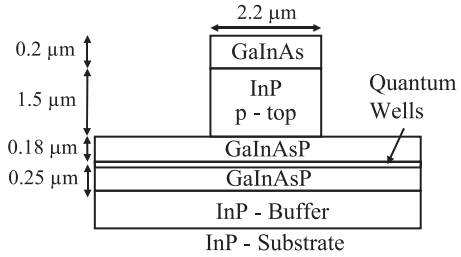

Fig. 3.38. Device structure of the SOA ridge waveguide

Table 3.4. Layer stack of the used SOA

no.	material	λ_g (nm)	thickness	dopand (cm^{-3})	function
1.	InP–Sn-sub.		360 µm		substrate
2.	InP-buffer		500 nm	Si : 3×10^{18}	buffer
3.	n-GaInAsP	1,150	250 nm	Si : 3×10^{18}	n-contact
4.	n-GaInAsP	1,290	10 nm	undoped	barrier
5.	Q 1% compressive strained		6 nm	undoped	6 × QW
6.	Q-1.29	1,290	10 nm	undoped	6 × barrier
7.	GaInAsP	1,150	180 nm	undoped	LD-WG
8.	InP		1,500 nm	Zn : 5×10^{17}	p-top
9.	GaInAsP	1,300	50 nm	Zn : 1×10^{18}	p-top
10.	InGaAs		200 nm	Zn : 1×10^{19}	p-contact

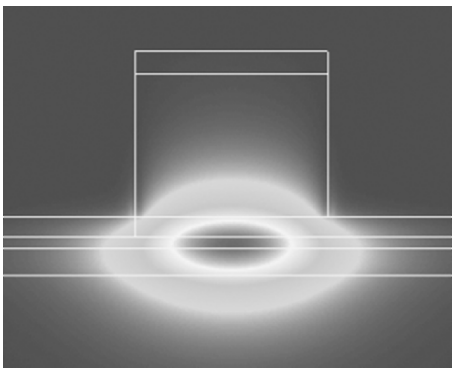

Fig. 3.39. Mode profile of the SOA (TE polarization)

The calculated mode field profile of the RW structure is given in Fig. 3.39. The quantum wells (QWs) and the barrier layers have been considered as one layer with an effective refractive index of $n_{\text{eff}} = 3.4$. Due to the multiquantum well structure, the SOA was designed for favoring TE polarization. The effective index of the SOA is determined to be $n_{\text{eff}} = 3.238$. The center of the guided mode in the RW structure is located lower compared with the passive waveguide structure. Thus, it is necessary for the integration process to adjust the height of the active–passive transition to assure minimal coupling losses.

The butt coupling losses at the passive–active waveguide interface have been calculated by the finite difference method (Fig. 3.40). The calculated vertical and lateral offset between the active and passive waveguide results in a minimum theoretical coupling loss of <1 dB.

The starting point for the calculation of the horizontal shift has been chosen so that the passive structure is located symmetrical in the center of the active section. The calculation of the vertical shift starts with the passive–active section, butt coupled at the position where the rib starts for the passive

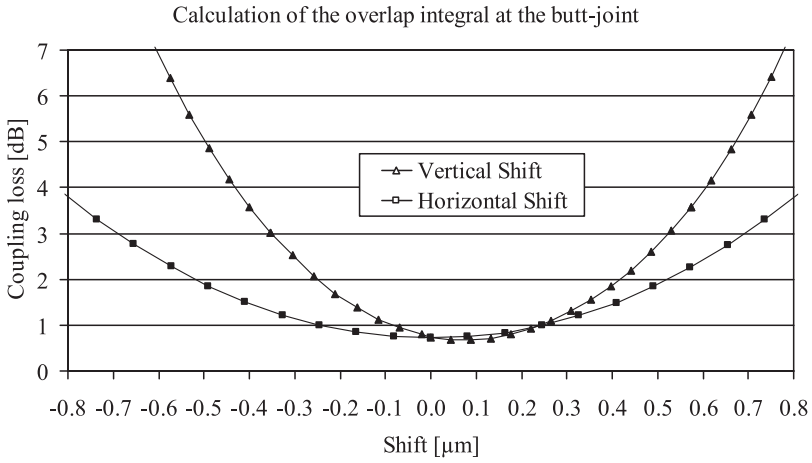

Fig. 3.40. Calculated butt-joint losses

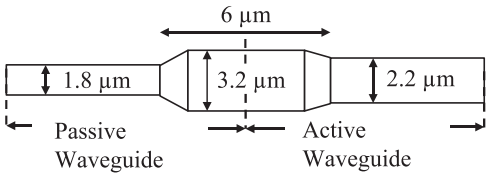

Fig. 3.41. Lateral dimensions of the active–passive waveguide interface

structure and in the middle of the active layers for the SOA section. The practical realization of the active–passive transition is done in using a special taper structure at the interface. The lateral design is shown in Fig. 3.41.

The use of the tapered structure enables the propagating wave coming from the passive waveguide to laterally broaden, interfere, and propagate into the active waveguide with a different refractive index and scale down to the dimension of the active waveguide.

Another technological challenge is the fabrication of a low resistance contact of the active section. As directly contacting the SOA on the ridge with a metal needle would destroy the SOA in the worst case, so called "support mesa" are designed at a distance of a few micrometer away from the SOA ridge on either side. The p-contact of the SOA is then located on these mesa for securely placing a measurement needle and for later wire bonding. The support mesas have the same active material layer stack as the SOA. The technological challenge lies in creating a low metal–semiconductor p-contact on the SOA. The isolation of the metal layer on top of the support mesa is performed with a SiN_x layer, which is removed only on top of the SOA waveguide. A sketch of the cross section of the SOA with support mesa is shown in Fig. 3.42. The n – contact is realized by metal coating the backside of the wafer.

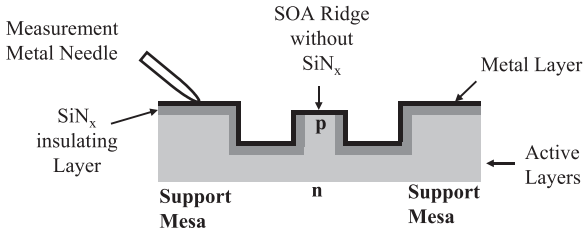

Fig. 3.42. Cross-section of the SOA section with support mesa

The fabrication starts with the epitaxial growth of the SOA layers by using MOVPE. The first CVD processing step is the deposition of an SiN_x layer which is ≈230 nm thick at a temperature of 370°C for the fabrication of the etching mask. The lateral active mesa structures are defined in a resist pattern by using standard photolithography (positive process, photoresist AZ5214, exposing time ≈24 s, developer MFI724, developing time ≈50 s). The resist pattern serves as an etching mask for the following reactive ion etching step (CHF_3 – 22 SCCM and O_2 – 2.2 SCCM, pressure = 0.012 mbar, power = 50 W). The photoresist is removed with an O_2 plasma (10 min, power = 500 W, T < 250°C) after this process. The p-top mesa are etched in the following step by using RIE (CH_4 – 8 ml min^{-1} and H_2 – 20 ml min^{-1}, pressure = 0.006 mbar, power = 200 W). In order to remove the polymer which is formed during reactive ion etching, an O_2 plasma (20 min, power = 550 W, T < 250°C) and a solution of KOH (20%) are used. The p-top is etched down to a distance of about 1.1–1.2 µm followed by a wet etching step by using a solution of 20 H_2O:5 HBr:H_2O_2. This wet etching process is the "undercut" etching. In this step, part of the sidewall is removed. A layer of InP protects the active sections underneath. The etching of the undercut is indispensable for the second epitaxial growth step of the passive waveguide. The undercut reduces the formation of high "rabbit ears" during selective area MOVPE at the vicinity of the mask and enables adequate control of the layer thickness in order to achieve the necessary vertical alignment within the active – passive transition. For further improvement of the SAMOVPE growth step, the "undercut" is covered by a layer of SiN_x which is realized by depositing the entire wafer with SiN_x and removing the material on the bottom of the wafer by reactive ion etching, leaving the sidewalls covered. The next step is the final etching of the p-top and the active layers using RIE (CH_4 – 8 ml min^{-1} and H_2 – 20 ml min^{-1}, pressure = 0.006 mbar, power = 200 W). The control of the etch depth is very important in order to adjust the regrowth of the passive material. The following step is the regrowth of the passive material using selective area MOVPE (SAMOVPE). The correct height of the passive material is defined by the thickness of an InP buffer layer. The regrowth process is followed by the removal of the entire SiN_x at the "undercut" using hydrofluoric acid (HF – 5%). After this step, the entire wafer

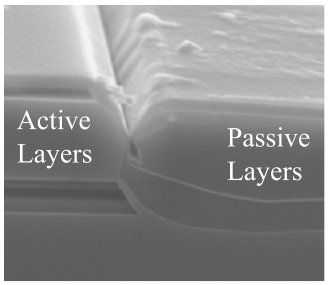

Fig. 3.43. Active–passive transition

is covered again with a SiN_x layer (≈190 nm) at a temperature of 370°C. An SEM photograph of the active – passive transition is shown in Fig. 3.43.

The SiN_x is removed at the top of the active mesa using a photolithographic step, followed by a dry etching step (CHF_3 – 22 SCCM and O_2 – 2.2 SCCM, pressure = 0.012 mbar, power = 50 W). The photoresist is removed after the dry etching step using KOH (20%). The following diffusion process (T = 575°C, 18 s) is carried out using zinc arsenide as the dopand. In the next step, the waveguide is etched together with the laser ridge in a so called self-aligning process, where the active–passive interface is generated using RIE (CH_4 – 6 ml min^{-1}, H_2 – 40 ml min^{-1}, O_2 – 0.3 ml min^{-1}, pressure = 0.02 mbar, power = 150 W). Due to the larger height of the laser ridge, the remaining material is etched by selective wet chemical etching using a solution of HCl and H_3PO_4 (1:4). The wet etching is automatically stopped, when the quaternary layers are reached. The deep etching of the passive waveguide, which is necessary in order to achieve sufficient optical confinement in small bent waveguides (radii <200 µm), is the next processing step. The etching mask material is again a SiN_x layer structured in a photolithographic and dry etching step. The SiN_x layer also serves as a protection layer for the laser ridge. The deep etching of the passive waveguide is done by reactive ion etching using CH_4 (8 ml min^{-1}) and H_2 (20 ml min^{-1}) with a pressure of 0.006 mbar and a power of 200 W. The SiN_x which was deposited for the protection of the SOA ridge has to be removed only at the very top of it, to be able to place a metal layer for realizing an electric contact. Therefore, the entire wafer is covered with photoresist and is exposed for a few seconds (≈14 s) at the areas of the SOA ridge which results in opening the tip of the laser ridge. The photograph of the top view of an SOA ridge with structured photoresist is shown in Fig. 3.44.

In this process the exposing time of the photoresist is the key figure. If the time is too high, the photoresist will become very thin between the SOA ridge and the support mesa and might uncover the insulating SiN_x layer which will be etched in the next fabrication step and so cause unwanted short cuts. On the other hand, if the exposing time is too short, only part of the photoresist on top of the SOA ridge is removed and the SiN_x layer can not entirely be

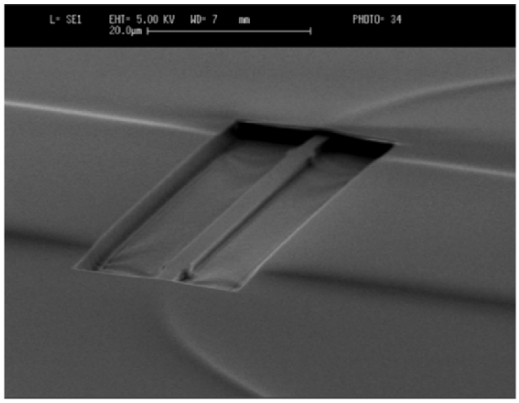

Fig. 3.44. Top view of an SOA ridge with structured photoresist

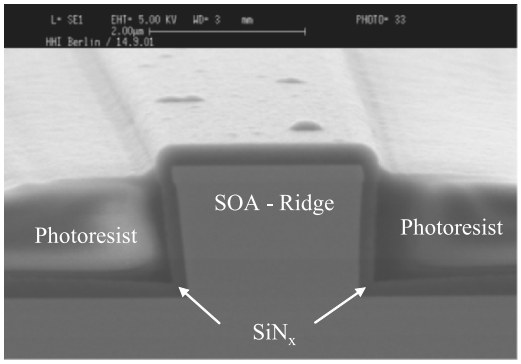

Fig. 3.45. SEM photograph of the cross section of a developed SOA ridge

etched away in the following process. The SEM photograph of the cross-section of a developed SOA ridge is shown in Fig. 3.45.

The SiN_x layer at the top of the SOA ridge is completely free of photoresist. The area in between the SOA ridge and the support mesa and also the entire wafer are covered by photoresist with a thickness of about 800 nm which is a sufficient amount for protecting the SiN_x layer from being etched in the next step. The SiN_x is removed from the p-top in a dry etching process (CHF_3 – 24 SCCM, H2 – 1 SCCM, pressure = 0.012 mbar, power = 50 W). Now, the metal contacts are fabricated starting with a photolithographic step for the definition of the contacts. The p-top of the SOA, the area in between the ridge and the support mesa and the top of the support mesa is deposited with titanium, platinum, and gold and the remaining metal is removed in a "liftoff" process using NMP (*n*-methyl-2-pyrrolidon, C_5H_9NO).

A vertically stacked asymmetric twin waveguide structure is used in Menon et al. (2004) to integrate an SOA into an MMI coupled single ring resonator notch filter. The asymmetric twin waveguide structure is grown on a (100)

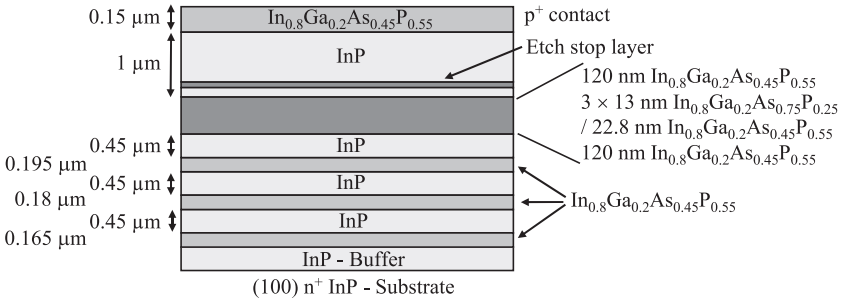

Fig. 3.46. Layer sequence of asymmetric twin waveguide structure

n^+ InP substrate using gas source MBE. The layer sequence is shown in Fig. 3.46. The width and height of the single mode passive waveguide is 4 µm and 1.9 µm, respectively. The SOA is formed by etching a 500 µm long stripe, and is coupled optically to the lower passive guide via two-section adiabatic lateral tapers. The width of the taper varies linearly from 3.5 to 2 µm over a 25 µm length followed by a second linear section that varies from 2 µm to 0.5 µm over a 150 µm length, resulting in a coupling loss of <0.5 dB per taper. The length and width of the MMI is 685 µm and 12 µm, respectively. The input and output waveguides are angled at 7°C to the cleaved edge of the chip in order to avoid Fabry–Perot resonances in the bus waveguide. The wafer is planarized using silicon nitride (SiN_x) followed by a short etch back to open the SOA ridges and the taper. Electron beam evaporation was used to deposit Ti–Ni–Au p-contacts on the active ridge including the tapers. The p-contacts are annealed at 415°C for 30 s. The wafer is thinned to 130 µm, and a Ge–Au–Ni–Au n-contact is deposited on the back of the substrate, and annealed at 360°C for 90 s.

Total internal reflection (TIR) mirror based GaInAsP ring resonator notch filters integrated with SOAs are presented in Kim et al. (2005b). The ring resonators are made out of four TIR mirrors, an MMI coupler with a length of 113 µm and the SOA (see also Fig. 5.36). The layer sequence of the active and passive waveguide is shown in Fig. 3.47.

The passive waveguide A which leads to the facet and the TIR mirrors is tapered down (taper length 15 µm) from a width of 1.5 µm to a width of 3 µm. The edge depth is 1.8 µm for this type of waveguide as well as for the active waveguide. The passive waveguide B is connected to waveguide A and differs only from type A by a deeper etch depth which is 4.5 µm. The fabrication of the device is started by growing the active layers on a n^+ InP substrate. The multiquantum wells consist of seven quantum wells, each 6.5 nm thick, separated by barrier layers with a thickness of 8 nm. The active layers are etched away in unwanted areas in the next step, which is followed by a regrowth step with passive material. Standard RIE and metallization techniques are used for realizing the device.

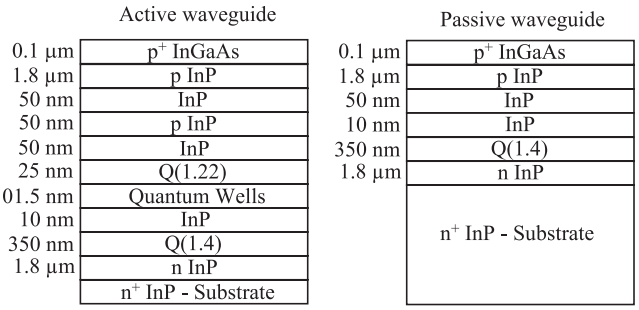

Fig. 3.47. Layer sequence of active and passive waveguide used in TIR ring resonator

Table 3.5. Layer sequence of active disk (Djordjev 2002)

layer no.	material	bandgap λ	thickness (nm)	doping
17	InP		300	$n^+, 10^6$
16	InP		700	n, 5×10^{17}
15	GaInAsP	1.1	400	n, 3×10^{17}
14	InP		800	n, 3×10^{17}
13	GaInAsP	1.25	170	
12	GaInAsP	1.55; 1% strain	4×8	
11	GaInAsP	1.25	3×10	
10	GaInAsP	1.25	170	
9	Inp		100	
8	InP		100	p, 3×10^{17}
7	InP		100	p, 5×10^{17}
6	InP		600	p, 1×10^{18}
5	InGaAs		200	$p^+, 1 \times 10^{19}$
4	InP		100	
3	InGaAs		200	
2	InP		100	n, 3×10^{18}
1	InP			n^+

Vertically coupled disks with radii of 10 µm employing gain are demonstrated in Djordjev et al. (2002b). The fabrication of the vertically coupled disk is based on the passive disk explained earlier (see Fig. 3.30). The layer sequence of the active disk is listed in Table 3.5. In order to limit the interaction of the optical field with the metal bond pads, a 3 µm thick layer of polyimide is applied between the surface of the substrate and the metal layer by using a standard liftoff process which leaves the active regions polyimide free for creating the metal contact.

Finally the sample is thinned down to a thickness of 100 µm, the n-metal contact is deposited and contact annealing is performed. Then the samples are cleaved into bars and deposition of AR coating on both facets is applied.

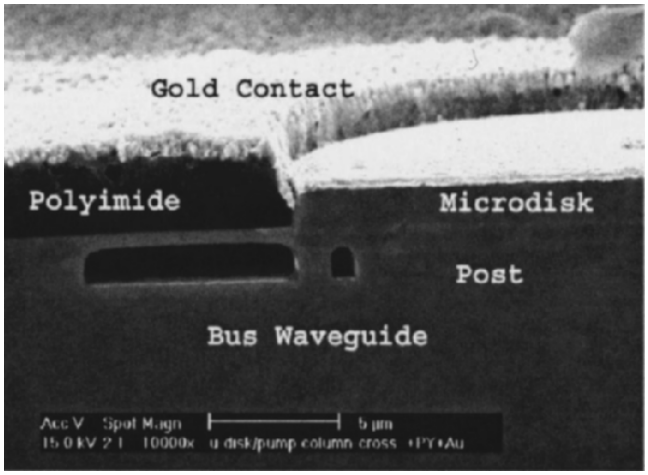

Fig. 3.48. Cross-sectional scanning electron microscope photograph of an active microdisk device.

Reused with permission from K. Djordjev, Applied Physics Letters, 80, 3467 (2002) ©2002 American Institute of Physics

A SEM photograph of the cross section of a vertically coupled disk is shown in Fig. 3.48.

These active disk resonators are the first of its kind employing gain to change the resonant filter characteristic.

A detailed theoretical analysis of vertical coupled ring resonators employing active and passive layers is presented in Tee et al. (2006). A design layout based on the calculations is developed.

3.5 Polymers

Polymer photonic integrated circuits have always been playing an important role in literature (Ma et al. 2002). Polymers have recently attracted again a lot of attention due to the lower cost of the material (if standard polymers are used), easier processibility and integration than semiconductor materials. Polymers can be doped with appropriate materials for engineering desired properties. Different polymer material systems exist on the market today for realizing not only purely passive devices, but also electro-optic and thermo-optic devices. In the following chapter polymer based ring resonators made by using different fabrication technologies will be presented.

3.5.1 Conventional Fabrication Techniques

In order to fabricate polymer waveguide based components, mainly two processing methods are used, which are well known from the semiconductor

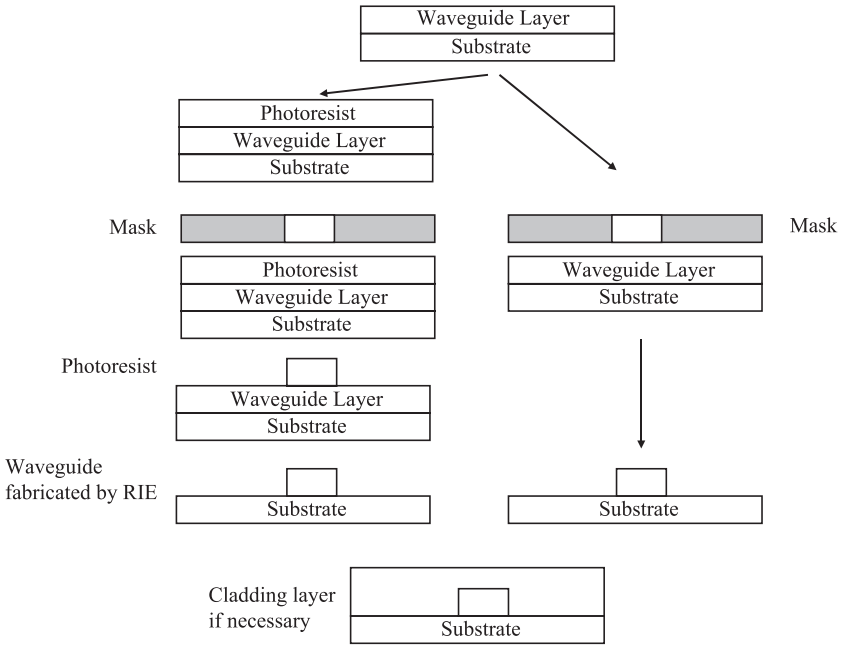

Fig. 3.49. Photoresist (*left*) and direct lithographic (*right*) patterning for realizing polymer waveguides

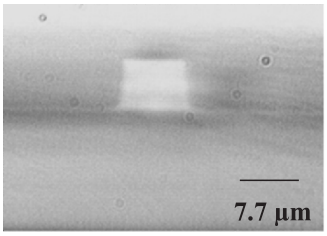

Fig. 3.50. Polymer waveguide realized by RIE and spin coating

field, namely photoresist based patterning and direct lithographic patterning (laser direct writing, photobleaching, electron beam direct writing). Both methods are briefly sketched in Fig. 3.49.

A polymer waveguide generally consist of a core and a cladding polymer where the refractive index of the core is higher than the cladding to enable the propagation of optical waves. Of course the cladding can also be left out and air can be used instead, which depends on the application. Figure 3.50 shows a typical photograph of the facet of a polymer waveguide, realized by RIE and spin coating in poly(perfluorocyclobutylaryl ether) (PFCB). As can be seen from the photograph the core waveguide has a nearly rectangular shape. RIE processes are aimed for obtaining smooth and vertical sidewalls to reduce scattering losses.

One of the first integrated polymer ring resonator add drop filters with a radius of 4.5 cm is presented in Haavisto and Pajer (1980). The ring resonator is fabricated by photopolymerization of doped polymethylmethacrylate (PMMA) films spun onto a silicon wafer. The patterns are written by a focused 325 nm He–Cd laser. The width of the achieved waveguides is 10 µm. The coupling gap is 17.5 µm, measured from the waveguide center to center. A prism coupling arrangement is used for measuring the device.

A ring resonator notch filter with a radius of 15.9 mm using polymers synthesized from deuterated[10] methacrylate and deuterated fluoromethacrylate are described in Hida et al. (1992). The ring resonator is fabricated on a silicon substrate by spin coating, photolithography and dry etching. The height and width of the waveguide core is 6.4 and 7.0 µm, respectively. The relative refractive index difference between the core and the cladding is set to 0.5% by controlling the copolymerization ratio of the two monomers. A coupling gap of 3 µm is realized between the bus waveguide and the ring.

Polymer ring resonator filters and modulators with vertically coupled input and output waveguides are demonstrated in Rabiei et al. (2002a). Two different kinds of ring resonator filters are fabricated, one with an index difference between core and cladding of 0.1 and a radius greater than 220 µm, and a second one with an index difference of 0.3 between core and cladding and radius greater than 25 µm. The layer sequence and the dimension of the waveguides used in the passive ring resonator filter are shown in Fig. 3.51. A photograph of a passive ring resonator filter is shown in Fig. 3.52.

The fabrication of the device with an index difference of 0.3 between core and cladding starts by spin coating a 2.8 µm Teflon film (11% solution of Teflon AF 1600 (Dupont) in 3M FC-40 solvent) on a silicon substrate. The Teflon layer is etched for 2 minutes in oxygen by RIE to improve the adhesion of the Teflon to the next layer. A 1.5 µm SU-8 (negative photoresist) layer is spin coated onto the etched Teflon layer and patterned by lithography to form the ring resonator. The ring resonator waveguides are planarized by spin coating a 4.5 µm thick Teflon layer. The Teflon layer is again etched by RIE in oxygen to increase the adhesion of the following polymer layer. The bus waveguides are

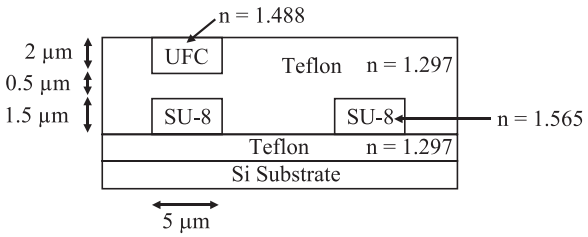

Fig. 3.51. Layer sequence and dimensions of waveguides (refractive indices are given for a wavelength of 1,550 nm)

[10] Introduction of deuterium into the chemical compound

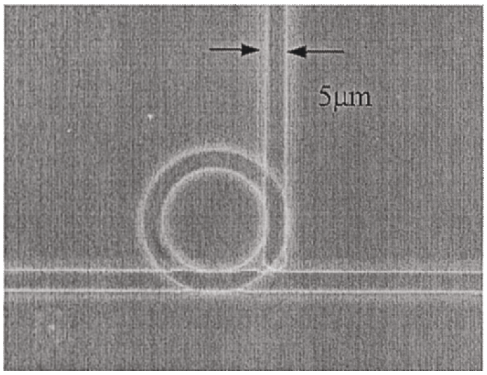

Fig. 3.52. Photograph of a passive polymer ring resonator add–drop filter.

Reprinted with permission from IEEE Journal of Lightwave Technology, vol. 20, pp. 1968–1975 ©2002 IEEE

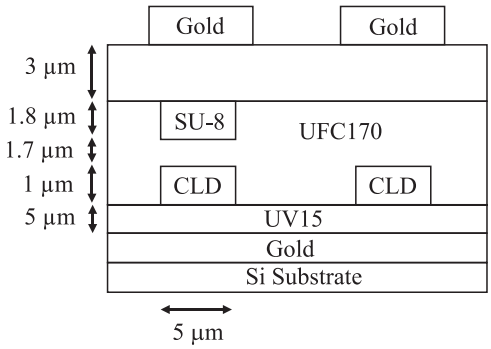

Fig. 3.53. Layer sequence and dimensions of waveguides used in the modulator

realized by lithographic patterning, RIE etching of the Teflon cladding layer, spin coating a UFC 170A (URAY Co., Korea) layer, UV curing, and baking. Remaining UFC 170A which is not part of the waveguide is removed using RIE. For the fabrication of the ring resonator filter with an index difference of 0.1 between core and cladding layers the cladding material is UFC 170A and the vertically coupled bus waveguides are made out of NOA61 (Norland Products). The fabrication of the polymer ring resonator modulator is in principal the same as for the passive device. The layer sequence of the ring resonator modulator is shown in Fig. 3.53.

The CLD1/APC polymer is aligned using corona polling for 30 min at a polling temperature of 145°C and an applied voltage of 10 kV. An upper gold electrode is deposited and patterned on top of the device to cover the ring resonator modulator. A photograph of a fabricated ring resonator modulator is shown in Fig. 3.54.

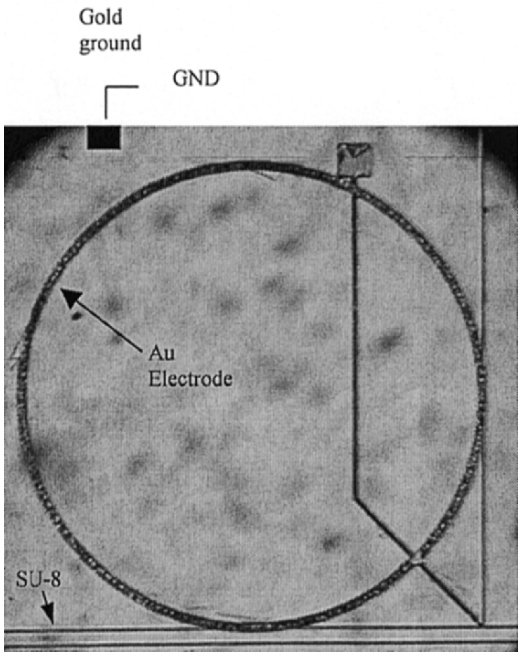

Fig. 3.54. Fabricated polymer ring resonator modulator.
Reprinted with permission from IEEE Journal of Lightwave Technology, vol. 20, pp. 1968–1975 ©2002 IEEE

A free standing polymer ring resonator notch filter is presented in Paloczi et al. (2003a), Huang et al. (2004). The polymer waveguides are embedded in a lower cladding of UV-15 ($n = 1.5, \lambda = 1.55\,\mu\text{m}$) and an upper cladding of OG-125 ($n = 1.46, \lambda = 1.55\,\mu\text{m}$). The waveguide cores which are made of SU-8 ($n = 1.57, \lambda = 1.55\,\mu\text{m}$) are $2\,\mu\text{m}$ wide and $1.6\,\mu\text{m}$ thick. The SU-8 waveguides are patterned by direct electron beam lithography and following development process. The upper cladding is spin coated and UV cured. The free standing feature is achieved by a thin gold layer deposited on to the silicon substrate onto which the UV-15 layer is spin coated. Due to the weak adhesion of the UV-15 layer, it is possible to peal of the polymer layer (thickness $\sim 10\,\mu\text{m}$) with the integrated ring resonators. Optical quality facets are realized by simple cutting with a scalpel.

One of the smallest ring resonator add drop filters with a radius of $10\,\mu\text{m}$ is demonstrated in Chen et al. (2004b) in the polymer BCB (Cyclotene 3022-46 from the Dow Chemical Company). An SEM photograph of a fabricated ring resonator is shown in Fig. 3.55.

Racetrack shaped ring resonators with bending radius of $10\,\mu\text{m}$ and $4\,\mu\text{m}$ straight coupling sections are also presented. The layer sequence of the device is shown in Fig. 3.56.

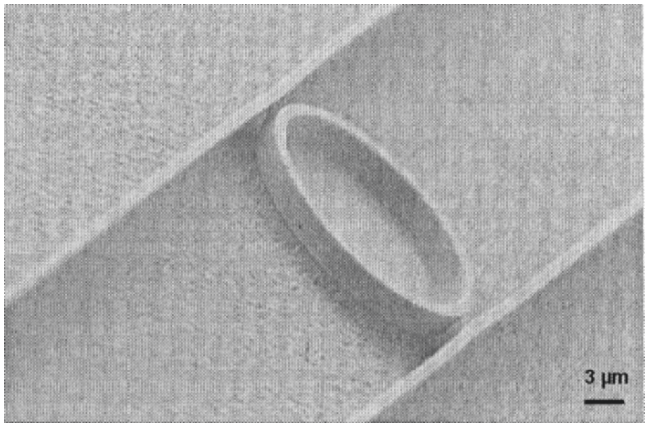

Fig. 3.55. BCB microracetrack resonator. The filter section has 0.9 µm wide waveguides, which are tapered to 2.5 µm at the input – output sections.

Reprinted with permission from IEEE Photonics Technology Letters, vol. 16, pp. 470–472 ©2004 IEEE

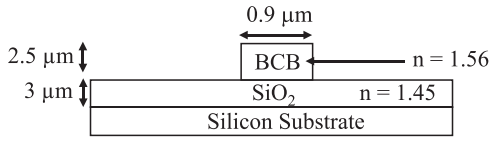

Fig. 3.56. Layer sequence of BCB ring resonator

BCB is cured at a temperature of 250°C. SiO_2 is used as an etch mask to transfer the patterns of the waveguides from photoresist to the used BCB. SiO_2 is etched using a trifluoromethane and oxygen plasma, BCB is etched using a sulfur hexafluoride and oxygen plasma. The etch mask is removed by buffered hydrofluoric acid. The width of the waveguides is 0.9 µm at the coupling gap and is tapered to 2.5 µm at the facets.

Laterally coupled organic–inorganic hybrid polymer ring resonator add drop filters with a radius of 50 µm are presented in Rezzonico et al. (2006). A photograph of a fabricated ring resonator and a cross-section of a waveguide are shown in Fig. 3.57.

The waveguides are made out of Ormocore, from the family of Ormocer®[11] a commercially available inorganic-organic hybrid polymer (negative photoresist, $n = 1.536$, 0.6 dB cm^{-1} at a wavelength of 1.55 µm, $T_g >$ 270°C). A two step lithography process is used to realize the laterally coupled ring resonator add drop filter. The layer sequence is similar to the one shown in Fig. 3.56 for the BCB ring resonator, substituting Ormocore for BCB. The SiO_2 layer used has a thickness of 4 µm. In a first step, the port waveguides

[11] Trademark of the Fraunhofer–Gesellschaft zur Förderung der angewandten Forschung e.V. München

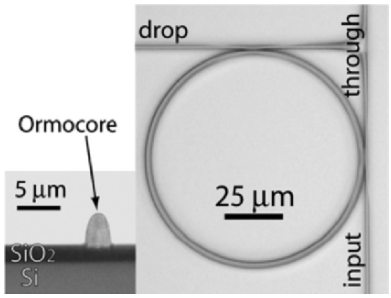

Fig. 3.57. *Left*: Microscopic front view of a cleaved sample showing the Si substrate, the SiO barrier, and the cross-section of a port waveguide. The structures are by about 10% thinner than the films before development since the oxygen at the surface reduces the polymerization during the exposure. *Right*: Microscopic top view of a laterally coupled ring resonator of Ormocore. The external radius of the ring is 50 µm with a cross-section of 3.8 µm width and 4.5 µm height; the port waveguides are 2.7 µm wide and 3.6 µm high. The gaps at the couplers are 0.3 µm wide.

Reprinted with permission from IEEE Photonics Technology Letters, vol. 18, pp. 865–867 ©2006 IEEE

are defined using an exposure in oxygen poor atmosphere through a negative chrome mask. The sample is developed in methylpentanone. Then the sample is spin coated again with Ormocore, patterned and developed for realizing the ring resonator. The gap between the ring and the bus waveguides is aimed to be 0.5 µm (measured 0.3 µm). The sample is hard baked at 150°C in inert atmosphere. The width and height of the bus waveguides is 2.7 and 3.6 µm, respectively. The width and height of the ring waveguide is 3.8 and 4.5 µm.

3.5.2 Replication and Nanoimprinting

One of the first ring resonators realized using a nanoimprint technique is presented in Chao and Guo (2002). Here waveguides made out of PMMA, polystyrene (PS) and polycarbonate (PC) are demonstrated. SEM photographs of directly imprinted polycarbonate racetrack and disk resonators are shown in Fig. 3.58.

Two fabrication methods are demonstrated, direct imprinting (Fig. 3.59) and template filling (Fig. 3.60).

The fabrication (Fig. 3.59) of the molding tool is performed in two steps. First, a silicon substrate is etched using RIE, realizing the first molding tool for imprinting the device pattern into PMMA which is used as a resist for the following Ti/Ni liftoff process. The remaining PMMA on the surface of the sample is etched using an oxygen RIE process, thus only leaving the structured PMMA in place. Ti/Ni which is deposited on to the sample is used as a hard mask for the following RIE process to etch the SiO_2 layer, realizing

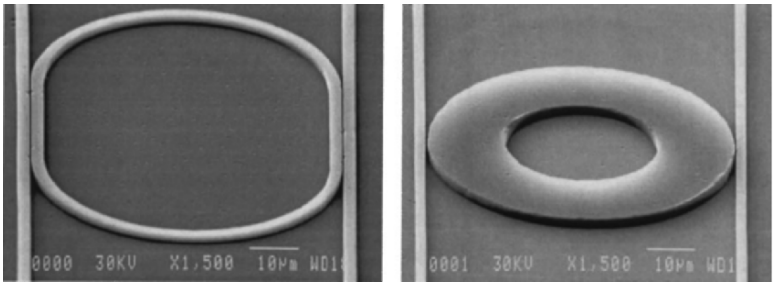

Fig. 3.58. Directly imprinted polycarbonate racetrack and disk resonators.

Reused with permission from Chung-yen Chao, Journal of Vacuum Science and Technology B, 20, 2862 (2002) ©2002 AVS The Science and Technology Society

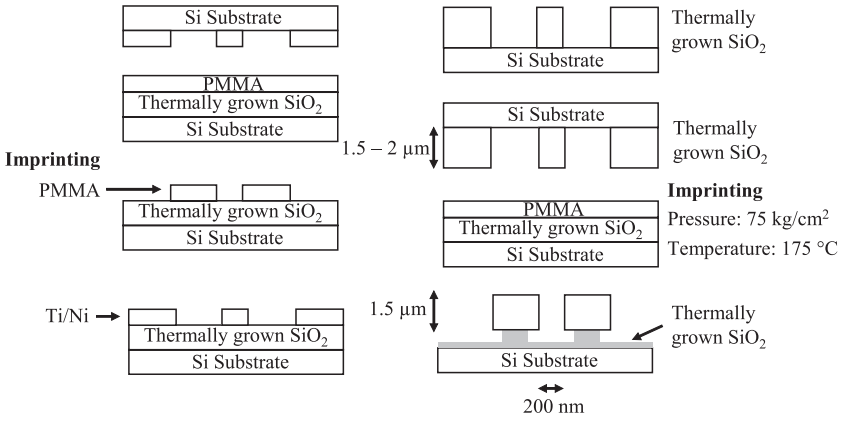

Fig. 3.59. Process flow for directly imprinting into a polymer

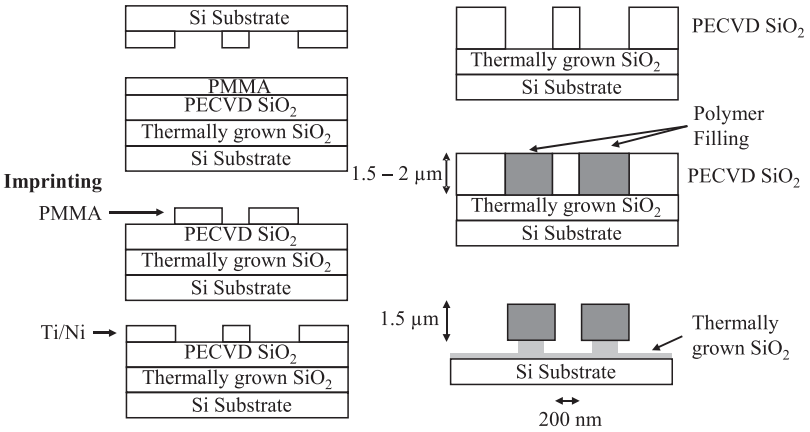

Fig. 3.60. Process flow for polymer template filling

the second and final molding tool for imprinting the waveguides again in PMMA with a molecular weight of 15,000 (imprinting time = 10 min). In order to increase the optical confinement of the mode in the waveguides, a buffered hydrofluoric acid (BHF) etch is performed, resulting in an undercut of the SiO_2 layer underneath the waveguides forming a pedestal. In order to separate the molding tool from the polymer waveguides, the molding tool is coated with a surfactant to provide a low surface energy. SEM photographs of PMMA waveguides sitting on top of a thermally grown SiO_2 pedestal are shown in Fig. 3.61.

In the template filling method (Fig. 3.60), a second layer of SiO_2 is grown by PECVD which is structured using the same processing steps as in the direct imprinting method for obtaining the molding tool, spin coating PMMA, imprinting and removal of residual PMMA by dry etching, deposition, and liftoff of Ti/Ni for the hard mask fabrication, dry etching of the PECVD SiO_2 layer and removal of the metal layer. The molding tool is filled with polymer. Planarization is done with a flat molding tool. The residual polymer is removed by RIE and the sample is heated to remove unwanted air bubbles in the polymer. Finally the sample is again etched with a buffered HF realizing the pedestal for the polymer waveguides. To reduce the surface roughness induced scattering loss and therefore increase the performance of the polymer ring resonator devices, the authors propose a thermal reflow technique in Chao and Guo (2004). Polymer ring resonator devices are heated with controlled time duration (60–150 s) in a temperature range of 10–20°C below the glass transition temperature of the polymer. This lowers the viscosity and enhances the fluidity of the polymer, resulting in a reflow which reduces the surface roughness significantly under the action of surface tension. The variance of

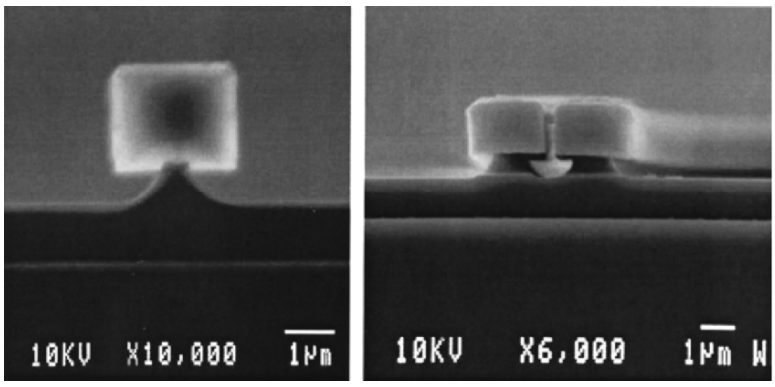

Fig. 3.61. Cross-section SEM picture of (**a**) rectangular PMMA waveguide sitting on top of a SiO_2 pedestal. (**b**) PMMA waveguides in the coupling region of a micro-ring device.

Reused with permission from Chung-yen Chao, Journal of Vacuum Science and Technology B, 20, 2862 (2002) ©2002 AVS The Science and Technology Society

surface roughness is estimated to decrease by 35–40 nm in the ring and by 15–20 nm in straight waveguides.

Replication of polymer ring resonators using a soft lithography method is demonstrated in Huang et al. (2003). The fabrication process is illustrated in Fig. 3.62. Ring resonators made out of SU-8 are presented.

The samples are cleaved after molding and curing to achieve optical quality facets. A photograph of a ring resonator is shown in Fig. 3.63.

This soft lithography method has also been used in Poon et al. (2004a) to fabricate ring resonator devices without cladding and cladding in polystyrene (PS) and SU-8, respectively. Here a 3 µm thick layer of OG-125 ($n = 1.456$,

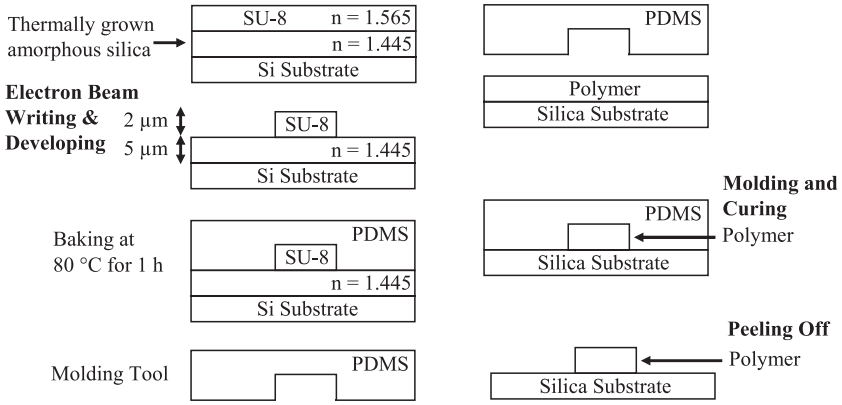

Fig. 3.62. Replication of polymer ring resonators by soft lithography

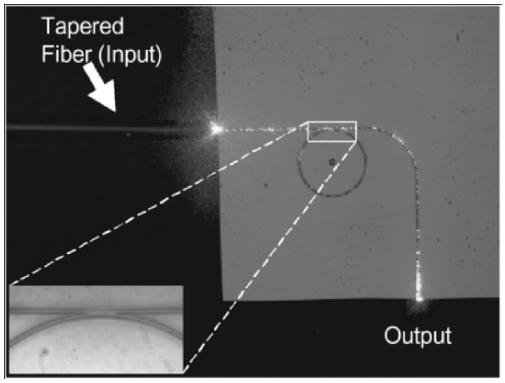

Fig. 3.63. Optical microscope image of microring optical resonator fabricated by soft lithography. The *inset* shows the detail of coupling region. The ring diameter is 200 µm, the waveguide width is 2 µm, and the gap between the straight waveguide and the microring is 250 nm.

Reprinted with permission from Y. Huang, Optics Express, vol. 11, no. 20, pp. 2452–2458 ©2003 Optical Society of America

a UV curable epoxy) is used as the under cladding instead of growing a SiO_2 layer with PECVD as previously done which is UV cured at 80°C for 2 min. The ring resonators without cladding are fabricated by deposition of 10 µl of PS solution (4 wt% in toluene) on the sample and pressing the mold against the chip with a force of 25 N for 20 min. The toluene evaporates through the PDMS mold, leaving behind a 200 nm residual film which does not influence the characteristic of the ring resonator. Finally, the chip is baked at 80°C for 3–5 min. The SU-8 ring resonator is fabricated in a similar way. The only difference is that SU-8 is UV cured and the sample is baked at 80°C for 3 min. Another layer of OG-125 with a thickness of 3 µm is spin coated, UV cured and baked at 80°C for 3–5 minutes to form the upper cladding. All samples are cleaved for device separation. The ring radius is 200 µm and the height and width of the waveguide is 1.5 and 1.9 µm, respectively.

Polymer racetrack shaped ring resonator notch filters with radii of 100 µm and 200 µm and a coupling length of 100 µm and 40 µm, respectively, fabricated using an imprinting technique with a smoothing buffer layer are presented in Kim et al. (2005a). The width of the coupling gap used is 200 nm. The layer sequence and dimensions of the used waveguide is shown in Fig. 3.64.

The stamp fabrication starts by patterning a quartz glass wafer coated with chromium using photoresist. After UV exposure, the chromium is etched and the so achieved hard mask is used to transfer the pattern to the substrate by RIE. The smoothing buffer layer is made by depositing an SiN film using LPCVD. The pattern on the stamp is transferred to the cladding of the sample by general imprinting, where the stamp is pressed against the polymer layer. The cladding is UV cured and the stamp is removed, leaving behind the trench for the core waveguide. The core polymer is spin coated onto the sample and cured. Finally the sample is cleaved and the devices are separated.

Imprinting technologies are an attractive way of realizing ring resonators, especially due to the fact that the manufactured stamp can be used several times. This aspect is important, when it comes to producing a large number of devices which is a requirement for realizing low cost products for the telecommunication and sensor market. The rise of these fabrication technologies enables a renaissance of polymer materials and opens up the way for new materials with appropriate manufacturing properties suitable for replication.

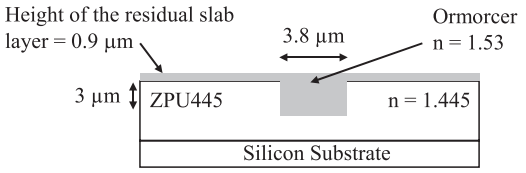

Fig. 3.64. Layer sequence and dimensions of waveguide

3.6 Temperature Insensitivity

Temperature stability of photonic integrated circuits is a key challenge which applies to all devices, especially resonant based devices like ring resonator filters. In ring resonator filters, the wavelength to be filtered out for example has to exactly match the rings resonance wavelength. Temperature shifts the resonance spectra of ring resonator filters depending on the materials used for fabricating the device. For stabilizing the resonance wavelength of ring resonator filters, a temperature control unit with a heater or a Peltier cooler is needed. This requires a permanent power consumption of a few watts and electronic control circuits. The major goal is therefore to eliminate these additional expenses and sources of defect. For this reason, temperature insensitive or athermal waveguide based devices have been investigated (Kokubun et al. 1993, Chu et al. 1999e, Keil et al. 2001). The temperature dependence of photonic integrated circuits (PICs) is mainly caused by the temperature dependence of the optical path length. In the case of ring resonator add/drop filters, the center wavelength of the passband is determined only by the optical path length of the ring resonator. The temperature induced effective index shift in a ring waveguide cannot be compensated by a similar induced effective index change of the bus waveguides.

The basic principle of an athermal waveguide is derived in the following using (Kokubun et al. 1997). The temperature dependence of the center wavelength of a device can be expressed by

$$\frac{\mathrm{d}\lambda_0}{\mathrm{d}T} = \left(\frac{1}{L}\frac{\mathrm{d}S}{\mathrm{d}T}\right) \cdot \frac{\lambda_0}{n_{\mathrm{eff}}}, \tag{3.1}$$

where λ_0 is the central wavelength, L is the waveguide length of the device, T is the absolute temperature and n_{eff} is the effective index of the waveguide (see also (2.4)).

S is the optical path length and is given by

$$S = n_{\mathrm{eff}} \cdot L. \tag{3.2}$$

The temperature dependence of the optical path length of an optical waveguide on a substrate is given by differentiating (3.2) with T, dividing both sides by L

$$\frac{1}{L}\frac{\mathrm{d}S}{\mathrm{d}T} = \frac{\mathrm{d}n_{\mathrm{eff}}}{\mathrm{d}T} + n_{\mathrm{eff}}\frac{1}{L}\frac{\mathrm{d}L}{\mathrm{d}T} = \frac{\mathrm{d}n_{\mathrm{eff}}}{\mathrm{d}T} + n_{\mathrm{eff}}\alpha_{\mathrm{th}}, \tag{3.3}$$

where α_{th} is the coefficient of thermal expansion.

In the case of a waveguide, the coefficient of thermal expansion is the one of the substrate, since the thickness of the substrate is much larger than the waveguide layer. Table 3.6 gives the coefficient of thermal expansion for some bulk materials.

Table 3.6. Coefficients of thermal expansion of some materials

material	coefficient of thermal expansion $\alpha_{\mathrm{th}}(\times 10^{-6}/^{\circ}\mathrm{C})$
BCB	42
MMA	68
Si	2.6
InP	4.6
GaAs	5.8
Au	14
Al	24
Ag	18
Pt	9

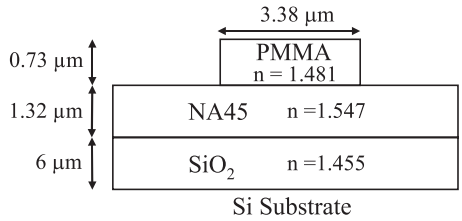

Fig. 3.65. Dimensions of athermal waveguide design

In order to achieve an athermal condition, the following equation has to be satisfied.

$$\frac{\mathrm{d}n_{\mathrm{eff}}}{\mathrm{d}T} + n_{\mathrm{eff}}\alpha_{\mathrm{th}} = 0 \quad \Rightarrow \quad \alpha_{\mathrm{th}} = -\frac{1}{n_{\mathrm{eff}}}\frac{\mathrm{d}n_{\mathrm{eff}}}{\mathrm{d}T}. \tag{3.4}$$

From (3.4), two possibilities exist of designing an athermal waveguide based device. Either a substrate with a negative value of α_{th} or a waveguide material with a negative value of $\mathrm{d}n_{\mathrm{eff}}/\mathrm{d}T$ can be chosen.

One of the first temperature independent ring resonator filters based on a strip-loaded athermal waveguide is presented in Kokubun et al. (1997). Here, a transparent material having a negative value of $\mathrm{d}n_{\mathrm{eff}}/\mathrm{d}T$ is chosen for the design of the waveguide. This gives more freedom in designing the waveguide, as the parameters of used bulk materials obviously cannot be changed. The structure and dimensions of the athermal waveguide used are shown in Fig. 3.65. The design makes use of the negative value of $\mathrm{d}n_{\mathrm{eff}}/\mathrm{d}T$ for PMMA which is -105×10^{-6} at $\lambda = 633\,\mathrm{nm}$ for bulk material.

The radius of the ring is 5 mm resulting in a free spectral range of 0.037 nm. The finesse is measured to be 2.6. The athermal design leads to a temperature coefficient for the central wavelength of $7 \times 10^{-4}\,\mathrm{nm\,K^{-1}}$.

Another ring resonator filter where the temperature dependence of the center wavelength is compensated by application of a polymer overlay is demonstrated in Chu et al. (1999e). The design of the waveguide is similar to the one described in Figs. 3.8 and 3.9. The material which is used as the polymer

overlay is a copolymer made by a combination of PMMA and tri-fluoroethylmethacrylate (TFMA). The refractive index at room temperature is 1.44 and the value of $\mathrm{d}n_{\mathrm{eff}}/\mathrm{d}T$ is $-1.44 \times 10^{-4}/^{\circ}\mathrm{C}$. The material is deposited onto the device using spin coating realizing a height of more than $3\,\mu\mathrm{m}$. The center wavelength shift due to rising temperature increases linearly without compensation by $0.0137\,\mathrm{nm}\,^{\circ}\mathrm{C}^{-1}$ from room temperature to 103°C. Using the polymer overlay, this value is decreased in the temperature range between 25°C and 55°C resulting in a wavelength shift of $-0.0025\,\mathrm{nm}\,^{\circ}\mathrm{C}^{-1}$. Above 55°C this value increases to $-0.03\,\mathrm{nm}\,^{\circ}\mathrm{C}^{-1}$ mainly due to the low glass transition temperature (T_g) of the polymer which is around 80°C. Polymers with a higher T_{g} like polymides are preferred in utilizing this method to realize an athermal behavior.

A similar method employing a birefringent polymer overlay can also be used to realize polarization independent ring resonator filters (Kokubun et al. 2001).

A different approach for realizing athermal waveguide based devices is presented in Keil et al. (2001). Here an all-polymer approach is used. Polymer materials are used for both the waveguide and the substrate. The substrate is chosen to have a positive coefficient of thermal expansion (CTE) and the polymer used for the waveguides is chosen to have a negative thermo-optic (TO) coefficient ($\mathrm{d}n_{\mathrm{eff}}/\mathrm{d}T$). An athermal (measured between 25°C and 65°C) and polarization independent arrayed waveguide grating (AWG) is demonstrated. The CTE of the substrate is $80\,\mathrm{ppm}\,\mathrm{K}^{-1}$. The temperature dependent drift of the center wavelength of the device is $\pm 0.05\,\mathrm{nm}$ over the entire temperature range between 25 and 65°C. This approach can readily be adapted for realizing athermal ring resonator devices.

3.7 Polarization Independence

Handling polarization has been and is an issue when developing photonic integrated circuits especially for telecommunication systems. A polarization insensitive ring resonator filter is desirable as different polarization states lead to undesired shifts in the filter spectrum of the resonator and degrade the optical performance of the filter.

A well-know method for realizing polarization insensitive devices is by using a so called polarization diversity architecture. The idea behind this method is to split the optical input signal into two signals having an orthogonal polarization state, like for example one arm is for TE polarized signals, the other arm is for TM polarized signals. In order to perform integrated polarization handling of the input signals, polarization splitters, and rotators are needed. Polarization converters using sharp bends are demonstrated for example in van Dam et al. (1996). An example of a polarization insensitive heterodyne receiver in InP employing polarization rotator and splitter elements is presented in Kaiser et al. (1996).

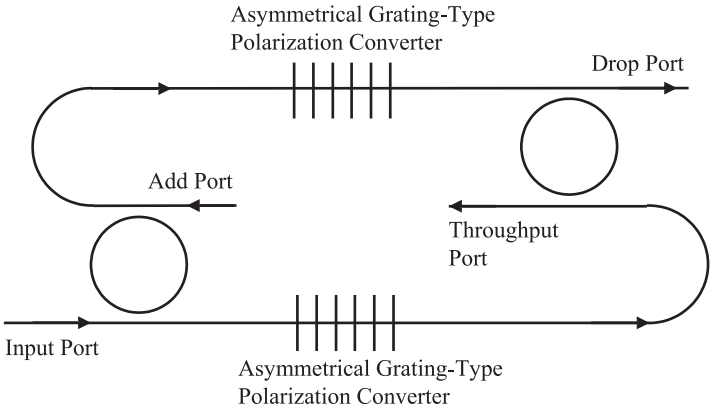

Fig. 3.66. Layout of a polarization independent filter

A theoretical analysis of a filter comprising two identical ring resonators, two identical polarization converters, straight and curved sections which is based on the polarization-dependent architecture is presented in Klunder et al. (2002b). The layout of the filter is sketched in Fig. 3.66.

The ring resonators are assumed to be ideal polarization splitters which drop the TE polarized light with wavelengths within the pass band completely and the TM polarized light and the remaining TE polarized light not in the passband, pass the ring resonator unaffected. The polarization converters are also assumed to ideally convert from one polarization state into the other without losses. The calculated polarization dependence of the filter for the drop port is 0.7 dB, using a polarization converter with a conversion efficiency of 98%.

A tunable ring resonator filter utilizing a Vernier architecture with polarization diversity is presented in Van et al. (2004). Here a polarization beam splitter separates TE and TM polarized light into a waveguide which leads to two third order ring resonator filters with two different FSRs, 575 and 650 GHz. The two waveguide arms are joined using a polarization beam combiner after the light passes the ring resonators. A polarization dependent loss of 0.4 dB and a differential group delay of better than 5 ps are obtained. A similar architecture is realized in Watts et al. (2005) using integrated polarization splitters and rotators and third-order ring resonators with a diameter of 16 µm.

Polarization converters with periodical spectral response based on ring resonators are theoretically proposed and discussed in detail in Morichetti and Melloni (2006). Several device layouts of parallel coupled and directly coupled ring resonator configurations are presented.

Polarization independent ring resonator filters are also analytically analyzed in Chin et al. (2004). Two approaches are being considered. In the first approach, laterally strong confined single mode waveguides with a large

etch depth are analyzed regarding the effective refractive index for TE and TM polarization depending on the width of the waveguide. The effective indices become equal at the critical width where the mode is circular. Another issue despite achieving a critical polarization independent waveguide width is the critical bending radius below which no etch-depth can meet the differential loss criterion, as losses for the fundamental modes also become to high for achieving an acceptable filter performance. In this case, this radius should not be smaller than 30 µm. The next approach is to realize polarization independent coupling. MMI couplers (see also Sect. 4.1.2) are proposed, which can be designed for polarization insensitive operation. Finally in adding polarization independent waveguides and couplers, polarization insensitive ring resonators can be fabricated.

The idea of polarization independent waveguides and couplers is used in Headley et al. (2004) for fabricating a racetrack shaped ring resonator notch filter in SOI. A layout and layer sequence of the waveguide used is shown in Fig. 3.67.

A coupling length of 500 µm and a bending radius of 400 µm are used in realizing polarization insensitivity within a shift of the resonance peaks of 2 pm between TE and TM polarized input over a spectral range of four times the FSR of 192 pm. The devices are covered with a passivating surface oxide after etching of the waveguides and the coupler, which helps to protect the waveguides during end facet preparation. The wafers are diced and the end facets are polished and AR coated in order to minimize Fresnel reflections and to reduce Fabry–Perot resonances inside the device.

One of the first polarization independent filters using a birefringent fluorinated polyimide overlay (birefringence = 0.11) is presented in Kokubun et al. (2001). Here a vertical coupling scheme is used together with single mode rib waveguides for achieving polarization independent operation. The geometry and layer sequence of the used waveguides is shown in Fig. 3.68.

All glass layers are deposited by RF sputtering and patterned by RIE. The polyimide cladding layer is spin coated onto the sample. The RIE parameters are: RF power (30 W), gas pressure (0.67 Pa), flow rate of CF_4 and O_2 (10:3 SCCM). An advantage in using a polymer overlay is that remaining polarization dependence can be eliminated by UV trimming of the polyimide film, due to the fact that the thickness of the film can be reduced by more

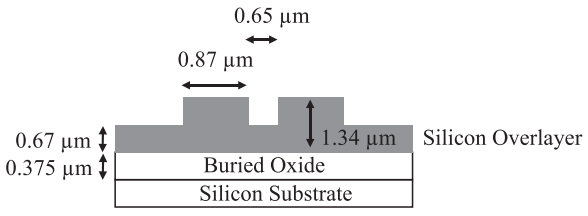

Fig. 3.67. Layer sequence and dimension of used waveguides

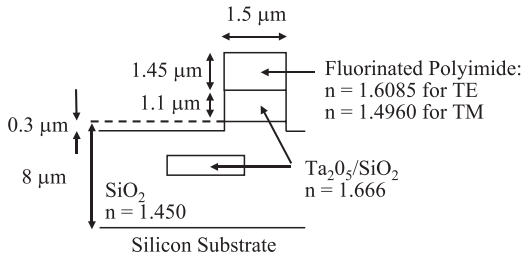

Fig. 3.68. Layer sequence and waveguide dimensions (the refractive indices are given for a wavelength of 1.55 µm)

than 20% by UV irradiation while keeping the refractive index and the birefringence constant (see also Sect. 5.2).

Several methods exist for realizing polarization insensitive devices and as can be seen, the chosen method again depends on the material system and the device layout for appropriate polarization compensation.

Now that ring resonator theory and device fabrication have been addressed, the focus in the following chapter lies on determining the performance of the devices, therefore possible characterization methods will be explained in Sect. 3.8.

3.8 Characterization Methods

The standard characterization of waveguide based devices usually involves fibers for in and out coupling of the device, a light source and a detector. Due to the advance in current fabrication methods, analyzing the performance of ring resonator filters with regard to where the loss occurs is necessary for improving the manufacturing process and thus improving the characteristic of the filter. Besides the standard optical fiber characterization setup, microscope examination, SEM and atomic force microscopy (AFM) measurements, several methods exist to analyze the performance of waveguide based devices such as cut-back (destructive), Fabry–Perot (requires single mode lasers) (Park et al. 1995), prism coupling method (requires a minimum length of the waveguide of several cm), optimum end-fire coupling (OEC) method (Haruna et al. 1992) and many others. The description of some of the mentioned characterization methods will be done in the following paragraphs.

The main goal of each method is to determine the losses of the device. In order to compare the loss parameters, a definition for the standard parameters is given in the following paragraph.

The insertion loss $\alpha_{\text{insertion}}$ of the device is the minimum transmission for a specific wavelength range for all polarization states. It represents the worst possible loss through the device. The insertion loss uniformity of a device is the difference between the insertion loss of the best-case and worst-case

channels. The insertion loss $\alpha_{\text{insertion}}$ is defined for an input intensity I_{in} and output intensity I_{out} as

$$\alpha_{\text{insertion}} = -10 \cdot \log \frac{I_{\text{out}}}{I_{\text{in}}}. \tag{3.5}$$

The total insertion losses $\alpha_{\text{insertion}}$ includes the intrinsic losses $\alpha_{\text{propagation}}$ and the fiber–chip coupling losses α_{coupling}

$$\alpha_{\text{insertion}} = \alpha_{\text{propagation}} + \alpha_{\text{coupling}} \quad \left(\text{dB}\,\text{cm}^{-1}\right). \tag{3.6}$$

The intrinsic losses can be described by the following equation:

$$\alpha_{\text{propagation}} = -\frac{1}{L}\left\{10 \cdot \log \frac{I_{\text{out}}}{I_{\text{in}}} + \alpha_{\text{coupling}}\right\} \quad \left(\text{dB}\,\text{cm}^{-1}\right), \tag{3.7}$$

where L is the total length of the measured waveguide.

3.8.1 Conventional Characterization

One of the standard setups for the measurement of ring resonator devices is shown in Fig. 3.69. Here an external cavity laser (ECL) is used as the light source which is connected via a polarization controller (PLC) and a tapered or lensed fiber to the input waveguide.

The transmitted signal is detected using for example the lock-in technique employing a photo diode and a lock-in amplifier. The ECL signal is coupled to the input waveguide by using for example a tapered fiber, which can be adjusted by a three axis piezo drive. Tapered fibers are usually used to couple into strong guiding waveguides and reduce the fiber to chip coupling loss considerably compared to a standard butt fiber due to the reduction of the mode field diameter which suits the high index contrast waveguides better than the large field diameter of the butt fiber. The near field of the output

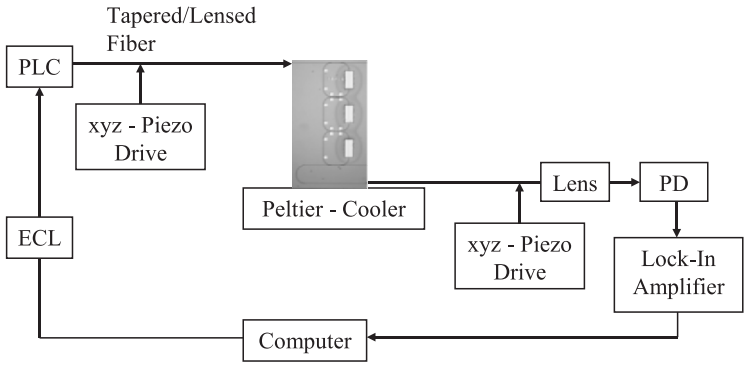

Fig. 3.69. Example of a standard optical measurement setup

waveguide can then be focused on a photodiode (PD) by using a microscope lens which has a sufficient aperture to guarantee correct power measurement. The device under test (DUT) is placed on a Peltier – cooler/heater so that all measurements are performed at a definite temperature. Instead of using a microscope lens on the output side, a tapered fiber can again be used to couple light from the drop or throughput port which is fed to an optical power meter or an optical spectrum analyzer.

This setup can now be used to extract various device parameters including the filter characteristic. The coupling losses can for example be calculated from measuring the loss of different waveguide lengths of the same device. This internationally recognized reference test method is known as the cut-back technique. The measured insertion loss is plotted against different lengths of the measured devices. The slope of the obtained curve is determined by the propagation losses of the waveguide. The coupling losses are obtained from the point, where the extrapolated measurement curve crosses the Y-axis at a device length of zero (unit length). The cut-back method is a destructive method to obtain the propagation and coupling losses of straight waveguides.

A nondestructive method which is commonly used is the Fabry–Perot method. This method has first been introduced in 1978 by Kaminow and Stulz. The chip is regarded as a Fabry–Perot resonator for waveguide losses $<1\,\mathrm{dB\,cm^{-1}}$, where the facets of the chip serve as the mirrors of the resonator. The optical wave is reflected back and forth within the waveguide. The resulting "filter" spectrum depends on the intrinsic losses and the reflection factor of the facets. The optical length is changed by varying the temperature of the whole chip or the wavelength exploiting the group velocity dispersion. The following calculations closely follow (Regener and Sohler 1985, Feuchter and Thirstrup 1994). The transmission spectrum of a Fabry–Perot resonator is given by

$$\frac{I_\mathrm{T}}{I_0\eta} = \frac{T^2 \mathrm{e}^{-\alpha_\mathrm{insertion} L}}{\left(1-\tilde{R}\right)^2 + 4\tilde{R}\sin^2\left(\frac{\phi}{2}\right)}, \qquad (3.8)$$

$$\tilde{R} = R \cdot \mathrm{e}^{-\alpha_\mathrm{insertion} L}.$$

The equation for describing the Fabry–Perot resonator is very similar to the one describing a single ring resonator notch filter. Here I_T is the transmitted intensity, I_0 is the intensity of the input laser signal, η is the coupling efficiency to the fundamental waveguide mode, $\phi = 2\beta L$ is the internal phase difference, R is the end-face reflectivity, L the length of the resonator and $\alpha_\mathrm{insertion}$ the insertion losses of the waveguide. The contrast K of the Fabry–Perot resonances, which is independent of I_0 and η, is given by

$$K = \frac{I_\mathrm{max} - I_\mathrm{min}}{I_\mathrm{max} + I_\mathrm{min}}. \qquad (3.9)$$

The transmitted maximum and minimum intensities can be described by

$$I_{\min} = \frac{(1-R)^2 \cdot \mathrm{e}^{-\alpha_{\text{insertion}} L}}{\left(1 + R \cdot \mathrm{e}^{-\alpha_{\text{insertion}} L}\right)^2} \tag{3.10}$$

$$I_{\max} = \frac{(1-R)^2 \cdot \mathrm{e}^{-\alpha_{\text{insertion}} L}}{\left(1 - R \cdot \mathrm{e}^{-\alpha_{\text{insertion}} L}\right)^2}. \tag{3.11}$$

From (3.10) and (3.11) K can be rewritten as

$$K = \frac{2\tilde{R}}{1+\tilde{R}^2}. \tag{3.12}$$

This leads to

$$\tilde{R} = \frac{1}{K}\left(1 - \sqrt{1-K^2}\right). \tag{3.13}$$

The value of K is taken from the measurement of the Fabry–Perot resonances. The maximum value of K is obtained for lossless waveguides. Increasing losses on the other hand reduces the contrast.

If the end-face reflectivity is known, the insertion loss of the device is given by

$$\alpha_{\text{insertion}} = \frac{4.34}{L}\left\{-\ln \tilde{R} + \ln R\right\} \quad \left(\mathrm{dB\,cm^{-1}}\right). \tag{3.14}$$

Equation (3.14) can also be written using $I_{\min}$ and $I_{\max}$ directly

$$\alpha_{\text{insertion}} = \frac{1}{L}\left\{\ln \frac{1+\sqrt{u}}{1-\sqrt{u}} + \ln R\right\} \quad \left(\mathrm{cm^{-1}}\right) \tag{3.15}$$

$$u = \frac{I_{\min}}{I_{\max}}.$$

When the reflection factor of the chip is unknown, it can be calculated from the insertion loss measurements plotted for different device lengths using (3.14) or (3.15). The measurement is approximated by a straight line from which the reflection factor can directly be taken. The slope of the curve is again the value for the intrinsic losses $\alpha_{\text{propagation}}$ of the waveguide, which is given by

$$4.34 \cdot \ln \frac{1+\sqrt{u}}{1-\sqrt{u}} \text{ or } -4.34 \cdot \ln \tilde{R} \quad \left(\mathrm{dB\,cm^{-1}}\right). \tag{3.16}$$

Another way of calculating the reflectivity of the end faces, which is valid for weak guiding waveguide structures, is by using:

$$R = \left(\frac{n_{\text{eff}} - 1}{n_{\text{eff}} + 1}\right)^2. \tag{3.17}$$

When the reflection factor is known, the intrinsic losses of the chip are easily determined without the necessity to cut the waveguide several times for characterization.

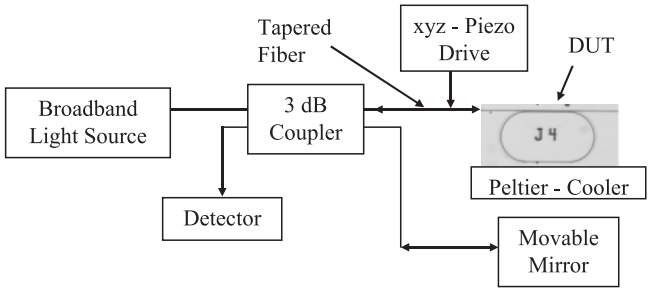

Fig. 3.70. Basic OLCR measurement setup in reflection mode

3.8.2 Optical Low Coherence Reflectometry

In optical low-coherence reflectometry (OLCR), the output of a low-coherence source is coupled into an optical fiber and split in a 3-dB coupler as sketched in Fig. 3.70. It is basically a white light Michelson's interferometer.

Half of the input signal travels to the DUT, while the other half is launched into free space towards a mirror on a scanning translation stage. When the optical path length from the coupler to the mirror equals the optical path length from the coupler to a reflection in the DUT, the signals from the two arms add coherently to produce an interference pattern which is measured in the detector arm of the coupler. When the optical path length difference becomes larger than the coherence length of the source, this interference signal fades and is lost eventually. Therefore the spatial resolution critically depends on the coherence length of the light source. Reflections with a spatial resolution better than 10 µm can be localized. Refractive index discontinuities less than 10^{-4} (dynamic range of ≈ -80 dB) in the device can be detected. The amplitude of the interference signal is proportional to the magnitude of the reflection from the DUT. Movement of the mirror allows the reflectivity of the DUT to be mapped as a function of distance, which allows the localization of waveguide discontinuities and imperfections. To achieve precise control of the fiber chip coupling and to record the transmission data, the output end of the setup can be coupled to an infrared-sensitive camera and an optical spectrum analyzer (OSA), respectively. This setup is referred to as the reflection mode. The reflection mode setup is used to characterize for example an active–passive butt joint, but can also be used to measure ring resonator devices without AR coated facets. Due to the AR coating of the facets, which is applied to most devices incorporating ring resonator filters, a setup called the transmission mode (Fig. 3.71) is used for the characterization of ring resonator devices.

A detailed analysis of ring resonator filters using OLCR is presented in Gottesman et al. (2004). An example of a so called reflectogram of a ring resonator notch filter without AR coating with a codirectional coupler (length = 150 µm, coupling gap = 0.9 µm) and radius r = 100 µm is shown

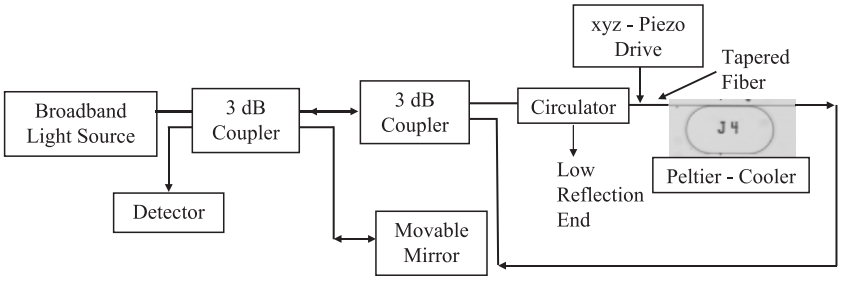

Fig. 3.71. OLCR measurement setup in transmission mode

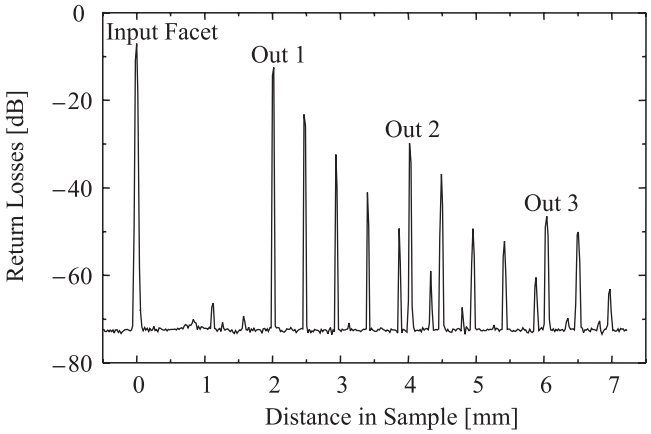

Fig. 3.72. Reflectogram of ring resonator with $r = 100\,\mu\text{m}$ without AR, measured in reflection mode

in Fig. 3.72. The first peak is measured at the input facet of the device. The second peak (out_1) is measured at the output facet. There are no significant reflection peaks in between those peaks coming from the ring resonator, which shows that the input signal has passed the resonator undisturbed. The peaks in between peak out_1, peak out_2, and peak out_3 result from multiple roundtrips in the ring resonator. The distance between the peaks out_{1-2} is 2 mm which corresponds to the chip length. The distance between two peaks coming from the ring resonator is equal to half of the cavity length which is measured to be $\approx$466 µm (physical value 464 µm).

A reflectogram of a ring resonator notch filter measured in transmission mode is shown in Fig. 3.73.

The first peak is the transmission passing the coupler without entering the ring. The second peak is the transmission from one roundtrip in the ring. The third peak is the transmission from two roundtrips and so on. The roundtrip loss is evaluated from the transmission data beginning from the second peak.

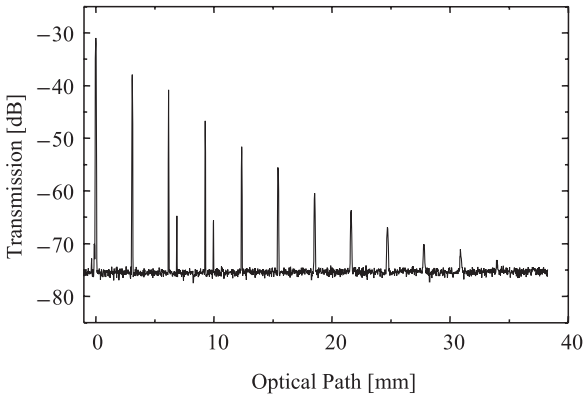

Fig. 3.73. Reflectogram of ring resonator with $r = 100\,\mu\text{m}$ without AR, measured in transmission mode

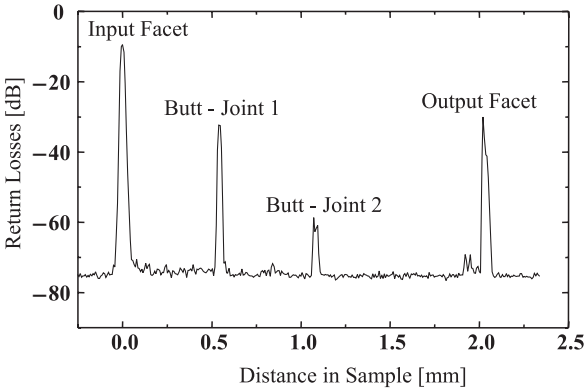

Fig. 3.74. Reflectogram of a straight waveguide with integrated SOA

In this calculation the loss in the straight waveguide is not considered and is contained in the coupling factor and the roundtrip loss. The length between the peaks is equal to half of the optical length of the ring resonator. The average optical length (in the ring) is taken from the measurement (e.g., distance between peak 2 and 3) and is equal to $6171.86\,\mu\text{m}$. The measured ring has a resonator length of $1776.64\,\mu\text{m}$. The group index is calculated from this data to be $n_{\text{gr}} = 3.47$. This is the average group index which the traveling light wave experiences when it passes the coupling region, the curved sections and the straight section in the resonator.

The active–passive transition can also be analyzed using the OLCR measurement. The result for a straight waveguide with a $500\,\mu\text{m}$ long SOA section, measured in reflection mode is shown in Fig. 3.74.

The facets are not AR coated which is shown in the high reflection peaks at the input and output facets. The return loss from the first butt joint is

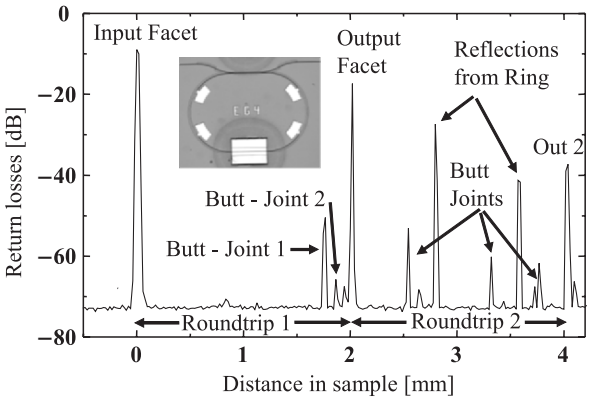

Fig. 3.75. Reflectogram of a ring resonator with integrated SOA

about −32 dB. The length of the SOA section can also be taken from the OLCR measurement and is proven to be 500 µm.

The reflectogram of a single ring resonator with SOA (see inset) is shown in Fig. 3.75.

The ring resonator has a radius of $r = 200\,\mu\text{m}$, a coupler length of 150 µm (coupling gap = 1 µm) and a gain length of 100 µm. The return loss resulting from the butt joint is only −50 dB which indicates a lower reflection than from the straight waveguide with SOA. This is due to the bending loss in the ring resonator, where part of the reflected intensity from the butt joint is lost, leading to a lower value for the return loss. There are again no reflection peaks due to imperfections in the resonator or straight waveguide which indicates a high quality cavity.

The OLCR method shows only a qualitative indication of the reflection coefficient, because OLCR takes into account the unknown absorption during propagation. A technique to evaluate the coupling efficiencies and reflection coefficients simultaneously at the butt-joint interface is presented in Song et al. (2005). The technique described here is based on the Hakki–Paoli method (Hakki and Paoli 1975), which is widely used to extract the gain spectra of semiconductor lasers and the reflectivity of the AR coating by measuring amplified spontaneous emission (ASE) spectra.

In summary, the OLCR measurement method enables an insight study of the quality of the ring cavity and has the potential to efficiently extract all necessary ring parameters to describe the spectral behavior of the ring resonator configuration.

3.8.3 Evanescent Field Measurement Methods

Near field techniques have become attractive for optical characterization. Probing the near field enables to overcome the diffraction limit of conventional

microscopy. Spatial resolutions much smaller than the optical wavelength can be obtained, approaching $\lambda/50$.

Near-Field Scanning Optical Microscopy

Near-field scanning optical microscopy (NSOM) or scanning near-field optical microscopy (SNOM) which is used as an alternative name is another scanning probe microscopy (SPM) related technique. An optic fiber is stretched and thinned such that it has a very sharp point. The fiber is coated with metal such that a small aperture (approximately 25 nm diameter) is formed at the tip of the fiber. This aperture serves to illuminate a small spot on the sample which is much smaller than the conventional diffraction limit. The sample is then scanned beneath the tip and the image is formed in the same fashion that a dot matrix printer prints a picture. The tip is brought very close to the surface. The tip–surface distance can be measured via the force acting between the two. The tip is scanned across the surface as in scanning tunneling microscopy (STM). NSOM (or SNOM), can detect objects below the diffraction limit (down to the nm regime) and thus represents a powerful new technique in optical microscopy. The significance of NSOM is that it allows spatial resolution with more than an order of magnitude improvement over the best conventional optical methods, including laser scanning confocal microscopy.

Although optical characterization is the most widespread method to analyze materials from biology to the semiconductor industry, it suffers from one inherent problem: the diffraction limit provides a spatial resolution limit of about half of the wavelength of light. Thus, features smaller than 250 nm can not be imaged or spectrally characterized with visible light. NSOM combines scanning probe microscopy instrumentation with optical microscopy and spectroscopy to provide optical characterization with, in some cases, 15 nm resolution in using visible light.

One of the first experiments using NSOM to measure the internal optical modes inside ring resonators with a radius of 25 µm is presented in Vander Rhodes et al. (2000). The ring resonators which are analyzed are described in detail in Chu et al. (1999c) and have also been described in Sect. 3.3.2. The setup used in the NSOM experiment consists of a standard optical measurement setup as described in Sect. 3.8.1 using a lensed fiber for coupling into the ring resonator, an ECL and a photodiode at the output port and in addition the NSOM probe, which is fed into an InGaAs detector to collect the light from the sample. A multimode fiber optic is used at the output facet of the ring resonator chip which enables the simultaneous monitoring of both the through and drop port of the ring resonator when performing the NSOM scans. The NSOM probe is scanned over the surface of the waveguide with a tip–surface separation of 10 nm using an interferometrically calibrated translation stage to scan the tip with an accuracy of ±0.3 nm. Results of NSOM scans of a ring resonator are shown in Fig. 3.76.

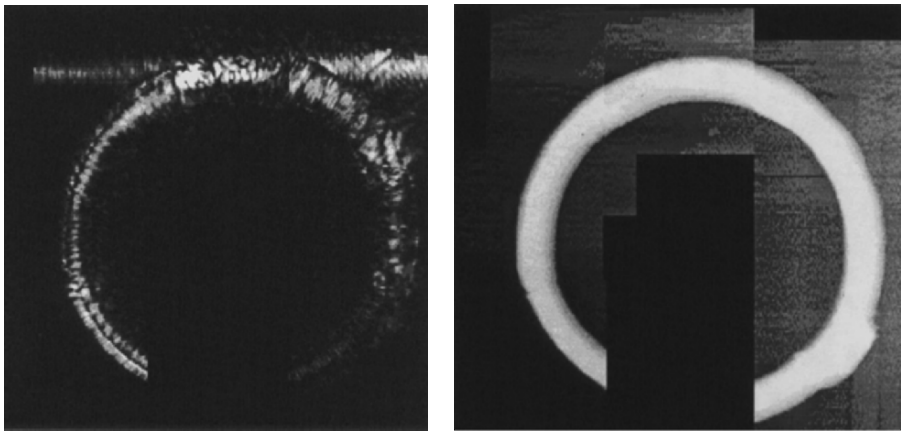

Fig. 3.76. Multiple NSOM scans of the ring resonator, stitched together for an image of almost the entire ring on resonance. Entire scan is 58 µm square: (**a**) shows the optical modes, clearly showing the light coming into the resonator in the upper right, with about half of that light leaving the resonator at the drop port in the *upper left*. The launch orientation used here is not especially efficient in coupling to the drop port, which is why very little light is seen at the drop port in the *upper right* and (**b**) is topography, with a height difference of 1.45 µm from black to white.

Reprinted with permission from IEEE Journal of Selected Topics in Quantum Electronics, vol. 6, pp. 46–53 ©2000 IEEE

Photon Scanning Tunneling Microscope

Photon Scanning Tunneling Microscope (PSTM) is another configuration of a scanning near field system described before. A PSTM is a device where the object is illuminated by an evanescent wave generated at the face of a prism or slide and the field is detected via a fiber probe in the near-zone of the sample (as in NSOM). PSTM measurements are inherently holographic since the sample is illuminated by an evanescent field and that same field serves as reference.

The PSTM tips are obtained in a similar way as NSOM probes, by pulling an optical fiber, coating it with about 7 nm of Cr, which results in no aperture at its very extremity. The PSTM tip scans at constant height. In this mode of operation, the signal detected by a PSTM is related to the spatial distribution of the intensity of the optical electric field in the near-field zone. Ring resonators have been analyzed using photon scanning tunneling microscopy in Quidant et al. (2004). A photograph of a fabricated ring resonator is shown in Fig. 3.77.

The used ring resonators are made of a 150 nm thick TiO_2 layer (residual roughness of 3 nm) coated on a glass substrate with a residual roughness

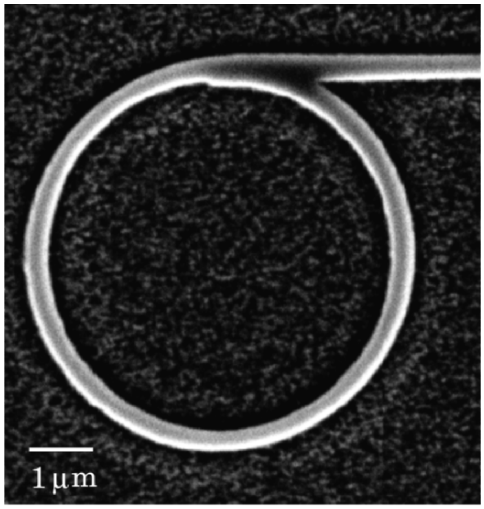

Fig. 3.77. Scanning electron microscopy picture of a TiO_2 ring coupled with a linear waveguide ridge. (Photograph courtesy of Dr. Romain Quidant[12])

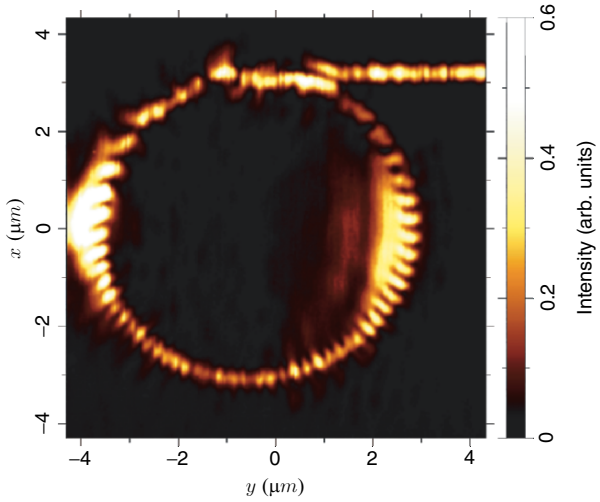

Fig. 3.78. PSTM image recorded above the microring. The probe tip scans in plane parallel to the sample located at 50 nm from the TiO_2 structures. (Photograph courtesy of Dr. Romain Quidant)

of 1 nm by ion assisted deposition. The waveguides are fabricated using RIE. The dimensions of the ring resonators are 6 µm in diameter, 250 nm wide and 150 nm high.

[12] ICFO – Institut de Ciències Fotòniques, Parc Mediterrani de la Tecnologia, Av. del Canal Olímpic s/n, 08860 Castelldefels, (Barcelona), Spain

In this PSTM experiment, an He–Ne laser (633 nm) injected in a lensed single mode fiber is used to illuminate the ring resonator. The end of the fiber is oriented in such a way that the beam can be focused at the interface between the dielectric ridge and the glass substrate. Only TM polarized incident light is being considered. The Gaussian beam is focused at the right end of the straight bus waveguide in such a way that the components of the incident wave vector parallel to the surface of the substrate align along the longitudinal axis of the bus waveguide. The tip is scanned at a constant height above the sample surface while monitoring the light intensity level. A photograph of the resulting image is shown in Fig. 3.78.

Several state-of-the-art characterization techniques have been described. Due to the decreasing dimensions of ring and disk resonator devices and the increase in integration density, a combination of several characterization methods is inevitable in the future to guarantee optimum device performance.

The following chapter deals with the building blocks of ring resonator devices which include bends and couplers.

4

Building Blocks of Ring Resonator Devices

Ring resonator devices comprise a bus waveguide and a ring which is made out of bend waveguides in the basic configuration. The material used for realizing the ring resonator filter already imposes restrictions onto the waveguide type and thus on the performance of the ring resonator. It is therefore important to analyze the building blocks of the envisaged ring resonator with respect to the wanted performance of the filter in advance once the material has been chosen.

The part where the bus and the ring come close to one another can be regarded as a coupler, also in the basic configuration, where the interaction path (coupler length) of the optical field in ring and coupler is extremely short. The performance of the ring resonator depends on the power coupling factor as one parameter besides several other factors already discussed in previous chapters. Several coupling schemes can be applied including vertical couplers, directional couplers, MMI couplers and Y-couplers. A detailed summary of the simulation and design of directional couplers and MMI couplers also with respect to polarization dependence is presented in Darmawan et al. (2005).

In order to fabricate ring resonators with low loss, it is essential to know the bending loss of the waveguides which depends directly on the used bending radius, which supplies the FSR of the ring resonator filter if this type of waveguide is used for fabricating the ring.

A fact which should be taken into account in the designing stage is the coupling of the bus waveguides to the outside world. Here several concepts exist like tapering the waveguides in vertical, horizontal (or both) directions to match the mode field profile of the bus waveguides to an optical fiber.

This chapter provides an introduction into the various building blocks making up a ring resonator filter.

4.1 Couplers

4.1.1 Directional Couplers

An important device used to couple light into and from ring resonators is the directional coupler. This type of coupler is preferably used to realize splitting ratios other than 3 dB. One of the first papers to deal with directional integrated optical couplers is presented in Marcatili (1969b).

Directional couplers have been studied extensively in the past and have found their way into many integrated optical devices like for example optical switches (Forber and Marom 1986) and vertical coupler beam splitters (Raburn et al. 2000).

The well known equations which describe the input and output field of the coupler shown in Fig. 4.1 are given by

$$\begin{bmatrix} E_3 \\ E_4 \end{bmatrix} = (1-\gamma)^{\frac{1}{2}} \begin{bmatrix} \sqrt{1-\kappa} & -\mathrm{j}\sqrt{\kappa} \\ -\mathrm{j}\sqrt{\kappa} & \sqrt{1-\kappa} \end{bmatrix} \cdot \begin{bmatrix} E_1 \\ E_2 \end{bmatrix}. \tag{4.1}$$

The relation between the in- and output intensity of a symmetrical directional coupler is given using

$$\begin{bmatrix} I_3 \\ I_4 \end{bmatrix} = (1-\gamma) \begin{bmatrix} 1-\kappa & \kappa \\ \kappa & 1-\kappa \end{bmatrix} \cdot \begin{bmatrix} I_1 \\ I_2 \end{bmatrix}, \tag{4.2}$$

where γ is the power loss coefficient, κ is the power coupling factor. If both waveguides have the same propagation constant which is the case in this configuration and the light is inserted into input port 1, then after a length L_c the energy will have coupled into the other waveguide and can be detected at output port 4.

The coupling behavior dependent on L_c for light inserted at input port 1 is expressed by

$$E_3(x) = E_1(1-\gamma)^{\frac{1}{2}} \cos\left(\frac{\pi}{2L_\mathrm{c}}x\right), \tag{4.3}$$

$$E_4(x) = \mathrm{j}E_1(1-\gamma)^{\frac{1}{2}} \sin\left(\frac{\pi}{2L_\mathrm{c}}x\right), \tag{4.4}$$

$$I_3(x) = E_3(x) \cdot \overline{E_3(x)} \text{ and } I_4(x) = E_4(x) \cdot \overline{E_4(x)}. \tag{4.5}$$

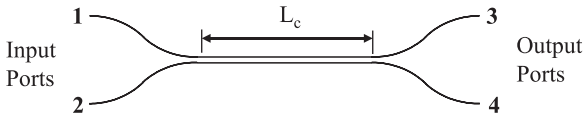

Fig. 4.1. The directional coupler

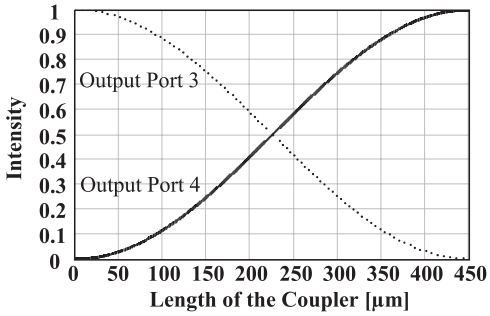

Fig. 4.2. Coupling behavior of a symmetrical directional coupler

The coupling behavior for a coupler with $L_c = 450\,\mu m, E_1 = 1, E_2 = 0$ is shown in Fig. 4.2. The intensity at both output ports is normalized to the sum of the output intensities

$$\text{Intensity at output port } 3 = \frac{I_3}{I_3 + I_4} \tag{4.6}$$

$$\text{Intensity at output port } 4 = \frac{I_4}{I_3 + I_4} \tag{4.7}$$

The power coupling factor κ is taken from the diagram (Fig. 4.2) for a specific coupling length x.

For example, the power coupling factor κ is equal to $\kappa = 0.9$ for a coupler with a length of $360\,\mu m$.

The separation between the waveguides in the directional coupler is the critical element regarding the fabrication. The resolution of the photolithography used (standard photolithography using a quartz/chromium mask, electron beam lithography, etc.) defines the minimum coupling gap. The fabrication of the gap depends mainly on the waveguide width and the etch depth in the gap. An example of a fabricated coupler is shown in Fig. 4.3. The etch depth in the gap is lower in this example than on the outer side of the coupler waveguides, which is due to the lower etch rate in the gap. The dry etching process is strongly dependent on the etch gases and conditions used and has to be modified if performed with other RIE systems to achieve similar results.

Integrated optical devices require directional couplers to provide the desired power splitting ratio, independent of wavelength or polarization. In wavelength division multiplexing systems, where ring resonator add drop filters are deployed, it is necessary to achieve a constant splitting ratio for all used wavelength channels. It is often impossible to achieve broadband polarization-insensitive performance, especially in planar integrated devices, unless several design consideration are incorporated and tradeoffs taken into account as is explained in Sect. 3.7. A wavelength- and polarization-insensitive directional coupler configuration is demonstrated in Little and Murphy (1997)

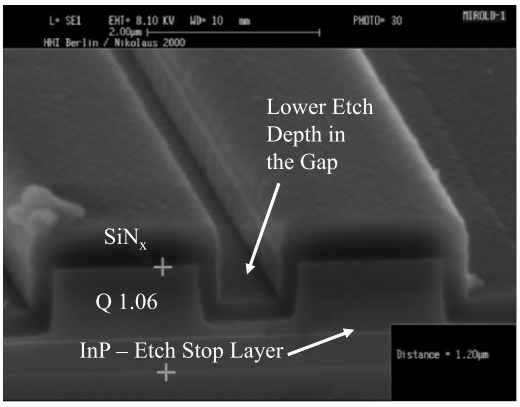

Fig. 4.3. SEM photograph of the input region of a directional coupler, gap = 0.8 µm

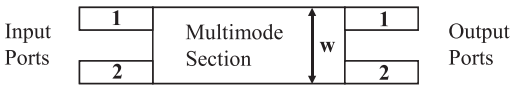

Fig. 4.4. Top view of an MMI coupler

and Murphy et al. (1999). Design rules towards polarization insensitive directional couplers employed in ring resonator filters are discussed and presented in Chin (2003).

4.1.2 Multimode Interference Couplers

A multimode interference (MMI) coupler consists of a broad center waveguide which supports several modes depending on the width and the layer sequence of the waveguide (Fig. 4.4). The self-imaging principle is used in MMI couplers for realizing various coupler configurations including a 2×2 coupler to be used in ring resonator devices. Self-imaging is a property of multimode waveguides by which an input field profile is reproduced in single or multiple images at periodic intervals along the propagation direction of the guide (Soldano and Pennings 1995).

Between these intervals, the input field is reproduced with only a fraction of the input intensity, divided symmetrically in the multimode section. A SEM photograph of the input region of a 2×2 MMI coupler is shown in Fig. 4.5.

An atomic force microscope (AFM) photograph of the input region of an MMI coupler is shown in Fig. 4.6 (Rabus 2002). The gap between the two input waveguides is 2.4 µm.

The main advantage of MMI couplers compared to directional couplers is the fabrication tolerance with respect to the splitting ratio which can be for example 3-dB in the case of 2×2 couplers used in ring resonators. If other coupling ratios are required, directional couplers are favored. The multimode section should support more than three modes to assure an appropriate

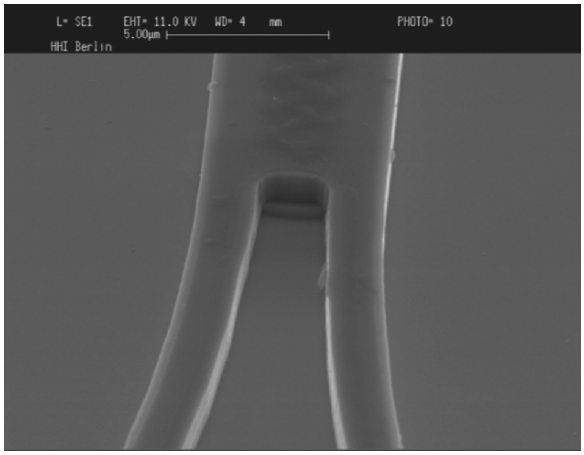

Fig. 4.5. SEM photograph of the input region of a 2×2 coupler

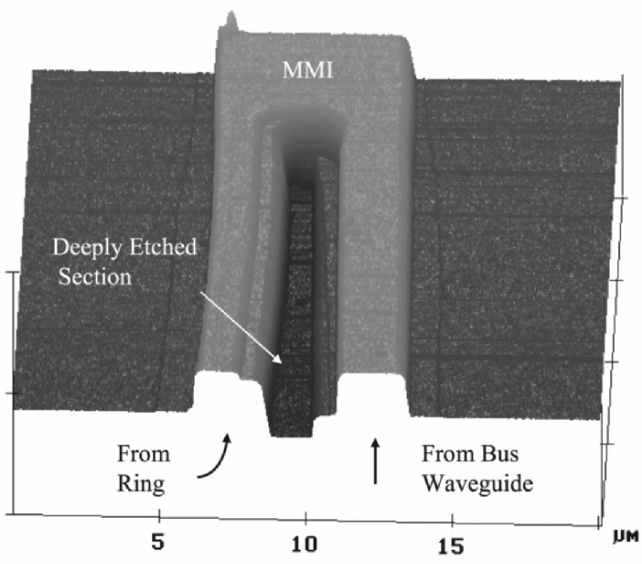

Fig. 4.6. AFM picture of the input region of an MMI coupler (Rabus 2002)

interference signal of the input mode. Finite difference time domain or beam propagation tools (Weinert and Agrawal 1995) are needed to calculate the behavior of MMI couplers which are commercially available.

The fundamental beat length of MMI is related to the waveguide parameters (step-index MMI section) by Soldano and Pennings (1995):

$$L_\pi = \frac{\pi}{\beta_0 - \beta_1} \cong \frac{4 n_{\text{eff}} \cdot w^2}{3\lambda_0}, \tag{4.8}$$

where β_0 and β_1 are the propagation constants of the fundamental and first order lateral modes, respectively, λ_0 is the wavelength, n_{eff} is the effective index and w is the width of the multimode section.

The 3 dB length of MMI couplers can also be approximated by the formula given in van Roijen et al. (1994):

$$L_{3dB} = \frac{3}{4}\frac{\lambda_0}{n_{\text{eff}0} - n_{\text{eff}1}} \approx 2\frac{n_{\text{eff}} \cdot w^2}{\lambda_0}, \tag{4.9}$$

where λ_0 is the wavelength, $n_{\text{eff}0}$ and $n_{\text{eff}1}$ are the effective indices of the fundamental and first order mode.

The usage of short couplers with defined splitting ratio is essential in ring resonators for achieving a high FSR due to a short roundtrip length. One of the first fabricated MMI couplers on InP having the shortest length at that time of only 107 µm for a 3 dB coupler are demonstrated in Spiekman et al. (1994). The width of the MMI is only 9 µm. A ridge waveguide design is used with an InGaAsP core with a bandgap wavelength of 1.3 µm and a thickness of 600 nm. An InP cap having a thickness of 300 nm is grown on top.

Extremely short InP–InGaAsP MMI 3-dB couplers with lengths between 15–50 µm are presented in Ma et al. (2000b).

Ring resonators ideally require a tunable coupler in order to adjust the coupling factor to the roundtrip loss in the case of passive resonators and to realize specific filter characteristics in the case of multiple coupled ring resonators. MMI couplers with a tunable splitting ratio are demonstrated in Nagai et al. (1999); Leuthold and Joyner (2000, 2001) and Jiang et al. (2005). MMI couplers are usually fabricated in semiconductor materials which enable the realization of strong guiding waveguides. Recently MMI couplers are proposed using weak guiding structures (West and Honkanen 2005) and fabricated in polymer materials (Mule' et al. 2004, Rabus et al. 2005b).

4.1.3 Y-Couplers

Y-couplers are a well-known class of integrated optical devices and have been used in several integrated systems to guide and manipulate light. Quite a lot of research has been performed on digital optical switches (DOS) in polymers using cascaded Y-couplers to create integrated $1 \times N$ splitters (Bernhard 2002, Hauffe 2002). An example of a Y-coupler is shown in the schematic in Fig. 4.7.

This example of a Y-coupler comprises single mode waveguides for in- and out coupling with width w, a taper and a coupling region. The taper region is designed in such a way, that the width at the end is slightly less than 2 times the width of a single mode waveguide. This assures, that only the fundamental mode is allowed to propagate in the beginning of the taper and in the end into the two output waveguides and not the next higher mode which would cause additional losses, as it is not supported by the geometry of the single mode waveguides. In the coupling region, both output waveguides have to

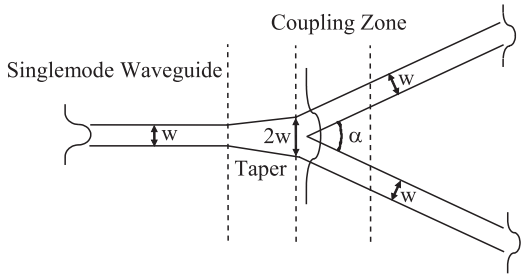

Fig. 4.7. Schematic of a symmetric Y-coupler

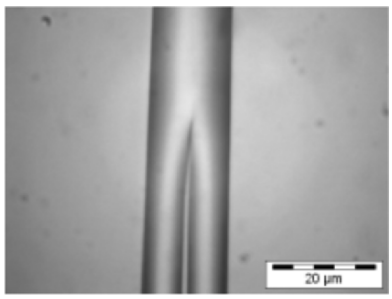

Fig. 4.8. Polymer Y-coupler

be treated using coupled mode theory to describe their behavior. This region is of importance when it comes to design a symmetric Y-coupler with equal power splitting in both output arms. If the angle α is chosen too small, power from one arm is able to couple to the other one being the cause for a different splitting ratio than intended. On the other hand making the angle too large causes additional losses. Therefore, a tradeoff has to be found for realizing a specific Y-coupler. Usually S-bends are used to separate the output arms and realize a certain distance between them. Due to manufacturing tolerances like proximity effect and etching, a sharp branching angle is not achieved in most cases and a compromise has to be made to find the optimum angle. An example of a fabricated Y-coupler in polymers is shown in Fig. 4.8 (Rabus et al. 2005b).

Y-couplers have found their way into ring resonators for example in ring lasers, where they have been specially designed to increase the output power. An example of an improved Y-junction splitter used in ring resonator lasers can be found in Burton et al. (1994). The design uses only rectangular sections which make it similar to an MMI coupler avoiding sharp tips at waveguide intersections, which are a challenge to fabricate. For more details on ring resonator lasers, see Sect. 5.6. Due to the fact that Y-couplers can be regarded as standard optical components which can be simulated with several commercially available BPM and FDTD software, further treatment of these devices will not be given.

4.2 Bends

Bends are inevitable building blocks of state-of-the-art integrated optical circuits and have therefore been always of interest in the optics community. One of the first papers dealing with the analysis of bends is described in Marcatili (1969a). Since then, many methods have been proposed and developed to describe the behavior of the mode field and lower the losses in bends for example, Neumann and Richter (1983), Bienstman et al. (2002), Melloni et al. (2001).

One method of describing a waveguide bend is to use a conformal transformation which is presented in Heiblum and Harris (1975). The curved waveguide is translated into an equivalent straight waveguide with a transformed index profile.

By using a cylindrical coordinate system (x, ρ, ϕ), propagation of light in circularly curved waveguides can be described in terms of modal propagation (Fig. 4.9). A mode in such a structure is given by Smit et al. (1993):

$$E_{\mathrm{Circ}} = U_{\gamma}(r)\, e^{\pm\gamma_{\phi}\phi}. \tag{4.10}$$

This mode has as an equi-phase front which propagates in the angular direction ϕ. γ_{ϕ} is regarded as a complex angular propagation constant and is described as:

$$\gamma_{\phi} = \alpha_{\phi} + \mathrm{j}\beta_{\phi}, \tag{4.11}$$

where α_{ϕ} is the attenuation coefficient, this time in angular direction, and β_{ϕ} is the real angular propagation constant in rad^{-1}.

Using a conformal mapping technique (see also Chin and Ho 1998), the problem of solving the wave equation in cylindrical coordinates can be transformed to rectangular coordinates by performing the following steps (Heiblum and Harris (1975), Smit et al. (1993)):

$$u = R_{\mathrm{t}} \ln\left(\frac{r}{R_{\mathrm{t}}}\right) \tag{4.12}$$

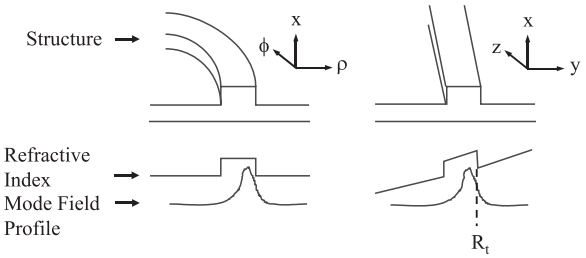

Fig. 4.9. Curved waveguide transferred to a straight waveguide using conformal transformation. Curved waveguide with real index profile (*left*). Equivalent straight waveguide with transformed index profile (*right*)

with R_t a freely selectable reference radius. Equation (4.10) can then be written as

$$\left[\frac{\partial^2}{\partial u^2} + \left\{k^2 n_\mathrm{t}^2(u) - \gamma_\mathrm{t}^2\right\}\right] U_\mathrm{t}(u) = 0, \tag{4.13}$$

where

$$n_\mathrm{t}(u) = n\left\{r(u)\right\} \mathrm{e}^{\frac{u}{R_\mathrm{t}}} \tag{4.14}$$

$$\gamma_\mathrm{t} = \frac{\gamma_\phi}{R_\mathrm{t}} \tag{4.15}$$

$$r(u) = R_\mathrm{t} \mathrm{e}^{\frac{u}{R_\mathrm{t}}} \tag{4.16}$$

The angular propagation and attenuation constants can now be derived using (4.15) as follows:

$$\beta_\phi = \beta_\mathrm{t} R_\mathrm{t}, \tag{4.17}$$

$$\alpha_\phi = \alpha_\mathrm{t} R_\mathrm{t}. \tag{4.18}$$

The radiation loss can then be expressed by

$$A_\phi = -20 \log_{10}\left\{\mathrm{e}^{\frac{-\alpha_\phi \pi}{2}}\right\} = 10\pi\alpha_\phi \log_{10} \mathrm{e}. \tag{4.19}$$

With this transformation an ordinary straight waveguide problem is obtained, which can be solved with the effective index method by using a staircase approximation for the transformed index profile in the u-direction (Fig. 4.9 right). The index profile $n(r)$ is transformed into an index profile $n_\mathrm{t}(u)$. The shape of the transformed profile can be qualitatively understood by considering that the longer path length of the light travelling in the outside bend has to turn up in the straight waveguide problem as a slower phase velocity, hence the higher index there. The center of gravity of the mode profile in a curved waveguide moves outward, an effect that increases by decreasing the radius of the bend.

An approximation can be made when R_t is chosen to be equal to the outer edge of the waveguide and $u/R_\mathrm{t} \ll 1$ in the vicinity of the waveguide, then

$$r \cong R_\mathrm{t} + u, \tag{4.20}$$

which leads to a transformed index profile

$$n_\mathrm{t}(u) \cong n(R_\mathrm{t} + u)\left(1 + \frac{u}{R_\mathrm{t}}\right). \tag{4.21}$$

A simple method for estimating bend radii of deeply etched rib waveguides (Fig. 4.9) is presented in Pennings et al. (1991). This method can be used for rib waveguides, where the rib is etched completely through the guiding layer. The effective index method (EIM) is used in this reference to describe the

rib waveguide by a one dimensional refractive index profile with an effective index n_{rib} under the rib and an effective index of 1 next to the rib (air). This one dimensional refractive index profile can now be treated as a straight slab waveguide with a propagation constant of

$$\beta = k n_{\mathrm{straight}}. \tag{4.22}$$

All modes with a refractive index n_{straigth} smaller than the refractive index of the substrate $n_{\mathrm{substrate}}$ are treated as below the cut of wavelength and are lost into the substrate. The straight waveguide problem is solved again by applying the conformal transformation method as discussed before with the refractive index of the bend n_{bend} related to the angular propagation constant γ by

$$n_{\mathrm{bend}} = \frac{\mathrm{Re}\,(\gamma_\phi)}{kR} = \frac{\alpha_\phi}{kR}. \tag{4.23}$$

The imaginary part of the angular propagation has been neglected due to the high index contrast between the waveguide and the surrounding air, which leads to a strong confinement of the mode in the waveguide and results in low radiation losses in the bend. The radius R is defined as being the length up to the outer side of the waveguide bend. Using the cutoff condition $R = R_{\mathrm{co}}$ when $n_{\mathrm{bend}} = n_{substrate}$ and the approximation

$$n_{\mathrm{straight}} - n_{\mathrm{bend}} = \frac{1}{2} n_{\mathrm{rib}} \frac{w}{R} \tag{4.24}$$

leads to the equation for the cutoff radius, which depends only on parameters of the straight waveguide

$$R_{\mathrm{co}} = \frac{w \cdot n_{\mathrm{rib}}}{2\,(n_{\mathrm{straight}} - n_{\mathrm{bend}})}. \tag{4.25}$$

The main cause for losses in bends is of course the bending losses themselves (4.19). One way to minimize the bending loss is by increasing the radius. This is of course limited when designing ring resonators with certain parameters and a specified filter performance. Therefore one way to reduce the bending loss is by changing the refractive index of the material on the outer side of the waveguide. This can also mean the complete removal of the material on the outer side of the waveguide and forming a trench. An analysis of this idea is presented in (Neumann 1982b, Seo and Chen 1996). Schematics of proposed waveguide geometries are shown in Fig. 4.10. Seo et al. not only suggested to use trenches on the outer side of the curved waveguide to reduce the bending losses, but analyzed also the slope of the rib with regard to the transition losses which can be lowered this way.

Another type of loss which is especially important when it comes to the design of racetrack shaped ring resonators is the transition loss which occurs at the interface between a straight waveguide and a bend. One of the first publications dealing with the reduction of these transition losses is (Neumann

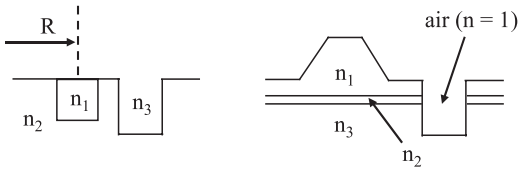

Fig. 4.10. Architectures of waveguide bends

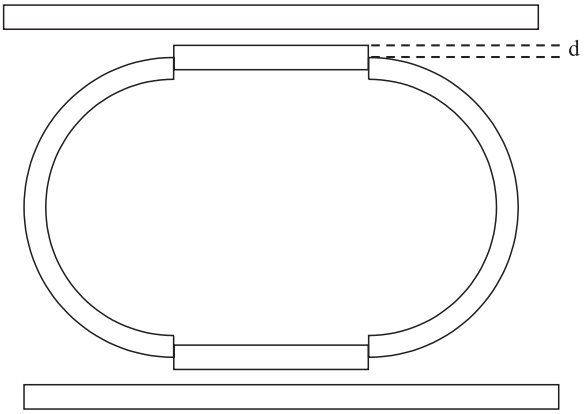

Fig. 4.11. Schematic of a racetrack shaped ring resonator with offsets between the curved and straight waveguide junctions

1982a). As described earlier, the center of the mode field in the curvature shifts with increasing radius to the outer side of the waveguide in the bend. This distance d of the mode shift in a waveguide having a width w[1] can be described by the following equation:

$$d = \frac{\pi^2 n_{\text{eff}}^2 w}{\lambda^2 R}. \tag{4.26}$$

One method of reducing the transition losses is therefore to apply an offset between the curved and the straight waveguide sections which is equal to a distance d. A schematic of a racetrack shaped ring resonator employing offsets at the respective interfaces is shown in Fig. 4.11. A fabricated racetrack shaped ring resonator in the material system GaAs–AlGaAs (Fig. 4.12) employing such offsets is presented in Van et al. (2001). Here, fabricated racetrack shaped ring resonators with offsets up to 0.08 µm are demonstrated. The parameters for the racetrack shaped ring resonators are a waveguide width of 0.52 µm, a coupling gap of 0.2 µm, an average bending radius of 4.7 µm, and straight-section length of 10.24 µm.

[1] Note that w can either be the actual width of the waveguide or the width of the mode, depending on the type of waveguide used.

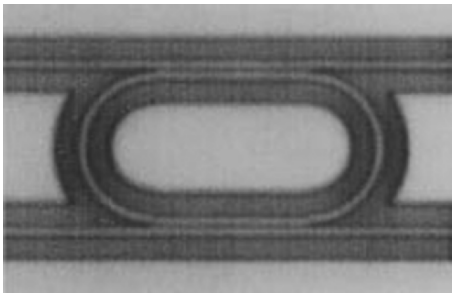

Fig. 4.12. Racetrack shaped ring resonator with lateral offsets between curved and straight waveguide sections.

Reprinted with permission from IEEE Journal of Lightwave Technology, vol. 19, pp. 1734–1739 ©2004 IEEE

The transmission from a straight to a curved waveguide for the case of rib channel waveguides is given by Subramaniam et al. (1997)

$$T_{\mathrm{SC}}(d) = \frac{\mathrm{e}^{\frac{-d^2}{2w^2}} \left[1 + \frac{(k \cdot n \cdot w)^2 d}{2R}\right]^2}{\left[1 + \frac{(k \cdot n \cdot w)^4 w^2}{2R^2}\right]}, \tag{4.27}$$

where w represents the mode width and n the effective refractive index of the rib in the center of the waveguide. Minimum transition loss is achieved when:

(a) The amplitude distributions of the two modes are matched
(b) The phase distributions are matched

Condition (b) is satisfied, condition (a) is a cause for the transition losses which can be evaluated using (4.27) or can be approximated by Neumann (1982a)

$$\alpha_{SC\text{-}losses} = 4.343 \left(\frac{d}{w}\right)^2 \quad \text{(dB)}$$

where w is either the width of the waveguide or the width of the mode.

These transition losses can be lowered by choosing the appropriate offset, trench or different material with a lower refractive index on the outer side of the waveguide in the bend and in addition selecting the right widths of both the straight and the bend waveguides (Smit et al. 1993).

Bends are not only used as "connecting" elements in integrated optics, but can also serve themselves as polarization rotators. An analysis of polarization rotation in bends is presented in Lui et al. (1998), Obayya et al. (2001). A compact polarization converter based on bends is demonstrated in van Dam et al. (1996). Polarization rotation can be of importance when designing ring resonator filters and depends on several influencing factors like type of material used, waveguide geometry and ring radius.

4.3 Spot Size Converters for Light In- and Outcoupling

Spot size converters are used to reduce the fiber–chip coupling losses when single mode fibers are butt coupled to an integrated waveguide structure or to a laser diode. The efficiency of the spot size converter depends again on the type of material used for realizing the integrated waveguide based device which results in possible waveguide parameters. Therefore in choosing an appropriate material for the fabrication of a ring resonator filter for example and with it a waveguide geometry, already sets the boundary conditions for the spot size converter. It is therefore important to design a photonic device taking into account not only fabrication aspects, but also the connections to the outside world.

An established way to realize a spot size converter is by incorporating tapered structures operating close to the mode cutoff, which expands their spot size area to enhance the optical coupling efficiency without deteriorating alignment tolerances. The use of these designs has improved the coupling efficiency and at the same time has enabled a more relaxed alignment tolerance of the fiber to the chip. Several taper designs have been demonstrated, such as lateral tapers (Kasaya et al. 1993), vertical tapers, or combinations of either lateral and vertical tapers (Yan et al. 2002) or waveguide configurations (Hamacher et al. 2000). An example of a spot size converter consisting of a lateral taper and a vertical coupling to a waveguide underneath is shown in Fig. 4.13.

Here an approach is applied which relies on an adiabatic coupling between a strong confined waveguide mode and a weak waveguide mode in a guiding layer 1 µm beneath the actual waveguide. The rib of the waveguide is laterally tapered down from 2 µm to 0.5 µm forcing the light to couple between the two modes. For a better lateral confinement of the weakly guided mode a second rib is etched in the tapered region only. An example of the integration of this spot size converter with a ring resonator is shown in Fig. 4.14.

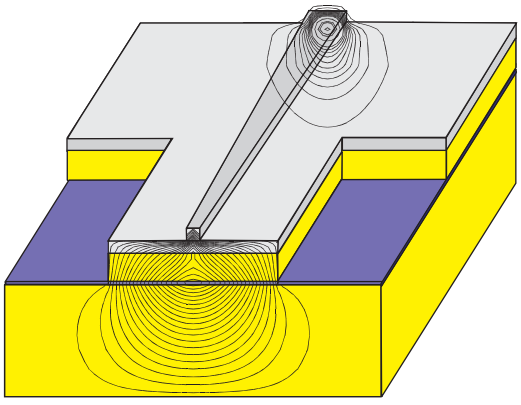

Fig. 4.13. Schematic of a spot size converter (Hamacher et al. 2000)

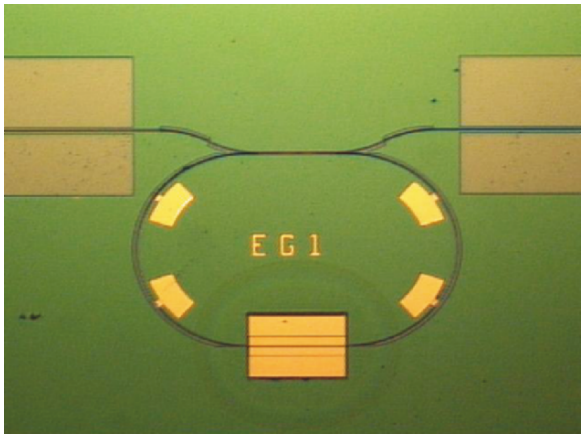

Fig. 4.14. Ring resonator with integrated SOA and spot size converter

A tradeoff between overall chip size and length of the taper region on both sides has to be found. A longer taper with a gradual enough taper slope will of course exhibit a lower loss. An optimization of compact lateral, vertical, and combined tapered spot size converters using the beam-propagation method is presented in Haxha et al. (2006).

In the previous chapters, simulation, fabrication, and building blocks of ring resonator devices have been described. The following chapter presents applications of ring resonator devices fabricated in different material systems using different architectures and building blocks.

5

Devices

This chapter is entirely devoted to highlighting the various applications of ring resonator devices developed to date using examples presented by the ring resonator community. Some ring resonators have already been described in Chap. 3, therefore only performance parameters like the free spectral range (FSR), the full width at half maximum (FWHM), the quality factor Q and the finesse F will be given in this chapter for selected devices.

Ring resonators have been primarily investigated to be implemented as optical add–drop filters in optical networks. Several optical filter designs have been proposed and realized in semiconductors and polymers, purely passive devices, ring resonators with integrated gain sections and devices made out of active material. Optical filters need to be tunable in order to be deployed in optical networks. This fact is even more important, when it comes to ring resonators, as the resonances of the ring resonator filter have to be aligned exactly to the required optical channel. Wavelength tuning and center wavelength trimming methods will be explained in this chapter.

Ring resonators can be used for flexible dispersion compensation and several fabricated devices will be explained.

In wavelength division multiplexing (WDM) applications, a square spectrum response is desirable. Periodic multiplexers and demultiplexers, which have a flat passband and a wide rejection region, can be realized integrating a modified Mach–Zehnder interferometer (MZI) with a ring resonator.

The application of ring resonators as lasers has been demonstrated already some time ago. It has gained attention again recently with the fact that combining ring resonators can enhance the tunability of ring lasers. Novel concepts have been proposed and realized using all active ring lasers and passive ring resonator coupled configurations with integrated semiconductor optical amplifiers (SOAs).

Due to the advancing state of the art in fabrication technology, ring resonators with very small radii have been built which opens up the possibility to use these elements as modulators and in optical signal processing systems as logic gates and as switching devices.

As equally important as creating a wavelength with ring lasers and filtering out a specific wavelength, wavelength conversion has been found to be possible using ring resonator devices.

Finally as a new technology trend is emerging which is currently known as biophotonics, ring resonators have again found their way into this new field in the form of sensors.

5.1 Filters

Ring resonator filters have been fabricated in many material systems as is described in Chap. 3. State-of-the-art manufacturing technologies have enabled the demonstration of filter characteristics and parameters useful for optical networks. The advantages of using ring resonator filters are obvious. Ring resonators can be integrated with other components such as lasers or SOAs to form complex photonic integrated circuits. Ring resonators do not require facets or gratings for optical feedback and can have very small dimensions which enables the realization of large scale photonic integrated circuits. Several examples will be presented in this chapter highlighting various results achieved for ring resonator filters with different geometries and materials.

5.1.1 Passive Devices

Single Ring Filters

One of the first passive single ring resonator add–drop filter with integrated throughput and drop–port is presented in Haavisto and Pajer (1980). A thin film of PMMA is used to fabricate the waveguides. The radius of the ring is 4.5 cm. The waveguide widths are 10 µm, with a 17.5 µm separation from center to center. A coupling strength of 2% is achieved. Prism coupling is used to couple in and out of the bus waveguides. A finesse of 16 is measured. The loss in the ring is found to be $0.05\,\mathrm{dB\,cm^{-1}}$, which includes coupling and radiation losses. Due to the large circumference of the ring, these ring resonator filters are limited in their use as channel dropping filters.

Improvement of fabrication methods and the coming up of new material systems (for example III–Vs) has made it possible to fabricate ring resonators with radii far below 100 µm. One of these first ring resonators is demonstrated in Rafizadeh et al. (1997b). Ring and disk resonators in the material system AlGaAs/GaAs with diameters of 10.5 µm (Fig. 5.1) and 20.5 µm are presented.

An FSR of 21.6 nm and an FWHM of 0.18 nm is measured for the disk resonator with a diameter of 10.5 µm, leading to a finesse of 120, and a cavity quality factor Q greater than 8,500. In the case of the ring resonator with a diameter of 10.5 µm, an FSR of 20.6 nm and an FWHM of 0.43 nm is measured, leading to a finesse of 48 and a Q-factor greater than 3,500. The FSR and the FWHM for the ring and disk resonators with a diameter of 20.5 µm are

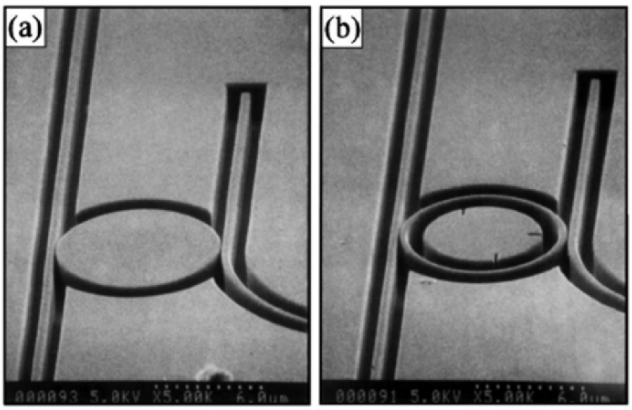

Fig. 5.1. SEM images of a 10.5-mm-diameter (**a**) disk and (**b**) ring.

Reprinted with permission from R. Rafizadeh, Optics Letters, vol. 22, no. 16, pp. 1244–1246 ©1997 Optical Society of America

10.2 nm/10.7 nm and 0.54 nm/0.12 nm, respectively. The FWHM is broader in the case of the ring resonator due to the loss caused by the additional sidewall.

Similar ring resonators in glass, vertically coupled to the bus waveguides with radii of 10 μm are presented in Little et al. (1999). An FSR of 20 nm and an FWHM of 5.2 nm are measured, leading to a finesse of 4 and a quality factor of 300. The low Q factor compared to the high Q factor for the similar AlGaAs/GaAs is due to a stronger coupling, leading to a broader FWHM and therefore to a lower Q factor. The transmission spectrum from both the throughput and the drop–port is shown in Fig. 5.2.

These ring resonators are used as building blocks in an 8 channel add–drop filter (Chu et al. 1999c). The ring resonators are connected in parallel to form a multichannel add–drop filter. Each ring resonator in the device has a different radius and thus a different resonance wavelength. In the fabricated device, the first ring resonator has a radius of 10.35 μm, while the remaining ring resonators decrease in radius by increments of 50 nm. The parallel drop–port waveguides are separated by 250 μm. A schematic of the 8-channel ring resonator add–drop filter is depicted in Fig. 5.3.

The transmission spectrum of the eight channel add–drop filter is polarization dependent. The FWHMs of the resonances for TE and TM polarization, from shortest to longest wavelengths, are 0.53, 0.63, 0.64, 0.71, and 0.92, 1, 1.06, 1.16 nm, respectively, leading to Q factors of 2,500 and 1,500. The average FSRs of the array is 20.1 nm and 20.2 nm for TE and TM, respectively. A junction induced crosstalk lower than −30 dB is achieved. The channel spacing achieved with this architecture is approximately 5.7 nm. The channel spacing can be adjusted to the required parameter by either changing the ring radius or the width of the waveguide, which results in a different propagation constant.

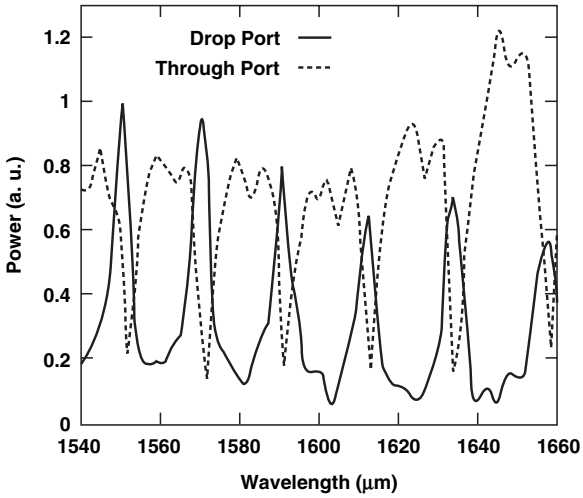

Fig. 5.2. TE polarized wavelength response of a 10 μm radius ring resonator. Reprinted with permission from B.E. Little, IEEE Photonics Technology Letters, vol. 11, pp. 215–217 ©1999 IEEE

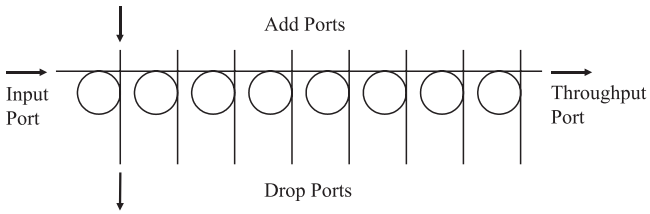

Fig. 5.3. 8-Channel add–drop filter

Vertically coupled ring resonators have not only been used in a parallel cascade to form a channel dropping filter, but have also been used in a 2×2 cross grid array for crosstalk reduction and spectrum cleanup in Chu et al. (1999a). A schematic of the 2×2 array consisting of three ring resonators is shown in Fig. 5.4.

The three ring resonators have the same parameters and therefore filter out the same wavelength. Resonator 1 is the first filter along the input bus waveguide. Resonator 2 having the same resonance wavelength as resonator 1 sends the filtered wavelength to the drop–port which increases the out-of-band signal rejection. This ring resonator configuration corresponds to a double ring resonator leading to a steeper roll off of the filter spectrum and consequently to a larger out-of-band rejection. Resonator 2 therefore, cleans up the drop–port spectrum. Signal power at the resonance wavelength that is not completely filtered out by resonator 1 is filtered out a second time by resonator 3. Resonator 3 therefore, cleans up the throughput spectrum.

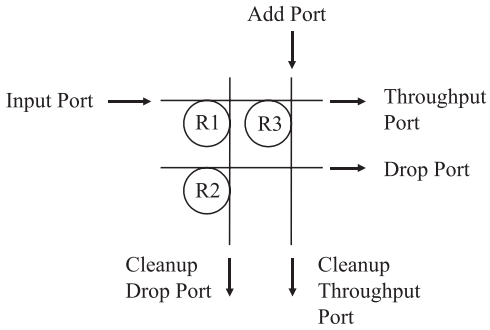

Fig. 5.4. 2×2 ring resonator add–drop node

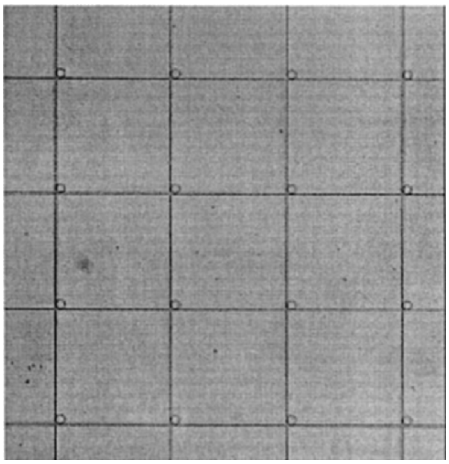

Fig. 5.5. Photograph of a portion of the 8×8 cross-grid vertically coupled glass ring resonator array.

Reprinted with permission from IEEE Photonics Technology Letters, vol. 12, pp. 323–325 ©2000 IEEE

The add port which does not have a path to the drop–port is cross connected to the input and throughput bus waveguide by resonator 3.

Finally, the vertically coupled glass ring resonators have been used to realize an 8×8 cross grid array (Little et al. 2000b). A photograph of the array is shown in Fig. 5.5. The height of the waveguide in the ring resonators is 1.5 µm, and the waveguide widths vary from 1 to 1.7 µm in increments of 100 nm. The ring resonators are identical along upward directed diagonals in the array. The spacing between the bus waveguides is 250 µm.

Vertically coupled ring resonators consisting of a dielectric material core (Ta_2O_5–SiO_2 compound glass with $n = 1.8$, or SiN with $n = 2$) and an air cladding have been proposed, designed and fabricated by the group of Kokubun. A summary of the work can be found in Kokubun (2005). Ring

resonators with radii between 10 and 20 µm, resulting in an FSR of 10–25 nm and an FWHM 0.1–1.0 nm have been demonstrated. These device parameters lead to high Q values between 1,500 and 15,000. Kokubun's group have pushed ring resonator technology not only in terms of ring size, but have also demonstrated polarization insensitive and tunable (center wavelength tuning and resonance tuning) ring resonators which are addressed in the relevant chapters of this book.

Laterally coupled ring resonators and vertically coupled disk resonators, with PMMA cladding and without cladding have been designed and realized in Si_3N_4 on SiO_2 in Klunder et al. (2001). A finesse of 136 has been achieved for a laterally coupled ring resonator without cladding and with a radius of 25 µm with a coupling gap of 750 nm. A finesse of 61 has been measured for a ring resonator with PMMA cladding. TE polarized light is used for the characterization of the devices at a wavelength of 1.55 µm. Vertically coupled disk resonators with a radius of 15 µm have been fabricated. The vertically coupled disk resonators are characterized using a wavelength of 640 nm. An FSR of 2.2 nm is measured which results in a finesse of 31. The finesse is limited by the linewidth of the laser used for characterizing the devices. A detailed analysis of the device performance of laterally coupled ring resonators in the same material system is presented by the group in Klunder et al. (2003b). Here ring resonators with coupling gaps of 0.5 µm (not completely open, due to fabrication imperfections), 0.75 µm and 1 µm have been fabricated and characterized. A photograph of a ring resonator with a coupling gap of 0.75 µm is shown in Fig. 5.6.

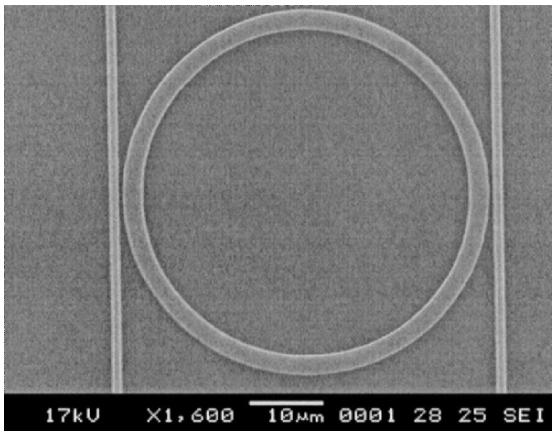

Fig. 5.6. Laterally coupled ring resonator in SiON with a radius of 25 µm and a coupling gap of 0.75 µm.

Reprinted with permission from IEEE Journal of Lightwave Technology, vol. 21, pp. 1099–1110 ©2003 IEEE

An FSR of 8 nm at a wavelength of 1,530 nm and a finesse of 120 are obtained for a ring resonator with a coupling gap of 0.75 µm and air cladding. A finesse of 22 is measured for the resonator with a coupling gap of 0.5 µm with air cladding. The values for the finesse of ring resonators with PMMA cladding are 61 and 25, respectively.

As has been mentioned in Chap. 3, recently several groups have demonstrated ring resonators not only in silicon, but also in GaAs and InP. One of the first racetrack shaped laterally coupled ring resonators in the material system AlGaAs with a cavity length of 31 µm (length of the straight sections is 6 µm and 4 µm) is presented in Chin et al. (1999). A photograph of a racetrack shaped ring resonator is shown in Fig. 5.7.

A gap between the bus waveguides and the racetrack of 200 nm is used. An FSR of 20 nm and an FWHM of 1 nm is achieved in the case of the 6 µm long straight sections, leading to a finesse of 20. An FWHM of 0.2 nm and a finesse of 100 are obtained in the case of the 4 µm long straight sections. The racetrack shaped ring resonators are surrounded by etched trenches which are 2.5 µm deep and 1 µm wide. The waveguide width is 0.4 µm and is tapered to 2 µm at the facets for easier fiber chip coupling.

Disk resonators with diameters of 5 and 10 µm in the material system GaInAsP are presented in Ma et al. 2000a. The disk resonators are vertically coupled using polymer (BCB) wafer bonding. The measured FSR of the disk resonators is nearly the same as for the devices described in this chapter, namely 38 nm for the disk with a diameter of 5 µm and 21 nm/20 nm for the disk with a diameter of 10 µm. The two values for the FSR for the 10 µm disk are due to the polarization dependence in this disk which is also visible in the transmission spectrum having two sets of resonance peaks. The FWHM is,

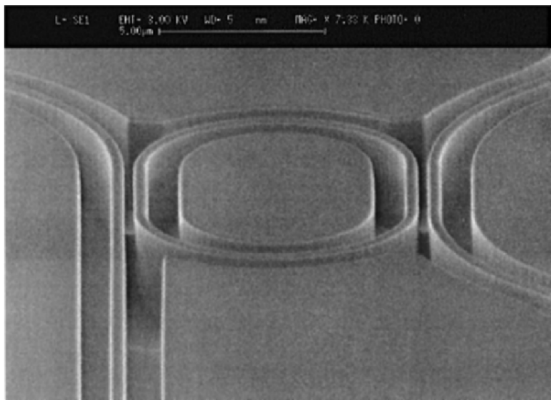

Fig. 5.7. Racetrack shaped ring resonator.

Reprinted with permission from IEEE Photonics Technology Letters, vol. 11, pp. 1620–1622 ©1999 IEEE

as expected, therefore also polarization dependent which leads to values of 0.25 and 0.22 nm. In the case of the 5 µm disk, the FWHM is measured to be 0.6 nm.

Vertically coupled disk resonators also in the material system GaInAsP fabricated by wafer bonding with radii ranging from 4 to 12 µm are presented in Dapkus et al. (2001) and Djordjev (2002). The parameters for a disk with radius of 12 µm are: an FSR of 10 nm, an FWHM of 0.22 nm leading to a Q factor of more than 7,000. The details of the fabrication method have been described in Chap. 3. Photographs of bus waveguides and a disk resonator are shown in Figs. 5.8 and 5.9.

One of the smallest racetrack shaped ring resonator notch filters in InP is demonstrated in Grover et al. (2003). A radius of 2.25 µm is realized. The

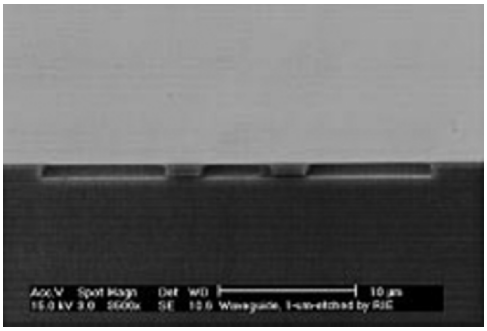

Fig. 5.8. Bus waveguides at the bonded interface and the remaining transparent InP layer after the etch of the microdisk mesa.

Reprinted with permission from IEEE Photonics Technology Letters, vol. 14, pp. 331–333 ©2002 IEEE

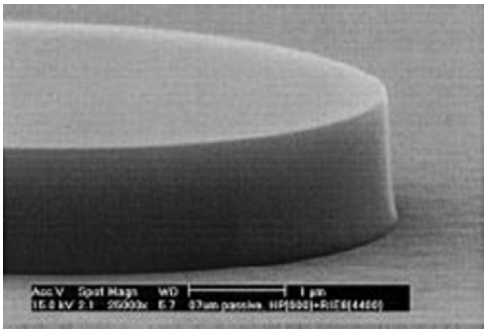

Fig. 5.9. A smooth 2.3 µm deep microdisk mesa formed by CH_4 based RIE etch. The bus waveguides are below the remaining thin membrane of InP.

Reprinted with permission from IEEE Photonics Technology Letters, vol. 14, pp. 331–333 ©2002 IEEE

straight waveguides have a length of 10 µm. An FSR of 19 nm at a wavelength of 1,550 nm is measured. A photograph of a ring resonator notch filter is shown in Fig. 5.10. The values for the finesse and the Q factor are 6 and 500. A transmission spectrum of a notch filter is shown in Fig. 5.11.

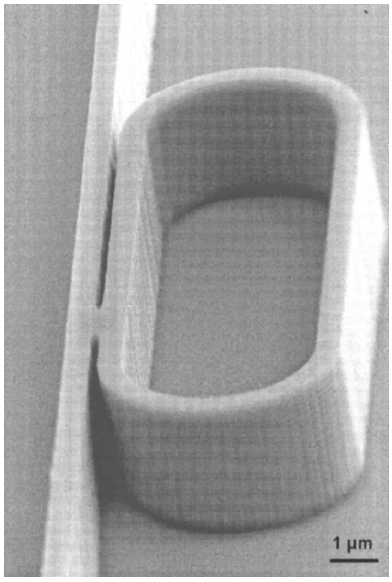

Fig. 5.10. One of the smallest ring resonator notch filters in InP.

Reprinted with permission from IEEE Photonics Technology Letters, vol. 15, pp. 1082–1084 ©2003 IEEE

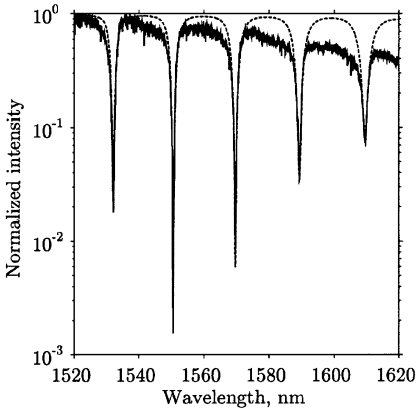

Fig. 5.11. Spectral behavior of InP racetrack shaped ring resonator notch filter. The *solid line* is experimental data, and the *dashed line* is a curve-fit.

Reprinted with permission from IEEE Photonics Technology Letters, vol. 15, pp. 1082–1084 ©2003 IEEE

A racetrack shaped ring resonator notch filter employing multimode interference couplers is presented in Rabus and Hamacher (2001). The curved sections have a rather large radius of 100 µm when compared to the previous examples. The length of the used MMI coupler is 150 µm. A photograph of a ring resonator and the transmission spectrum are shown in Figs. 5.12 and 5.13. An FSR of 0.8 nm (corresponding to 100 GHz in the frequency domain at a wavelength of 1.55 µm) and a finesse of 6 are measured.

Single ring resonator notch or add–drop filters have been studied extensively in the past and have been realized in major material systems as was demonstrated in this section. The use of single ring resonator devices as filters in optical networks is limited by the Lorentzian like function of the transfer function. Filters employed in optical networks require a rectangular, box-like passband shape. Multiple coupled ring resonator devices fulfill this request and have been fabricated in several material systems.

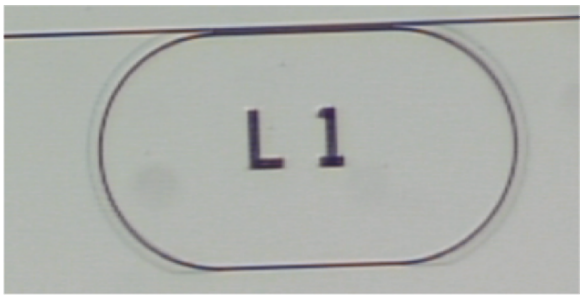

Fig. 5.12. MMI coupled racetrack shaped ring resonators

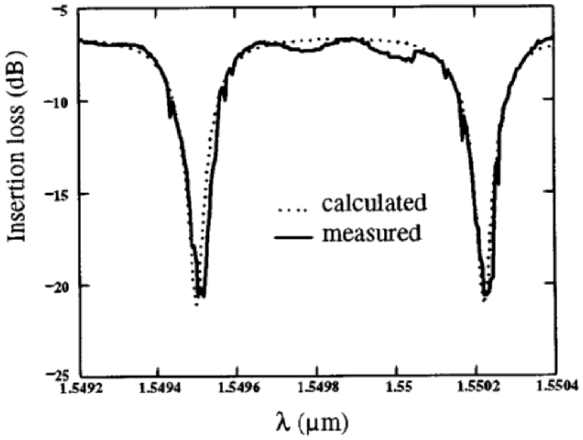

Fig. 5.13. Transmission spectrum of an MMI coupled racetrack shaped ring resonator with a radius of 100 µm

Double Ring Filters

One of the first integrated double ring resonator filters in silicon which is also used in a frequency-shift keying (FSK) optical transmission experiment is presented in Oda et al. (1994). The group had previously demonstrated a double ring resonator with an overall FSR of 40 GHz in Oda et al. (1991). In Oda et al. (1994) a double ring resonator consisting of ring resonators with different radii is used. The use of two ring resonators with different radius (3.33 and 3.82 mm in this case) opens up the possibility to increase the FSR (see (2.77)). The FSRs of the ring resonators are 14.29 and 12.50 GHz at a wavelength of 1,550 nm, leading to an overall FSR of 100 GHz or 0.8 nm. The finesse achieved is 200 for this configuration. A 10 GHz spaced, 8-channel, 622 MB s^{-1} FSK direct detection distribution experiment over 40 km is demonstrated using this double ring resonator configuration. A similar double ring resonator consisting again of two ring resonators with different radius is presented by the same group in Suzuki et al. (1995). The double ring resonators consist of two ring resonators with FSR's of 12.5 and 14.29 GHz, whose ring radii are 1.75 and 2.0 mm, respectively. The designed overall achieved FSR is again 100 GHz (98 GHz measured). The finesse is 138. In these two ring resonator experiments thin film heaters are integrated to be able to match the resonances of the two rings. Matching of the resonances in multiple coupled ring resonators is of utmost importance to achieve an optimum device performance and to realize the designed filter response. The tuning of the resonances and the center wavelength of ring resonator devices will be addressed in Sect. 5.2.

A double ring resonator where the ring resonators and the bus waveguides are coupled to one another by multimode interference couplers is presented in Rabus and Hamacher (2001). The radius of the curved sections is 100 µm. The length pf the MMI coupler is 150 µm, leading to an FSR of 0.8 nm at a wavelength of 1,550 nm. A photograph of an MMI coupled double ring resonator is shown in Fig. 5.14.

Vertically coupled double ring resonators in the material system Ta_2O_5–SiO_2 are presented in Kokubun et al. (2002). Double ring resonators with a finesse of 39.8, an FSR of 16.7 nm and an FWHM of 0.42 nm have been designed, fabricated and characterized. Due to the double ring resonator structure, a box-like filter response is obtained.

The design and characterization of a polarization independent double ring resonator filter with a designed FSR of 50 GHz (47.6 GHz measured) at a wavelength of 1,550 nm by use of SiO_xN_y technology is presented in Melloni et al. (2003a). The photograph of a double ring resonator is shown in Fig. 5.15.

The coupling between the ring resonators is realized by directional couplers with coupling coefficients of 0.4, 0.28, and 0.4 for realizing a Butterworth type filter response. A 15 dB extinction ratio and a bandwidth at −1 dB of 7.4 GHz are measured. The transmission spectrum of a double ring resonator filter is shown in Fig. 5.16.

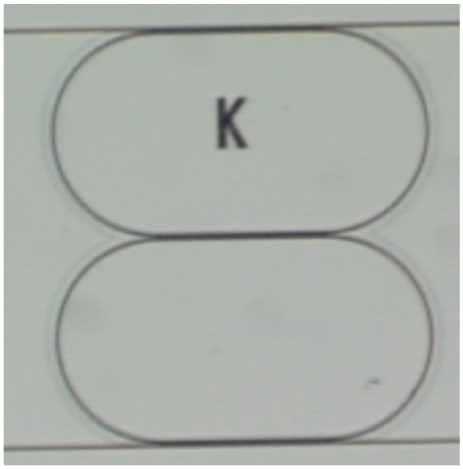

Fig. 5.14. MMI coupled double ring resonator

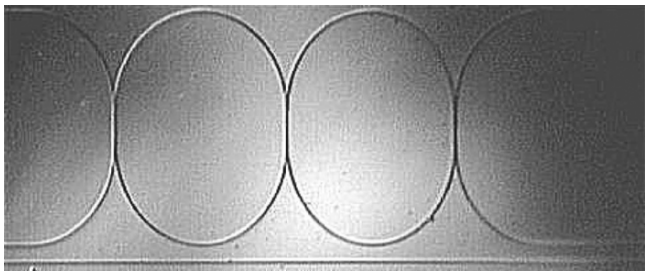

Fig. 5.15. Photograph of a double ring resonator filter.

Reprinted with permission from A. Melloni, Optics Letters, vol. 28, no. 17, pp. 1567–1569 ©2003 Optical Society of America

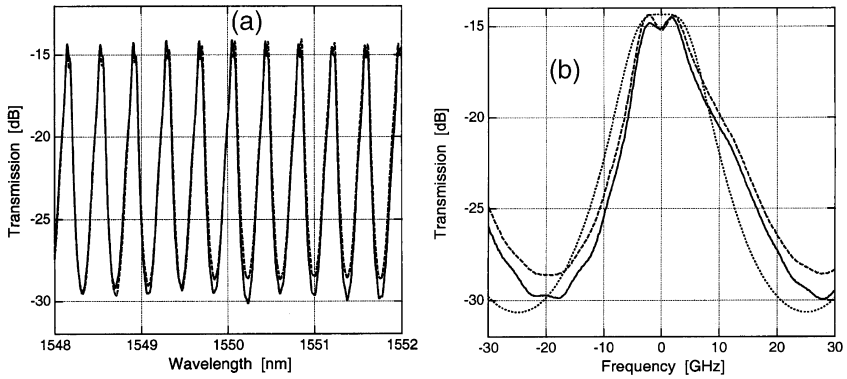

Fig. 5.16. Drop–port TE (*solid curves*) and TM (*dashed curves*) measured spectral responses of the double-ring filter. (**a**) Response over a 4-nm span and (**b**) detail of the response centered at 1551.2 nm. The *dotted curve* in (b) is the theoretical response.

Reprinted with permission from A. Melloni, Optics Letters, vol. 28, no. 17, pp. 1567–1569 ©2003 Optical Society of America

Double ring resonator filters are a first step to enable the realization of box-like filter functions. Using double ring resonators as was demonstrated by the examples in this chapter also makes enlargement of the FSR possible. In order to improve the roll-off and out-of-band rejection, multiple coupled ring resonator filters are required.

Multiple Coupled Ring Filters

Serially coupled, racetrack shaped, AlGaAs–GaAs triple ring resonators with radii of 4.5 µm and straight sections with lengths between 0 and 10 µm are demonstrated in Hryniewicz et al. (2000). A photograph of a triple ring resonator is shown in Fig. 5.17.

The waveguide width, bus waveguide – ring resonator gap and inter ring resonator coupling gap is between 0.18 and 0.32 µm. The box-like filter response of a triple ring resonator is shown in Fig. 5.18.

Parallel cascaded third- and fifth-order disk resonators in the material system GaInAsP/InP are presented in Ma et al. (2001). Photographs of the realized devices are shown in Fig. 5.19.

The disks have diameters of 10 µm and are only coupled to the bus waveguides and not to each other. The coupling gap between the bus waveguide and the disk resonator is about 0.15 µm. The distance between two adjacent resonators is 23.85 µm, leading to a $\pi/2$ phase shift. The chosen distance between the resonators introduces in-phase responses among the parallel cascaded disk resonators. A box like filter response is obtained due to the constructive interference formed at the drop–port which can be seen in the spectral response of a fifth-order disk filter in the measurement of the drop–port in Fig. 5.20. The FSR of the fifth-order filter is about 20 nm and the FWHM is approximately 3.5 nm.

Parallel, vertically coupled triple ring resonators in the material systems GaAs–AlGaAs and GaInAsP–InP are demonstrated in Grover et al. (2002). A photograph of a triple ring resonator is shown in Fig. 5.21.

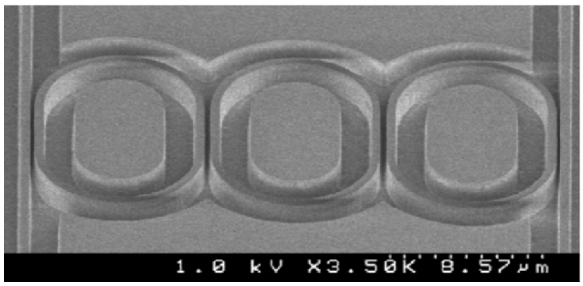

Fig. 5.17. Serially coupled triple ring resonator.

Reprinted with permission from IEEE Photonics Technology Letters, vol. 12, pp. 320–322 ©2000 IEEE

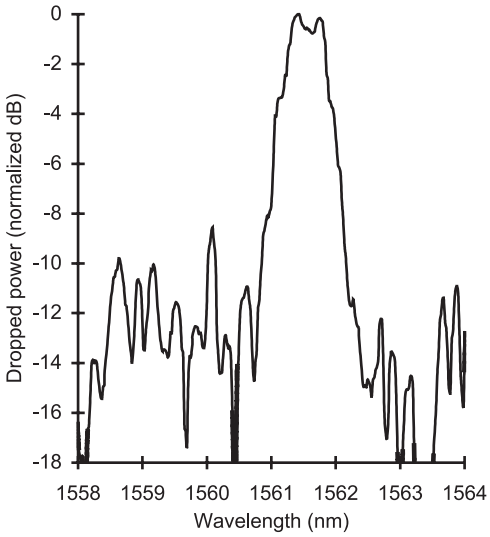

Fig. 5.18. Transmission spectrum at drop–port of triple resonator filter.

Reprinted with permission from IEEE Photonics Technology Letters, vol. 12, pp. 320–322 ©2000 IEEE

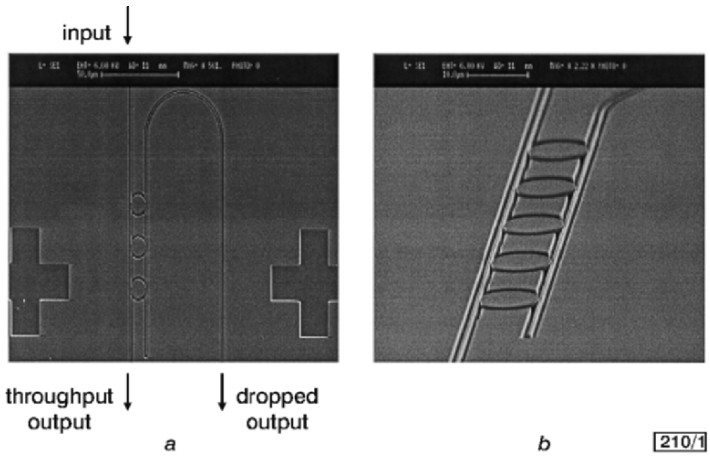

Fig. 5.19. Photograph of third- and fifth-order disk resonators.

Reprinted with permission from Y. Ma, Electronics Letters, vol. 37, no. 9, pp. 564–565 ©2001 IEEE

The width of the single mode waveguides is 0.8 µm. The waveguides are tapered to a width of 2 µm at the facets to improve fiber chip coupling. The radius of the rings is 9.55 µm. The distance between the rings is chosen to be 20 µm (center-to-center). The achieved overall FSR of the triple ring

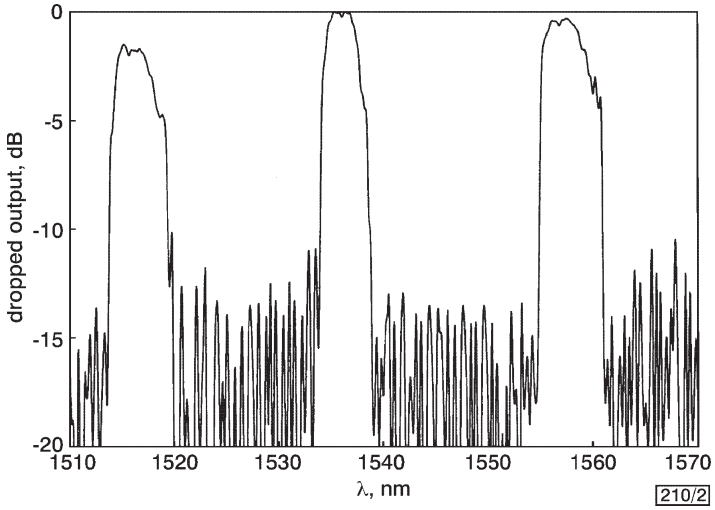

Fig. 5.20. Measured filter responses of fifth-order cascaded microdisk resonator filter for TM polarization.

Reprinted with permission from Y. Ma, Electronics Letters, vol. 37, no. 9, pp. 564–565 ©2001 IEEE

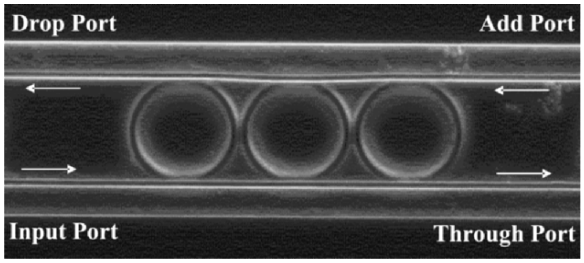

Fig. 5.21. Photograph of a vertically coupled triple ring resonator filter. The ring resonators are on the lower level.

Reprinted with permission from IEEE Journal of Lightwave Technology, vol. 20, pp. 900–905 ©2004 IEEE

resonator is 34 nm. The transmission spectrum of the GaAs–AlGaAs ring resonator is shown in Fig. 5.22.

The increase in the FSR in the case of the third-order ring resonator filter compared to a single ring resonator device is due to the Vernier effect (see Sect. 2.2.2). The cavities which interfere with one another are each of the ring resonators and part of the ring resonators with the bus waveguides. Fabrication tolerances can introduce an unwanted Vernier effect also and have an influence on the device performance. A difference in the radius of the rings of 0.04% is reported for this device.

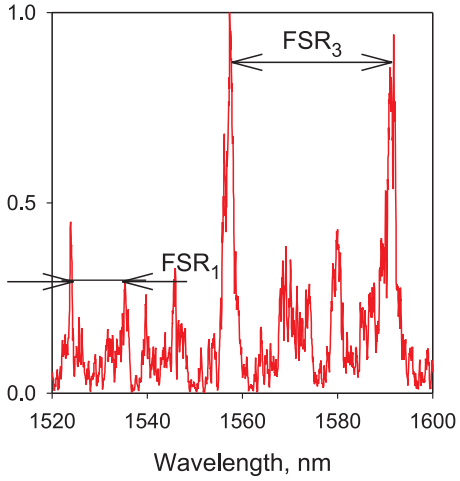

Fig. 5.22. Response of the drop–port of a parallel, vertically coupled triple ring resonator.

Reprinted with permission from IEEE Journal of Lightwave Technology, vol. 20, pp. 900–905 ©2004 IEEE

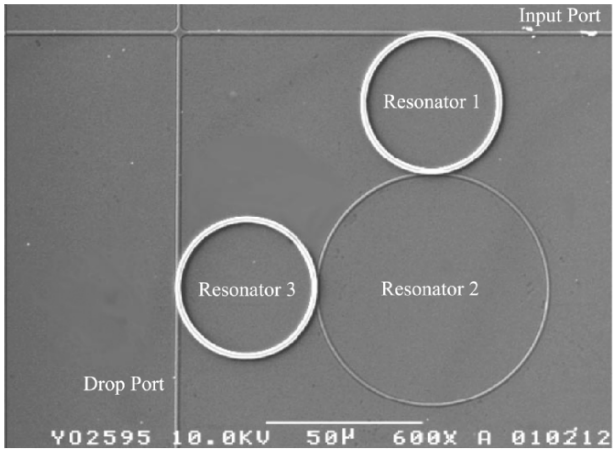

Fig. 5.23. Vertically coupled triple ring resonator.

Reprinted with permission from IEEE Journal of Lightwave Technology, vol. 20, pp. 1525–1529 ©2002 IEEE

Vertically, serially coupled triple ring resonators are presented in Yanagase et al. (2002a). The ring resonators are fabricated in the material system Ta_2O_5–SiO_2. A photograph of a triple ring resonator is shown in Fig. 5.23.

The bus waveguides and ring resonator 2 are in the lower layer and ring resonators 1 and 3 are located in the upper layer. The coupling strength between

the resonators and the resonators with the bus waveguides is controlled by the thickness of the buffer layer. This is one of the advantages of using a vertically coupled ring resonator configuration. One triple ring resonator configuration presented by the authors has the following parameters: the radius of ring resonator 1 and 3 is 22.78 µm resulting in an FSR of 10 nm, the radius of ring resonator 2 is 39.32 µm leading to an FSR of 6 nm. The measured overall FSR expanded to 25.8 nm (theoretical value: 30 nm), which is larger than the FSR of each of the ring resonators. In determining the value for the overall FSR, one has to take into account different values for the propagation constant in the buried ring resonator and the ring resonators on top. A transmission spectrum of the response of the drop–port of a single resonance is shown in Fig. 5.24. The mentioned shape factor is defined here as the width of the bandwidth at −1 dB divided by the width of the bandwidth at −10 dB.

One of the first and so far only demonstration of 6 and 11 serially coupled ring resonator filters using the material Hydex^{TM1} which is a glass based material, is presented in Little et al. (2004). The ring resonators are laterally coupled to each other. The outer rings are vertically coupled to the bus waveguides. A photograph of a serially coupled sixth-order ring resonator is shown in Fig. 5.25. The width and thickness of the cores of the waveguides are approximately 1.5 µm. The vertical gap between the bus waveguides and the outer ring resonators varies from 200 to over 1,000 nm depending on the desired filter linewidth. The gaps between the laterally coupled ring resonators vary from 500 to 1,400 nm depending again on the application. The drop–port

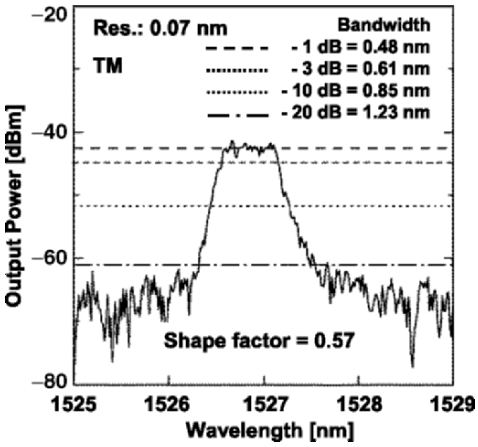

Fig. 5.24. Measured filter response of a triple ring resonator with radii of 28.52 µm for resonators 1 and 3 and 39.32 µm for resonator 2.

Reprinted with permission from IEEE Journal of Lightwave Technology, vol. 20, pp. 1525–1529 ©2002 IEEE

[1] See www.nomadics.com for more information.

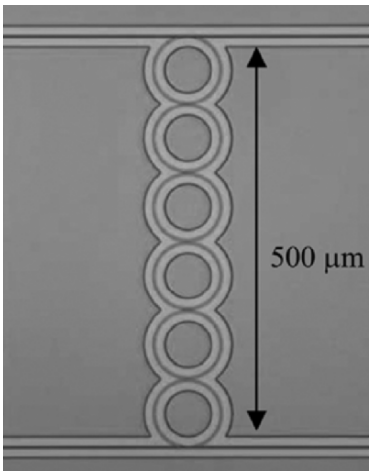

Fig. 5.25. Example of a sixth-order ring resonator filter fabricated with 17% index contrast Hydex.

Reprinted with permission from IEEE Photonics Technology Letters, vol. 16, pp. 2263–2265 ©2004 IEEE

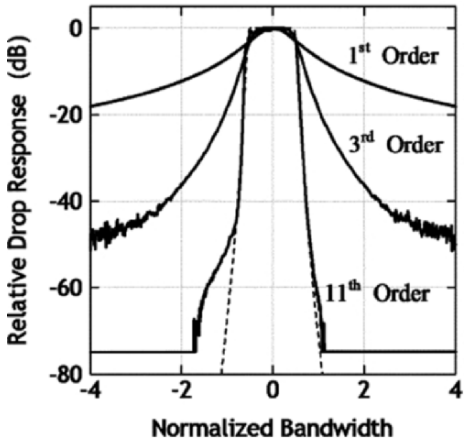

Fig. 5.26. Measured response for first-, third-, and 11th-order ring resonator filters similar in fabrication to the device shown in Fig. 5.25. The responses have been normalized to their 3-dB bandwidths. The *dashed curve* is the theoretical fit to the 11th-order filter.

Reprinted with permission from IEEE Photonics Technology Letters, vol. 16, pp. 2263–2265 ©2004 IEEE

response of first-, third-, and 11th-order ring resonator filters is shown in Fig. 5.26. Filters with high quality factor and large out of band rejection have been realized. As can be seen, maximal flatness of the filters response is obtained by increasing the number of coupled ring resonators. Polarization

independent resonances can be achieved by this technology by choosing the correct aspect ratio for the waveguides.

The examples in this section have demonstrated that fabrication methods of ring resonator filters in several material systems are available for realizing devices with adjustable performance parameters suitable for implementation in future all-optical networks. In order to increase the device functionality of ring resonator filters, gain can be introduced into the cavity. Examples of devices with gain inside the ring resonator are presented in the following section.

5.1.2 Devices with Gain Section

Ring resonator lasers have of course been around quite some time and examples will be presented in Sect. 5.6. This chapter focuses on ring resonator filters with integrated gain sections for realizing improved and loss reduced filter functions.

One of the first devices with gain inside the resonator is presented in Djordjev et al. (2002b). Disk resonators with gain region, vertically coupled to the bus waveguides are used to demonstrate gain trimming of the resonant response. The fabrication of the devices has been described in Sect. 3.4.7. The response from the throughput port of a disk with a radius of 10 µm is shown in Fig. 5.27.

The device has an FSR of 10 nm. A quality factor of 5,700 and a finesse of 40 are measured. The coupling coefficient is estimated to be 3.6%. As can be seen in Fig. 5.27 it is possible with active devices to adjust the response of the disk resonator. When the applied current supplies enough gain inside the

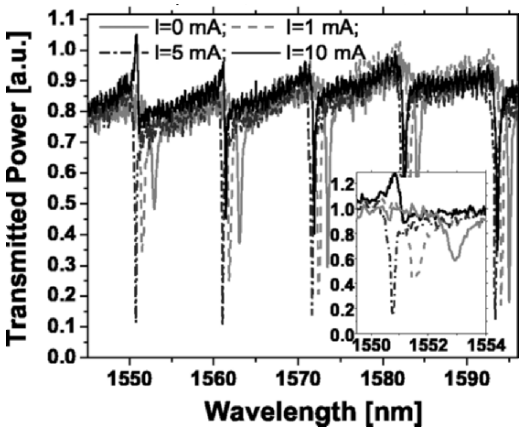

Fig. 5.27. Gain trimming of the transmission response of a disk with radius 10 µm. Reused with permission from K. Djordjev, Applied Physics Letters, 80, 3467 (2002) ©2002 American Institute of Physics

resonator to equal the internal losses, the resonator becomes lossless and the obtained filter spectrum is ideal.

Racetrack shaped ring resonators with integrated SOAs are presented in Rabus et al. (2002c). A minimum radius of 100 µm which is one magnitude larger than the ones presented in the previous paragraph is used. Single, double and triple serially coupled ring resonator add–drop filters with integrated SOAs are demonstrated. The fabrication details and the layer sequence of the devices have been described in Sect. 3.4.7. A photograph of a serially coupled triple ring resonator with SOAs is shown in Fig. 5.28. The output port is transferred to the right side of the chip via another half circle for a better accessibility when measuring the transfer response. The devices realized have FSRs of 12.5, 25, and 50 GHz at a wavelength of 1,550 nm.

The lossless filter response of a single ring resonator with an FSR of 25 GHz is shown in Fig. 5.29.

The radius of the ring resonator is 363 µm and the length of the SOA is 400 µm. The length of the couplers is 200 µm (gap = 0.9 µm), which results in power coupling factors of 0.17. The y-axis has been normalized to the fiber–chip coupling loss. The on–off ratio is measured to be more than 22 dB. The FWHM is determined to be 0.012 nm. The finesse of the ring resonator is $F = 17$, leading to a Q factor of more than 130,000. The filter response is measured by sweeping the external cavity laser (ECL) signal with a resolution of 4 pm. The SOA is operated at a current of 90 mA which provides lossless operation of the ring resonator as is seen in the transmission spectrum. The response from the drop–port on resonance is as high as the response from the throughput port off-resonance.

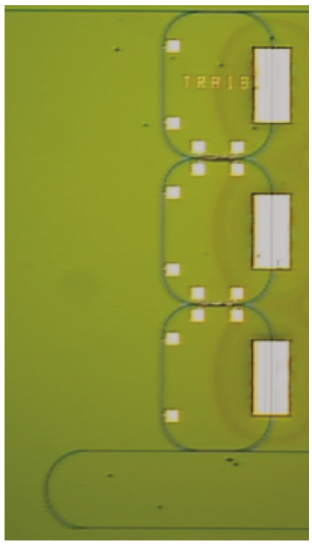

Fig. 5.28. Serially coupled triple ring resonator with integrated SOAs

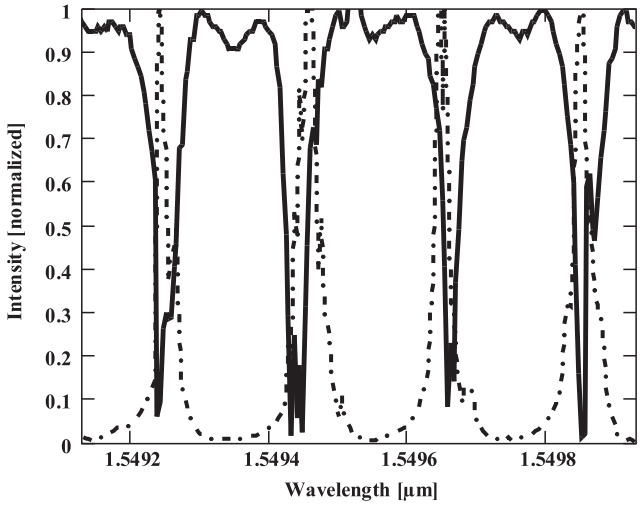

Fig. 5.29. Single ring resonator with two straight input/output waveguides and directional couplers (length = 200 μm, gap = 0.9 μm), r = 363 μm, gain length = 400 μm, FSR = 25 GHz

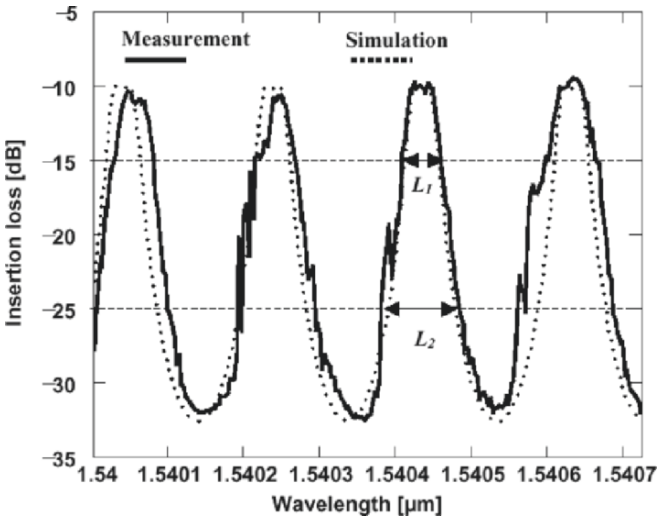

Fig. 5.30. Drop–port response from a double ring resonator with two straight input/output waveguides, two MMI couplers and a directional coupler (length = 150 μm, gap = 1 μm), r = 347 μm, SOA length = 500 μm, FSR = 25 GHz

The response from the drop–port of a double ring resonator with integrated SOAs is shown in Fig. 5.30. The double ring resonator is made up of two straight input/output waveguides, two 3 dB MMI couplers for the outer couplers (length = 150 μm, width = 6 μm) and a directional coupler in the

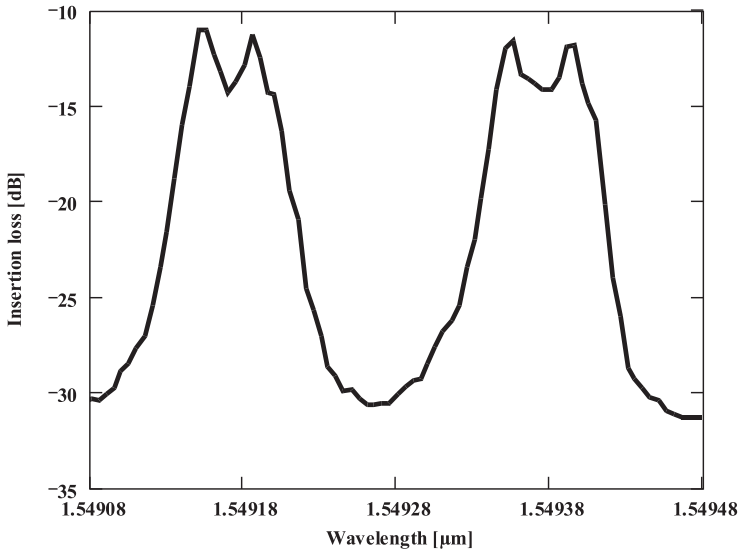

Fig. 5.31. Filter response of the drop–port of a triple ring resonator with $r = 323\,\mu\text{m}$, length of the couplers $= 325\,\mu\text{m}$, gain length $= 400\,\mu\text{m}$, FSR $= 25\,\text{GHz}$

center (length $= 150\,\mu\text{m}$, gap $= 1\,\mu\text{m}$), $r = 347\,\mu\text{m}$, SOA length $= 500\,\mu\text{m}$ which results in an FSR of 25 GHz.

The driving current for each SOA is 50 mA. The shape factor which is defined in this case as L_1 divided by L_2, achieved for this configuration is 0.5. The FWHM is measured to be 0.04 nm, leading to a finesse of 5.

The drop–port response of a triple serially coupled ring resonator is shown in Fig. 5.31.

The measured triple ring resonator has a radius of $323\,\mu\text{m}$. The length of an SOA is $400\,\mu\text{m}$. The length of the couplers is $325\,\mu\text{m}$ with a gap of $0.8\,\mu\text{m}$ for the outer couplers and $1\,\mu\text{m}$ for the couplers in the center. The achieved FSR is 25 GHz. The driving current for each of the three SOAs is 50 mA. The steep roll-off can be seen from the measurement. The two ripples result from a slight resonance mismatch between the three ring resonators. The on–off ratio for the fabricated triple ring resonator is more than 18 dB including the ripples.

Ring resonators integrated with SOAs have not only been fabricated in the serially coupled configuration, but have also been demonstrated in the parallel architecture. The photograph of a parallel coupled triple ring resonator is shown in Fig. 5.32.

The ring resonators have a radius of $117\,\mu\text{m}$, a coupler length of $200\,\mu\text{m}$ (gap $= 0.9\,\mu\text{m}$) and a gain length of $300\,\mu\text{m}$. An FSR of 50 GHz is realized. The driving current for each SOA is 50 mA. The distance between the resonators was chosen to be equal to half of the circumference of a single ring resonator. The filter characteristic of the drop–port of the parallel, triple coupled ring resonator is shown in Fig. 5.33.

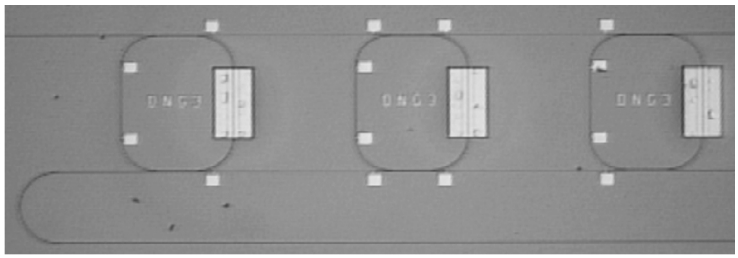

Fig. 5.32. Photograph of a fabricated triple coupled ring resonator in a parallel configuration

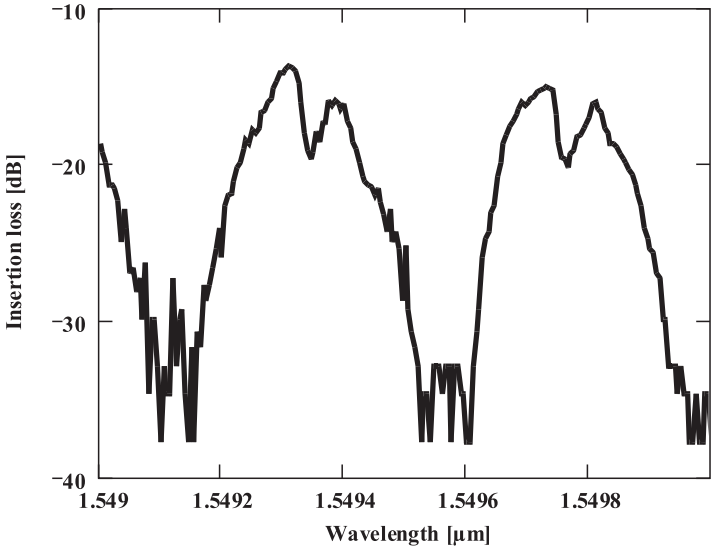

Fig. 5.33. Drop–port response of a parallel coupled triple ring resonator with integrated SOA, length of the couplers = 200 µm, r = 117 µm, gain length = 300 µm, FSR = 50 GHz

The ripples are due to a slight resonance mismatch due to fabrication tolerances. The resonances can be matched when integrated platinum resistors (see Sect. 5.2) in the ring resonators or adjusted SOA currents are used.

Another example of the integration of ring resonators with SOAs is presented in Menon et al. (2004). In this example, a vertically stacked asymmetric twin waveguide structure is used to integrate the SOA with the passive waveguides. The ring resonator is racetrack shaped and is designed as a notch filter with only one input/output bus waveguide. A photograph of the fabricated chip as well as a schematic of the design is shown in Fig. 5.34. In addition to the SOA in the resonator, another SOA has been integrated on the side of the input port. Details on the fabrication have been described in Sect. 3.4.7.

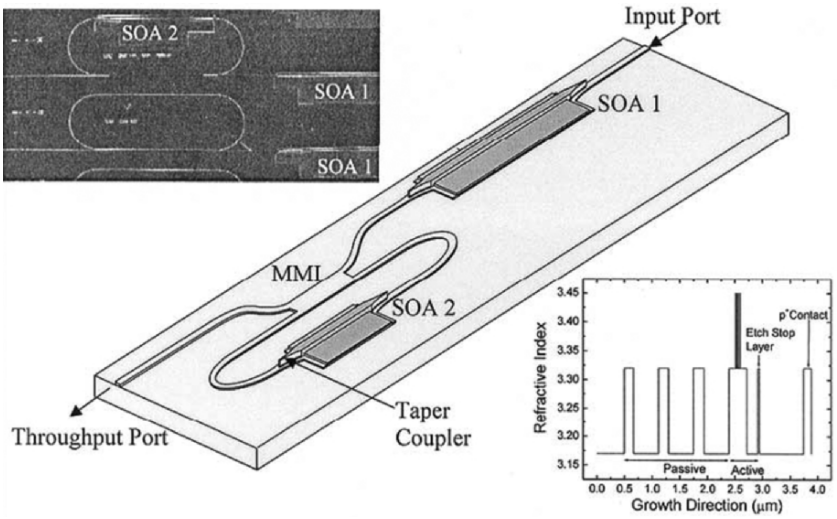

Fig. 5.34. Schematic of the microring resonator with integrated SOAs at the input and in the ring. *Upper left inset*: Scanning electron microscope image of the fabricated devices with and without an SOA in the ring. *Lower right inset*: Refractive index profile and layer structure of the ring resonator with integrated SOA.

Reprinted with permission from IEEE Photonics Technology Letters, vol. 16, pp. 1343–1345 ©2004 IEEE

The racetrack shaped ring resonator has an FSR of 0.25 nm. A multimode interference coupler is used as in the previous example to couple into and from the ring. The length of the MMI is 685 µm and the width is 12 µm. The length of SOA 1 is 1,000 µm and the length of SOA 2 is 500 µm. The overall length of the resonator is 3,020 µm. The availability of an SOA inside a ring cavity enables the tuning of parameters of the resonator like the FWHM, the extinction ratio and thus also the Q factor and the finesse. The tuning of these parameters is shown in Fig. 5.35.

A fabricated ring resonator employing an SOA, an MMI and total internal reflection (TIR) mirrors is demonstrated in Kim et al. (2005b). Details on the layout and a photograph of a TIR based ring resonator are shown in Fig. 5.36.

An FSR of 2 nm at a wavelength of 1,568 nm is obtained. The on–off ratio achieved is 14 dB, an FWHM of 0.3 nm is measured leading to a finesse of more than 6, and a Q factor of more than 4,900. The length achieved for the MMI coupler is one of the shortest reported. The SOA current dependable tunability of the resonance characteristic of the device is shown in Fig. 5.37.

All integration schemes have in common that they require temperature stabilization. Another effect which takes place is the resonance shift due to increase in SOA current. This is due to the current dependency of the refractive

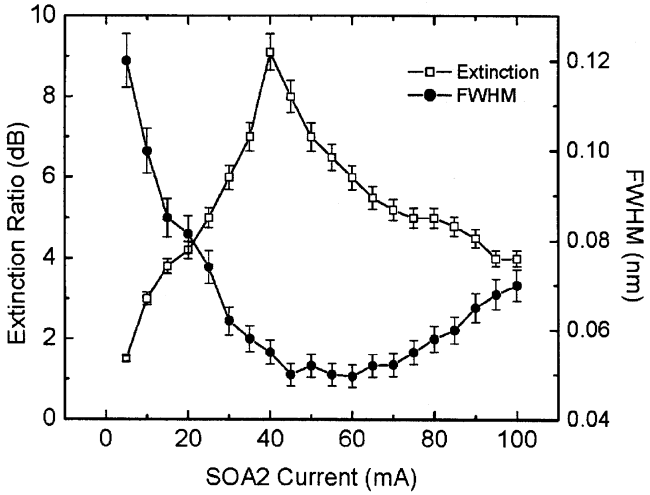

Fig. 5.35. Measured extinction ratio and FWHM as a function of the ring SOA 2 current.

Reprinted with permission from IEEE Photonics Technology Letters, vol. 16, pp. 1343–1345 ©2004 IEEE

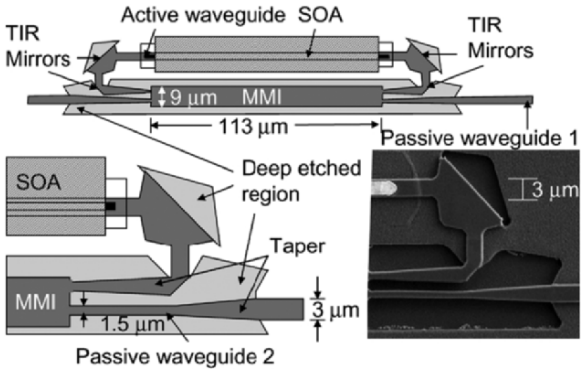

Fig. 5.36. Total internal reflection mirror-based GaInAsP ring resonators integrated with optical amplifiers.

Reprinted with permission from IEEE Photonics Technology Letters, vol. 17, pp. 1899–1901 ©2005 IEEE

index of the SOA. Despite these unwanted effects, SOAs inside ring resonators offer tunability of essential parameters and enable lossless switching devices, which can also be used for lasers, wavelength converters and nonlinear operation. Examples will be given later on in this chapter.

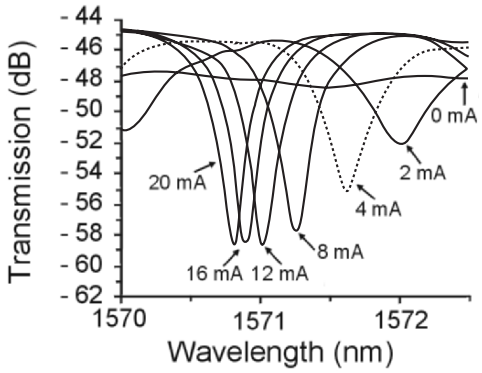

Fig. 5.37. Tuning of the resonator extinction ratio via the SOA current.

Reprinted with permission from IEEE Photonics Technology Letters, vol. 17, pp. 1899–1901 ©2005 IEEE

5.2 Tunability Methods

Tunability is essential for the system application of optical filters. In the case of periodic filters, like ring resonators, it is important to fit the transmission curve to the defined channel spacing (e.g., ITU-Grid). Several tunability methods exist either for trimming the center wavelength of the filter after processing or for tuning the resonance wavelength when the ring resonator add–drop filter is in operation. These methods including examples are briefly explained in the following chapters. The physical mechanisms behind these methods are:

Thermo-optic tuning. Thermo-optic tuning is realized by heating the component for example by fabricating a metal heater on top of the waveguide in the ring resonator. The refractive index of the material is changed through the heat which in turn shifts the resonances. The heating process is fairly slow but can be used to trim resonances in for example a double ring resonator because it is very difficult to fabricate ring resonator devices with exactly the same resonant wavelength. By adding heating elements and using the same, negligible additional loss is obtained. On the other hand, using heaters, limits the density of devices to maintain thermal isolation, and requires significant power consumption to maintain the tuned status.

Another used tuning mechanism is *electro-optic tuning*. Here an electric field is applied to change the properties of the material, which means either the refractive index or the absorption. Changes in the refractive index are realized by using a bandgap wavelength of the material which is far away from the signal wavelength so as not to interfere with it. This effect is quite small compared to the effect produced by the heating elements. The refractive index increase is maximized when ring resonators with narrow peaks and low losses are used. The change in the refractive index by using the electro-optic

effect is weak in III–V materials like InP, but has the advantage of being fast compared to the thermo-optic effect described before. One has to be careful when applying higher voltages which lead to significant losses. Changes in the absorption of the material are obtained, when the bandgap wavelength is closer to the signal wavelength. Only a small electric field is necessary to induce a large loss. This can be used advantageously in switching devices which shall be explained in the following chapter.

Carrier injection (or free carrier injection for example in InP) is another means of changing the refractive index, absorption or gain. Introducing gain in ring resonators is an advantage of using carrier injection. As is and will be demonstrated in the following chapters, gain can be used to change the response of ring resonators, the extinction ratio, the Q factor and the maximum transmission. Ring resonators can be switched between dropping and transmitting a signal by changing the loss/gain inside the cavity. When gain is introduced into the ring resonator, attention has to be paid to design and fabricate a heat sink which is necessary to suppress the unwanted thermo-optic effect.

5.2.1 Wavelength Tuning

Wavelength tuning is essential for realizing optical filters to be implemented in optical network. Tunability offers the network suppliers flexibility when designing and operating a network.

Thermo-Optic Tuning

A common and well-known method of tuning semiconductor and polymer based integrated optical devices is by using temperature. The simplest way is to heat the entire device and thus change the resonance spectrum in the case of ring resonators. This method is of course only useful for materials with a large temperature coefficient. A more effective way is to use local heating elements on top of the waveguides in the ring resonator for changing the refractive index and so for changing the resonance wavelength of the device. A detailed theoretical analysis with implementation on thermal tuning in ring resonators is described in Geuzebroek (2005).

One of the first papers dealing with the integration of such heating elements in ring resonators made in silicon is presented in Katila et al. (1996) and Heimala et al. (1996). The ring resonator is made out of silicon nitride (Si_3N_4) rib waveguides with a height of 40 nm. The silica undercladding layer and the silicon nitride layer thicknesses are 3 µm and 300 nm, respectively. The diameter of the ring is 2 mm. The resistors are made out of a phosphorous doped polysilicon layer. Aluminum with a thickness of 900 nm is used to create the bondbads. The layout and the layer sequence are shown in Fig. 5.38.

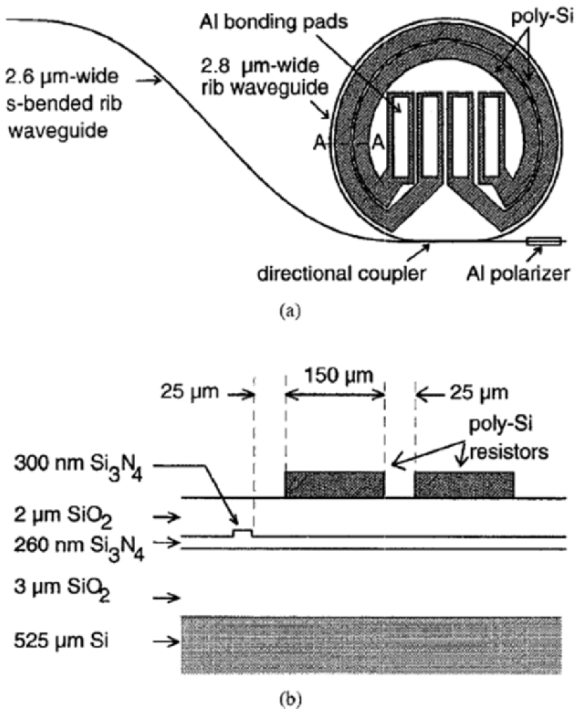

Fig. 5.38. (**a**) The schematic layout and (**b**) the cross-section (A–A) of the temperature-controlled ring resonator.

Reprinted with permission from IEEE Journal of Lightwave Technology, vol. 14, pp. 2260–2267 ©1996 IEEE

Temperature tuning of the entire chip is used in Rafizadeh et al. (1997a) to tune a disk resonator. A temperature tuning of 1.3 nm per 10°C is obtained. An overall tuning range of 6.3 nm over a temperature range of 50°C is demonstrated. The tunability is mainly due to physical thermal expansion of the cavity.

Triple ring resonators incorporating thermo-optic phase shifters for wavelength and passband shape tuning are demonstrated in Madsen and Zhao (1997) and Coppinger et al. (1999). In Madsen and Zhao (1997), double and triple serially coupled ring resonator filters in silicon with chromium heating elements inside the ring resonators are presented. A minimum bend radius of 4 mm is achieved leading to an FSR of 0.066 nm. The response of the filter is adjusted by the integrated heating elements and is analyzed by a developed algorithm. Triple serially coupled ring resonators integrated in a silica waveguide technology with diameters of 8.5 mm are presented in Coppinger et al. (1999). The FSR of the filter is 7.5 GHz and a bandwidth of 1.5 GHz is measured. The application of this rather large ring resonator filter is the

filtering of microwave signals to obtain a microwave transfer function. The integrated phase shifters (heating elements) cover part of the waveguide in the ring. As will be explained in the following paragraph in more detail using another ring resonator example, these heating elements are used to match the resonances of each ring to one another which leads to an improved passband of the filter. Once the desired passband characteristic is achieved, the power of the heating elements is increased by the same amount which enables wavelength tuning of the entire filter.

Another method applied successfully to achieve wavelength tuning is by using platinum as a heating element inside a GaInAsP/InP based ring resonator (Rabus et al. (2002b)). The platinum layer which enables the local heating of waveguide segments of the ring resonators via the thermo-optic effect is deposited directly on the waveguides. Before the platinum is deposited, the entire device is covered with a SiN_x layer. This layer assures that no metal will diffuse into the waveguide material and no waveguide mode couples to the metal and increases the propagation losses. A photograph of a part of a Pt-resistor in a ring resonator is shown in Fig. 5.39. The pads for contacting the Pt-resistor are composed of layers of titanium, platinum and gold. A triple ring resonator with integrated Pt-resistors is shown in Fig. 5.40.

The Pt-resistors have two functions. The first function is the tuning to specific wavelengths. The second function is the resonance matching of multiple coupled ring resonators to each other. A demonstration of resonance matching of a double ring resonator is shown in Rabus et al. (2002a).

The tunability of a single ring resonator notch filter is shown in Fig. 5.41. The Pt-resistors enable a finer tuning to a specific wavelength and so an improved on–off ratio is obtained.

The second feature of the Pt-resistors, the resonance matching, is demonstrated with a double ring resonator ($r = 200\,\mu m$, upper and lower coupling factors $\kappa_{0,2} = 0.5$, middle coupling factor $\kappa_1 = 0.055$, coupler lengths $= 150\,\mu m$). The unmatched transmission spectrum of the double ring resonator is shown in Fig. 5.42. The upper curve shows the response of the throughput port and the lower curve that of the drop–port. This device has not been antireflection coated, which leads to Fabry–Perot resonances in the straight

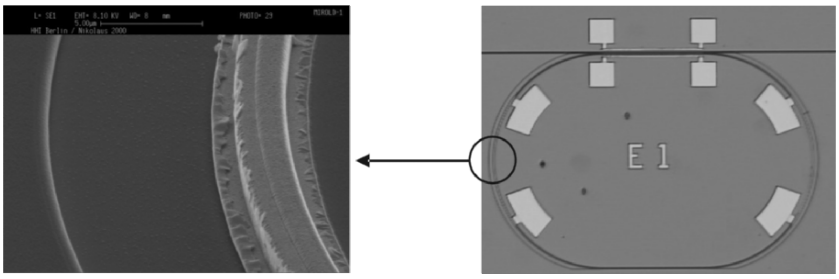

Fig. 5.39. SEM picture of waveguide with platinum layer

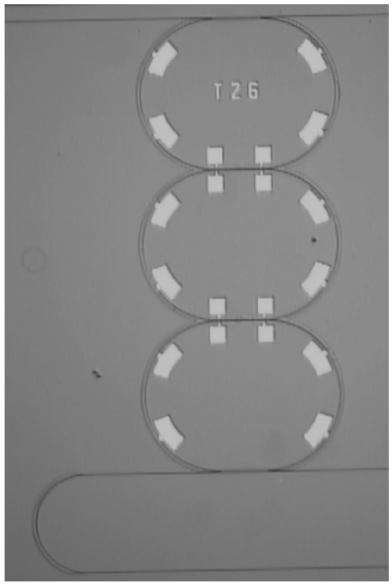

Fig. 5.40. Triple ring resonator with integrated platinum heaters on top of the waveguides in the curvatures and adjacent contact pads

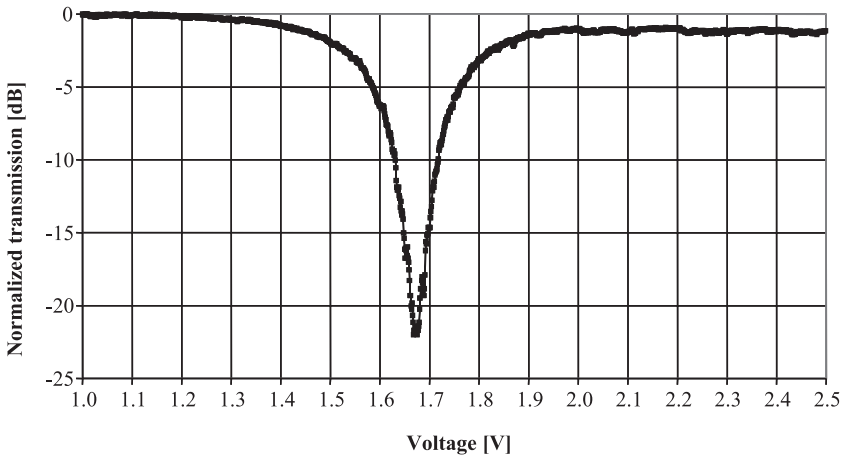

Fig. 5.41. Tunability of a single ring resonator notch filter with Pt resistors

waveguides. The resonances are visible in the transmission spectrum of the throughput port. The typical filter characteristic of the double ring resonator is not disturbed despite the Fabry–Perot resonances. It depends on the application, if antireflection coating is required. The contrast of the throughput port is 16 dB and that of the drop–port 13 dB. The simulated filter response reveals a difference of the effective refractive index of about 0.0003, which

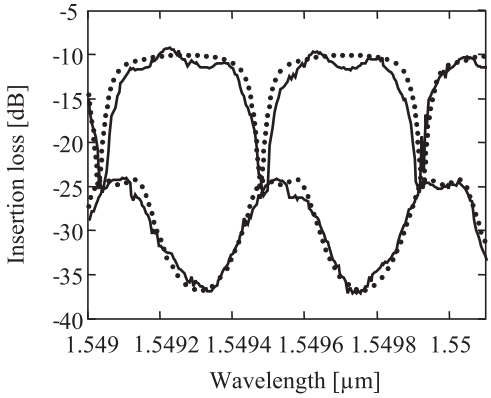

Fig. 5.42. Unmatched transmission spectrum of a double ring resonator. *Dotted line* – simulation, *solid line* – measurement

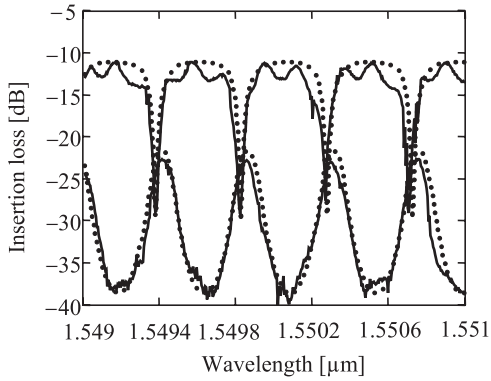

Fig. 5.43. Resonance matched double ring resonator. *Dotted line* – simulation, *solid line* – measurement

is also the origin of the different contrast values. According to the calculation, the refractive index is lower in the upper ring. This is mainly due to fabrication tolerances which occur during the deep etching on the outer side of the waveguide in the curvatures. The physical lengths of the resonators are the same. In order to match the resonance frequency in both ring resonators, the upper Pt-resistors are used. A voltage of 0.5 V is applied to match the resonance frequency. The temperature coefficient of InP can be approximated in this example to (see Sect. 3.4):

$$\frac{\mathrm{d}n}{\mathrm{d}T} \approx 0.0001\,\mathrm{K}^{-1} \tag{5.1}$$

The local temperature increase is therefore approximately 3 K. The result of the resonance matched double ring resonator is shown in Fig. 5.43.

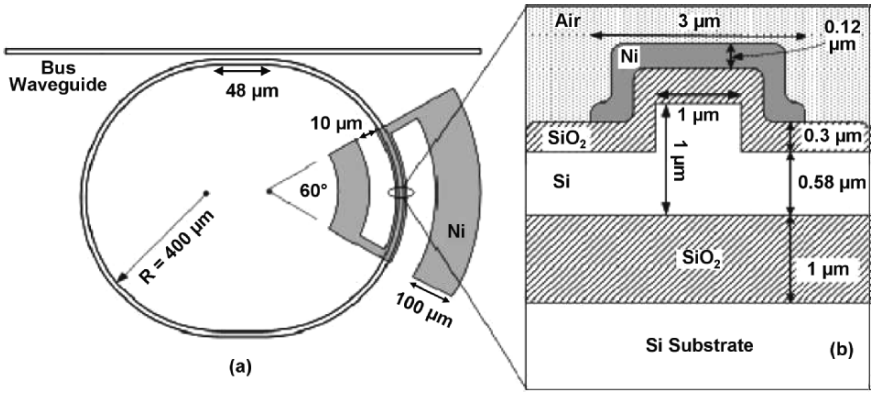

Fig. 5.44. Schematic views showing critical dimensions. (**a**) Top view of SOI resonator and (**b**) cross-sectional view of SOI rib waveguide.

Reprinted with permission from IEEE Photonics Technology Letters, vol. 18, pp. 364–366 ©2006 IEEE

The tuning to a specific wavelength can be performed after the frequency matching in such a way, that both of the Pt-resistors in the two rings are used. The driving voltage of the Pt-resistors is different in both ring resonators due to the previous frequency matching but has to be increased by the same amount in order to shift to a specific wavelength.

A tunable racetrack shaped ring resonator notch filter in SOI is demonstrated in Kiyat et al. (2006). Details of the ring resonator and the used waveguide are shown in Fig. 5.44. A directional coupler with a coupling gap of 0.8 µm and a length of 48 µm is used, which results in a coupling factor of 0.45. The FSR of the ring resonator is determined to be 248 pm. The FWHM is measured to be 40 pm leading to a Q-factor of 38,000 and a finesse of 6.2. A heater electrode made out of nickel is used for tuning the resonance wavelengths of the filter. The electrode covers part of the waveguide in the curvature as in the previous example where platinum is used as the electrode material. The resistance of the heating element including the bond pads is 170 Ω. The tuning of the resonance wavelength against power consumption is shown in Fig. 5.45.

Electro-Optic Tuning

One of the first electro-optic tunable, racetrack-shaped ring resonator notch filters in GaInAsP/InP is presented in Grover et al. (2004). The racetrack shaped ring resonator filter is also one of the smallest reported, with a radius of curvature of 2.25 µm and straight sections with a length of 1 µm leading to an FSR larger than 30 nm. The electrodes are made on top of a BCB layer which is used to planarize the device after the waveguides have been etched. The top

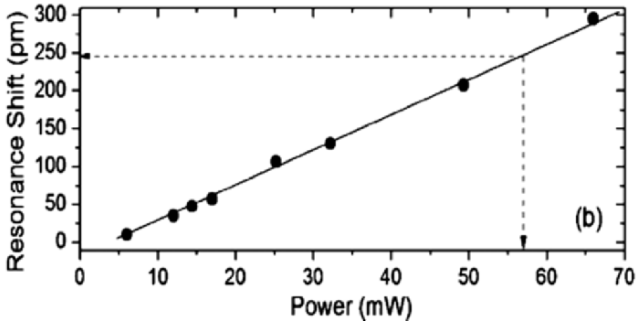

Fig. 5.45. Shift in resonance wavelength as function of applied power (*dotted line* with *arrows* indicate the tuning parameters for reaching the FSR).

Reprinted with permission from IEEE Photonics Technology Letters, vol. 18, pp. 364–366 ©2006 IEEE

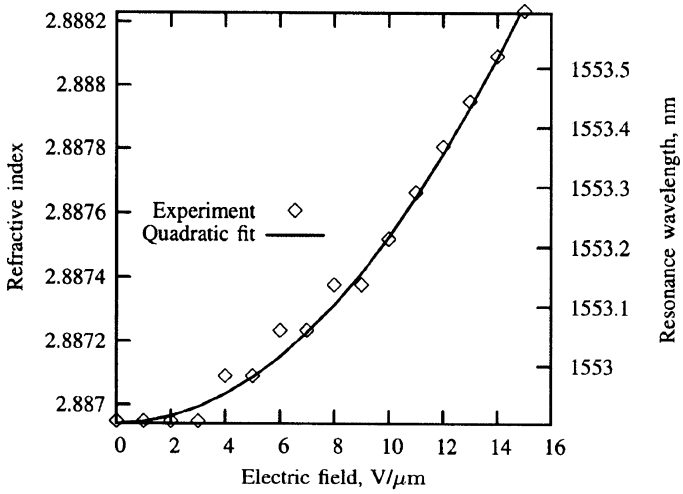

Fig. 5.46. Effective refractive index vs. electric field, assuming all the bias appears across the core. Corresponding value of the resonance wavelength is shown on the right side. Refractive index in the absence of electric field is obtained from simulations. Quadratic fit provides us the quadratic electro-optic coefficient for the waveguide. Value of the coefficient for the waveguide is a lower bound for the quadratic electro-optic coefficient of the core.

Reprinted with permission from IEEE Photonics Technology Letters, vol. 16, pp. 467–469 ©2004 IEEE

contact (p-side) is made out of deposited Ti–Pt–Au. The bottom contact is made out of deposited Pd–Sn–Au–Pd–Au after the chip has been thinned. The change of the refractive index and the tuning of the resonance wavelength of the ring resonator filter with applied electric field are shown in Fig. 5.46.

The quadratic electro-optic coefficient can be calculated from the measurement and is determined to be $-9.8 \times 10^{-15}\,\mathrm{cm^2\,V^{-2}}$. A tuning range of 0.8 nm which corresponds to 100 GHz at a wavelength of 1,550 nm is realized.

A narrowband, widely electro-optically tunable filter based on a whispering gallery mode cavity using $LiNbO_3$ is demonstrated in Savchenkov et al. (2003). The device has an FSR of 10 GHz and can be used in microwave photonics communication systems. The obtained tuning speed of the filter is approximately 10 ns. The actual spectrum shifting time is determined by the 30 MHz bandwidth of the filter and does not exceed 30 ms. A channel crosstalk suppression of −20 dB for a 50 MHz channel spacing is measured.

Carrier Injection Tuning

One of the first vertically coupled disk resonators with a radius of 10 µm using carrier injection for increasing the refractive index and tuning the resonance of the resonator is demonstrated in Djordjev et al. (2002d). The device has an FSR of 10 nm and a Q value of 5,500. The fabrication of the device has been explained in Sect. 3.4.7. The tunability of the device is $1.1\,\mathrm{nm\,(mA)^{-1}}$. The refractive index change is $\Delta n = -2.1 \times 10^{-3}$. The linewidth of the resonances is 0.28 nm. A transmission measurement of the tuning of the disk resonator is shown in Fig. 5.47.

The vertically coupled disk resonator can also be used as an on/off switch. A demonstration of the switching behavior is shown in Fig. 5.48. The switch

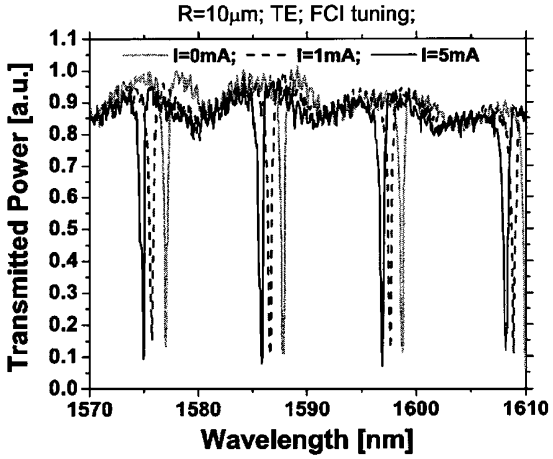

Fig. 5.47. The free carriers injected into the disk resonator change the modal refractive index, which blue-shifts the resonant wavelengths.

Reprinted with permission from IEEE Photonics Technology Letters, vol. 14, pp. 828–830 ©2002 IEEE

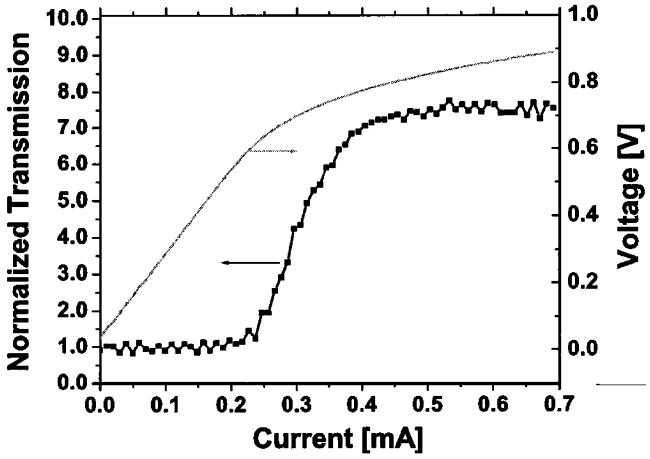

Fig. 5.48. Switching behavior of a disk at a wavelength of 1,598 nm. Change in the drive current by $\Delta I = 200\,\mu\text{A}$ is enough to toggle the switch from the off to the on state. The voltage change required for this transition is $\Delta V = 0:1\,\text{V}$.

Reprinted with permission from IEEE Photonics Technology Letters, vol. 14, pp. 828–830 ©2002 IEEE

is operated by changing the drive current from 200 µA to 400 µA requiring a voltage of only 0.1 V. A contrast between the on and off state of 10 dB is achieved.

Two different types of tunable disk resonators vertically coupled to bus waveguides are presented in Choi et al. (2004d): a disk resonator coupled to air-guided rib bus waveguides and another one fabricated on buried heterostructure bus waveguides. Diagrams and SEM photographs of both types of resonators are shown in Fig. 5.49. The disk resonators have a radius of 12 µm. The two types of disk resonators have Q values of 8,000 and 3,000, respectively. A tunability of 1.5 nm and 2.1 nm is demonstrated at a current of 3 mA due to free carrier injection.

5.2.2 Center Wavelength Trimming

In the previous chapter, examples of tuning mechanisms have been presented which enable the selection of resonance frequencies inside a ring resonator filter. Postfabrication methods which enable the permanent fitting of the entire resonance spectrum to a desired resonance frequency grid are explained in this chapter.

Ring resonators once fabricated offer practically no way to change the resonance spectrum besides heating the entire sample and thus changing the refractive index which in turn shifts the resonance spectrum. Therefore it is highly desirable to have methods which can be applied after the ring resonator filters have been fabricated to change the resonance spectrum. One way is to

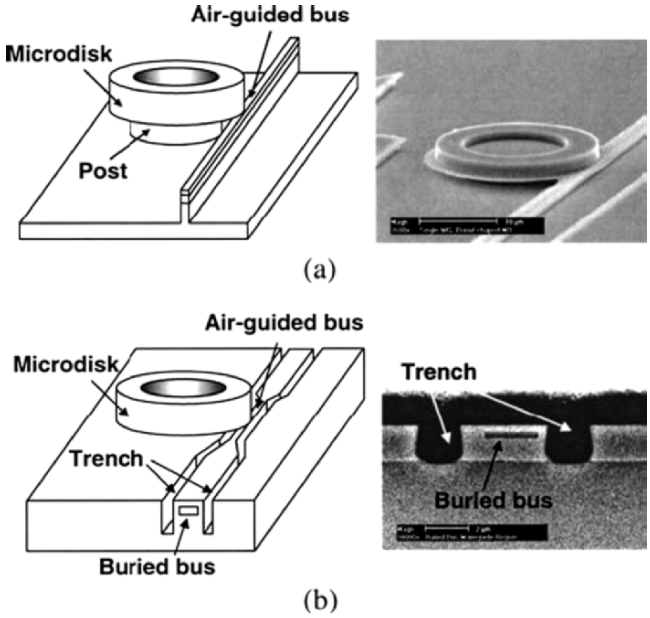

Fig. 5.49. Schematic drawings and SEM images of: (**a**) a disk vertically coupled to a single air-guided bus waveguide, type 1, and (**b**) a disk built on a buried bus line, type 2, respectively. The SEM image in (**b**) shows a stain-etched cross-sectional view of a buried bus waveguide section.

Reused with permission from S.J. Choi, Applied Physics Letters, 84, 651 (2004) ©2004 American Institute of Physics

use a UV sensitive polymer overlay to change the resonance spectrum (Chu et al. 1999d). Polysilane is used as a polymer overlay to change the resonance spectrum of vertically coupled glass ring resonators with a radius of 19 µm. The FSR of the device before UV exposure for TE and TM polarized input light is 10.54 and 10.56 nm, respectively. Dip coating of the resonator is used which results in a thickness of the polymer of 2 µm. An Hg-lamp UV source (Toshiba Lightec TOSCURE 251), having a center wavelength of 370 nm and an irradiance of 38 mW cm^{-2} is used for the UV exposure. The trimming of one resonance using TM polarized input light is shown in Fig. 5.50. The wavelength shifts obtained for the resonances are 7.62 and 9.14 nm for TE and TM polarized input light. No change has been observed to a device after UV exposure which was measured again after one month.

A similar polysilane UV trimming technique has been used in Suzuki et al. (2002) to trim the resonance wavelengths of a vertically coupled 1×8 filter array. A radius of 15 µm is used for all rings in the array. The ring resonators are made on a SiO_2 substrate. The ring and bus waveguides are made out of Ta_2O_5/SiO_2 compound glass. The cores of the ring resonator waveguides are covered by polysilane with a thickness of 10 µm using dip

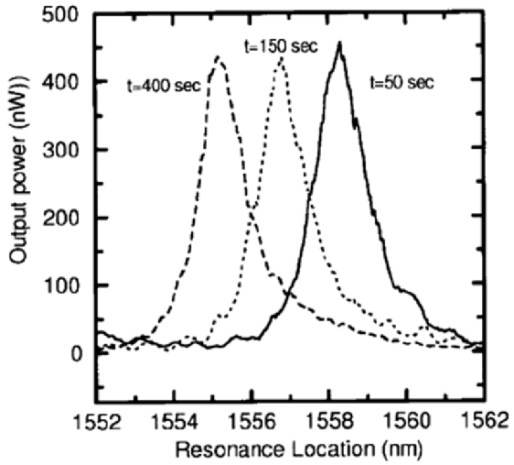

Fig. 5.50. The detailed TM spectra around one resonance after three different UV time exposures.

Reprinted with permission from IEEE Photonics Technology Letters, vol. 11, pp. 688–690 ©1999 IEEE

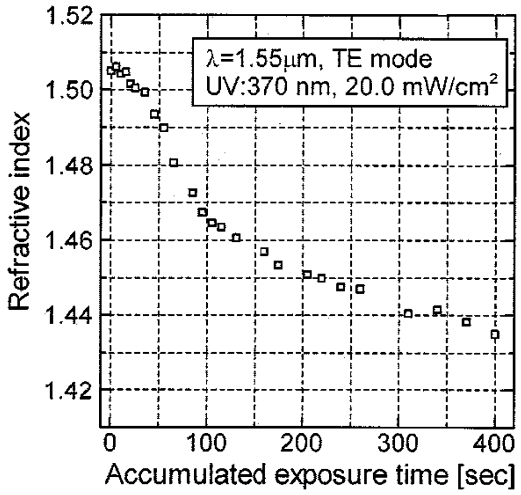

Fig. 5.51. Measured refractive index change of polysilane vs. UV exposure time.

Reprinted with permission from IEEE Photonics Technology Letters, vol. 20, pp. 745–750 ©2002 IEEE

coating. The change of the refractive index of polysilane versus UV exposure time is shown in Fig. 5.51.

The authors report, that the center wavelength change which is caused by the index change of the polysilane overcladding is due to the effect of oxidation or humidity absorption during UV exposure of the polysilane. The authors also

report on an aging effect which makes hermetic packaging of the device after UV trimming necessary.

A polysilane overcladding has also been used in Sparacin et al. (2005) to trim the resonance spectrum of Si_3N_4 ring resonators fabricated on a $3\,\mu m\,SiO_2$ under-cladding layer on a (100) silicon substrate with a diameter of $100\,\mu m$. The ring resonators are designed for a wavelength of $\lambda = 1{,}550\,nm$. The difference to the aforementioned polysilane trimming method which utilizes dip coating is that the used polysilane is brought on to the ring resonators using a vapor phase technique. The polysilane used is (PECVD 6M2S). The UV exposure is carried out with a MINERALIGHT® handheld lamp (model UVGL-25) emitting at a wavelength of $\lambda = 254\,nm$ at an intensity of $1.7\,\mu W\,cm^{-2}$. The refractive index decreased exponentially by $\sim$4 %, from 1.52 to 1.46 at a wavelength of $\lambda = 1{,}550\,nm$. The overall spectrum shift obtained is 12.8 nm for the TE mode and 23.5 nm for the TM mode.

Another UV trimming method is presented in Haeiwa et al. (2004) where the refractive index of the waveguide material SiN is exposed to UV light which imposes a refractive index change in the material. The refractive index change of an SiN film versus UV exposure time is shown in Fig. 5.52. The UV light source used is an Ar ion second harmonic generation laser with a wavelength of 244 nm and an output power of 100 mW.

Details on the used ring resonator can be taken from the inset in Fig. 5.52. The maximum refractive index change is $\Delta n = -1.3\times10^{-2}$, leading to a center wavelength shift of $-11.4\,nm$. This UV induced index change is reported to be stable for more than 1,200 h without any further treatment. A side effect of the UV induced index change is that coupling strength and loss inside the

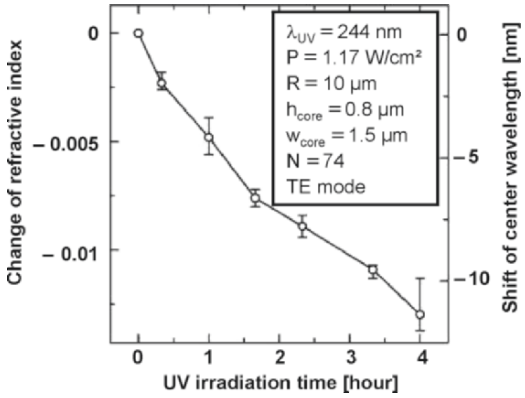

Fig. 5.52. Refractive index change of SiN film by UV irradiation and calculated center wavelength shift.

Reprinted with permission from IEEE Photonics Technology Letters, vol. 16, pp. 135–137 ©2004 IEEE

ring resonator are affected due to the absorption of UV radiation, changing the performance of the ring resonator filter. The FWHM in the presented example changed from an initial value of 0.34 to 1.02 nm after UV irradiation for 24 h.

A different approach of trimming the resonance spectrum of SiN ring resonators is demonstrated in Wang et al. (2005). Oxygen plasma treatment is used to convert the ring resonator material into SiO_xN_y changing the refractive index and thus affecting the resonance spectrum. The refractive index of SiO_xN_y depends on the amount of oxygen incorporated in the SiN layer and can be tuned over a large range between 1.45 (SiO_2) and 2.0 (Si_3N_4). A schematic of the used ring resonators is shown in Fig. 5.53. The radius of the ring resonator filter is $r = 25\,\mu m$. The length of the zero-gap coupler is $4\,\mu m$. The waveguide width is $1\,\mu m$ for the bus waveguides and $2.5\,\mu m$ for the ring resonator waveguides. An overall change in the resonance wavelength of 8.9 nm is demonstrated.

In the previous examples, tuning of semiconductor based ring resonators has been addressed. In the following example, a polymer ring resonator notch filter fabricated by soft lithography (Poon et al. 2004b) is tuned via a photobleaching technique of CLD-1 chromophores. The radius of the ring resonator is $207\,\mu m$, and the height and width of the waveguides are approximately 1.6 and $1.4\,\mu m$, respectively. The coupling gap is 430 nm wide. The trimming is performed using a visible broadband light source which is focused on one part of the ring resonator. The wavelength shift achieved is 8.73 nm after an exposure time of 1.75 h. The stability of chromophores, as it is well known,

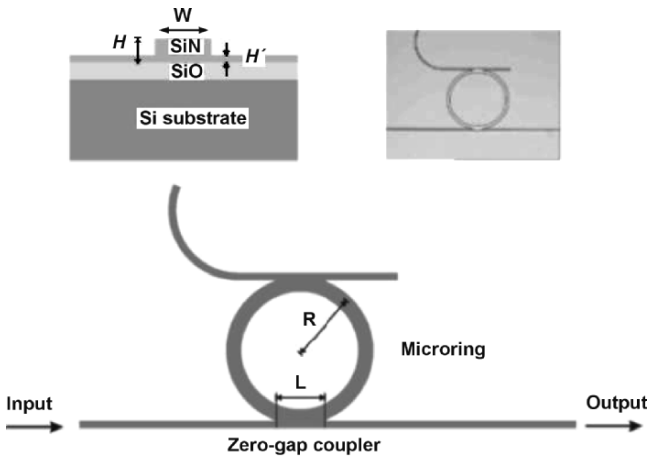

Fig. 5.53. Ring resonator filter. (*Inset*: (*upper-left*) SiN waveguide structure; (*upper-right*) photograph of fabricated ring resonator filter).

Reprinted with permission from IEEE Photonics Technology Letters, vol. 17, pp. 582–584 ©2005 IEEE

can degrade the performance of this material by the presence of oxygen. Therefore hermetic sealing and an inert gas atmosphere are needed for practical applications.

Tunability of the resonance spectrum of ring resonators by changing the refractive index with different methods has been presented, highlighting several practical examples. These methods have only affected the FSR and have had sometimes as a side effect, changed the shape of the resonances which is seen by an increase/decrease of the FWHM. A way of definite tuning of the resonance shape is by implementation of tunable couplers.

5.2.3 Tunable Couplers in Ring Resonators

Tunable couplers have been fabricated and demonstrated as has been described in Sect. 4.1. Their implementation in ring resonators is so far limited by the size and technologies used. A widely used technique for realizing tunable couplers in ring resonator filters is by applying heaters on top of the waveguides in the coupling region. This also affects the resonance spectrum which is also shifted and has to be compensated with another heater inside the ring cavity.

Tunable couplers enable the exact matching of the coupling coefficient to the loss inside ring resonator filters realizing a critically coupled state with maximum on–off ratio. One of the first disk resonators on an SOI platform, employing tunable couplers is presented in Lee and Wu (2005). Microelectromechanical system (MEMS) actuated deformable waveguides are used to tune the shape of the resonance. The layout and an SEM photograph of the MEMS disk is shown in Figs. 5.54 and 5.55, respectively.

The disk has a radius of 10 µm and the gap is 1.4 µm wide when no voltage is applied. A voltage of 70 V is needed to obtain a zero-gap coupler. One advantage of using MEMS couplers is the elimination of electron beam lithography to define the coupling gaps smaller than 500 nm. In this example a single standard lithographic step is required to pattern both the disk and the bus waveguides simultaneously.

Another MEMS approach is described and demonstrated in Nielsen et al. (2004), where a MEMS parallel plate structure is placed above the ring resonator enabling switching by lowering the plate and elevating it thus creating a change in the effective refractive index and a change in resonance wavelength. A detailed theoretical analysis of tunable couplers in ring resonators is presented in Kaplan (2006). Tunable couplers are one possibility of realizing perfectly matched ring resonator filters apart from gain implementation inside the ring cavity as was described in Sect. 5.1.2. Due to the advancing state-of-the-art of manufacturing technologies, it will only be a matter of time until tunable couplers are widely incorporated in ring resonator filters realizing various types of devices.

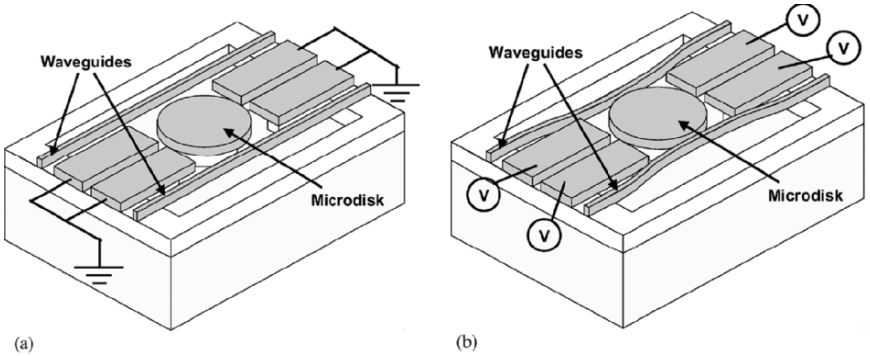

Fig. 5.54. Schematic structure of the disk resonator with deformable waveguides. (**a**) At zero bias, the disk is completely uncoupled since the suspended waveguides are far away from the disk. (**b**) With voltage applied on the electrodes, the waveguides are bent toward the disk, increasing the coupling between the waveguides and the disk.

Reprinted with permission from IEEE Photonics Technology Letters, vol. 17, pp. 1034–1036 ©2005 IEEE

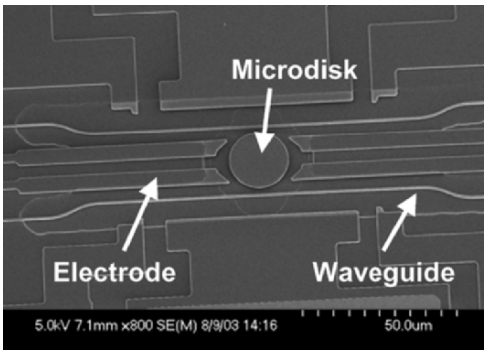

Fig. 5.55. SEM photograph of MEMS actuated disk resonator.

Reprinted with permission from IEEE Photonics Technology Letters, vol. 17, pp. 1034–1036 ©2005 IEEE

5.3 Dispersion Compensators

In classical optics, "dispersion" is used to denote the wavelength dependence of the refractive index in matter, ($\mathrm{d}n/\mathrm{d}\lambda$, where n is the refractive index and λ is the wavelength) caused by interaction between matter and light. In communication technology, "dispersion" is used to describe any process by which an electromagnetic signal propagating in a physical medium is degraded because the various wave components (i.e., frequencies) of the signal have different propagation velocities within the physical medium.

Material dispersion causes different wavelengths to travel at different speeds due to the variation of the refractive index of the fiber core with wavelength. However, part of the light also travels in the cladding of the fiber, which has a different refractive index. This portion of the light propagates therefore right through the cladding at different speeds to the core – an effect known as waveguide dispersion. Material and waveguide dispersion are combined to give an overall effect called "chromatic dispersion."

Chromatic dispersion is caused by a variation in the group velocity of light traveling within a fiber with changes in optical frequency. A data pulse always contains a spectrum of wavelengths. As the pulse travels along the fiber, the shorter wavelength components travel faster (negative dispersion) than the longer wavelength components (positive dispersion). This effect broadens the pulse and causes it to interfere with neighboring pulses and distort the transmission signal. The allowed chromatic dispersion in an optical network is inversely proportional to the square of the transmitted bit rate, so as data rates increase, dispersion tolerances decrease dramatically. While $2.5\,\mathrm{Gbit\,s^{-1}}$ networks can tolerate $16{,}000\,\mathrm{ps\,nm^{-1}}$ of dispersion, $10\,\mathrm{Gbit\,s^{-1}}$ networks can tolerate only $1{,}200\,\mathrm{ps\,nm^{-1}}$ and in $40\,\mathrm{Gbit\,s^{-1}}$ networks, the tolerance drops to only $60\,\mathrm{ps\,nm^{-1}}$ of dispersion. In addition, $40\,\mathrm{Gbit\,s^{-1}}$ systems require a wider modulation spectrum. A 12 GHz wide spectrum is typical for $10\,\mathrm{Gbit\,s^{-1}}$, for $40\,\mathrm{Gbit\,s^{-1}}$, it can be as high as 50 GHz, which means the total dispersion per channel is higher. Chromatic dispersion has a fixed, stable component in addition to a dynamic one. Most of the fixed dispersion is caused by the fiber and is predictable as a function of the type of fiber and the distance. In addition, the optical components present in the optical path add a smaller, fixed contribution. A dynamic contribution must be added to the fixed one. Since many passive components do not have a simple flat or linear dispersion curve, laser drift (caused by aging or temperature change) can lead to dispersion fluctuations that are nonlinear and hard to predict.

Another important type of dispersion is the polarization mode dispersion (PMD). PMD is caused by light traveling faster in one polarization plane compared to another. Fundamentally, it is caused by the core of the fiber not being perfectly round in cross-section and by birefringence which is introduced by mechanical forces. As a result, the optical thickness is not absolutely identical on every possible axis. PMD is a special case for modal dispersion or intermodal dispersion, which is caused by multimode propagation of light. Each mode travels with a different group velocity. The modes can be higher order modes of the same polarization, or modes of different polarization, as is it is the case for PMD. Intermodal dispersion is of no concern under single mode operation.

Finally, there is structural dispersion also known as quadratic dispersion which is effectively the second derivative of the transmission phase with respect to frequency. Structural dispersion is determined by the architecture and layout of the photonic integrated circuit.

Ring resonators can be used as dispersion compensators and examples presented in literature will be highlighted in this chapter. Practical dispersion compensators should have a limited tunability, uniform insertion loss upon tuning of dispersion and should enable the operation at multiple wavelengths. Ring resonators can be used to enhance the physical length by forcing the light to traverse the physical distance many times. Resonant enhancement, however, comes at the price of finite bandwidth. A large enhancement results in a narrower bandwidth. Ring resonators allow large compensation for multiple wavelengths simultaneously in a so far limited frequency range.

The building block of a multistage dispersion compensator using ring resonators is shown in Fig. 5.56. The group delay of a ring resonator follows a periodic curve. Cascading multiple loops enables synthesization of various delay curves.

A tutorial overview on ring resonators used as dispersion compensators highlighting various configurations is given in Schwelb (2004).

Dispersion compensators utilizing ring resonator architectures have been investigated by Madsen and coworkers extensively and some examples will be given in the following section. One filter type is of special interest, the optical all pass filter (APF). APF's are devices that allow phase correction or equalization without introducing any amplitude distortion (Lenz and Madsen 1999). One of the first experimental demonstration of a multistage all pass filter dispersion compensator that uses ring resonators in planar waveguides is demonstrated in Madsen et al. (1999b). A two stage optical filter consisting of two parallel coupled ring resonator notch filters with a bend radius of 2.2 mm is realized. Ge-doped silica waveguides on a silicon substrate are used for the waveguides. A coupling gap of 3 µm is used for the directional couplers. The phase shifter inside the ring resonators is made out of chrome with a resistance of 55 Ω, which is deposited on the upper cladding of each ring. The FSR of the device is 12.5 GHz. The parameters of the filter are: $D = 4{,}200\,\mathrm{ps\,nm^{-1}}$, ±5 ps group delay ripple, <3 dB loss, and a 4.5 GHz passband width. The filter is used in a transmission experiment using 320 km of fiber. The filter is capable of compensating negative and positive dispersion. Due to the birefringence of the used waveguides, the filter is polarization dependent and therefore to avoid PMD, either TE or TM polarized input light is used.

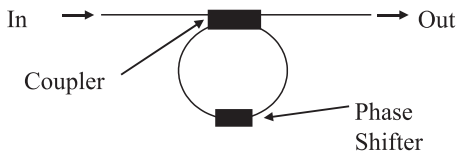

Fig. 5.56. Single ring resonator filter building block of multistage dispersion compensator

Four stage ring resonator dispersion compensating filters are presented in Horst et al. (2000). Ring resonators with an FSR of 25, 33, and 50 GHz are fabricated in SiON technology. Metal heaters are deposited on top of the waveguides to allow for tunable phase shifting. A dispersion of $-415\,\mathrm{ps\,nm^{-1}}$ over a usable bandwidth of 22 GHz for a filter with an FSR of 50 GHz is obtained. The filter is as the previous example polarization dependent which means that accurate polarization control has to be maintained.

A new architecture combining ring resonators and MZIs to be used for dispersion compensation is presented in Madsen et al. (1999b). A schematic of a single stage ring resonator filter with an MZI design is shown in Fig. 5.57. The MZI design enables a tunable APF by incorporating phase shifters in the ring and the MZI. The phase shifter in the MZI enables a tunable coupling ratio while the phase shifter in the ring resonator is for resonance tuning.

Four stages of the ring resonator/Mach–Zehnder combination are cascaded yielding a dispersion of $1{,}800\,\mathrm{ps\,nm^{-1}}$ and a passband of 14 GHz, which is greater than 50% of the FSR. A low group delay ripple of 15 ps peak is achieved. The device is realized in Ge-doped silica planar waveguides. The directional coupler lengths are 477 μm. The radius used is 1 mm, and the FSR of the filter is 25 GHz (at 1,490 nm).

A device consisting of ring resonators coupled to arms of an MZI are used in Madsen et al. (2004) to compensate and emulate PMD. A photograph of a similar realized device is shown in Fig. 5.58. The device which is used for

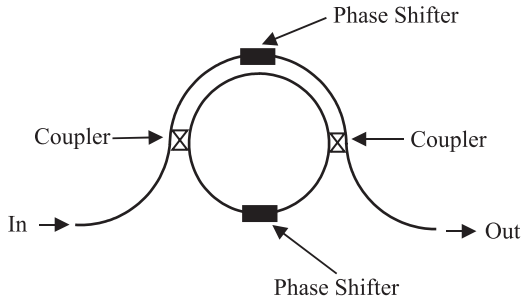

Fig. 5.57. Ring resonator with asymmetric Mach–Zehnder interferometer

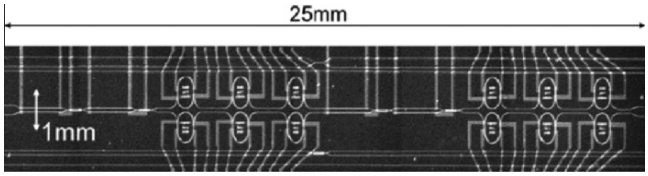

Fig. 5.58. A two-section planar waveguide chip with three-stage all-pass filters in the upper and lower arms of each section.

Reprinted with permission from IEEE Journal of Lightwave Technology, vol. 22, pp. 1041–1050 ©2004 IEEE

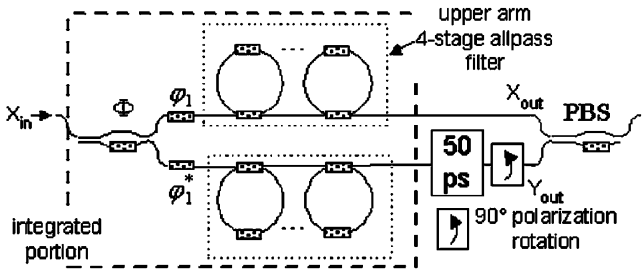

Fig. 5.59. Experimental device.

Reprinted with permission from IEEE Journal of Lightwave Technology, vol. 22, pp. 1041–1050 ©2004 IEEE

PMD measurements consists of a directional coupler, which is fed into an MZI which has ring resonators attached at each arm. A schematic of the used configuration is shown in Fig. 5.59.

The experimental device based on Ge-doped silica waveguides is a four stage all pass filter. The radius of the ring resonators used is 350 µm, leading to an FSR of 74.4 GHz. A discrete polarization beam splitter (PBS) on the output side and a linearly polarized input signal with the polarization aligned to either the TE or TM axis is used in the measurement setup. The authors demonstrate a differential group delay (DGD) tuning range over 100 ps for 10 Gbit s^{-1} and 25 ps for 40 Gbit s^{-1} data. Second order PMD with a tuning range of 255 ps^2 and third order PMD with a range of 2,430 ps^3 are also demonstrated.

Ring resonators combined with MZIs can not only be used for dispersion compensating optical devices. Other applications will be addressed in the following chapter.

5.4 Mach–Zehnder Interferometers Combined with Ring Resonators

MZIs are well known and have found their way into integrated optics. A basic MZI consist of two waveguides of different lengths, which are joined at both ends using 3 dB couplers. A schematic is shown in Fig. 5.60.

The transfer characteristic has a periodic $\sin^2$ shape over wavelength assuming that the two 3 dB couplers are wavelength independent regarding their coupling behavior. The distance between the minima and maxima in terms of wavelength depend on the length difference in both arms of the MZI. The 3 dB bandwidth of the filter in the frequency domain is given by

$$\Delta f = \frac{c_0}{2n_{\text{eff}}\Delta L} \tag{5.2}$$

where ΔL is the length difference between both arms.

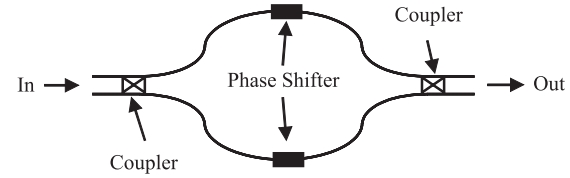

Fig. 5.60. Layout of a basic MZI

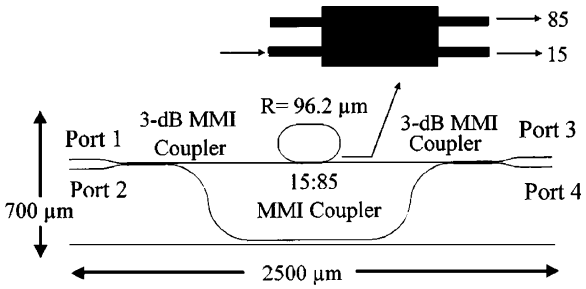

Fig. 5.61. Configuration of the periodic multi/demultiplexer with a ring resonator. Reprinted with permission from IEEE Photonics Technology Letters, vol. 12, pp. 1174–1176 ©2000 IEEE

Optical filters deployed in optical networks are required to have a "box-like" filter response as was described earlier. One way to do this is by using multiple coupled ring resonators. MZIs can also be modified to realize a more rectangular transfer function by introducing a ring resonator into one of the arms. A ring resonator has one 2π phase shift per FSR. In order to obtain passband flattening of the transfer characteristic of the MZI, two ring resonator phase shifts per FSR of the MZI are required. This means that the FSR of the ring resonator has to be half of the FSR of the MZI. Translated into length requires the circumference of the ring to be twice as large as the delay length of the MZI.

A periodic multi/demultiplexer with a square spectrum response having an FSR of 200 GHz is presented in Kohtoku et al. (2000). A schematic of the device layout including design parameters is shown in Fig. 5.61. The device is fabricated on an InP substrate. MMI couplers are used in the device which enables lower manufacturing tolerances regarding the splitting ratio. The circumference of the ring resonator is 876.6 µm leading to an FSR of 100 GHz which is half of the FSR of the MZI. A suitable coupling ratio for the coupler in the ring resonator has to be chosen to obtain a rectangular transfer characteristic with a large rejection bandwidth and a high extinction ratio. The MMI coupler in the ring resonator has a splitting ratio of 15:85. The transmission characteristic of the device is shown in Fig. 5.62.

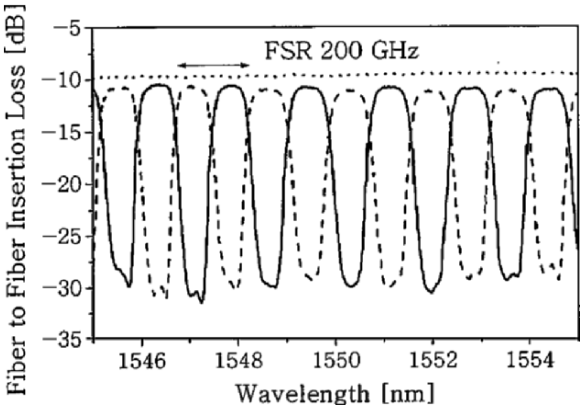

Fig. 5.62. Transmission spectra of the fabricated device with 200 GHz FSR. The *solid line* indicates ports *1–3*. The *dashed line* indicates ports *1–4*. The *dotted line* indicates the reference waveguide.

Reprinted with permission from IEEE Photonics Technology Letters, vol. 12, pp. 1174–1176 ©2000 IEEE

In the following example, a balanced MZI with one arm coupled to a ring resonator in AlGaAs–GaAs is presented (Absil et al. 2000b). The motivation in using a balanced MZI is by realizing a notch filter and thus introducing a zero pole filter when speaking in terms of the Z-transformation (see Chap. 2). When the round-trip loss in the ring resonator is small compared to the waveguide coupling strength, the ring resonator introduces a phase shift of π at resonance. The resonant phase shift is independent of the coupling coefficient, and minimum transmission occurs. A photograph of the device is shown in Fig. 5.63. The amplitude transfer response of this kind of device is given by Absil et al. (2000b):

$$T = \frac{1}{2}\left(1 + \frac{t - \mathrm{e}^{-(\alpha+\mathrm{j}\beta)2\pi R}}{1 - t\mathrm{e}^{-(\alpha+\mathrm{j}\beta)2\pi R}}\mathrm{e}^{-\mathrm{j}\phi}\right), \qquad (5.3)$$
$$t = \sqrt{1-\kappa^2},$$

where ϕ is the phase imbalance between the two arms of the MZI. The Y-splitters are assumed of having a 3 dB splitting ratio with a wavelength independent loss. The device has only one input and one output port coupled to 3 dB Y-splitters. The transfer spectrum obtained is slightly deviated from the theoretical notch filter response due to an imbalance in the arms of the MZI of only 110 nm. The spectrum is shown in Fig. 5.64.

These two examples show how different transfer functions can be realized with a ring resonator coupled to one arm of an MZI. The response depends on the length of the arms (balanced/unbalanced), on the type of response desired and on the coupling coefficient from one arm to the ring resonator.

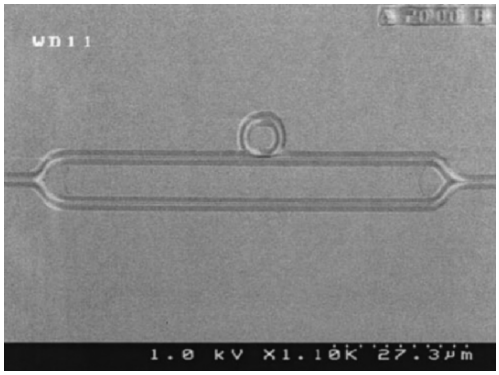

Fig. 5.63. SEM micrograph of the fabricated MZI in GaAs–AlGaAs.

Reprinted with permission from IEEE Photonics Technology Letters, vol. 12, pp. 398–400 ©2000 IEEE

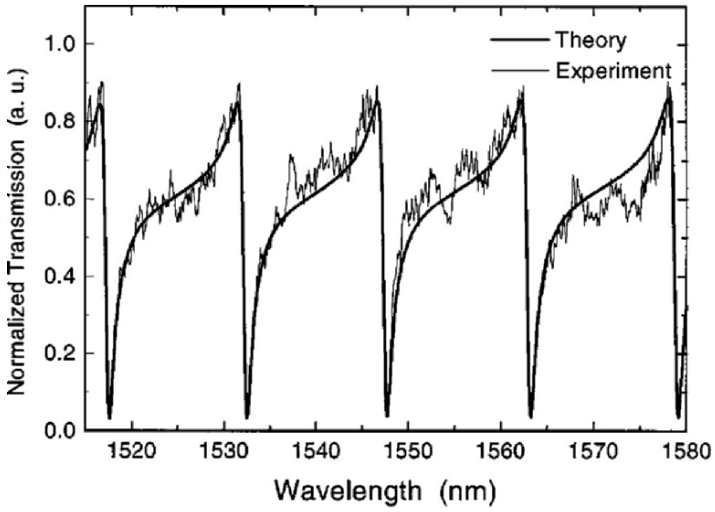

Fig. 5.64. Measured Mach–Zehnder transmission spectrum and analytical fit showing imbalanced arms.

Reprinted with permission from IEEE Photonics Technology Letters, vol. 12, pp. 398–400 ©2000 IEEE

Recently a novel geometry for ring resonators coupled to an MZI has been demonstrated in polymer in Paloczi et al. (2003b). A photograph of the proposed and fabricated device is shown in Fig. 5.65. The device is realized in SU-8. The ring resonators are racetrack shaped and have a bending radius of 100 µm. The straight coupling sections have a length of 50 µm. The designed coupling gap is 750 nm. The ring resonators have an FSR of 2.2 nm for TE polarized light at a wavelength of 1,550 nm. Complicated phase properties and

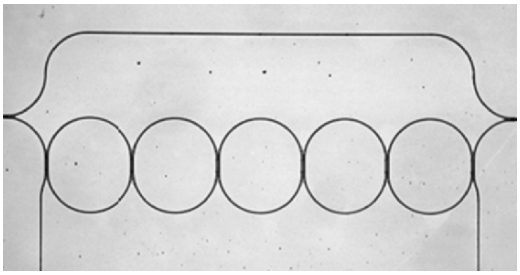

Fig. 5.65. Novel design of ring resonators coupled to an MZI. The size of the device is approximately 1.2 mm.

Reprinted with permission from G.T. Paloczi, Optics Express, vol. 11, no. 21, pp. 2666–2671 ©2003 Optical Society of America

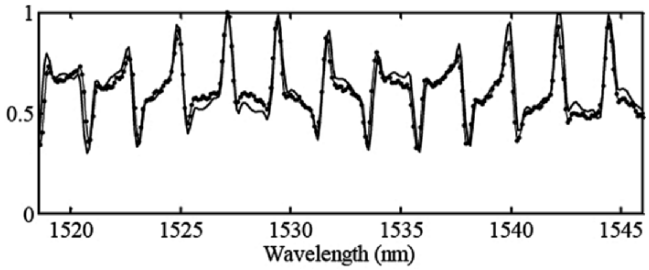

Fig. 5.66. Experimental data (*dotted*) and the theoretical fit (*line*). The fitting parameters used for the fit were: polarization 93% TE and 7% TM, effective indices 1.48475 for TE and 1.48555 for TM, power coupling coefficients 0.46 for TE and 0.85 for TM, and waveguide loss of $30\,\mathrm{dB\,cm^{-1}}$.

Reprinted with permission from G.T. Paloczi, Optics Express, vol. 11, no. 21, pp. 2666–2671 ©2003 Optical Society of America

a periodic spectral response of the absolute field amplitude are observed. The transmission spectrum of the device is shown in Fig. 5.66.

MZIs with ring resonators have also been demonstrated to be used for all optical switching (Heebner et al. 2004).

Optical switching in ring resonators will be described in Sect. 5.8. Ring resonators coupled to MZIs have also been investigated for implementation as modulators Tazawa and Steier (2005).

The properties of ring resonator modulators are addressed in the following chapter.

5.5 Modulators

Wavelength division multiplexing (WDM) and dense WDM systems require modulators to generate the required optical signals to be transmitted. Electro-optic (EO) modulators based on an MZI are used for fulfilling this task so far.

Resonator based modulators are of increasing interest as they can be operated in principle with a lower driving voltage and have a more compact design which is a prerequisite for integrated devices. One of the earliest resonator based modulators is of course the Fabry–Perot resonator. Ring resonator modulators have recently gained attention due to the improvement of fabrication technologies which enable very small devices as was demonstrated in previous chapters, and due to improved and novel material properties. In contrast to MZI based EO devices, ring resonator modulators have a rather small bandwidth which limits their applications so far to systems requiring a modest radio frequency (RF) bandwidth but operate at high carrier frequencies. A single wavelength is used as the input signal for a ring resonator modulator. The operating wavelength of the ring resonator modulator is tuned, so that the steepest slope of one of the resonances in the throughput port spectrum is used. Applying a voltage through an electrical field in the ring resonator induces a shift in the position of the resonance peak, resulting in an intensity change at the throughput port.

The main bandwidth limitation is the time which is needed to build up the optical field in the ring resonator. The time of one roundtrip in the resonator is given by (see also Chap. 2):

$$\tau_{\mathrm{Roundtrip}} = \frac{2\pi R n_{\mathrm{g}}}{c_0} \tag{5.4}$$

The total time needed for a ring resonator to build up a resonance (also referred to as cavity ring-down time) is given by

$$\tau_{\mathrm{Cav}} = m \cdot \frac{2\pi R n_{\mathrm{g}}}{c_0} \tag{5.5}$$

The cavity ring-down time can be related to the quality factor Q of a ring resonator by Leinse (2005)

$$\tau_{\mathrm{Cav}} = \frac{\lambda Q}{2\pi c_0} \tag{5.6}$$

The cavity ring-down time can also be written in terms of the finesse F of the ring resonator using (2.31) to:

$$\tau_{\mathrm{Cav}} = \frac{F R n_{\mathrm{g}}}{c_0} \tag{5.7}$$

Instead of using the group refractive index, the effective refractive index can also be used. The group refractive index takes into account the wavelength dependency of the effective refractive index and therefore a more accurate value for the cavity ring-down time is obtained. The relationship between the bandwidth of the filter spectrum response and the maximum transmission capacity is analyzed theoretically and experimentally in Suzuki et al. (2001). A vertically coupled ring resonator add–drop filter with a radius of 20 µm is used for the experiment. An FWHM of 0.75 nm is obtained. A pulsewidth of

3.4 ps is measured at the output port of the ring resonator, when an input pulse of 1.2 ps with a sech pulse shape from a fiber laser is inserted at the input port. A maximum transmission capacity of $50\,\mathrm{Gbit\,s^{-1}}$ is estimated for this type of ring resonator filter. Linear and nonlinear pulse propagation in ring resonator filters is analyzed theoretically in Melloni et al. 2003b. In particular, the so-called slow wave structures consisting of a chain of directly coupled ring resonators are investigated.

In the following paragraph a relationship between the bandwidth and the driving voltage based on Rabiei et al. (2002a) is given.

Since the traditional switching voltage V_π in MZI based modulators cannot be used for a ring resonator modulator a switching voltage of V_{FWHM} is defined, which is the voltage required to shift the resonant wavelength by the FWHM. Sometimes other definitions are used which define the voltage needed for a specific extinction ratio (e.g., $V_{10\,\mathrm{dB}}$ or $V_{20\,\mathrm{dB}}$).

The modulation bandwidth BW of a ring resonator is given by

$$BW = \frac{1}{2\pi\tau_{\mathrm{Lifetime}}}, \tag{5.8}$$

where τ_{Lifetime} is the finite lifetime for the photons in the resonator. Using the frequency relationship for the FWHM

$$\Delta\omega_{\mathrm{FWHM}} = \frac{1}{\tau_{\mathrm{Lifetime}}}. \tag{5.9}$$

The bandwidth can be rewritten as

$$BW = \Delta\upsilon_{\mathrm{FWHM}} \tag{5.10}$$

The index change Δn_{eff} required to shift the resonance by $\Delta\upsilon_{\mathrm{FWHM}}$ is given by

$$\frac{\Delta n_{\mathrm{eff}}}{n_{\mathrm{eff}}} = \frac{\Delta\upsilon_{\mathrm{FWHM}}}{\upsilon}, \tag{5.11}$$

where n_{eff} is the effective refractive index of the ring resonator and υ is the optical frequency. The index change relation for EO materials is given by

$$\Delta n_{\mathrm{ef}} = \frac{1}{2} K n_{\mathrm{EO}}^3 r_{33} \frac{V}{d}, \tag{5.12}$$

where K is the confinement factor, V is the applied voltage, n_{EO} is the refractive index of the EO material, and d is the distance between the electrodes. Using these equations, the relationship between the bandwidth and the driving voltage is obtained, yielding the fundamental limitations of these kind of modulators:

$$\frac{BW}{V_{\mathrm{FWHM}}} = \frac{K\upsilon n_{\mathrm{EO}}^3 r_{33}}{2 n_{\mathrm{eff}} d}. \tag{5.13}$$

The polymer based ring resonator modulator presented in Rabiei et al. (2002a) has a bandwidth of 2 GHz and a transmission experiment has been carried out demonstrating an open eye diagram at 1 Gbit s^{-1}. Detailed expressions for the modulation bandwidth and drive voltage for optical resonator based modulators can be found in Gheorma and Osgood (2002). Ring resonator-based travelling wave modulators are also analyzed theoretically in Tazawa and Steier (2006). Theory on ring resonator modulators, device design, and characterization is presented in Rabiei (2003) and Leinse (2005). In Leinse (2005), modulators consisting of a ring resonator coupled to an MZI are also demonstrated.

Polymer ring resonator modulators with diameters of 50, 70, and 150 µm are demonstrated in Rabiei et al. (2002b). The modulators have FSRs of 1,100, 770, and 300 GHz at a wavelength of 1,330 nm. The fabrication and layer sequence of the ring resonators has been described in Sect. 3.5.1. The bandwidth of the devices is 18, 16, and 12 GHz, respectively. The authors propose a multiwavelength ring resonator modulator and filter configuration for implementation in WDM systems shown in Fig. 5.67.

In order for the system to be realized, the FSRs of each of the ring resonator modulators and filters have to be greater than the wavelength spectrum used in the WDM system. Each ring resonator has to be frequency hence wavelength stabilized to modulate or filter out the correct wavelength with high extinction ratio. The device consisting of several ring resonators is feasible with current state-of-the-art manufacturing methods and as was described in a previous chapter, wavelength stabilization can be performed with several methods.

Modulators based on ring resonators on silicon on insulator are presented in Pradhan et al. (2005), Xu et al. (2005). A ring resonator notch filter is used with a rib waveguide structure. Photographs of the ring resonator and the metal contacts are shown in Fig. 5.68.

Electro-optic modulation of the refractive index is achieved by a p–i–n junction integrated with the ring resonator. The *p*- and *n*-doped regions are on the inner and outer side of the ring waveguide having a concentration of 10^{19} cm^{-3}. The width and height of the ring and bus waveguides are 450 and

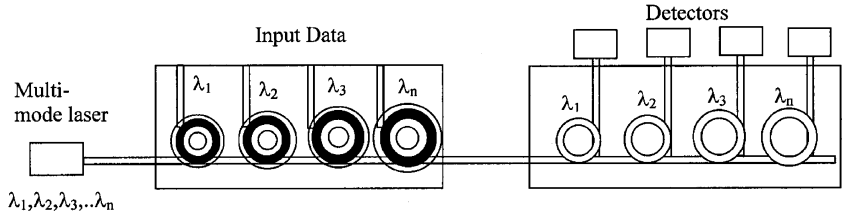

Fig. 5.67. Integrated WDM system using microring modulators and filters.

Reprinted with permission from IEEE Journal of Lightwave Technology, vol. 20, pp. 1968–1975 ©2002 IEEE

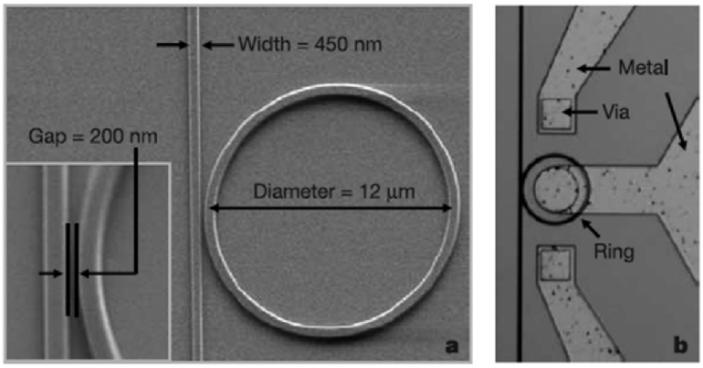

Fig. 5.68. SEM and microscope images of the fabricated device. (**a**) Top view SEM image of the ring coupled to the waveguide with a close-up view of the coupling region. (**b**) Top view microscope image of the ring resonator after the metal contacts are formed. The metal contact on the central p doped region of the ring goes over the ring with a 1 µm thick silicon dioxide layer between the metal and the ring.

Reprinted by permission from Macmillan Publishers Ltd: Nature, Xu, vol. 435, pp. 325–327 ©2005

250 nm, respectively. A coupling gap of 200 nm is realized. The diameter of the ring resonator is 12 µm leading to an FSR of 15 nm. The FWHM of a resonance around 1,550 nm is measured to be 0.04 nm. The cavity ring down time for this type of modulator using (5.6) is calculated to be $\tau_{\mathrm{Cav}} = 33\,\mathrm{ps}$. The performance of the device is demonstrated using a nonreturn-to-zero (RZ) signal at $0.4\,\mathrm{Gbit\,s^{-1}}$ and an RZ signal at $1.5\,\mathrm{Gbit\,s^{-1}}$.

Vertically coupled disk modulators on InP are demonstrated in Sadogopan et al. (2005). The operation of the device is based on a depletion width translation mechanism which involves the transfer of optical energy between two waveguides at the resonance of a ring or disk resonator that couples the two waveguides. A photograph of a fabricated ring modulator as well as a sketch of the cross-section is shown in Fig. 5.69.

The fabricated device has an outer radius of 12 µm and an inner radius of 8.5 µm. The 3 dB modulation BW of the device is 8 GHz. A wavelength shift of 0.2 nm at a driving voltage of 0.9 V leads to an extinction of the signal wavelength of 10 dB. The device shows open eye diagrams at $10\,\mathrm{Gbit\,s^{-1}}$ which demonstrates the functionality at these speeds.

Ring and disk resonators with a high Q-factor enhance the coupling between waveguides, thus a low voltage modulation of the resonator Q can modulate the power transfer, enabling high speed operation. Examples of techniques for fabricating ring and disk resonators modulator circuits have been demonstrated in this chapter and ongoing research will enable faster and smaller devices.

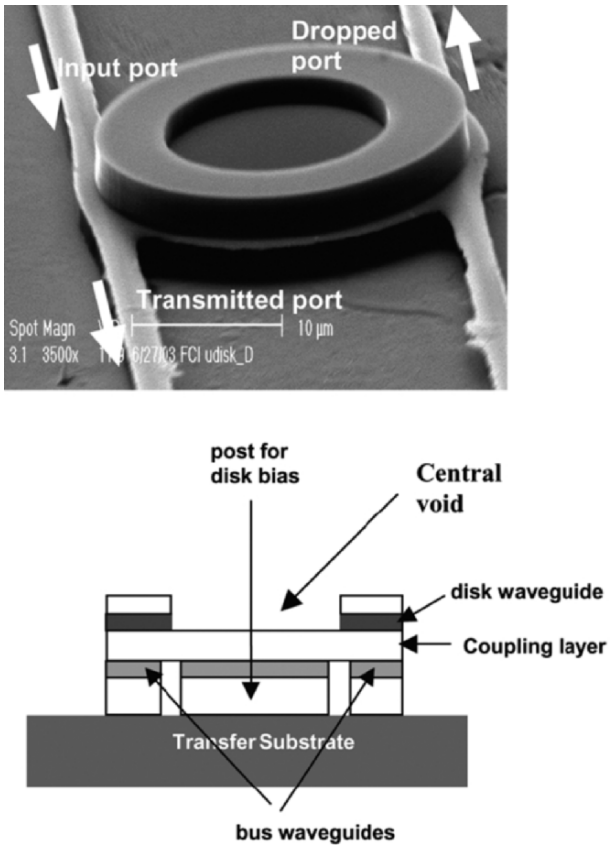

Fig. 5.69. SEM photograph of fabricated ring modulator. The cross-section of the device shows the three-dimensional coupling which is necessary for the depletion mechanism.

Reprinted with permission from IEEE Photonics Technology Letters, vol. 17, pp. 567–569 ©2005 IEEE

5.6 Lasers

Semiconductor ring lasers have been investigated in the past and have recently gained attention again because they can be readily integrated with other optoelectronic devices and do not require gratings or facets for optical feedback. Ring lasers avoid spatial hole burning by traveling wave operation, which results in single mode operation and reduced sensitivity to feedback. Different types of active and passive coupling configurations have been used in ring resonator lasers including Y-splitters, directional couplers and multimode interference couplers. MMI couplers have attracted widespread attention, because they allow increased fabrication tolerances compared to directional couplers as has been described in Chap. 4.

Ring lasers have been described in detail in literature, therefore only brief highlights will be given and different types of laser configuration will be discussed in the following chapter.

5.6.1 All Active Lasers

In this chapter ring resonator-based lasers fabricated using gain material for realizing ring and bus waveguides are described. These ring lasers will be referred to as all active ring lasers.

One of the first demonstrations of the principle of a ring resonator laser is presented in Weber and Ulrich (1971). A rhodamine 6G[2] doped polyurethane film which serves as the waveguide is coated on the surface of a cylindrical glass rod with a diameter of 5 mm providing the ring resonator geometry. This film is pumped with a N_2 laser having a wavelength of 337 nm emitting a beam with a sheet like output characteristic, enabling the pumping of only a short width of approximately 0.2 mm of the film coated glass rod. In using this pump method, a ring resonator laser is obtained. A prism coupler is used to couple light out of the ring resonator. One of the first integrated ring resonator lasers is presented in Liao and Wang (1980). The ring laser is made in the material system GaAs–GaAlAs and has a straight branching waveguide serving as the output. The output waveguide is in principle a Y-splitter. A ring radius of 100 µm is realized. The lasing wavelength observed is around 873 nm under pulse operation. The threshold of the laser is above 300 mA. In order to prevent the output waveguide from acting as a second cavity, it was made 3 mm long and the facets have been scratched to lower or eliminate the reflectivity.

One of the first continuous wave (cw) operating integrated disk resonator lasers in the GaAs material system with integrated Y-splitter for output coupling is presented in Krauss et al. (1990). The disk has a diameter of 84 µm and a threshold current of 24 mA. The low threshold current is achieved by only depositing a metal contact layer on the outer side of the disk with a width of 4 µm, forming a metal ring and isolating the inner disk with a polyimide layer. One of the first integrated ring resonator lasers in GaAs/AlGaAs with a radius of 150 µm and a threshold current of 72 mA is demonstrated in Hohimer et al. (1991). A Y-splitter is used to couple out of the ring resonator. The width of the used waveguide is 8 µm. A side mode rejection ratio of 22 dB is measured for current values greater than 50 mA, which was one of the highest side mode rejection ratios at that time. The laser emits at a wavelength of 852 nm. The output power has been increased significantly for similar ring laser devices in Hohimer et al. (1992) by tilting the output waveguide (tilt angle = $5°, 10°$), eliminating a back reflection of modes which compete with the laser mode for gain. Controlled back reflection is also investigated for unidirectional lasing in ring resonator lasers suppressing the counter propagating wave. Ring lasers in GaAs–AlGaAs having Y-splitters as output couplers

[2] Formula: $C_{28}H_{31}N_2O_3Cl$

with tilted output waveguides are also presented in Tsai et al. (1998). Tilt angles from 0° to 15° between the waveguide orientation and the normal of the cleaved facet are realized. Ring lasers having a radius of 200 µm and 300 µm are demonstrated.

Unidirectional ring lasers using racetrack geometry are presented in Hohimer and Vawter (1993). Inside the racetrack cavity is an equal-radius crossover S-waveguide that is independently electrically contacted. This S bend waveguide enables unidirectional lasing. Single mode operation at wavelengths around 870 nm with an output power greater than 10 mW is reported. This group around Hohimer has performed extensive research on ring resonator lasers and has published numerous papers on the subject. Therefore only an excerpt of relevant publications from this group is presented in this chapter.

One of the first ring resonator lasers in the material system GaInAsP is demonstrated in Hansen et al. (1992). The ring resonator laser has a diameter of 3 mm and emits at a wavelength of 1.54 µm. The threshold current is measured to be 157 mA. The ring laser is coupled to a straight waveguide with a gap of 1.5 µm. The ring laser is fabricated using buried passive rib waveguides and two buried heterostructure active sections with multiple quantum wells. The length of the active sections is 500 µm each, placed on opposite sites of the ring laser. Continuous wave operation is achieved with a side mode suppression of 28 dB.

InP-based ring lasers employing MMI couplers are presented and analyzed in detail in Pennings et al. (1993, 1994) and van Roijen et al. (1994). An output power of 9 mW under cw operation at a wavelength around 1.6 µm with a side mode suppression of 35 dB is obtained. Two types of ring resonator geometries are analyzed and fabricated. A schematic of the devices is shown in Fig. 5.70. Completely active ring resonators are fabricated. Two types of MMI couplers

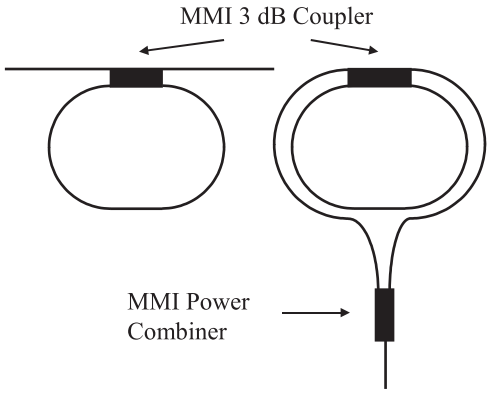

Fig. 5.70. Ring laser employing MMI couplers – design

are used, output couplers with a width of 7 µm with lengths between 185 and 233 µm and combiners with a width of 8 µm and lengths between 61 and 75 µm.

The use of MMI couplers in ring resonator lasers has also been investigated and demonstrated in Krauss et al. (1994, 1995b). Racetrack shaped ring resonators in the GaAs/AlGaAs material system with a radius of 400 µm and a length of 320 µm for the straight section and the 3 dB MMI coupler are used. The device has a threshold current of 140 mA and emits at wavelengths around 870 nm. Ring lasers having directional couplers, MMI couplers and Y-splitters as output configurations are analyzed, fabricated and compared in Krauss et al. (1995a).

A square ring resonator laser in GaAs–AlGaAs with an MMI output coupler is presented in Kim et al. (1997). A schematic of the laser is shown in Fig. 5.71. The round-trip length of the square ring resonator laser is determined by the width of the used waveguide. A waveguide width of 6 µm results in a 3 dB coupling length of 283 µm and for a waveguide width of 8 µm, a 3 dB coupling length of 509 µm is determined. The width of the coupling waveguide is 2 µm for the 6 µm ring waveguide and 3 µm for the 8 µm ring waveguide. Threshold currents of 200 mA and 250 mA are measured at lasing wavelengths around 800 nm.

A ring laser with a triangular shape in InP–GaInAsP is presented in Ji et al. (1997). A photograph of the device is shown in Fig. 5.72. The lasing wavelength of a presented device is around 1.26 µm with a threshold current of 64 mA ($\theta = 25°$) under pulsed operation (100 ns pulsewidth, and 20 µs period). A side mode suppression ratio of 25 dB is achieved. The width of the waveguide is 4 µm and the cavity length is 300 µm. The Q of the cavity is determined by the so called structural angle θ which defines the output angle ϕ. The dependence of these angles on the output power is investigated experimentally.

One of the first photonic integrated circuits in GaAs–AlGaAs comprising a mode-locked ring laser, an optical amplifier, and a high speed photodetector is fabricated and demonstrated in Vawter et al. (1997). A schematic of the device is shown in Fig. 5.73.

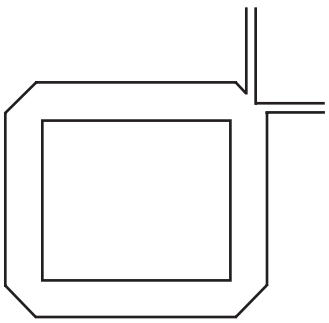

Fig. 5.71. Layout of square ring resonator laser

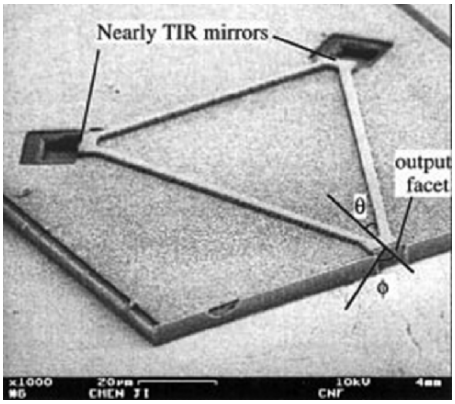

Fig. 5.72. SEM fabricated triangular ring laser, cavity length 300 µm, structural angle θ and light output angle ϕ are defined in the diagram.

Reprinted with permission from IEEE Photonics Technology Letters, vol. 9, pp. 1469–1471 ©1997 IEEE

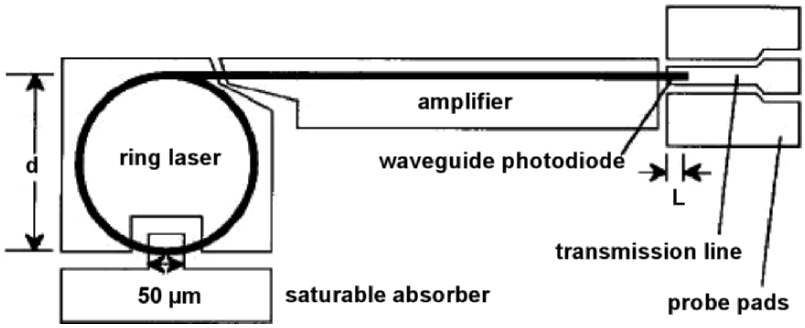

Fig. 5.73. Schematic of photonic integrated circuit.

Reprinted with permission from IEEE Photonics Technology Letters vol. 9, pp. 1634–1636 ©1997 IEEE

The device is used to generate mm wave signals at frequencies of 30, 60, and 90 GHz depending on the radius of the ring laser. The radii of the used ring lasers are 860, 430, 290 µm, respectively. Passive mode locking of the ring laser is realized by a saturable absorber, generating pulses between 1 and 10 ps.

Mode locking in ring lasers is investigated both theoretically and experimentally in Yu et al. (1998) with respect to different configurations of intracavity saturable absorbers. A schematic of the designs analyzed is shown in Fig. 5.74.

Low-threshold GaInAsP all active ring lasers are presented in Griffel et al. (2000). The layer sequence has already been described in Chap. 3. The threshold current of the cw operated ring laser is 66 mA with a side mode suppression ratio of 26 dB at wavelengths around 1.6 µm.

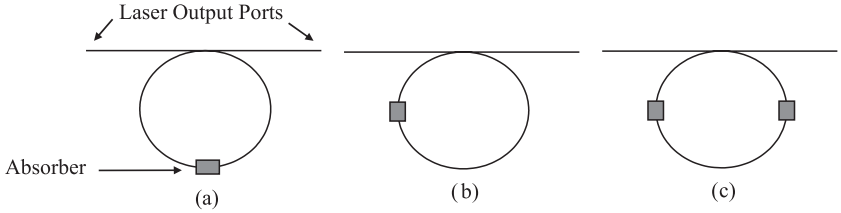

Fig. 5.74. Configurations: (**a**) symmetric, (**b**) asymmetric and (**c**) dual absorber

Unidirectional bistability in circular waveguide InGaAs/GaInAsP semiconductor lasers has been observed and demonstrated in Sorel et al. (2002). A ring diameter of 1.2 mm is used for the cw ring laser having a threshold current of 125 mA. The FSR obtained is 0.166 nm. Three operating regimes regarding the clockwise and counter clockwise propagating modes are observed. Operation regime one is between 125 and 135 mA, and both modes oscillate. Operation regime two is between 135 and 220 mA, unidirectional operation is observed, either in one or the other direction, depending on the driving current. The extinction ratio between the lasing and nonlasing output is measured to be more than 30 dB. Operation regime three is above 220 mA, here the modes randomly switch to the output ports. Bistability is imposed by two electrodes (see Fig. 5.75), each on one side of the output waveguide. For example by applying a short pulse to either of the two electrodes when the ring laser is operated in regime two, changes the direction of the mode in the ring laser. Operating regimes of ring laser in the material system GaAs–AlGaAs are also investigated by this group in Sorel et al. (2003). A photograph of a ring laser where the contact layout can be seen which was also used for the InP based devices is shown in Fig. 5.75. The presented ring laser is integrated together with three photodiodes (PD) realized in a simple manner by placing contacts on top of the active waveguides. Their position can be taken from the photograph.

The radius of the ring lasers investigated is 1 mm. A directional coupler with a coupling gap of 1 μm is used to couple light out of the ring. The output waveguide is tilted at an angle of 5° to reduce back reflection of the light from the cleaved facets below a reflectivity of 0.5%. Different operating regimes are analyzed both theoretically and experimentally. In addition to the operating regimes described previously, a bidirectional regime is observed, where the two counterpropagating modes undergo harmonic alternate oscillations.

Defined mixing of clockwise and counterclockwise ring laser modes of two ring lasers fabricated in InGaAs/GaAs/AlGaAs is used in Cao et al. (2005) to obtain frequency beating. The application of such integrated circuits is in ring laser gyros and optical rotation sensors. The ring lasers in the form of racetracks have a radius of 1 mm and a straight section length of 2 mm. Clockwise and counterclockwise operation is achieved by integrated absorbing spiral elements coupled to the ring waveguide located inside one ring and on

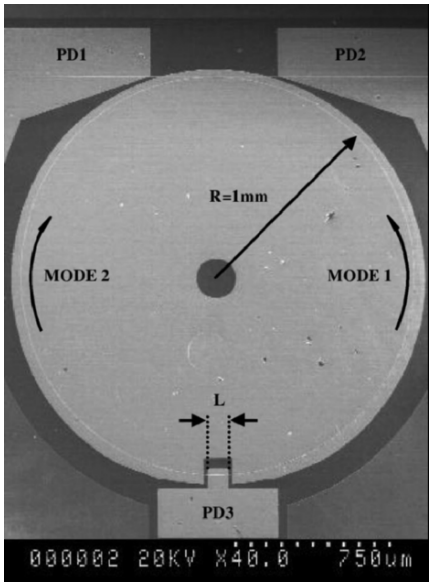

Fig. 5.75. Ring laser with contact pad layout.

Reprinted with permission from IEEE Journal of Quantum Electronics, vol. 39, pp. 1187–1195 ©2003 IEEE

the outside of the other ring. Tunability of the lasing wavelength of each ring is realized by integrated heaters.

Single mode ring resonator laser operation using two coupled active ring lasers is demonstrated in Hamacher et al. (2003). The ring lasers are fabricated in the GaInAsP/InP material system. A photograph of the device is shown in Fig. 5.76.

The ring laser consists of two coupled ring resonators having a radius of 50 µm. The ring resonators, the couplers and the bus waveguides can be driven independently by separate electrical contacts. Each ring resonator laser generates an individual slightly shifted comb like laser spectrum with respect to the driving current. Wavelength tuning to specific single mode emission is achieved using the Vernier effect. A measured single mode spectrum of the double ring laser configuration is shown in Fig. 5.77. A high side mode suppression ratio of >40 dB and a maximum output power of 6.5 mW per facet at a driving current of 250 mA is obtained.

A single mode ridge waveguide (RW) laser coupled to two ring resonators using MMI couplers also in the material system GaInAsP/InP has been realized and demonstrated in Bach et al. (2003). The layout of the device is shown in Fig. 5.78.

The diameter D_1 and D_2 of the ring resonators is 50 µm and 60 µm, respectively, leading to an overall FSR of 18 nm. The FSR of the ridge waveguide

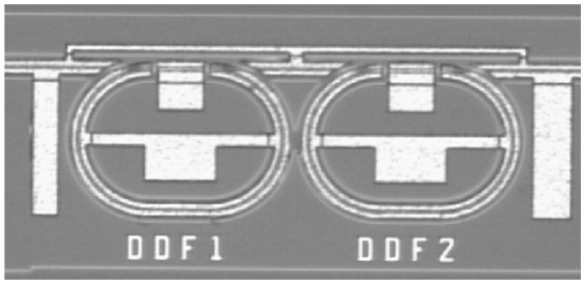

Fig. 5.76. Single mode operating double ring laser

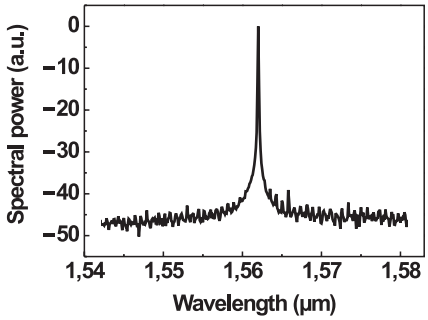

Fig. 5.77. Single mode output spectrum of a double ring laser

Fabry–Perot cavity is 0.5 nm and is small compared to the FSR of each of the ring resonators. Therefore only the FSRs of the ring resonators will contribute to the mode selection. The width w of the ridge waveguide is 4 μm. The facet width e inside the ring resonators is given by

$$e = \sqrt{2} \cdot w. \tag{5.14}$$

The ring resonators are not metal contacted and are only pumped through the straight ridge waveguide by a lateral carrier flow over the cap layer. A measured spectrum of such a double ring resonator laser is given in Fig. 5.79.

Ring lasers have been made with deeply etched structures to provide a stronger confinement of the optical mode in the waveguide. This, however, comes at the price of higher threshold currents due to surface recombination and scattering losses. Another drawback is the fact that deeply etched structures lase in multiple lateral modes because of the large index step. Other types of waveguide designs used for realizing ring lasers like ridge waveguides or buried heterostructures with small index steps exhibit a better lateral mode confinement and have lower threshold currents. A detailed analysis of the lateral and longitudinal mode discrimination of ring lasers is presented in Nabiev et al. (1993).

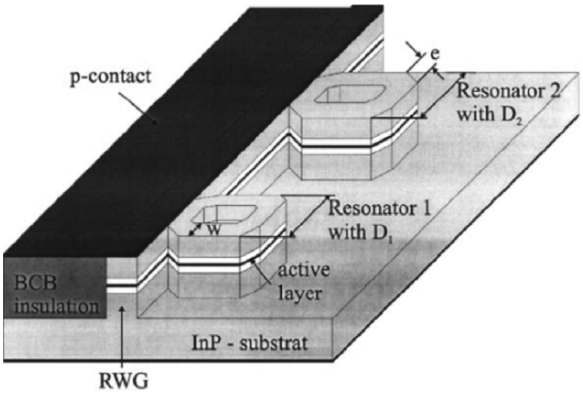

Fig. 5.78. Layout of double ring laser. The ring resonators are also covered with BCB which is left out for illustration purposes.

Reprinted with permission from IEEE Photonics Technology Letters, vol. 15, pp. 377–379 ©2003 IEEE

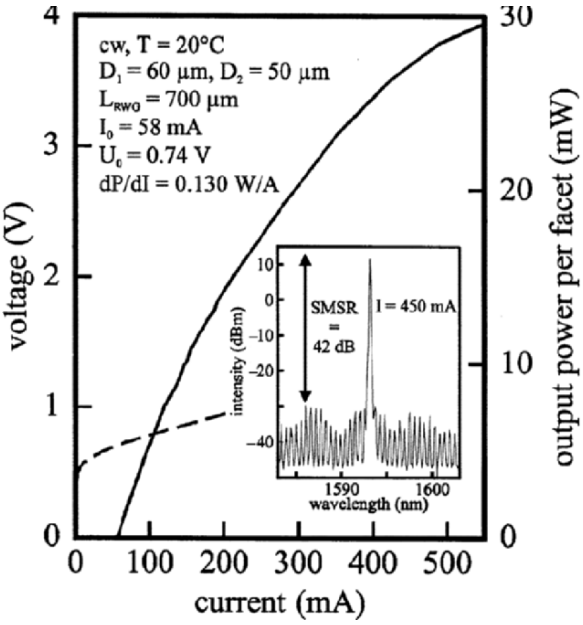

Fig. 5.79. cw laser characteristics at room temperature of a 700 µm long device with 50 and 60 µm ring resonators. The inset shows the emission spectrum at a drive current of 450 mA.

Reprinted with permission from IEEE Photonics Technology Letters, vol. 15, pp. 377–379 ©2003 IEEE

Ring lasers with different architectures (circular, square, and triangular ring cavities) and waveguide designs having a radius down to 50 µm have been described in this chapter. A theoretical comparison of photon recycling in circular, square, and triangular ring laser cavities is given in Numai (2000).

Smaller devices have been fabricated by several groups and examples are given in Sect. 6.3.

5.6.2 Devices with Gain Section

Merits of integrated ring resonators have been pointed out throughout this book. This chapter demonstrates again some of them, like the integration capability with active sections to enhance the characteristics of ring lasers.

One of the first integration of an SOA with passive silica waveguides and coupler is demonstrated in Hibino et al. (1992). The gain in the ring resonator consists of a GaInAsP buried heterostructure SOA. The facets of the SOA are coated with antireflecting films made from SiO. Both facets of the SOA are coupled to lensed optical fibers with a lens radius of 7 µm. The SOA module is inserted into the passive integrated silica ring resonator using etched fiber grooves. The size of the module is 1.2 mm × 1.2 mm × 3 mm. The fibers are fixed to the passive waveguides using an UV curable resin. The total resonator length is 10.2 cm leading to an FSR of 2 GHz at a wavelength of 1.3 µm. A comb like lasing spectrum is obtained with a threshold current of only 17 mA. The device is temperature stabilized with a Peltier cooler.

An active resonator with passive Y-coupler and outcoupling waveguides has been realized in the material system InGaAs-GaAs in Cockerill et al. (1994). The ring laser is made out of strained-layer InGaAs–GaAs buried heterostructure waveguides. The integration of the passive Y-coupler is made by selective area growth. The radius of the ring laser is 200 µm. The facets are antireflection coated to avoid back reflections. The laser operates at a wavelength around 1 µm with a threshold current of 25 mA. A side mode suppression of 24 dB is achieved.

Passive circular sections, an SOA and a saturable absorber in the material system GaInAsP are used in Ohno et al. (2002) to fabricate a modelocked ring laser. The radius of the curved sections is 100 µm. Modelocking at frequencies of 29.5, 41.2, and 61.7 GHz is obtained for three different devices with corresponding SOA lengths of 1,000, 650, and 300 µm and saturable absorber lengths of 30, 20, and 20 µm, respectively. An MMI coupler is used for output coupling.

Ring lasers with MMI output couplers have been showed to have superior operation characteristics to devices with Y-junction couplers (examples have been given in this chapter and in the previous chapter for both coupling versions). A further improvement in performance of MMI coupled ring lasers as suggested in Pennings et al. (1994) is by the use of a single active gain section in the ring, and making the MMI coupler and outcoupling waveguides of passive waveguide material.

The realization of a racetrack shaped ring resonator laser employing an SOA as the gain element, where the input and output waveguides, the MMI coupler and the curved ring sections are made out of passive material is described in the following paragraph. The passive waveguide is made from quaternary GaInAsP with a bandgap wavelength of 1.06 µm. The ring radius is 117 µm. The length of the MMI coupler is 150 µm. The fabrication details and the layer sequence of the passive waveguide have already been described in Chap. 3. A photograph of the ring laser with integrated SOA is shown in Fig. 5.80.

A standard ridge waveguide laser structure was used for the 500 µm long SOA section, which required an additional epitaxial growth step. The SOA is butt-coupled to the passive waveguide using a self-alignment process. The detail of the SOA as well as the fabrication process has been described in detail in Chap. 3.4.7. The butt coupling losses have been determined to be <2 dB each. The facets of the input and output waveguides have been antireflection coated. The ring laser has been designed to have an FSR of 50 GHz. The ring laser is operated at $T = 17°\mathrm{C}$. The lasing spectrum was measured using a tapered fiber and an optical spectrum analyzer. The relationship between the lasing power in the fiber and the injection current in the SOA is shown in Fig. 5.81.

The threshold current is as can be seen from the diagram as low as 25 mA. The kinks in the L–I curve of the ring laser are accompanied by mode-hops and can be explained by coupled cavity effects, the second cavity being formed by the output path which includes the MMI coupler (Krauss et al. 1995a). The kinks have also been observed for fabricated ring lasers which do not have an antireflection coating on the facets of the outcoupling waveguides. The SOA does not form a cavity with the butt-joints. This has been verified by using a straight waveguide with integrated SOA (Fig. 5.82) where the input and output waveguides have been antireflection coated.

No lasing has been observed in such a device with a 500 µm SOA. An interesting feature observed was that the same threshold current of 25 mA

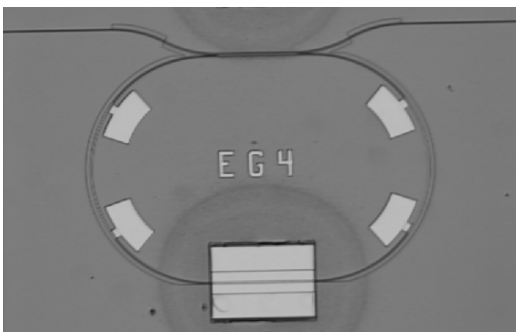

Fig. 5.80. Photograph of a ring resonator laser with integrated SOA

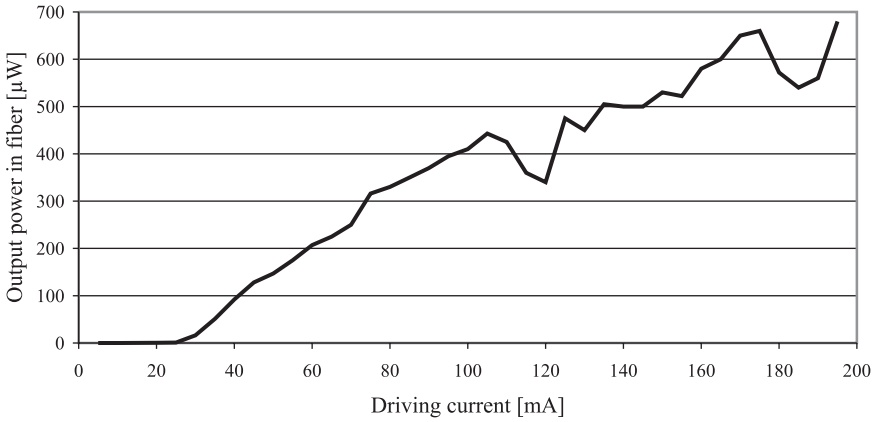

Fig. 5.81. Output power characteristic of a racetrack laser

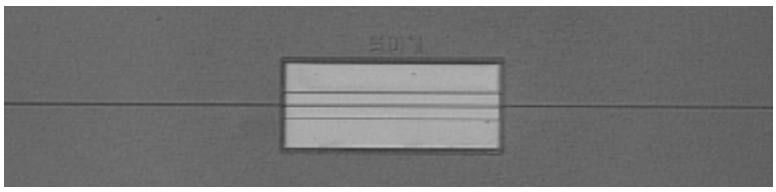

Fig. 5.82. Photograph of a straight passive waveguide with integrated SOA

is obtained for a device which was not antireflection coated (Fig. 5.83). The measurement has been performed monitoring the output power directly using a photodiode. If Fig. 5.83 is compared to the output power characteristic of the ring laser (Fig. 5.81), the fiber–chip coupling loss which has been determined to be ∼5 dB, has to be improved. This can be done for example by using a vertical taper.

In the output power characteristic there are no kinks visible which leads to the assumption, that the kinks in the ring laser L–I curve are mainly attributed to the output path which includes the passive waveguides and the MMI coupler. This also indicates that the threshold current is only dependent on the butt-joint losses. The curved waveguide sections have negligible bending losses.

The lasing spectrum of the racetrack laser at a drive current of 162 mA is shown in Fig. 5.84. An Advantest optical spectrum analyzer Q8384 with a maximum resolution of 10 pm in this wavelength range is used. The measured FWHM is therefore smaller than 1.25 GHz. The total power in the fiber is 0.6 mW per facet. As can bee seen from the lasing spectra, the side mode suppression ratio (SMSR) is 45 dB. The spectrum shows the designed FSR of 50 GHz of the ring resonator.

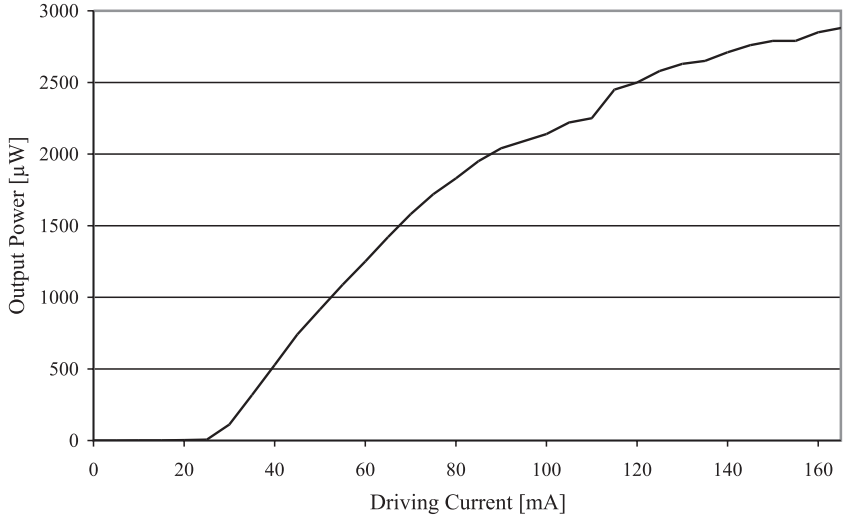

Fig. 5.83. Output power characteristic of a straight waveguide with integrated SOA without antireflection coated input and output passive waveguides

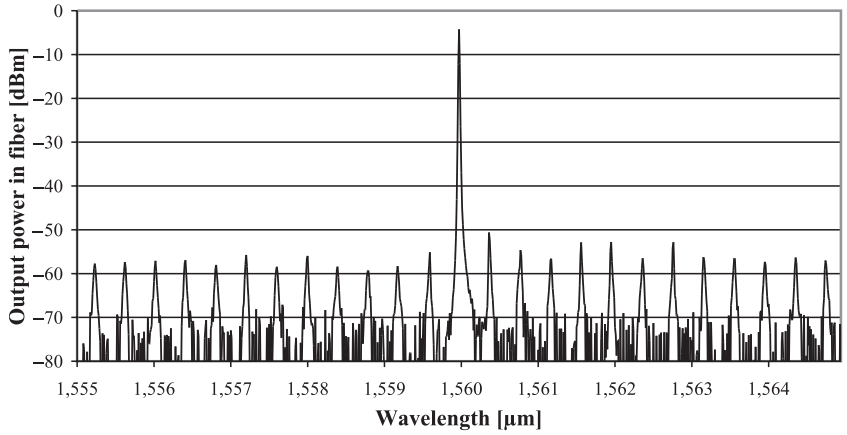

Fig. 5.84. Lasing spectra of a racetrack laser at a drive current of 162 mA, showing single mode operation with SMSR = 45 dB

The lasing spectra covering the entire 50 nm gain spectrum is shown in Fig. 5.85. It can be clearly seen that there is only one lasing mode.

Ring lasers fabricated by a combination of active and passive waveguide sections enable the lowering of the threshold current as compared to all active devices, where the whole structure needs to be electrically contacted. Special attention has to be made when joining active and passive elements. Mode field profiles of both waveguides have to match as close as possible to minimize transition losses.

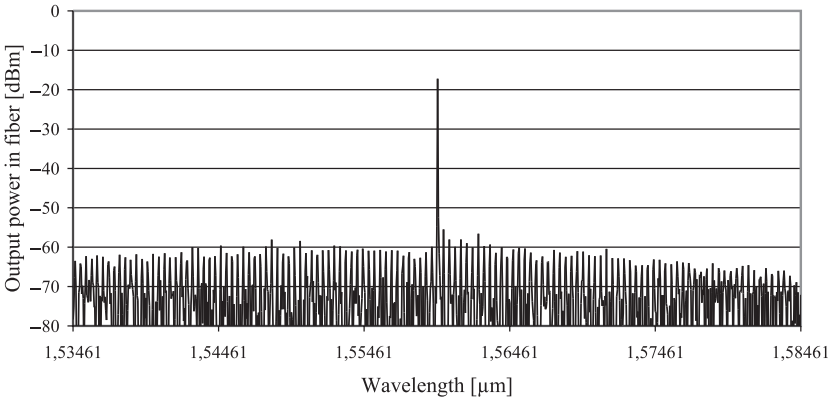

Fig. 5.85. Lasing spectrum of a racetrack laser showing single mode operation over a 50 nm gain spectrum

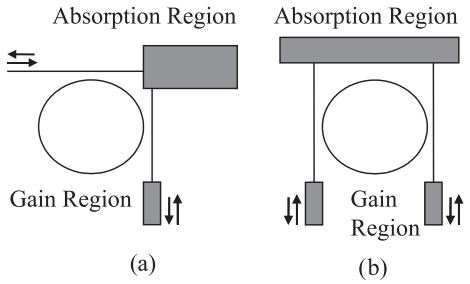

Fig. 5.86. Examples of passive ring resonator coupled lasers

5.6.3 Passive Ring Resonator Coupled Lasers

Ring resonator coupled lasers are different from the ring lasers in the previous chapter as the gain medium is placed outside the ring resonator cavity. Passive ring resonators serve as optical filters which enable single mode operation and tunability of the laser. Several examples including different architectures are described in this chapter.

Ring resonator coupled lasers offer many promising advantages over conventional tunable lasers, including ultra wide wavelength tuning range, high side mode suppression ratio, uniform threshold and efficiency, narrow linewidth, and low frequency chirp. The integration of active gain sections, passive waveguides and ring resonators forming a ring resonator coupled laser has recently been proposed and analyzed in Liu et al. (2001). A schematic of the two proposed architectures is shown in Fig. 5.86.

A detailed analysis of a single passive ring resonator coupled laser having a design like the one shown in Fig. 5.86b, with only one gain region as the output waveguide (the other waveguide is also passive like the ring) is given in Bian et al. (2003).

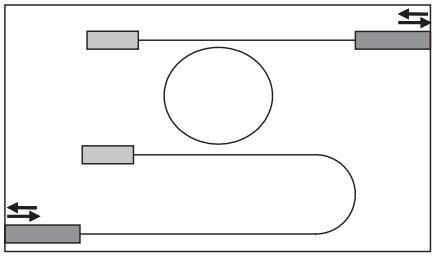

Fig. 5.87. Ring resonator coupled laser

One of the first fabricated passive single ring resonator coupled lasers is presented in Park et al. (2002). A schematic of the layout of the device is shown in Fig. 5.87. One material is used for the ring coupled laser. The ring is operated in a transparent mode. Only the waveguides at the facets introduce gain into the device. The waveguides not leading to the facets act as absorbers. The ring coupled laser is made using the material system GaInAsP on InP. Three types of devices having a radius of 5, 10 and 20 µm are fabricated. The width of the waveguides is 0.4 µm. Directional couplers with a coupling gap of 0.2 µm are used. The bus waveguides are tapered to a width of 2 µm having a taper length of 200 µm. The FSR of the ring resonator is chosen large enough that a resonance is in the middle of the gain spectrum to achieve single mode operation. The threshold of the laser is 70 mA under pulsed operation. The lasing wavelength is measured to be 1.549 µm.

In order to achieve single mode operation, the radius of the ring resonator has to be small, in the order of 10–20 µm. Another way to achieve single mode operation using passive coupled ring resonators is by using a double ring architecture. The ring resonators have slightly different radii which leads to an increase of the overall FSR as was described in Chap. 2. Passive double ring resonator coupled lasers (DR-RCLs) are analyzed theoretically in Liu et al. (2002a).

A double ring coupled laser is demonstrated in Rabiei and Steier (2003) using an integrated tunable polymer double ring filter, fiber coupled to an erbium-doped fiber amplifier, serving as the gain medium. Thermo-optic and electro-optic tunable devices are presented. The layer sequence of the device as well as the fabrication is similar to the ones described in Chap. 3. The radius of the ring resonators is 240 and 246 µm. The overall obtained FSR is approximately 39 nm at a wavelength of 1,550 nm. A layout of the double ring resonator structure is shown in Fig. 5.88.

One of several advantages of using a double ring resonator is the possibility of a higher tuning enhancement factor using the Vernier effect. The tuning enhancement factor is given by

$$T = \frac{1}{1 - \dfrac{L_1}{L_2}} = \frac{R_2}{R_2 - R_1}, \tag{5.15}$$

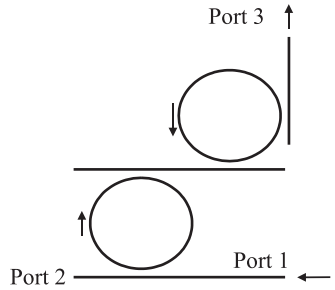

Fig. 5.88. Layout of double ring resonator structure

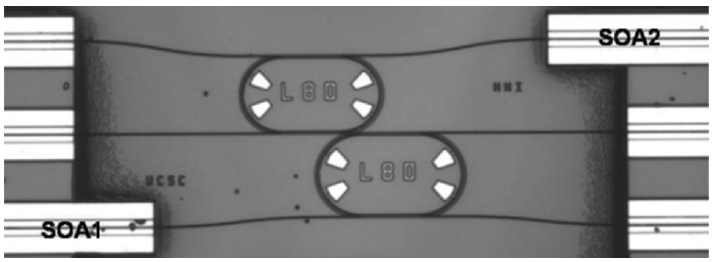

Fig. 5.89. Photograph of a DR-RCL

where L_1 and L_2 are the cavity lengths of each ring and R_1 and R_2 the radius, respectively. The tuning range of a double ring resonator is T times the tuning range of a single ring. The polymer double ring resonator configuration has a tuning enhancement factor of 40. The transmission experiments are performed using TM polarized input light, fed to the input port of the double ring resonator from an erbium doped fiber amplifier which serves as the gain medium. An output power of 1 mW and a side mode suppression ratio of 30 dB are measured for both the thermo-optic and the electro-optic device.

One of the first integrated double ring resonator coupled lasers in GaInAsP combining passive ring resonators with integrated SOAs is presented in Rabus et al. (2005a). A photograph of a DR-RCL is shown in Fig. 5.89. The layer sequence and the dimensions of the waveguides are the same as is described in Chap. 3 for the passive ring resonator and the integration of an SOA into the ring cavity.

Two configurations of DR-RCLs are investigated and the radii of the rings are 100 and 108 µm for the first configuration and 100 and 104 µm for the second configuration. An FSR of approximately 15 and 30 nm is obtained respectively. The coupling between the bus waveguides and the ring resonators is realized by a codirectional coupler with a length of 500 µm and a coupling gap of 1 µm. The coupling from the bus waveguide to the ring depends critically on the separation. The achieved splitting ratio is 3 dB. The laser cavity consists of SOA1 and SOA2 (see Fig. 5.89) which have a length of 500 µm each and

the two ring resonators. The chip length is 2 mm. The remaining SOAs are not biased and they are used as absorbers to suppress the lasing of sub cavity modes. The end facets of the chip are as cleaved and are uncoated, which could be improved to increase the performance in the future. The output of the DR-RCL is collected using a tapered fiber at SOA2.

The spectrum of the DR-RCL with an FSR of 15 nm is shown in Fig. 5.90, when the driving currents for SOA1 and SOA2 are 110 and 90 mA, respectively. Due to the fact that the FSR of the double ring resonator does not cover the entire gain spectrum, another lasing mode is present. The power difference between the two lasing modes is 13 dB. The threshold of the DR-RCL is about 30 mA when SOA1 is biased above 40 mA.

The spectrum of the DR-RCL with an FSR of 30 nm is shown in Fig. 5.91. A side mode suppression ratio of >35 dB is obtained which is limited by the dynamic range (−35 dB) of the used optical spectrum analyzer (OSA). The linewidth of the lasing wavelength is also limited by the bandwidth of the OSA which is 0.06 nm. From calculations, the linewidth is estimated to be <2 MHz. The driving currents for SOA1 and SOA2 are 100 and 90 mA, respectively.

The output power varies with the currents supplied to SOA1 and SOA2 (Fig. 5.92). The threshold of the DR-RCL is about 25 mA when SOA1 is biased above 40 mA.

An output power exceeding 1 mW is demonstrated in Bian et al. (2006). The resonance wavelength of the rings can be tuned by the integrated platinum resistors on top of the passive waveguides in the ring resonators. Varying the current of one heater results in a shift of resonance wavelength of the corresponding ring resonator due to the thermo-optic effect and the lasing can jump from one mode to the next one where the transmission peaks of the double ring resonators overlap. Figure 5.93 shows a series of lasing spectra when varying the heater current between 0 and 30 mA. When the current of

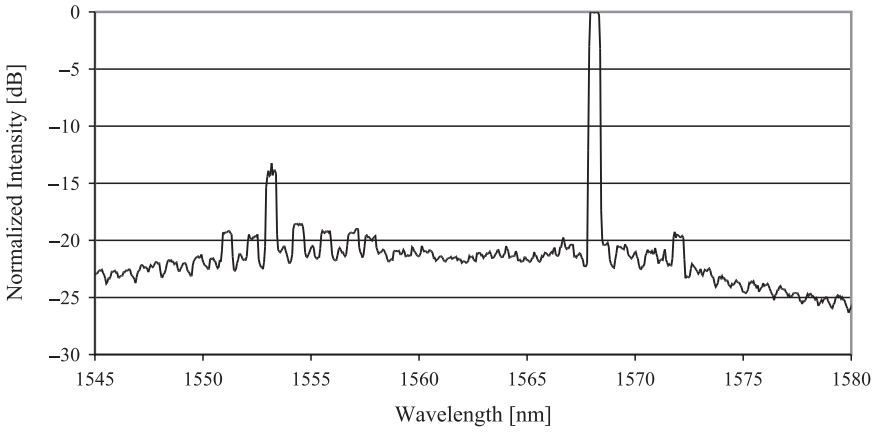

Fig. 5.90. Spectrum of a DR-RCL with an FSR of 15 nm

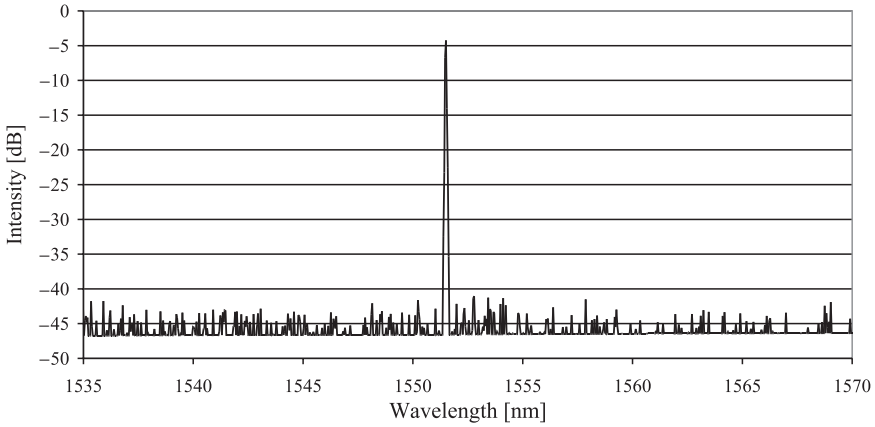

Fig. 5.91. Spectrum of a DR-RCL with an FSR of 30 nm

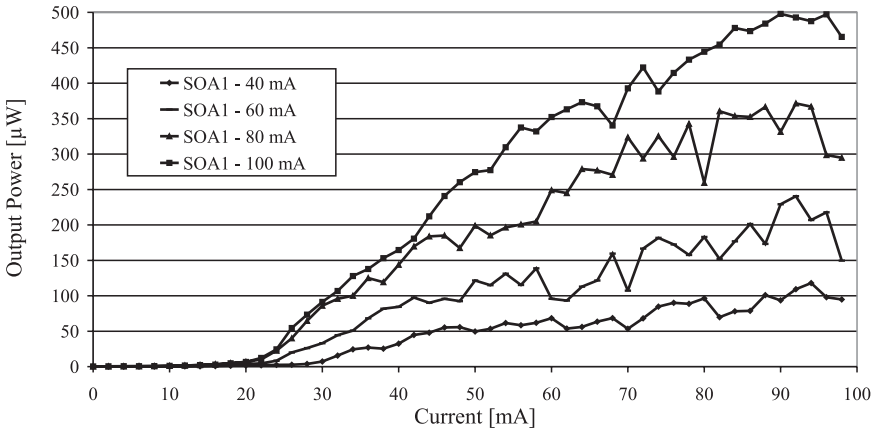

Fig. 5.92. PI-curve of the DR-RCL with an FSR of 30 nm changing the current at SOA2

the integrated heater is changed, the laser produces 20 different modes, which are spread uniformly over a 17 nm wavelength range.

Another architecture for a double ring resonator coupled laser is analyzed theoretically in Chung et al. (2005). The device consists of a coupled ring reflector and an active straight waveguide providing lasing activity. A schematic of the proposed device is shown in Fig. 5.94.

The properties and formulas describing the behavior of coupled ring reflectors have been addressed in Chap. 2. The radius of the ring resonators is chosen to be different enabling a larger FSR for the coupled device utilizing the Vernier effect. Two different ring radii enable an enhanced tuning factor as is described in this chapter. The reflective properties are obtained by allowing inter ring coupling.

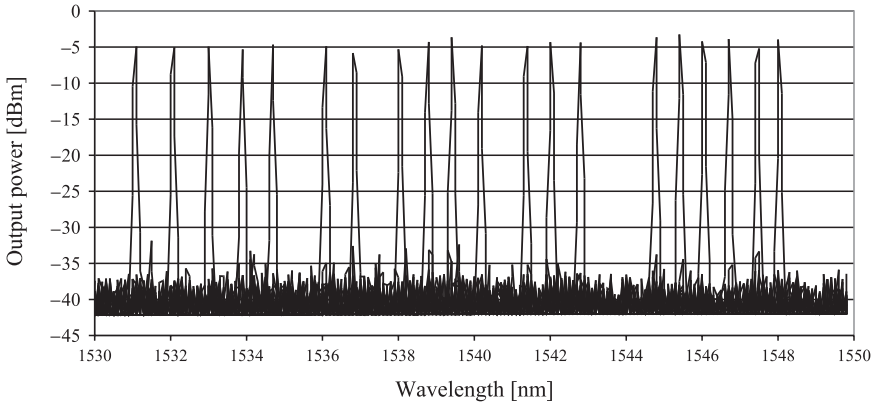

Fig. 5.93. Wavelength tuning by applying a current between 0 and 30 mA to the integrated Platinum heater

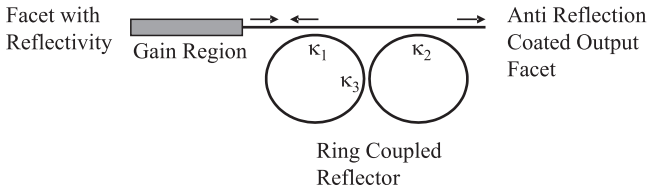

Fig. 5.94. Schematic of a ring resonator reflector coupled laser

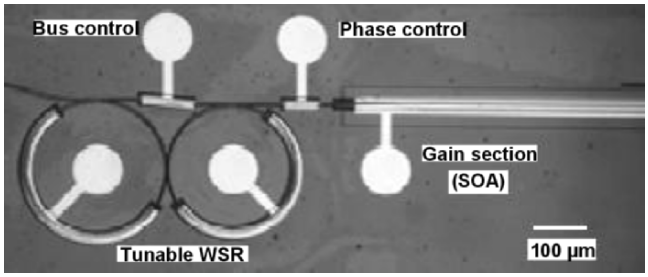

Fig. 5.95. Photograph of a fabricated coupled ring reflector laser. (Photograph courtesy of Prof. Dapkus[3])

A tunable laser based on a coupled ring reflector laser is fabricated and demonstrated in Choi et al. (2005). The device is fabricated by using a buried heterostructure waveguide design in the material system GaInAsP/InP. A photograph of the device is shown in Fig. 5.95.

[3]University of Southern California, Department of Electrical Engineering – Electrophysics, VHE 314, Vivian Hall of Engineering, Los Angeles, CA 90089, USA

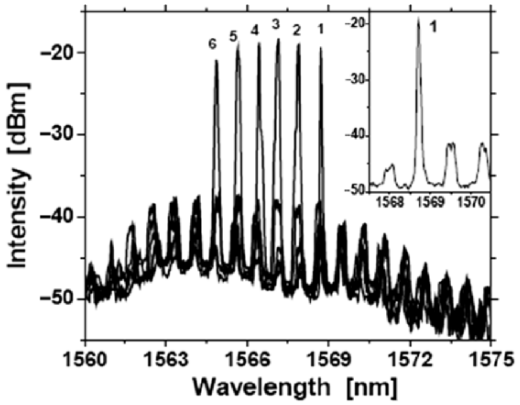

Fig. 5.96. Measured tuning characteristics. (Photograph courtesy of Prof. Dapkus)

The radius of the used ring resonators is 130 and 140 µm, giving an FSR for each of the rings of 0.8 nm and 0.75 nm. The overall FSR is determined to be 12 nm. Tuning of the device is realized through the free carrier injection (FCI) method which shifts the resonance wavelengths by the free carrier plasma effect. The tunability of the device is shown in Fig. 5.96. Carriers are injected into the ring resonator having an FSR of 0.75 nm leading to a shift of the resonance wavelength of 0.8 nm which corresponds to 100 GHz at a wavelength of 1,550 nm.

Examples of ring resonator coupled lasers with different architectures have been presented in this chapter and due to this relative new research field, an improvement of the device parameters is expected in the coming years. Technological progress will also add to advancement in device performance.

Ring resonator based devices both active and passive can be used for wavelength conversion as will be demonstrated in the following section.

5.7 Wavelength Converters

The four wave mixing (FWM) effect can be applied to passive and active ring resonators, enabling efficient wavelength conversion for all-optical communication systems. Ring resonators based on GaAs or InP combine both advantages of a high nonlinear susceptibility and a high linear gain. In contrast to other active resonant structures like distributed feedback (DFB) lasers or SOAs, ring resonators enhance both, the optical power of the signal wavelength at frequency ω_S and that of the converted wavelength at ω_C. Maximum conversion efficiency is achieved, when ω_S and ω_C fit one of the resonance wavelengths of the ring resonator. No stop-band has to be taken into account. Operating at wavelengths not being one of the resonance wavelengths of the ring resonator results in a reduced conversion efficiency. The internal optical

field enhancement and the FSR can be designed by the radius and the power coupling ratio between the ring resonator and the bus waveguides.

A passive GaAs racetrack shaped ring resonator is used in Absil et al. (2000a) to demonstrate wavelength conversion by four wave mixing with an improved conversion efficiency compared to a straight waveguide. A photograph of the device is shown in Fig. 5.97. The increase in efficiency is attributed to the increase of the interaction length and the enhancement of optical power inside the ring resonator cavity. Optical propagation losses limit so far the overall performance. A spectrum of the FWM measurement is shown in Fig. 5.98. The ring resonator used in the experiment has a radius of 4.2 µm. A coupling strength of 0.27 is obtained for the directional coupler.

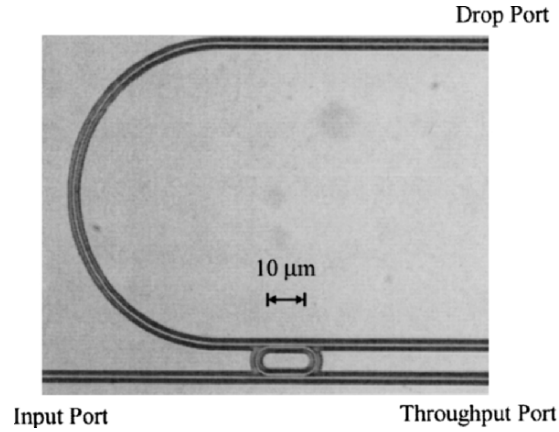

Fig. 5.97. Optical micrograph of a racetrack-shaped resonator with defined ports.

Reprinted with permission from P.P. Absil, Optics Letters, vol. 25, no. 8, pp. 554–556 ©2003 Optical Society of America

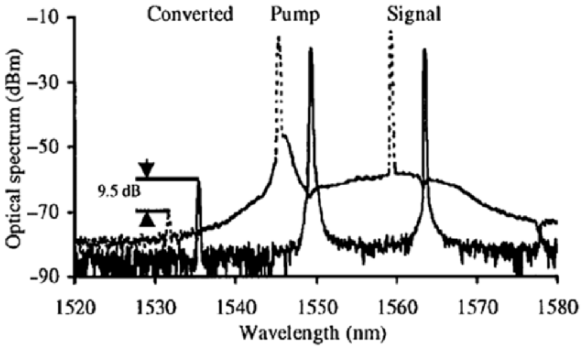

Fig. 5.98. Optical spectra for on-resonance (*solid curve*) and off-resonance (*dotted curve*) cases.

Reprinted with permission from P.P. Absil, Optics Letters, vol. 25, no. 8, pp. 554–556 ©2003 Optical Society of America

The properties of an all-optical wavelength converter with reshaping characteristics, based on FWM in a passive GaAs–AlGaAs ring resonator notch filter are investigated in Mikroulis et al. (2004). A detailed theoretical analysis of the static and dynamic reshaping characteristics of the wavelength converter is carried out.

Improved conversion efficiency is expected in ring resonators fabricated as all-active ring resonators. An active ring resonator architecture used for wavelength conversion is demonstrated in Hamacher et al. (2003). A photograph of an electrically contacted ring resonator is shown in Fig. 5.99. The ring resonator has a radius of 182 µm including two 160 µm long MMI couplers which can be electrically driven separately to couple the light from the straight bus waveguide into the ring and vice versa.

In analogy to FWM in DFB lasers the ring cavity itself can be used as the pump signal source. A proper choice of the driving currents provides a sufficient side mode suppression ratio of greater than 35 dB. An ECL acting as a cw signal source is used in the FWM experiment. The result of this experiment with a cw output power of 2 dBm measured in the feeding fiber is shown in Fig. 5.100. A conversion efficiency of −5 dB is derived from the measurement of the output power. Taking into account that the input signal will be increased due to the high power enhancement of the active ring structure, the conversion efficiency can be corrected by a factor of 8 dB, resulting in an "effective" conversion efficiency of 3 dB.

Instead of selecting a single mode laser spectrum by using a ring resonator with a small radius and/or a proper choice of driving currents as mentioned in the previous example, it is also feasible to obtain a mode selection by injection locking. If the frequency of the master laser (in the test set-up a second ECL, amplified by an erbium-doped fiber amplifier) is close enough to the ring resonator's free-running frequency and the signal amplitude is large enough, the device is locked to the master frequency over a certain bandwidth. This

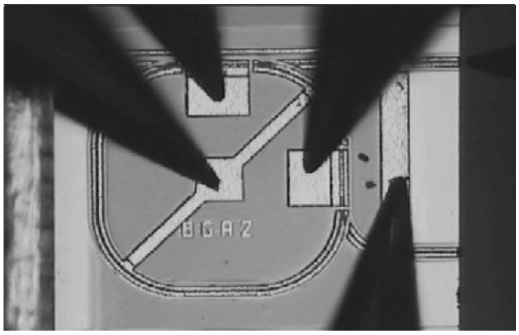

Fig. 5.99. All active ring resonator

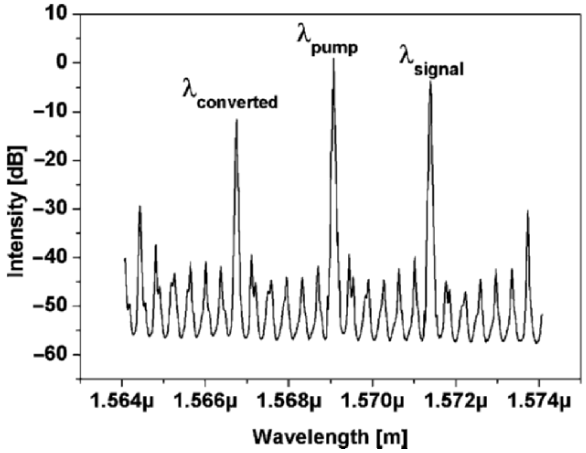

Fig. 5.100. Optical cw spectrum measured at the throughput port exhibiting a conversion efficiency of −5 dB (relation of the intensities in the feeding fibers)

approach may be favored for practical use in a real system in order to realize a well controlled resonator of specified FSR for FWM and to control the pump signal by injection locking in a separate device (master laser).

To demonstrate the FWM capabilities of an all active device, an all-optical cw channel switching experiment is performed. In this experiment the cw signal at ω_S is kept fixed at a resonance wavelength of the ring resonator of 1567.9 nm. For maximum conversion efficiency the injection locked pump wavelength ω_P is chosen to fit one of the resonances of the ring resonator. When the detuning of the pump wavelength is changed stepwise by multiples of the FSR, the converted signals at $\omega_C = 2\omega_P - \omega_S$ fit the resonances of the ring resonator as well. In this way the conversion efficiency can be kept at a maximum level over a tuning range of multiples of the FSR, which is verified in the experiment. Due to a high coupling factor of 0.7, the enhancement effect of the ring is limited and a conversion efficiency of approximately −20 dB is obtained. The result of the measurement is shown in Fig. 5.101, where λ_C is the converted wavelength, λ_P is the pump wavelength and λ_S is the signal wavelength.

Wavelength conversion can also be performed using passive ring resonators with integrated SOAs (Fig. 5.80) as the pump laser and inserting a signal wavelength into the bus waveguide placed on a resonance of the ring resonator. A spectrum of the ring resonator operating as a laser without signal and pump wavelength is shown in Fig. 5.102. The result of an FWM experiment using this racetrack shaped ring resonator with integrated SOA is shown in Fig. 5.103. The ring resonator has a radius of 117 µm. A directional coupler with a gap of 1 µm and a length of 150 µm is used for coupling into and from the resonator. The overall FSR is 0.4 nm which corresponds to 50 GHz at a

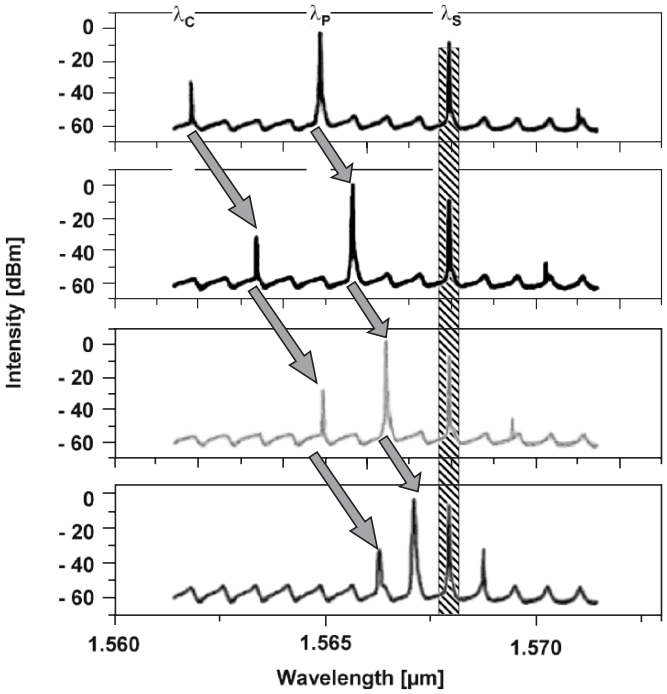

Fig. 5.101. All optical channel switching experiment in cw operation using injection locking. The signal wavelength is fixed and the pump wavelength routes the conjugated signal

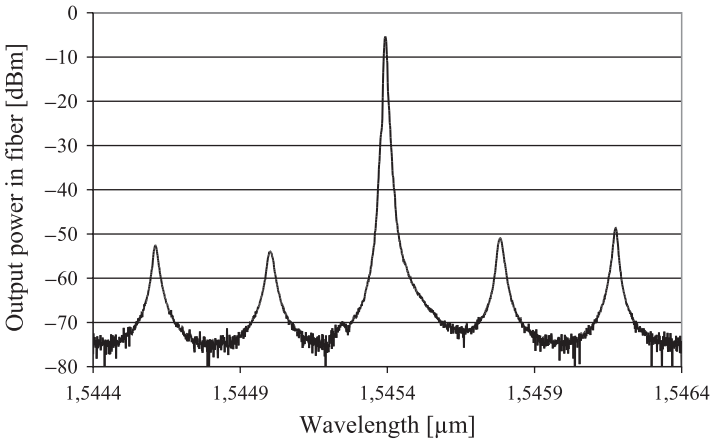

Fig. 5.102. Passive ring resonator with integrated SOA in laser operation

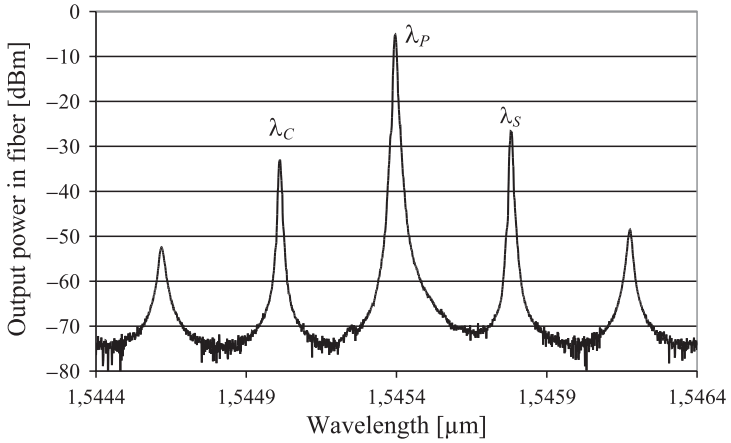

Fig. 5.103. FWM in a ring resonator with integrated SOA

wavelength of 1,550 nm. A conversion efficiency of approximately −6 dBm is achieved. The driving current for the SOA is 119 mA. The signal wavelength is inserted into the ring resonator from an ECL which is amplified by an erbium doped fiber amplifier (EDFA) to a total signal power of 3 mW.

Wavelength conversion using integrated ring resonators is a relative novel research direction as it requires either low loss passive ring resonators or active devices to achieve comparable conversion efficiencies as if using straight SOAs for example. This chapter proves again the versatility of ring resonator devices.

In the following chapter, an emerging field will be introduced with several practical examples: optical signal processing using ring resonators.

5.8 Optical Signal Processing

Optical signal processing (OSP) is one of the research areas which are receiving an increasing amount of interest from the all-optical network community. In OSP, light is used to influence, switch and control light. OSP has several advantages compared to electrical signal processing. One of them is the higher processing speed, which has been demonstrated to be as high as 100 Gbit s^{-1}. Elements used for OSP can be fabricated with current state-of-the-art technologies and are easier to be realized than compared to similar solutions in electrical signal processing. Several books can be found dealing with the fundamentals of OSP.

The focus in this chapter is on integrated ring resonators in optical signal processing. Ring resonators can be used for realizing all-optical switches, multiplexers, and logic gates.

5.8.1 Logic Gates

All-optical logic gates have evolved in the last couple of years and have received considerable attention. Examples of potential applications in optical signal processing systems are optical bit-pattern recognition, bit-error rate monitoring, payload separation and all-optical packet addressing.

One of the most obvious applications of ring resonators in connection with logic gates is the use as optical delay lines. In optical logic gates, control signals need to be overlapped in time with incoming data signals. As was shown in an earlier chapter, ring resonators used as all pass filters can address this application. Optical delay lines can also serve as an optical buffer to delay signals until the system is ready to process them. A detailed analysis of all pass filters used as optical delay lines is given in Lenz et al. (2001). Multiple coupled all pass filters are investigated theoretically in Azaña and Chen (2002) for optical signal processing applications, especially for real-time Fourier transformation (RTFT) and pulse repetition rate multiplication (PRRM).

Optical signal processing using fabricated nonlinear integrated ring resonators is presented in Van et al. (2002a). Applications of the ring resonators to switching, time-division demultiplexing, pulse routing, and wavelength conversion (see Sect. 5.7) using four wave mixing are demonstrated. The authors also propose architectures for realizing OR, AND, and XNOR optical logic gates with ring resonators. A schematic of the proposed logic gates is shown in Fig. 5.104.

The used input signals A, B, and C are tuned to resonances of the ring resonator. Signal C can be regarded as a constant bias to the gate in the case of asynchronous operation, or as a clock in the case of synchronous operation. In the case of the OR and AND gate, the signal wavelength C is not detected at the output D when signals A and B are not inserted. In the XNOR configuration, the MZI is balanced only when signal C is present, leading to a signal at output D. In all three configurations, a bandpass filter (BPF) only allows the wavelength λ_{out} to pass through.

In the OR configuration, signal C is brought off-resonance by either signal A or B which can then be detected at output port D. In the AND configuration, both signals A and B need to be present for signal C to be off-resonance so that it can be detected at output port D. In the case of the XNOR gate, signal C will be off-resonance either by the presence of signal A or B, inducing a π phase shift in the MZI and thus leading to destructive interference at output port D which means no signal is detected. A signal at output port D is detected on the other hand if both signals A and B are inserted into the gate, signal C is off-resonance, the MZI is balanced and signal C can be detected at output D. As described in Sect. 5.5, the speed of operation depends on the cavity ring-down time of the ring resonators.

All optical AND and NAND logic gates are demonstrated experimentally in Ibrahim et al. (2003b). The nonlinear effect used in the experiment is the change in refractive index from free carriers generated by two-photon

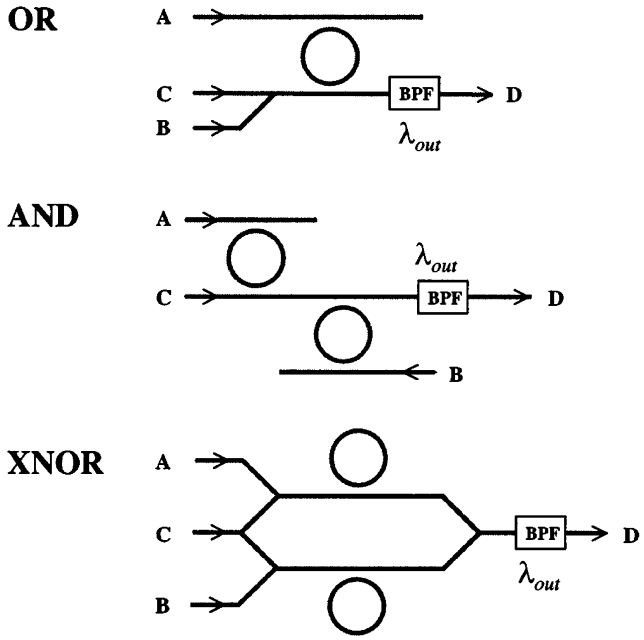

Fig. 5.104. Optical logic gates using ring resonators. Signals A and B are tuned to resonance wavelength λ_{in}; signals C and D are at resonance wavelength λ_{out}; BPF: bandpass filter.

Reprinted with permission from IEEE Journal of Selected Topics in Quantum Electronics, vol. 8, pp. 705–713 ©2002 IEEE

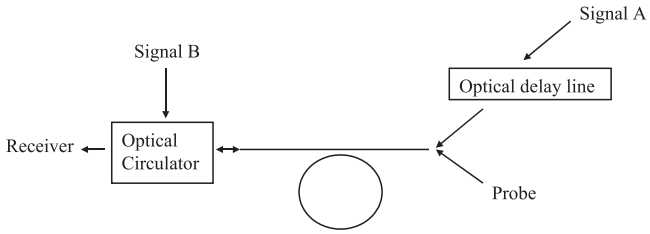

Fig. 5.105. Signal paths leading to AND/NAND operation in a racetrack shaped ring resonator filter

absorption. InP and GaAs-based racetrack shaped notch filters are used. The InP device has a radius of 10 µm and a 3 µm long straight section. A schematic of the signal paths is shown in Fig. 5.105. The intensity of the pump beams A and B are alone not strong enough to induce switching of the probe beam. The probe signal which is initially tuned to one of the resonance wavelengths of the ring resonator leading to a "0," is detected at the receiver when both input signals A and B are fed into the ring resonator corresponding to a "1."

When the probe beam is slightly "blue" shifted and out of resonance obtaining a "1," NAND gate operation is achieved when both input signals A and B are fed into the ring resonator leading to a shift of the probe beam into a resonance wavelength resulting in a "0" at the receiver.

The experiment using the InP device is performed with a mode-locked laser at 5.6 GHz, externally modulated at 140 MHz. The pump pulse has a pulsewidth of 35 ps and energy of 20 pJ. The result of the measurement demonstrating AND logic gate operation is shown in Fig. 5.106.

The GaAs sample, similar to the InP device, exhibits an FSR of 11 nm. A gain-switched laser diode at 8.4 GHz and externally modulated at 140 MHz, is used for the data source. The pump pulse energies of 80 pJ per pulse are inserted in to the input port of the device. The measurement of the device showing AND/NAND operation is given in Fig. 5.107.

An all optical AND logic gate based on the four wave mixing (FWM) effect is theoretically analyzed in Mikroulis et al. (2005). A GaInAsP ring resonator notch filter is used for the calculation with a cavity length of 69 μm.

Optical logic gates realized with ring resonator filters are a promising approach which has room for improvement in the future as smaller devices and material configurations are fabricated and investigated.

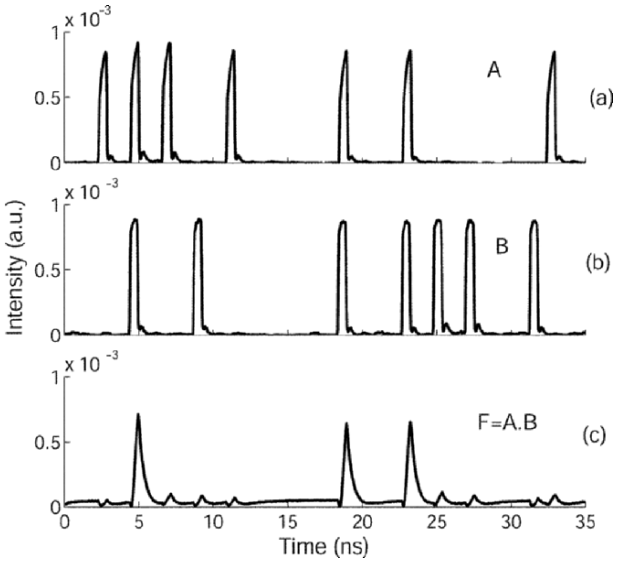

Fig. 5.106. Time traces showing an AND logic gate using the InP ring resonator: (**a**) "A" and (**b**) "B" are the two input pumps tuned to the resonance at 1,550 nm and (**c**) "F = A · B" is the output probe signal tuned to the next higher resonance at 1,560 nm.

Reprinted with permission from IEEE Photonics Technology Letters, vol. 15, pp. 1422–1424 ©2003 IEEE

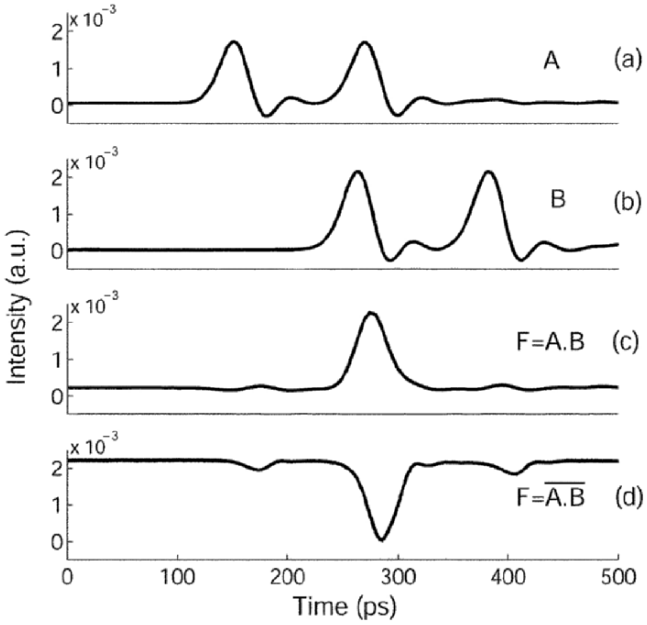

Fig. 5.107. Time traces showing logic operation using the GaAs resonator: (**a**) and (**b**) are the inputs "A" and "B" tuned to the resonance at 1,548 nm; (**c**) output "F" when the probe was initially in resonance at 1,559 nm; and (**d**) output "F" when the probe was initially blue tuned out of resonance at 1558.6 nm.

Reprinted with permission from IEEE Photonics Technology Letters, vol. 15, pp. 1422–1424 ©2003 IEEE

5.8.2 Switching

All optical switches rely on the control of light by light (the principle of optical signal processing) as was shown in the previous section for logic gates. In order to induce switching, an optical control signal is used to change the optical properties of a nonlinear medium. The device, in this case the ring resonator, then switches the data signal, which experiences the changed transmission properties when it passes through. In all-optical switches MZIs with SOAs have been used so far where the SOAs provide the nonlinear media. In the case of ring resonators, material systems providing nonlinearity are required which does not necessarily mean to introduce electrically contacted gain into the cavity. Ring resonators are ideal for optical switching as they have a high Q-factor and can be monolithically integrated. A high field enhancement and finesse in the ring can lower the switching threshold significantly.

One of the first experimental demonstrations of all optical switching in GaAs ring resonators is given in Van et al. (2002b). Switching is accomplished by a refractive index change in the ring resonator due to free carriers generated

by two-photon absorption. This switches the probe wavelength in and out of resonance. The radius of the used vertically coupled ring resonator notch filter is 10 μm. The parameters of the device are as follows: FWHM = 0.16 nm, Q-factor = 9,800, $F = 70$, calculated field enhancement factor = 7.3, calculated cavity lifetime = 40 ps. The switching experiment is carried out using an externally modulated laser diode, producing a 300 ps pump pulse signal with a 20 MHz repetition rate with an average input power of 10 mW. A 3 mW cw signal is used for the probe wavelength. The pump wavelength is slightly out of resonance whereas the probe signal is placed on a resonance of the ring resonator. The result from the experiment is shown in Fig. 5.108. Both pump and probe beams are inserted at the input port of the ring resonator via a fiber coupler. After passing through the ring resonator notch filter, the pump and probe beams are amplified and separated by a bandpass filter. Switching times of the probe beam of approximately 100 ps is observed.

A similar ring resonator geometry is used in Ibrahim et al. (2002) to demonstrate all-optical time division demultiplexing and spatial pulse routing. The radius of the ring resonator add–drop filter is 10 μm. The cavity lifetime of the ring is measured to be approximately 30 ps. Switching is again accomplished by a refractive index change induced by two-photon absorption.

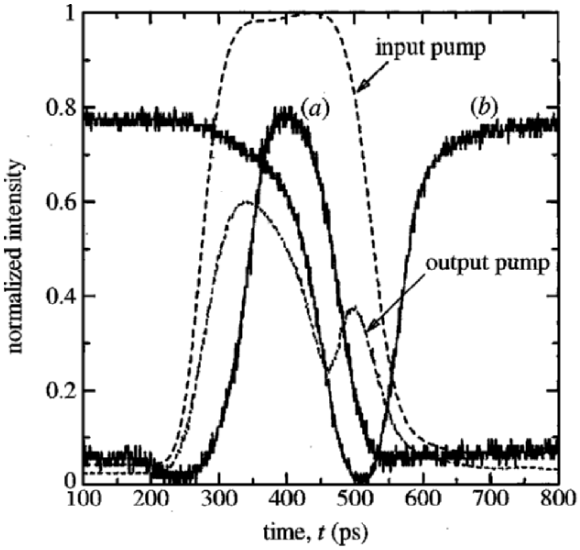

Fig. 5.108. Measured time traces of the pump-and-probe beam intensities with (**a**) probe beam initially on resonance (low transmission) and (**b**) Probe beam initially off-resonance (high transmission). The transmitted probe intensity is normalized with respect to the maximum transmittance at resonance.

Reprinted with permission from IEEE Photonics Technology Letters, vol. 14, pp. 74–76 ©2002 IEEE

A data pulse inserted into the ring resonator is demultiplexed and collected at the drop–port of the ring resonator filter. An on–off contrast ratio of 8 dB is achieved.

A detailed theoretical analysis of the nonlinear transfer functions of ring resonators is given in Blair et al. (2002). Ring resonators are compared to straight nonlinear sections of different lengths. Ring resonators are demonstrated to have a higher nonlinear phase shift induced by linear and two-photon absorption when compared to nonlinear straight devices. Based on the simulated results, a design for an MZI with integrated ring resonator is presented.

One of the first disk resonators with an electro-absorptive active region is presented in Djordjev et al. (2002f). The disk uses the quantum confined Stark effect (QCSE) to loss trim the frequency response of the resonator cavity. The disk vertically coupled to two bus waveguides has a radius of 10 μm, an FSR of 10.5 nm, a Q-factor of 5,700 and an F of 40. The transmission and dropped coefficients can be changed by introducing additional loss into the cavity at a particular wavelength. One advantage of using electro-absorptive ring or disk resonators is that the light is not absorbed as strongly as it would be in an MZI configuration. Switching in ring or disk resonators is done by changing the resonance characteristics which directs the light to the drop–port for example.

All-optical switching in a racetrack shaped laterally coupled ring resonator add–drop filter by carrier injection induced by single photon absorption is demonstrated in Ibrahim et al. (2003a). Single photon absorption is achieved by optically pumping the used material above its bandgap energy, generating electron–hole pairs, which in turn alter the gain–loss coefficient and the refractive index. In comparison to two photon absorption, the pump beam does not need to be located on a resonance of the ring resonator, reducing the cavity ring-down time leading to a reduction in the switching time. The parameters of the used ring resonator add–drop filter is: FWHM = 1.3 nm, $Q = 1,200$, FSR = 18 nm, and a finesse of 14. In the experiment, the ring resonator is pumped from the top with a Ti:Sapphire laser with a wavelength of 800 nm. A switching window of 20 ps is obtained. Two switching schemes are demonstrated. In the first, the inserted wavelength is located near a resonance causing it to be on a resonance when the ring resonator is pumped. The signal is then switched to the drop–port. In the other scheme the signal is tuned to a resonance and by pumping the ring, the signal is switched to the throughput port. In this way, a modulator is implemented. A switching contrast of approximately 7 dB is achieved.

A switching time of only 20 ps is demonstrated in Hill et al. (2004) using integrated ring lasers in GaInAsP/InP having radii of 8 μm. A photograph of the fabricated device is shown in Fig. 5.109. The width of the waveguides is 2 μm. The lasers are operated at 281 K in pulsed mode, with current pulses of 80 ns duration every 13.5 ms. The threshold current is approximately 30 mA. The double ring laser device can have two stable states. In one state, light from ring laser A injection locks ring laser B, forcing it to lase only in the clockwise

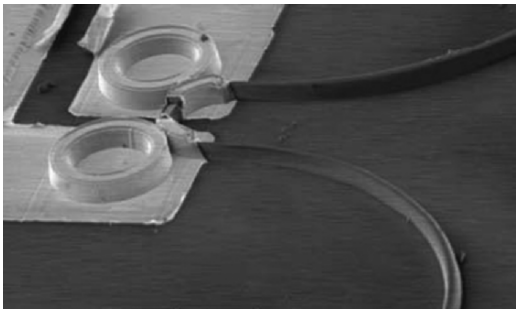

Fig. 5.109. A memory element formed by two 16 mm diameter microring lasers coupled via a waveguide on an InP/GaInAsP photonic integrated circuit. Scale bar, 10 mm. The microring lasers were fabricated in active areas of the integrated circuit containing bulk 1.55 mm bandgap GaInAsP in the light guiding layer. Separate electrical contacts allowed each laser's wavelength to be individually tuned by adjusting the laser current. Passive waveguides connected the microring lasers to the integrated circuit edges.

Reprinted by permission from Macmillan Publishers Ltd: T.M. Hill, Nature 432:206–209 ©2004

direction. In the second state, ring laser B injection locks ring laser A, forcing it to lase only in the anticlockwise direction. Pulses of light at the chosen input can set the system in the corresponding state.

Optical signal processing using ring resonators is a useful alternative to for example MZIs and progress in research on the switching behavior of these devices will eventually lead to an implementation in all-optical networks.

5.9 Sensors

Integrated optical sensors are and have been investigated since a long period of time and have found their way into many applications. Ring resonator can be used as sensing elements for example by measuring the resonance frequency shift, which is induced by a change in the effective refractive index. Integrated waveguide based sensors have gained attention since the downturn of the telecommunication industry left several research groups looking for other fields of application. But this is not the only cause. The focus of research has turned more and more towards biology where single molecule and single cell detection are the envisaged goal.

This chapter provides an overview of sensors based on integrated ring resonators including biosensors.

A silicon based integrated ring resonator notch filter with a radius of 3 cm is used in Adar et al. (1991) to measure the loss in phosphorus-doped silica on silicon waveguides. The finesse of the resonator is 45. The measuring principle used is the fact that waveguide loss is related to the width of the resonances

(see Chap. 2). The ring resonator is placed on a temperature controlled surface. An ECL kept at a constant wavelength, with a linewidth smaller than the width of the resonances of the ring resonator is used as the input source. The temperature is changed and the response of the ring resonator is measured, revealing the filter function characteristic for ring resonator notch filters. As the FSR is known from the parameters of the ring resonator, the width of the resonances can be taken directly from the transmission experiment leading to the waveguide loss.

An integrated ring resonator sensor is analyzed theoretically in Kiyat et al. (2004) to be implemented in a setup to measure the displacement in scanning probe microscopy. A schematic of the proposed device is shown in Fig. 5.110.

The displacement of the cantilever changes the refractive index of the ring resonator which changes the transmission spectrum. Several designs including racetrack-shaped ring resonators are simulated and compared. The highest sensitivity is obtained for a racetrack-shaped ring resonator. Sensitivities as high as $10^{-4}\,\text{Å}^{-1}$ are calculated.

Waveguide birefringence is measured in Carriere et al. (2004) by using an integrated ring resonator with a radius of 14 mm, fabricated by ion exchange in glass. The waveguide birefringence is defined as the difference between the effective refractive indexes of transverse electric and transverse magnetic modes. The birefringence Δn_{Bi} is calculated using the FSR of a ring resonator as follows (Carriere et al. 2004). Using (2.21) where the group refractive index is used, the shift in wavelength between the two polarization states seen in the FSRs is given by

$$\Delta\text{FSR}_{\text{Bi}} = \text{FSR}_{\text{TM}} - \text{FSR}_{\text{TE}} = \frac{\lambda^2}{L}\left(\frac{1}{n_{\text{g TM}}} - \frac{1}{n_{\text{g TE}}}\right). \tag{5.16}$$

The waveguide birefringence is defined as

$$\Delta n_{\text{Bi}} = n_{\text{eff,TE}} - n_{\text{eff, TM}}. \tag{5.17}$$

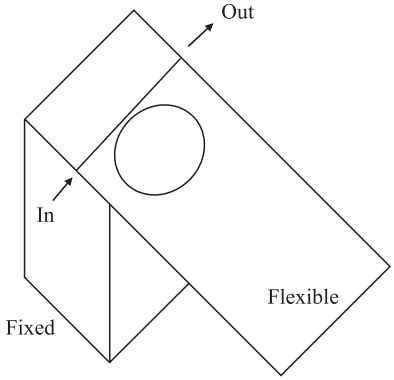

Fig. 5.110. Integrated microring resonator displacement sensor for scanning probe microscopies

Using (2.20), the waveguide birefringence in terms of the FSRs is given by

$$\Delta n_{\mathrm{Bi}} = \frac{\lambda^2}{L} \cdot \frac{\Delta \mathrm{FSR}_{\mathrm{Bi}}}{\mathrm{FSR}\,(\mathrm{FSR} - \Delta \mathrm{FSR}_{\mathrm{Bi}})}. \tag{5.18}$$

This equation is straight forward and the birefringence is easily calculated from the measurement of the FSRs. In order to differentiate the birefringence induced by the curved sections of a ring resonator, racetrack-shaped and full circle resonators can be compared in terms of their birefringence. The difference is only due to the contribution of the straight waveguide sections.

Ring resonators are not only used for measuring birefringence in waveguides, but can also be applied to determine strain. In Bhola et al. (2005) a polymer ring resonator strain sensor is demonstrated. A photograph and a cross-section of the fabricated device are shown in Fig. 5.111. A sketch and a photograph of the strain sensor attached to a micrometer stage are shown in Fig. 5.112. An advantage of using ring resonators as strain sensors is that the direction of the strain does not matter due to the ring geometry. The sensitivity can be increased by using a racetrack shaped ring resonator. In this case two racetrack-shaped ring resonators perpendicular to one another can be used to determine the direction of the strain.

These examples demonstrate a small variety of sensors realized with integrated ring resonators in different materials. Lately biosensors have attracted a lot of attention and ring resonators are again focus of research in this new emerging field.

A biosensor based on a disk resonator is proposed and analyzed in Boyd and Heebner (2001). The disk is weakly coupled to a bus waveguide which allows the field to build up to high values in the disk resonator which is necessary for sensing. The device designed has the following parameters: a waveguide width of 0.4 µm, a coupling gap of 0.25 µm and a disk radius of 2.54 µm. The device is operated in TM polarization. A dielectric constant of the device of 4 is assumed. The achieved simulated sensitivity is expected to be approximately 100 molecules.

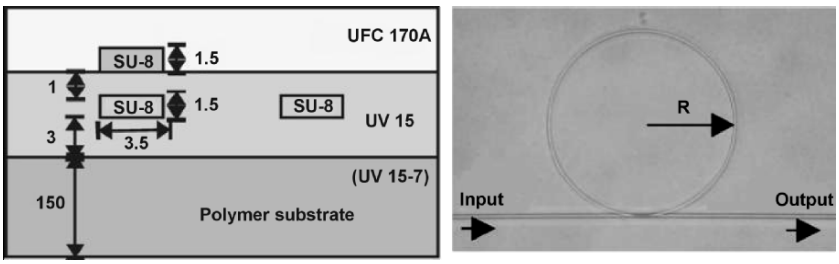

Fig. 5.111. Cross-section and photograph of the polymer ring resonator used for the strain sensor. Dimensions are in µm.

Reprinted with permission from IEEE Photonics Technology Letters, vol. 14, pp. 867–869 ©2005 IEEE

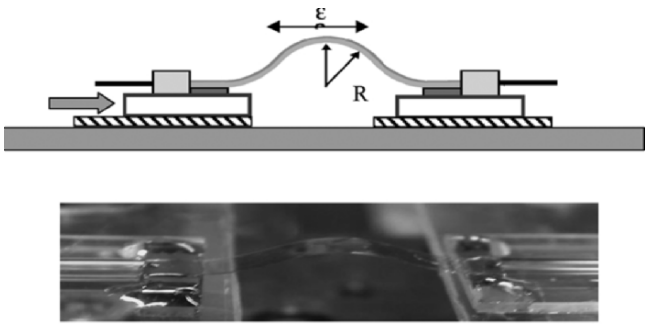

Fig. 5.112. Application of controlled strain using a micrometer stage. ε is the strain and R the radius of the bend.

Reprinted with permission from IEEE Photonics Technology Letters, vol. 14, pp. 867–869 ©2005 IEEE

A detailed analysis of resonant-enhanced evanescent-wave fluorescence biosensing in ring and disk resonators is presented in Blair and Chen (2001). Design layouts are given and the sensitivity and the enhancement factor are derived.

A sensor using a disk resonator vertically coupled to a bus waveguides is fabricated and demonstrated in Krioukov et al. (2002). The layer sequence and layout of the device is shown in Fig. 5.113. Similar to the previous simulated example, the disk resonator is weakly coupled to the underlying bus waveguide, allowing modes in resonance with the disk to build up. The response from the disk is measured using water, ethanol and a mixture of water and glucose in different concentrations as cladding. A shift in the resonance wavelength indicates the different solutions.

A glucose concentration sensor is realized in Chao and Guo (2003) using polymer nanoimprinting. The racetrack shaped ring resonator notch filter includes partially reflecting junctions in the bus waveguide creating so called Fano resonances (Fan 2002). A schematic of the devices is shown in Fig. 5.114. Details on the fabrication have been described in Chap. 3 where a similar device is realized. The measurement is performed by tuning a laser near one of the resonances of the ring and detecting the change in the spectra. The ring resonator is placed in different glucose concentrations. A minimum detectable concentration change of glucose solution is estimated to be 0.024%, or $24\,\mathrm{mg\,(dl)^{-1}}$. Since the Q-factor is proportional to the sensitivity, an increase in the Q-factor of the ring resonator will also enhance the sensitivity. The shift in the resonance wavelength is linear with increasing glucose concentration.

So far solids or liquids are detected with ring resonators. A gas sensor is fabricated and demonstrated in Ksendzov et al. (2004) which utilizes a polymer sensing layer. The racetrack-shaped ring resonator add–drop filter has a radius of 1.5 mm. The straight sections have a length of 0.1 mm with a

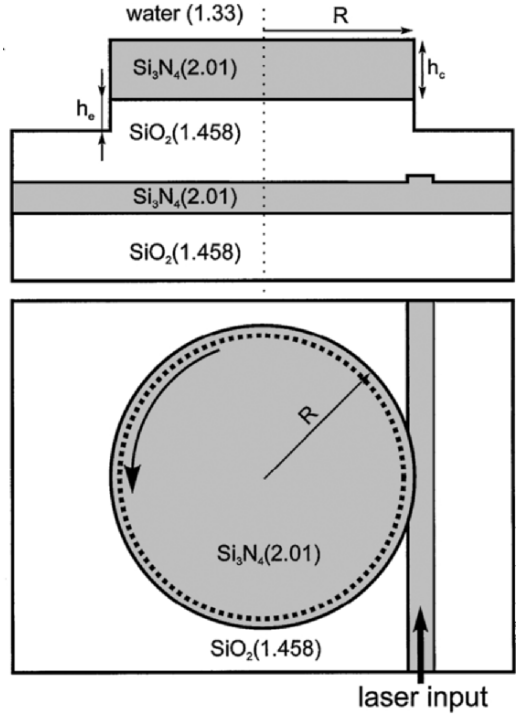

Fig. 5.113. Cross-section and view of an integrated optical MC sensor. Light from a tunable laser is coupled into the excitation waveguide, and the scattering is measured from the top of the MC as a function of the wavelength with various solutions in the sensing area. *Dotted line*, localization of a high-Q whispering-gallery mode; its propagation direction is shown by an arrow around the circumference. Device parameters: $R = 15\,\mu\text{m}$, $h_c = 255\,\text{nm}$, $h_e = 150\,\text{mm}$.

Reprinted with permission from E. Krioukov, Optics Letters, vol. 27, no. 7, pp. 512–514 ©2002 Optical Society of America

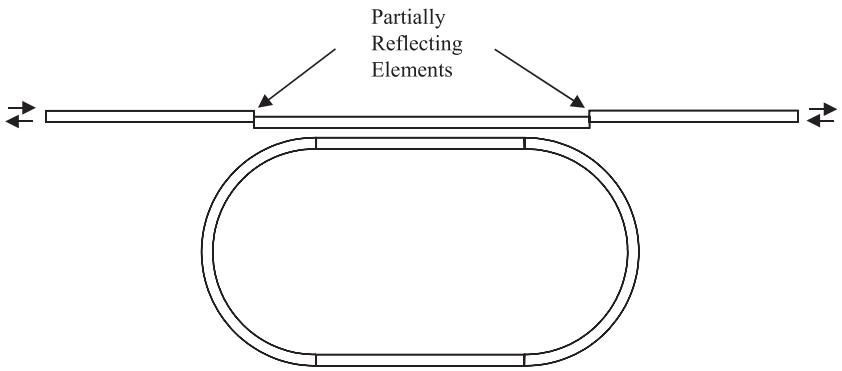

Fig. 5.114. Racetrack-shaped ring resonator with partially reflecting waveguide junctions

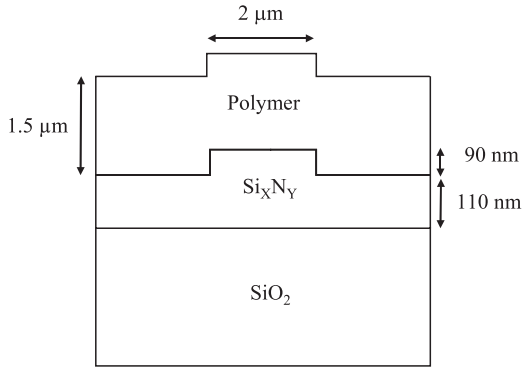

Fig. 5.115. Layer sequence of waveguide in a ring resonator gas sensor

coupling gap of 2 µm. The layer sequence of the waveguide used is shown in Fig. 5.115.

The polymer swells in the presence of the analyte and changes its refractive index due to chemical permeating. The resonance wavelength is monitored with a tunable laser and the shift is detected in dependence of the concentration of the analyte. The fabricated ring resonator is brought into a sealed chamber and a controlled mixture of air, water vapor, and isopropanol is inserted. Sensitivity to isopropanol of 50 ppm is shown experimentally.

One of the first demonstrations of a ring resonator used for sensing biomolecules is given in Yalçin et al. (2006). The functionality of the device is proven by using avidin–biotin binding on the surface of a vertically coupled glass ring resonator. The radius of the ring resonator is 60 µm. The penetration depth of the mode into the medium (deionized water) is calculated to be approximately 360 nm at a wavelength of 1,550 nm assuming an effective refractive index of the waveguide of 1.5. The ring resonator parameters are as follows: FSR $= 4.2\,\mathrm{nm}$, FWHM $= 0.126\,\mathrm{nm}$, $F = 33$, $Q = 12,000$. The measurement principle is again the monitoring of the resonance shift due to a change in the refractive index caused by the binding of biomolecules. The refractive index sensitivity of the system is 1.8×10^{-5}.

Ring resonators are ideal for use in sensing biomolecules or even cells, as only a few molecules are required to induce a change in the resonance wavelength. Going into the direction of single molecule detection requires so called whispering gallery mode resonators which will be briefly described in the following chapter.

6

Whispering Gallery Mode Devices

Whispering gallery mode (WGM) resonators and lately photonic crystal resonator based devices are attractive due to their potential applications in photonics and recently in biophotonics as is described in Chap. 5. Applications which have been realized include for example lasers, filters, optical switches, and biosensors. This chapter introduces WGM devices, although some examples which have been given in this book have dimensions of whispering gallery mode resonators. This chapter serves as a brief introduction into the topic as a significant number of books and other publications exist on this subject (for example, Vahala 2003, 2004).

6.1 Whispering Gallery Modes

WGMs are named after the whispering gallery at St. Paul's Cathedral in London and have been studied by Lord Rayleigh in 1910 (Rayleigh 1910, 1912). WGMs occur at particular resonant wavelengths depending on the size of the resonator. At these particular wavelengths, light undergoes total internal reflection at the surface of the resonator creating resonances in the transmission spectrum of the resonator. Whispering gallery resonators are dielectric structures in which light waves are confined by continuous total internal reflection. WGMs can be observed in droplets and glass spheres for example. In this chapter, examples are limited to planar integrated WGM resonators.

The light in WGM resonators is concentrated near the circumference of the device and is assigned a mode number and a mode order. The mode number, m_n, reveals the number of wavelengths around the circumference, and the mode order, m_o, reveals the number of maxima in the radial dependence of the electromagnetic field within the resonator. These modes can have very high Q factors if the losses due to reflection at the surface of the resonator are low. In addition to high Q-values, a high finesse is also obtained. The high Q-factor makes these resonators very attractive to be used as lasers.

In order to couple light in or out of these resonators, the evanescent field of the WGMs has to overlap with the evanescent field of a phase-matched optical bus waveguide. This in-and-out coupling of WGM resonators is one of the major technological challenges and was only recently achieved due to the advance of fabrication technology, as was demonstrated in several examples in this book.

A review of the basic properties of WGM resonators is presented in Matsko and Ilchenko (2006a).

6.2 WGM Filters

Optical filters are one of the first applications when considering optical devices having wavelength dependent resonances. As in ring resonators, WGM resonators have a wavelength dependent resonance spectrum. Due to the small size of WGM resonators, they have large FSRs, high Q-factors and high finesse. A review paper presenting applications of both WGM and ring resonators is given in Matsko and Ilchenko (2006b).

One of the challenging research tasks is to achieve in and output coupling of these very small (diameter$<10\,\mu$m) WGM resonators. Several groups have and are working on this subject. Before being able to couple in and out of a WGM device, WGM modes must circulate in the device to build up a resonance spectrum. This is only achieved when the WGM device has sufficiently low internal losses, especially a low surface roughness. Both of these aspects are theoretically investigated in Little and Chu (1996). The coupling between a WGM disk resonator and a bus waveguide is simulated in Dehmubed and Diament (1998).

Design and fabrication of laterally coupled ring and WGM disk resonators in the material system AlGaAs/GaAs is presented in Hagness et al. (1997), Rafizadeh et al. (1998). The layer sequence of the device has been described in Chap. 3. Photographs of the fabricated ring and WGM disk resonator are shown in Fig. 6.1. The diameter of the ring and disk resonator is $10.5\,\mu$m. A waveguide width of $0.5\,\mu$m is used. The coupling gap between the bus waveguide and the ring and disk is $0.1\,\mu$m. A trench is fabricated around the waveguides with a width of $1\,\mu$m.

A detailed description of cylindrical WGM multimode resonators verified by experimental results realized in silicon oxynitride technology is presented in Klunder et al. (2002a, 2003a). The layer sequence of the fabricated cylindrical WGM resonator is shown in Fig. 6.2. The intensity distribution inside the WGM resonator is analyzed using photon scanning tunneling microscope (PSTM) and effects like polarization conversion and counter propagation is detected. A simulation model is derived for calculating the finesse, bending losses and FSRs of fundamental quasi guided modes in this cylindrical WGM resonator.

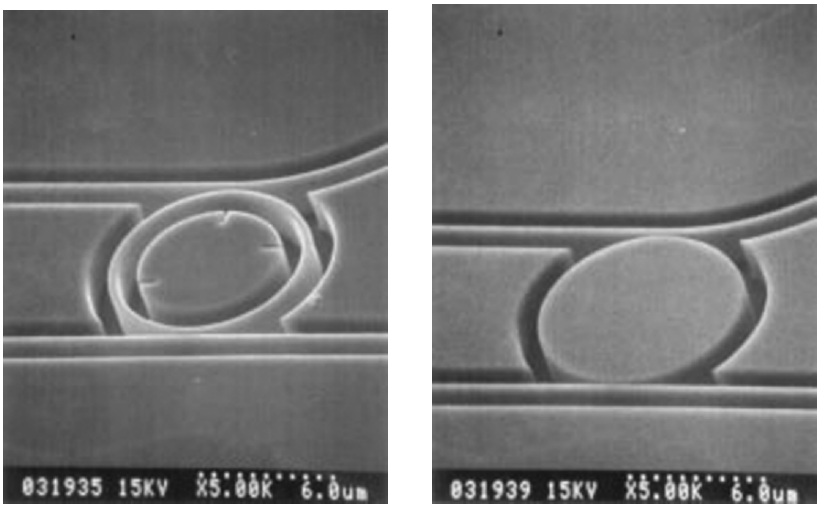

Fig. 6.1. SEM images of a 10.5 µm diameter GaAs/AlGaAs microcavity ring and disk resonator coupled to 0.5 µm-wide waveguides.

Reprinted with permission from IEEE Journal of Lightwave Technology, vol. 15, pp. 2154–2165 ©1997 IEEE

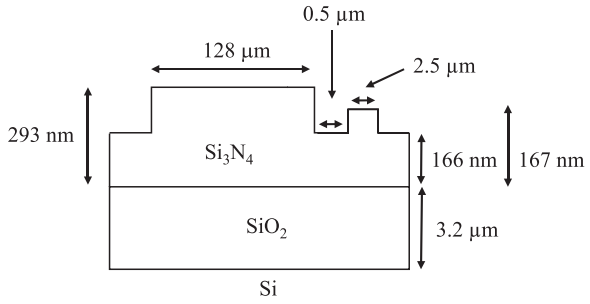

Fig. 6.2. Layer sequence of cylindrical WGM resonator

Another form of WGM resonator is designed and analyzed in detail in Maolatou et al. (1999) and Hammer (2002). The WGM resonator is in the shape of a rectangle coupled to bus waveguides. A schematic of the rectangular WGM resonator is shown in Fig. 6.3. Rectangular-shaped resonators are slightly different from ring or disk resonators treated so far in this book with respect to the intensity distribution at the output ports. As can be seen from Fig. 6.3, some of the input power is reflected back to the same port and dropped at all the remaining ports. This is in contrast to ring or disk resonators, where there is a preferred direction of the light passing the resonator in the on or off-resonance state, leading to only one drop and one throughput port.

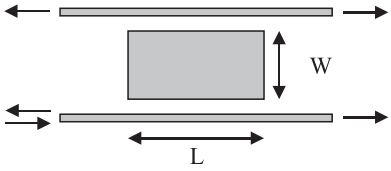

Fig. 6.3. Rectangular WGM resonator

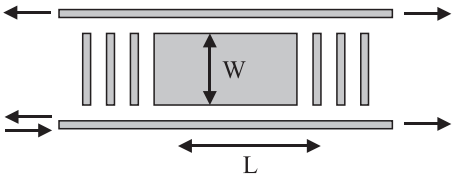

Fig. 6.4. Grating assisted rectangular WGM resonator

Several configurations have been simulated in Hammer (2002) using an operation wavelength of 1.55 µm. The length L and width W of the rectangular WGM resonator is varied between 0.81–6.902 µm and 0.81 µm–3.696 µm, respectively. The width of the bus waveguides and the coupling gap is varied between 0.035–0.13 µm and 0.32–0.49 µm, respectively. The refractive index of the WGM resonator and the bus waveguides is assumed to be 3.4, whereas the surrounding refractive index is defined to be 1.45.

This type of resonator is coupled to gratings on either side of the WGM resonator which leads to a superior add–drop filter characteristic. The device design is presented in Hammer et al. (2004). A schematic of the proposed device is shown in Fig. 6.4.

The fabrication of WGM resonators has only been possible recently due to an advance in nanofabrication technologies. Especially in the case of WGM resonator filters, in and out coupling is the greatest technological challenge. When these tasks are overcome, tunability of WGM resonators is the next goal.

Tuning of WGM resonators is addressed in Boriskina et al. (2003). Filter tuning is proposed by changing the shape of the resonator from circular to elliptic, which reduces the dependence of the coupling efficiency on the width of the air gap. The elliptic shape can be compared to a racetrack shaped ring resonator, where the effect in increasing the coupling length is the same. Two alternative coupling designs are suggested for monolithic and hybrid integration technologies. The first one is based on increasing the coupling length. The other makes use of the field concentration at the increased curvature portion of the deformed WGM resonator.

Another method of tunability (either wavelength or filter shape) in resonators is by introducing gain into the resonator as described in Chaps. 3 and 5. Active disk resonators are simulated and designed in Djordjev et al. (2002a) for use as modulators, switches and wavelength routers.

Totally active devices can of course be used as lasers. WGM lasers have been investigated and demonstrated earlier than WGM resonator filters, which is obvious, because light only needs to be collected from the WGM resonator and not coupled into it for detecting the spectrum. In the following chapter, a brief introduction is given with examples of fabricated WGM lasers.

6.3 WGM Lasers

WGM lasers are expected to be the light sources of future photonic integrated circuits and optical computer boards due to their extremely small size. Other advantages are similar to ring and disk resonators and include their compactness and their integration ability. Further more, no grating or facet is required for optical feedback which is the main advantage when thinking of several WGM lasers on a chip placed at different locations. Some examples described in Chap. 5.6.1 can be regarded as WGM resonator lasers and are therefore not addressed in this chapter.

WGM lasers having diameters of 3, 5, and 10 µm are fabricated in the material system GaInAsP/InP and demonstrated in McCall et al. (1992). Optically pumped InGaAs quantum wells are used to achieve lasing at wavelengths of 1.3 and 1.5 µm. The WGM lasers have the shape of a "mushroom" with an InP pedestal holding the disk with the quantum well layers. The thickness of the InGaAs quantum wells is 10 nm, the thickness of the GaInAsP barriers is 10 nm as well. The GaInAsP end caps have a thickness of 20 nm. The mushroom like shape is achieved by selective chemical etching of the InP below and around the quantum wells, resulting in a disk on a pedestal.

Even smaller WGM disk lasers are presented in Slusher et al. (1993). Disks with a diameter of 2.2 µm and 5 µm in the same material as the previous ones are fabricated. Six quantum wells with a thickness of 10 nm of the material $In_{0.53}Ga_{0.47}As$ are used together with five 10 nm thick GaInAsP barriers. The bandgap wavelength of the GaInAsP material is 1.1 eV at room temperature. The disks are optically pumped with an HeNe laser at a wavelength of 633 nm. A mode spacing of 87 nm is obtained for the small disk and 37 nm for the larger disk. Q-values of 260 and 500 are measured at pump powers below threshold.

A "submicron" WGM disk laser is presented in Levi (1994) having a radius of 0.8 µm and a thickness of 0.18 µm. The disk consists of six 12 nm thick InGaAs quantum wells separated by five 12 nm thick GaInAsP barriers. The disk is optically pumped with a diode laser having a wavelength of 850 nm. Pulses with a length of 8 ns and a repetition period of 100 ns are used for the pumping. A conformal mapping technique is used in Frateschi and Levi (1995) to determine the radial and azimuthal eigenvalues and eigenvectors of leaky optical modes of this WGM disk laser.

Quantum cascade (QC) WGM disk lasers with an emission wavelength at 5 µm are fabricated and demonstrated in Faist et al. (1996). A mushroom like

device structure is again used. A photograph of a fabricated QC disk laser is shown in Fig. 6.5. The layer sequence of the device is shown in Fig. 6.6.

Disks with diameters of 17, 25, 45, 80, and 125 µm are fabricated. The measurement of the devices is done at a temperature of 15 K. The disks are contacted from top and are operated using 50 ns pulses. A threshold current of 2.85 mA is measured for the QC disk with a diameter of 17 µm. QC WGM disk lasers in the material system InGaAs/AlInAs, emitting at a wavelength of 16 µm, being one of the longest wavelengths reported for disk lasers, are presented in Tredicucci et al. (2000). The disk lasers are electrically contacted and operated in pulsed mode. Measurements are performed at temperatures of 10 K.

Electrically pumped GaInAsP–InP strained quantum well WGM disk injection lasers with diameter between 2 and 10 µm are presented in Baba (1997) and Baba et al. (1997). A photograph of WGM disk lasers with diameters of 8, 3, and 2 µm are shown in Fig. 6.7.

The disks are made of compressive strained multiple quantum wells. Four quantum well layers with a thickness of 3–4 nm sandwiched between barrier layers with a bandgap wavelength of 1.2 µm having a thickness of 10 nm. The

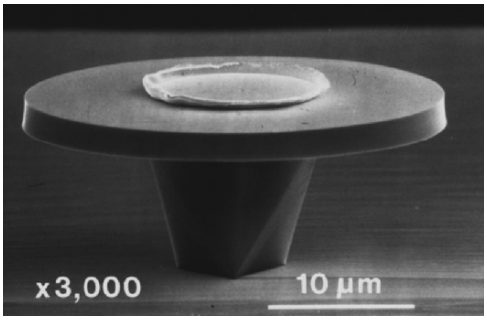

Fig. 6.5. Scanning electron microscope image of a 25 µm diameter QC disk laser with total height 15.5 µm.

Reused with permission from J. Faist, Applied Physics Letters, 69, 2456 (1996) ©1996 American Institute of Physics

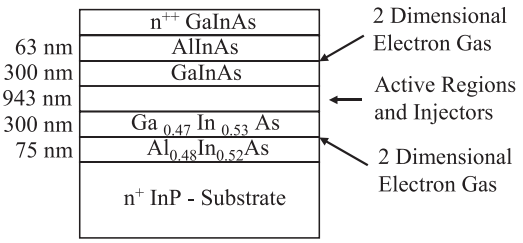

Fig. 6.6. Layer sequence of the QC WGM disk laser

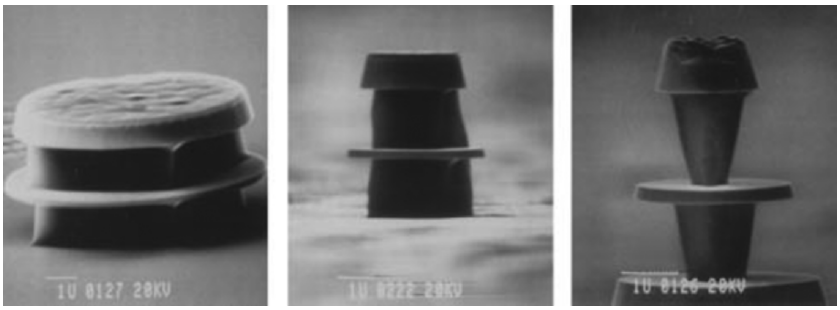

Fig. 6.7. WGM disk injection lasers with diameters of 8, 3, and 2 µm (from *left* to *right*).

Reprinted with permission from IEEE Journal of Selected Topics in Quantum Electronics, vol. 3, pp. 808–830 ©1997 IEEE

active layers include 50 nm thick guide layers with a bandgap wavelength of 1.2 µm and 30 nm thick gradient index (GRIN) layers with a bandgap wavelength of 1.1 µm. The total thickness of the active layers is 0.2 µm. A threshold current of 0.2 mA is measured for the disk with a diameter of 2 µm under pulsed operation at a temperature of 286 K. Lasing is achieved at wavelengths around 1.55 µm.

Optically pumped disk and ring lasers in InGaAs with diameters between 3.5 and 9 µm, fabricated using substrate removal and material transfer to a glass substrate by liftoff processing are presented in Corbett et al. (1996). This process is used in Corbett (1998) to fabricate ring and disk lasers with diameters between 6 and 28 µm having a single compressively strained 3 nm, $In_{0.7}Ga_{0.3}As$ quantum well cladded by a 20 nm GaInAsP layer having a bandgap wavelength of 1.25 µm and a 100 nm GaInAsP layer with a bandgap wavelength of 1.15 µm, lattice matched to InP with a total thickness of 245 nm. The devices are optically pumped continuous wave (cw) with the 514 nm line of an Ar-ion laser at liquid nitrogen temperatures. An optically pumped threshold of 2 µW is obtained. The lasing wavelength observed is between 1.4 and 1.55 µm. Multimode operation of the lasers is observed at wavelengths corresponding to whispering gallery modes.

Determining the optical modes in WGM resonators requires a different approach as the one presented in Chap. 2 for calculating the transmission spectrum of ring resonator filters. As these WGM resonators can be extremely small as is demonstrated in this chapter, the three dimensional Maxwell equations can not be reduced to a one dimensional problem. A method for calculating optical modes in WGM disk resonators giving an eigenvalue equation for optical modes and providing the distribution of the optical field in exact forms is described in detail in Wang and Dumitrescu (1998). Based on the results of the optical modes, the emitted optical modes are determined. Disks with a radius between 0.5 and 1.5 µm having a thickness of 50, 100 nm and 150 nm are simulated.

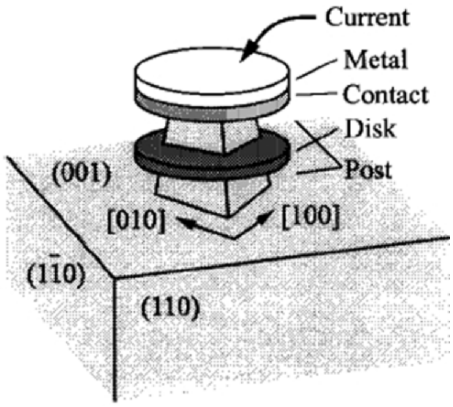

Fig. 6.8. Schematic of a WGM disk injection laser.

Reprinted with permission from IEEE Journal of Selected Topics in Quantum Electronics, vol. 5, pp. 673–681 ©1999 IEEE

One of the first cw operating, current injection WGM disk lasers in the material system GaInAsP/InP is presented in Fujita et al. (1999). A schematic of a WGM disk injection laser is shown in Fig. 6.8. Whispering gallery modes travel round near the edge of the disk by total internal reflection at the semiconductor/air boundary. The current is flowed from the top contact. Carriers are injected into the active layer from the posts.

A record threshold value of 150 µA is measured for a disk with a diameter of 3 µm at a temperature of 298 K. The measurement curve is shown in Fig. 6.9.

Two resonant modes are seen at a wavelength of 1.63 µm. The lasing mode has an FWHM of 0.5 nm. The nonlasing mode has an FWHM of 0.7 nm. The calculated Q factors for both of them are 3,300 and 2,300, respectively.

WGM resonators have not only been realized in GaAs or GaInAsP, but have also been demonstrated in the material system InGaN/GaN using multiple quantum wells (MQW). An example of realized WGM ring and disk resonator devices is described in Zeng et al. (1999). Both realized devices are optically pumped. A schematic diagram of the InGaN/GaN MQW WGM ring resonators is shown in Fig. 6.10. The response from a WGM disk resonator is shown in Fig. 6.11.

Different fabrication techniques and material systems have been used to fabricate WGM disk and ring resonators. A wafer fusion method is described in Song et al. (2000) to fabricate optically pumped GaInAsP disk lasers on Al_xO_y. Continuous wave room temperature operation is achieved for devices with a diameter of 2.2 µm. The output power and the spectrum of an optically pumped disk are shown in Fig. 6.12. The FSR of adjacent whispering gallery modes is 110 nm. The threshold pump power is 1.13 mW, as can be seen in the measurement.

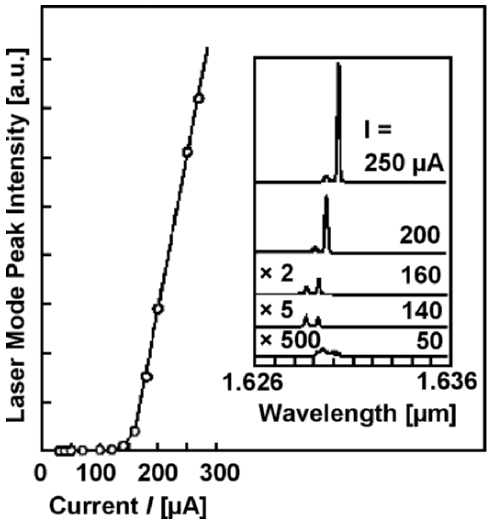

Fig. 6.9. Laser mode peak intensity versus current characteristic and lasing spectra observed under cw condition at 298 K for a 3 μm diameter device.

Reprinted with permission from IEEE Journal of Selected Topics in Quantum Electronics, vol. 5, pp. 673–681 ©1999 IEEE

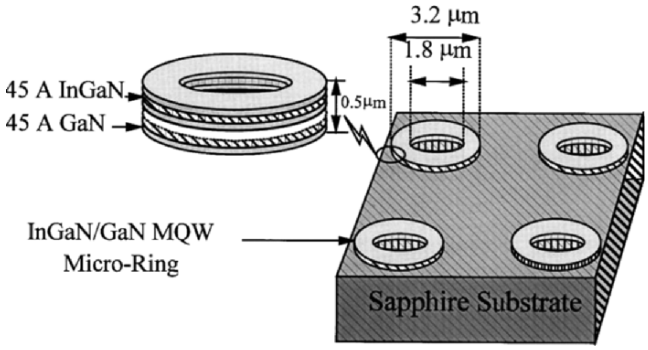

Fig. 6.10. Schematic diagram of representative InGaN/GaN MQW microring fabricated by photolithography patterning and dry etching.

Reused with permission from K.C. Zeng, Applied Physics Letters, 75, 2563 (1999) ©1999 American Institute of Physics

So far, WGM disk and ring lasers are measured by placing an optical fiber near the edge of the disk or ring to collect the emission which is then fed to an optical spectrum analyzer. In addition to the collection of the output light, cooling of some devices and measuring in pulsed mode is required. One of the first disk lasers with a radius of 10 μm vertically coupled to underlying bus waveguides in the material system GaInAsP/InP is presented

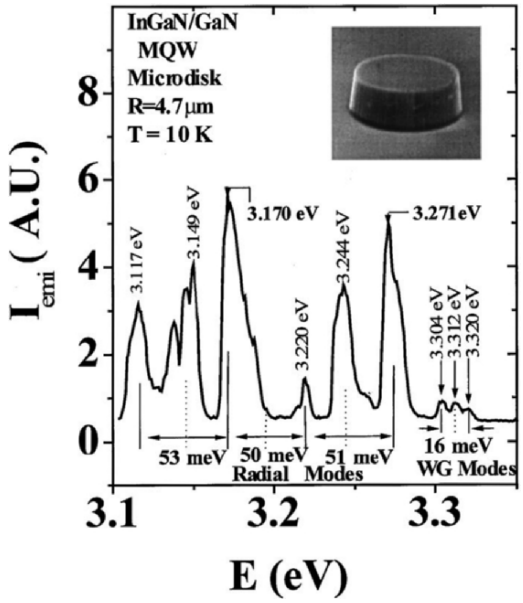

Fig. 6.11. Optical emission spectrum of an InGaN/GaN MQW microdisk with a diameter of 9.4 mm. Both the WG and radial modes are observed in the microdisks.

Reused with permission from K.C. Zeng, Applied Physics Letters, 75, 2563 (1999) ©1999 American Institute of Physics

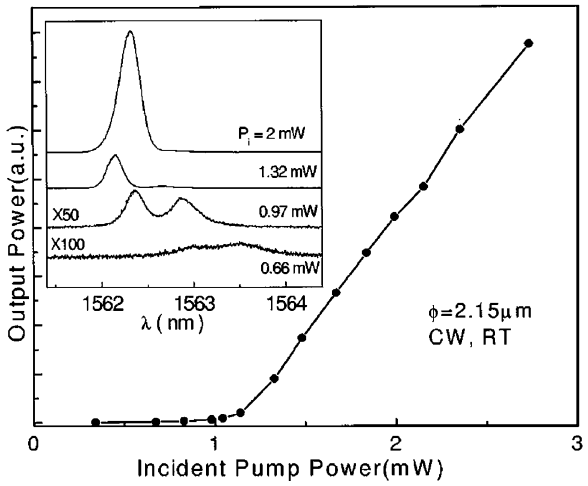

Fig. 6.12. Output power against incident pump power for the 2.2 μm diameter microdisk laser pumped by 1,064 nm Nd:YAG laser. The spectra are measured by optical spectrum analyzer (OSA) with 0.24 nm resolution.

Reprinted with permission from IEEE Photonics Technology Letters, vol. 12, pp. 954–956 ©2000 IEEE

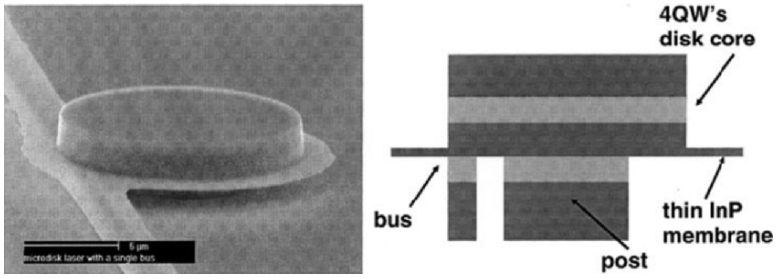

Fig. 6.13. SEM image (*left*) and schematic cross-sectional view of the microdisk vertically coupled to a bus waveguide. Picture was taken after the disk formation. A thin InP membrane remains along the edges.

Reprinted with permission from IEEE Photonics Technology Letters, vol. 15, pp. 1330–1332 ©2003 IEEE

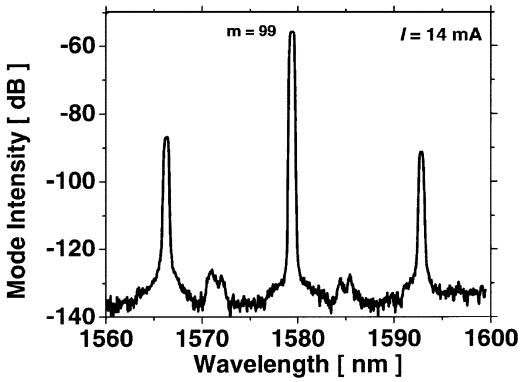

Fig. 6.14. Lasing spectrum for an 8 µm radius microdisk laser measured at $I = 14\,\mathrm{mA}$.

Reprinted with permission from IEEE Photonics Technology Letters, vol. 15, pp. 1330–1332 ©2003 IEEE

in Choi et al. (2002a). The device operates cw at room temperature, has a side mode suppression ratio of 20 dB and emits at a wavelength around 1.52 µm. The layer sequence and the fabrication of the device are similar to the ones described in Chap. 3. A disk laser based on the same fabrication process, vertically coupled to a single bus waveguide with a radius of 8 µm is demonstrated in Choi et al. (2003). A photograph of a vertically coupled disk and a schematic of the cross-section are shown in Fig. 6.13.

The width of the bus waveguide is 0.7 µm. The waveguide is antireflection coated to avoid Fabry–Perot resonances. A spectrum of the disk laser at an operating current of 14 mA is shown in Fig. 6.14. The disk laser has a threshold current of 4.5 mA. The FSR of the disk is 13 nm and the side mode suppression ratio is greater then 30 dB as can be seen in the diagram. Q-factors between 5,000 and 6,000 are measured for this device. These disk lasers are used in

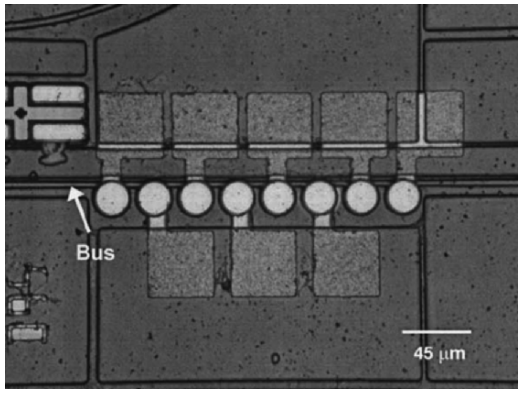

Fig. 6.15. Micrograph showing the top view of the fabricated eight-channel microdisk array vertically coupled to a single bus waveguide.

Reprinted with permission from IEEE Photonics Technology Letters, vol. 16, pp. 356–358 ©2004 IEEE

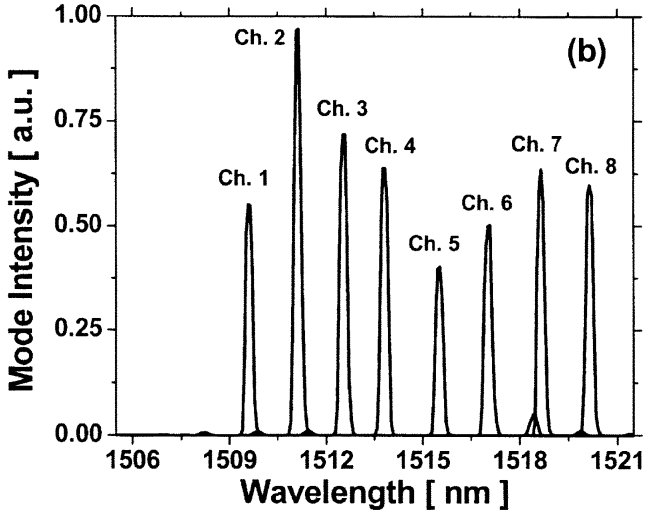

Fig. 6.16. The microdisks for channels 6–8 are pumped at $I = 13\,\mathrm{mA}$, while the current injection levels for the other disks are maintained at $I = 10\,\mathrm{mA}$.

Reprinted with permission from IEEE Photonics Technology Letters, vol. 16, pp. 356–358 ©2004 IEEE

Choi et al. (2004c) to fabricate an eight channel laser array. A photograph of the device is shown in Fig. 6.15.

The radius of the disks varies from 10.6 to 10.95 μm with 0.05 μm difference leading to spectral spacing of the channels of 1.6 nm. The FSR of the disks is approximately 9 nm. The bus waveguide is AR coated. The output spectrum of the laser array is shown in Fig. 6.16. An FWHM of 0.25 nm and a side mode

suppression ratio of 20 dB are obtained. Different current levels are used to tune the resonance wavelength to realize a channel spacing of 1.6 nm.

With increasing advance in nanofabrication and modeling, photonic crystal based devices have made it into real devices. Many applications of ring resonators presented in this book can be transferred to photonic crystal structures and some have already been demonstrated and described in several books and journal publications. Therefore only a few examples of photonic crystal based lasers will be described in the following paragraph to show the potential and possible future direction.

An optically pumped two-dimensional (2D) photonic crystal (PhC) laser in the material system GaInAsP/InP is fabricated and demonstrated in Painter et al. (1999). A schematic of the cross section of the 2D PhC laser is shown in Fig. 6.17. Four 0.85 % compressively strained quaternary quantum wells with an emission wavelength at 1.55 µm are used as the gain source. The membrane has a thickness of 211 nm and a width of approximately 8 µm. The lattice spacing is 500 nm. The holes have a radius of 160 nm. An SEM photograph showing a top view of the fabricated device is shown in Fig. 6.18. For measuring the properties of the cavity, a semiconductor laser with an emission wavelength of 830 nm is used. The measurement is performed under pulsed operation of the pump source. Lasing at a wavelength of 1,580 nm is observed. The absorbed threshold pump power of the PhC laser is estimated to be 500 µW. An upper limit for the Q-factor is derived to be approximately 600.

A similar layout is used in Kim et al. (2002) for fabricating an optically pumped hexagonal PhC ring laser in GaInAsP/InP emitting around 1.55 µm. A photograph of the device is shown in Fig. 6.19.

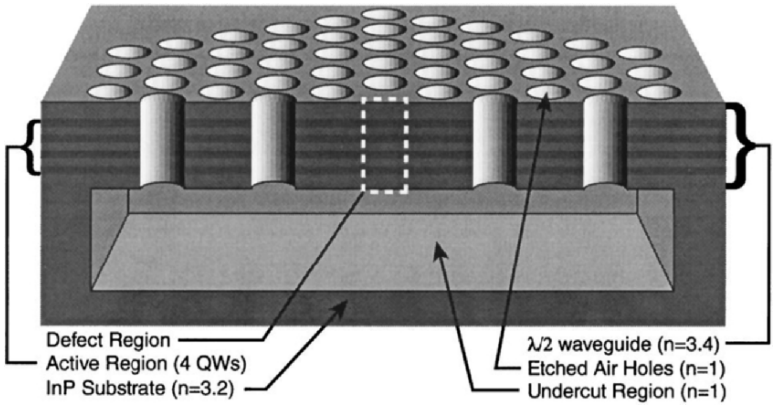

Fig. 6.17. Illustration of a cross-section through the middle of the photonic crystal microcavity. Photons are localized to the defect region by TIR at the air/slab interface and by Bragg reflection from the 2-D photonic crystal.

Reprinted with permission from IEEE Journal of Lightwave Technology, vol. 17, pp. 2082–2088 ©2004 IEEE

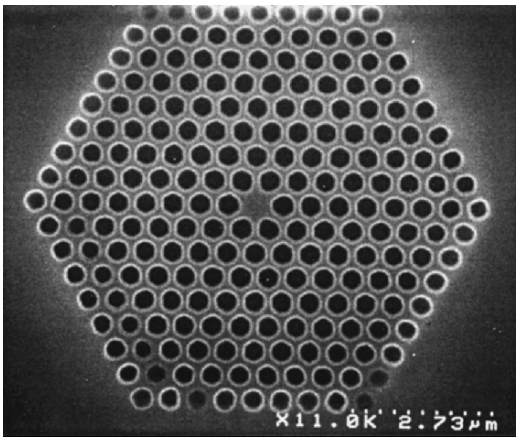

Fig. 6.18. *Top view* of a microfabricated 2D hexagonal array of air holes with a single central hole missing. The interhole spacing, a, is 500 nm, and the radius of the holes are approximately 160 nm.

Reprinted with permission from IEEE Journal of Lightwave Technology, vol. 17, pp. 2082–2088 ©2004 IEEE

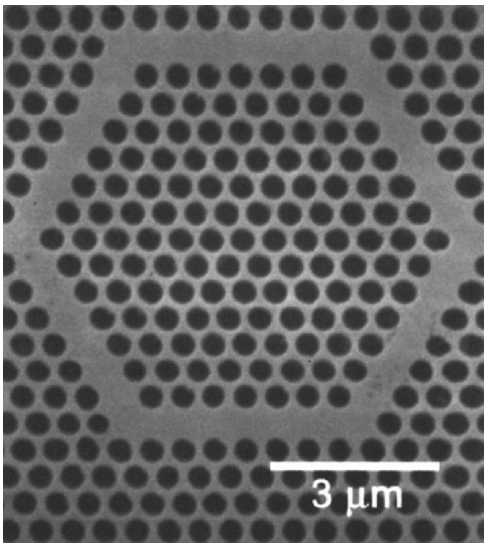

Fig. 6.19. The scanning electron microscope image of a fabricated laser sample. The photonic crystal ring cavity consists of six waveguides and six 120° bends. Thus the resonant mode has similar properties to the guided mode of photonic crystal waveguides. In this picture, lattice constant a is $\sim$0.57 mm and the air hole radius r is $\sim$0.36a.

Reused with permission from Se-Heon Kim, Applied Physics Letters, 81, 2499 (2002) ©2002 American Institute of Physics

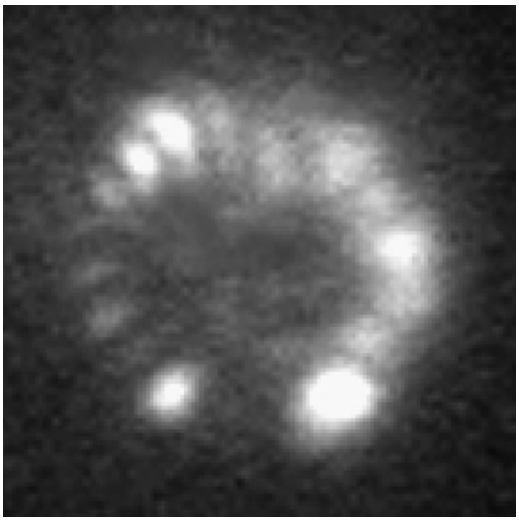

Fig. 6.20. Experimentally measured laser mode using a CCD. This laser sample has 15 air holes along the ring diameter. Lattice constant a of this laser sample is $\sim$0.58 mm and the air hole radius r is $\sim 0.41a$. A hexagonal ring mode pattern shows that the laser is emitted mainly from the ring region.

Reused with permission from Se-Heon Kim, Applied Physics Letters, 81, 2499 (2002) ©2002 American Institute of Physics

The diameter of the device is 8 μm. The measurement of the device is performed using a pump laser with a wavelength of 980 nm at room temperature with pulses having a width of 10 ns. A near field photograph of the standing wave mode in the PhC ring laser is shown in Fig. 6.20.

The threshold pump power of the laser is measured to be 3 mW. The wavelength of the lasing mode observed is $\sim 1,625$ nm. A Q-factor of more than 2,000 is obtained for this PhC ring laser. A detailed analysis of the resonant modes in 2D PhC lasers is presented in Park et al. (2002). Simulations are compared with two types of fabricated devices, air-based free standing (similar to the one in Fig. 6.17) and SiO_2-based epoxy bonded structures. These exemplary examples demonstrate novel types of devices which have a great potential for the future in photonic integrated circuits. Compared to the history of disk or ring resonator structures, active PhC resonator structures are on the way to being electrically contacted with the ability to connect to the outside fiber world using integrated PhC bus waveguides.

7

Outlook

Ring resonators are ideal candidates for realizing all devices ranging from optical filters to lasers for future all optical telecommunication networks. They can be integrated with other semiconductor based devices even electronics and are thus being in the focus of current and future research.

The increasing knowledge of ring resonator devices and the fast improving state-of-the-art in manufacturing technologies lead to novel devices with greater flexibility and higher level of integration. Miniaturization and nanofabrication technologies have already led to multiple coupled ring resonators and integrated gain. Enhancement of device performance will be the next step in ring resonator research, as functionality has been demonstrated as shown by several examples in Chap. 5. Parallel to semiconductor processing, polymer materials, and polymer manufacturing technologies like embossing or nanoimprinting will play an increasing role also due to the "bio" component of the current worldwide research direction.

Regarding the future of optical devices, WGM resonators as is pointed out in Chap. 6, have been developed and characterized since quite some time and their performance parameters are improving with every new fabricated device. These kinds of miniature devices will eventually be able to form the key devices for all-optical computers or even quantum computers.

A key question which remains and which is of a general nature in every optical device is the connection to the outside world, meaning the optical fiber. Here new waveguide designs and fabrication technologies will be the answer.

Ring resonators will certainly not loose their attractiveness as their versatility will increase rather than decrease which is also demonstrated by several examples given in this book. Recently ring resonators have proven their versatility in sensors and even biosensors as have been described in this book opening up new fields of applications. Ring resonators used as biosensors are an emerging class of new devices with increasing interest.

In summary, one could say that ring resonators are ever attracting devices which never loose their fascination once beginning resonating.

References

Absil, P.P.: Microring resonators for wavelength division multiplexing and integrated photonics applications. Ph.D. Thesis, University of Maryland, College Park (2000)

Absil, P.P., Hryniewicz, J.V., Little, B.E., Cho, P.S., Wilson, R.A., Joneckis, G., Ho, P.T.: Wavelength conversion in GaAs micro-ring resonators. Opt. Lett. **25**, 554–556 (2000a)

Absil, P.P., Hryniewicz, J.V., Little, B.E., Wilson, R.A., Joneckis, L.G., Ho, P.T.: Compact microring notch filters. IEEE Photon. Technol. Lett. **12**, 398–400 (2000b)

Absil, P.P., Hryniewicz, J.V., Little, B.E., Johnson, F.G., Ritter, K.J., Ho, P.T.: Vertically coupled microring resonators using polymer wafer bonding. IEEE Photon. Technol. Lett. **13**, 49–51 (2001)

Adar, R., Shani, Y., Henry, C.H., Kistler, R.C., Blonder, G.E., Olsson, N.A.: Measurement of very low-loss silica on silicon waveguides with a ring resonator. Appl. Phys. Lett. **58**, 444–445 (1991)

Alexe, M., Gösele, U. (eds.): Wafer Bonding. Applications and Technology. Springer, Berlin Heidelberg New York (2004)

Azaña, J., Chen, L.R.: Multiwavelength optical signal processing using multistage ring resonators. IEEE Photon. Technol. Lett. **14**, 654–656 (2002)

Baba, T.: Photonic crystals and microdisk cavities based on GaInAsP–InP system. IEEE J. Select. Top. Quantum Electron. **3**, 808–830 (1997)

Baba, T., Fujita, M., Sakai, A., Kihara, M., Watanabe, R.: Lasing characteristics of GaInAsP–InP strained quantum-well microdisk injection lasers with diameter of 2–10 μm. IEEE Photon. Technol. Lett. **9**, 878–880 (1997)

Bach, L., Reithmaier, J.P., Forchel, A., Gentner, J.L., Goldstein, L.: Wavelength stabilized single-mode lasers by coupled micro-square resonators. IEEE Photon. Technol. Lett. **15**, 377–379 (2003)

Barwicz, T., Popovic, M.A., Rakich, P.T., Watts, M.R., Haus, H.A., Ippen, E.P., Smith, H.I.: Microring-resonator-based add–drop filters in SiN: fabrication and analysis. Opt. Express **12**, 1437–1442 (2004)

Bernhard, W.: Digitale thermo-optische Schalter mit integrierten Modulatoren zur Erhoehung der Uebersprechdaempfung. Ph.D. Thesis, Technical University, Berlin (2002)

Bhola, B., Song, H.C., Tazawa, H., Steier, W.H.: Polymer microresonator strain sensors. IEEE Photon. Technol. Lett. **14**, 867–869 (2005)

Bian, Z., Liu, B., Shakouri, A.: InP-based passive ring-resonator-coupled lasers. IEEE J. Quantum Electron. **39**, 859–865 (2003)

Bian, Z., He, W.J., Rabus, D.G., Shakouri, A.: A wavelength-tunable monolithically integrated double ring resonator coupled laser. Proc. CLEO (2006)

Bienstman, P., Six, E., Roelens, A., Vanwolleghem, M., Baets, R.: Calculation of bending losses in dielectric waveguides using eigenmode expansion and perfectly matched layers. IEEE Photon. Technol. Lett. **14**, 164–166 (2002)

Blair, S., Chen, Y.: Resonant-enhanced evanescent-wave fluorescence biosensing with cylindrical optical cavities. Appl. Opt. **40**, 570–582 (2001)

Blair, S., Heebner, J.E., Boyd, R.W.: Beyond the absorption-limited nonlinear phase shift with microring resonators. Opt. Lett. **27**, 357–359 (2002)

Boriskina, S.V., Benson, T.M., Sewell, P., Nosich, A.I.: Tuning of elliptic whispering-gallery-mode microdisk waveguide filters. IEEE J. Lightwave Technol. **21**, 1987–1995 (2003)

Boyd, R.W., Heebner, J.E.: Sensitive disk resonator photonic biosensor. Appl. Opt. **40**, 5742–5747 (2001)

Burton, R.S., Schlesinger, T.E., Munowitz, M.: Improved Y-junction splitter for ring waveguides. Electron. Lett. **30**, 956–957 (1994)

Butterworth, S.: On the Theory of Filter Amplifiers. Experimental Wireless and the Radio Engineer **7**, 536–541 (1930)

Cao, H., Liu, C., Ling, H., Deng, H., Benavidez, M., Smagley, V.A., Caldwell, R.B., Peake, G.M., Smolyakov, G.A., Eliseev, P.G., Osiński, M.: Frequency beating between monolithically integrated semiconductor ring lasers. Appl. Phys. Lett. **86**, 041101 (2005)

Carriere, J.T.A., Frantz, J.A., Youmans, B.R., Honkanen, S., Kostuk, R.K.: Measurement of waveguide birefringence using a ring resonator. IEEE Photon. Technol. Lett. **16**, 1134–1136 (2004)

Caruso, L., Montrosset, I.: Analysis of a racetrack Microring resonator with MMI coupler. IEEE J. Lightwave Technol. **21**, 206–210 (2003)

Chao, C.Y., Guo, L.J.: Polymer microring resonators fabricated by nanoimprint technique. J. Vac. Sci. Technol. B **20**, 2862–2866 (2002)

Chao, C.Y., Guo, L.J.: Biochemical sensors based on polymer microrings with sharp asymmetrical resonance. Appl. Phys. Lett. **83**, 1527–1529 (2003)

Chao, C.Y., Guo, L.J.: Reduction of surface scattering loss in polymer microrings using thermal-reflow technique. IEEE Photon. Technol. Lett. **16**, 1498–1500 (2004)

Chen, W., Chen, W., Chen, Y.J.: A characteristic matrix approach for analyzing resonant ring lattice devices. IEEE Photon. Technol. Lett. **16**, 458–460 (2004a)

Chen, W.Y., Grover, R., Ibrahim, T.A., Van, V., Herman, W.N., Ho, P.T.: High-finesse laterally coupled single-mode benzocyclobutene microring resonators. IEEE Photon. Technol. Lett. **16**, 470–472 (2004b)

Chin, M.K.: Polarization dependence in waveguide-coupled micro-resonators. Opt. Express **11**, 1724–1730 (2003)

Chin, M.K., Ho, S.T.: Design and modeling of waveguide-coupled single-mode microring resonators. IEEE J. Lightwave Technol. **16**, 1433–1446 (1998)

Chin, M.K., Xu, C., Huang, W.: Theoretical approach to a polarization insensitive single-mode microring resonator. Opt. Express **12**, 3240–3250 (2004)

Chin, M.K., Youtsey, C., Zhao, W., Pierson, T., Ren, Z., Wu, S.L., Wang, L., Zhao, Y.G., Ho, S.T.: GaAs microcavity channel-dropping filter based on a race-track resonator. IEEE Photon. Technol. Lett. **11**, 1620–1622 (1999)

Choi, S.J., Djordjev, K., Choi, S.J., Coleman, J.J., Dapkus, P.D.: Microdisk laser vertically coupled to output waveguides. Proc. ISLC 2002, Paper ThB6 (2002a)

Choi, S.J., Djordjev, K., Choi, S.J., Dapkus, P.D.: CH4-based dry etching of high Q InP microdisks. J. Vac. Sci. Technol. B **20**, 301–305 (2002b)

Choi, S.J., Djordjev, K., Choi, S.J., Dapkus, P.D.: Microdisk lasers vertically coupled to output waveguides. IEEE Photon. Technol. Lett. **15**, 1330–1332 (2003)

Choi, S.J., Djordjev, K., Choi, S.J., Dapkus, P.D., Lin, W., Griffel, G., Menna, R., Connolly, J.: Microring resonators vertically coupled to buried heterostructure bus waveguides. IEEE Photon. Technol. Lett. **16**, 828–830 (2004a)

Choi, S.J., Djordjev, K., Peng, Z., Yang, Q., Choi, S.J., Dapkus, P.D.: Laterally coupled buried heterostructure high-Q ring resonators. IEEE Photon. Technol. Lett. **16**, 2266–2268 (2004b)

Choi, S.J., Peng, Z., Yang, Q., Choi, S.J., Dapkus, P.D.: Eight-channel microdisk cw laser arrays vertically coupled to common output bus waveguides. IEEE Photon. Technol. Lett. **16**, 356–358 (2004c)

Choi, S.J., Peng, Z., Yang, Q., Choi, S.J., Dapkus, P.D.: Tunable microdisk resonators vertically coupled to bus waveguides using epitaxial regrowth and wafer bonding techniques. Appl. Phys. Lett. **84**, 651–653 (2004d)

Choi, S.J., Peng, Z., Yang, Q., Hwang, E.H., Dapkus, P.D.: A semiconductor tunable laser using a wavelength selective reflector based on ring resonators. Proc. OFC/NFOEC 2005, Paper PDP20 (2005)

Chremmos, I., Uzunoglu, N.: Reflective properties of double-ring resonator system coupled to a waveguide. IEEE Photon. Technol. **17**, 2110–2112 (2005)

Christiaens, I.: Vertically coupled microring resonators fabricated with wafer bonding. Ph.D. Thesis, Ghent University, ISBN 90-8578-020-9 (2005)

Christiaens, I., Roelkens, G., De Mesel, K., Van Thourhout, D., Baets, R.: Thin-film devices fabricated with benzocyclobutene adhesive wafer bonding. IEEE J. Lightwave Technol. **23**, 517–523 (2004)

Chu, S.T., Little, B.E., Pan, W., Kaneko, T., Kokubun, Y.: Cascaded microring resonators for crosstalk reduction and spectrum cleanup in add–drop filters. IEEE Photon. Technol. Lett. **11**, 1423–1425 (1999a)

Chu, S.T., Little, B.E., Pan, W., Kaneko, T., Kokubun, Y.: Second-order filter response from parallel coupled glass microring resonators. IEEE Photon. Technol. Lett. **11**, 1426–1428 (1999b)

Chu, S.T., Little, B.E., Pan, W., Kaneko, T., Sato, S., Kokubun, Y.: An eight-channel add–drop filter using vertically coupled microring resonators over a cross grid. IEEE Photon. Technol. Lett. **11**, 691–693 (1999c)

Chu, S.T., Pan, W., Sato, S., Kaneko, T., Little, B.E., Kokubun, Y.: Wavelength trimming of a microring resonator filter by means of a UV sensitive polymer overlay. IEEE Photon. Technol. Lett. **11**, 688–690 (1999d)

Chu, S.T., Pan, W., Suzuki, S., Little, B.E., Sato, S., Kokubun, Y.: Temperature insensitive vertically coupled microring resonator add/drop filters by means of a polymer overlay. IEEE Photon. Technol. Lett. **11**, 1138–1140 (1999e)

Chung, Y., Kim, D.G., Dagli, N.: Widely tunable coupled-ring reflector laser diode. IEEE Photon. Technol. Lett. **17**, 1773–1775 (2005)

Cockerill, T.M., Osowski, M.L., Lammert, R.M., Coleman, J.J.: A strained-layer InGaAs–GaAs buried heterostructure circular ring laser with integrated y-coupled passive waveguide by selective-area metalorganic chemical vapor deposition. Proc. ISLC 195–196 (1994)

Coppinger, F., Madsen, C.K., Jalali, B.: Photonic microwave filtering using coherently coupled integrated ring resonators. Microwave Opt. Technol. Lett. **21**, 90–93 (1999)

Corbett, B.: Spectral characteristics of single-InGaAs quantum-well microring lasers. IEEE Photon. Technol. Lett. **10**, 3–5 (1998)

Corbett, B., Justice, J., Considine, L., Walsh, S., Kelly, W.M.: Low-threshold lasing in novel microdisk geometries. IEEE Photon. Technol. Lett. **8**, 855–857 (1996)

Dapkus, P.D., Choi, S.J., Choi, S.J., Djordjev, K., Sadagopan, T., Tishinin, D.: Microresonator devices for DWDM systems. Proc. OFC Paper WK 1–3 (2001)

Darmawan, S., Lee, S.Y., Lee, C.W., Chin, M.K.: A rigorous comparative analysis of directional couplers and multimode Interferometers based on ridge waveguides. IEEE J. Select. Top. Quantum Electron. **11**, 466–475 (2005)

Dehmubed, R.S., Diament, P.: Coupling of a planar waveguide and a dielectric disk. IEEE Trans. Microwave Theory Tech. **46**, 1461–1470 (1998)

Della Corte, F.G., Cocorullo, G., Iodice, M., Rendina, I.: Temperature dependence of the thermo-optic coefficient of InP, GaAs, and SiC from room temperature to 600 K at the wavelength of 1.5 μm. Appl. Phys. Lett. **77**, 1614–1616 (2000)

Djordjev, K.: Active microdisk resonant devices and semiconductor optical equalizers as building blocks for future photonic circuitry. Ph.D. Thesis, University of Southern California (2002)

Djordjev, K., Choi, S.J., Choi, S.J., Dapkus, P.D.: Active semiconductor microdisk devices. IEEE J. Lightwave Technol. **20**, 105–113 (2002a)

Djordjev, K., Choi, S.J., Choi, S.J., Dapkus, P.D.: Gain trimming of the resonant characteristics in vertically coupled InP microdisk switches. Appl. Phys. Lett. **80**, 3467–3469 (2002b)

Djordjev, K., Choi, S.J., Choi, S.J., Dapkus, P.D.: High-Q vertically coupled InP microdisk resonators. IEEE Photon. Technol. Lett. **14**, 331–333 (2002c)

Djordjev, K., Choi, S.J., Choi, S.J., Dapkus, P.D.: Microdisk tunable resonant filters and switches. IEEE Photon. Technol. Lett. **14**, 828–830 (2002d)

Djordjev, K., Choi, S.J., Choi, S.J., Dapkus, P.D.: Study of the effects of the geometry on the performance of vertically coupled InP microdisk resonators. IEEE J. Lightwave Technol. **20**, 1485–1492 (2002e)

Djordjev, K., Choi, S.J., Choi, S.J., Dapkus, P.D.: Vertically coupled InP microdisk switching devices with electroabsorptive active regions. IEEE Photon. Technol. Lett. **14**, 1115–1117 (2002f)

Dumon, P., Bogaerts, W., Wiaux, V., Wouters, J., Beckx, S., Van Campenhout, J., Taillaert, D., Luyssaert, B., Bienstman, P., Van Thourhout, D., Baets, R.: Low-loss SOI photonic wires and ring resonators fabricated with deep UV lithography. IEEE Photon. Technol. Lett. **16**, 1328–1330 (2004)

Emelett, S.J., Soref, R.: Design and simulation of silicon microring optical routing switches. IEEE J. Lightwave Technol. **23**, 1800–1807 (2005)

Faist, J., Gmachl, C., Striccoli, M., Sirtori, C., Capasso, F., Sivco, D.L., Cho, A.Y.: Quantum cascade disk lasers. Appl. Phys. Lett. **69**, 2456–2458 (1996)

Fan, S.: Sharp asymmetric line shapes in side-coupled waveguide-cavity systems. Appl. Phys. Lett. **80**, 908–910 (2002)

Feuchter, T., Thirstrup, C.: High precision planar waveguide propagation loss measurement technique using a Fabry–Perot cavity. IEEE Photon. Technol. Lett. **6**, 1244–1247 (1994)

Fiedler, F., Schlachetzki, A.: Optical parameters of InP-based waveguides. Solid-State Electron. **30**, 73–83 (1987)

Forber, R., Marom, E.: Symmetric directional coupler switches. IEEE J. Quantum Electron. **22**, 911–919 (1986)

Frateschi, N.C., Levi, A.F.J.: Resonant modes and laser spectrum of microdisk lasers. Appl. Phys. Lett. **66**, 2932–2934 (1995)

Fujita, M., Sakai, A., Baba, T.: Ultrasmall and ultralow threshold GaInAsP–InP microdisk injection lasers: Design, fabrication, lasing characteristics, and spontaneous emission factor. IEEE J. Select Topics Quantum Electron. **5**, 673–681 (1999)

Georgakilas, A., Deligeorgis, G., Aperathitis, E., Cengher, D., Hatzopoulos, Z., Alexe, M., Dragoi. V., Gösele, U., Kyriakis-Bitzaros, E.D., Minoglou, K.,

Halkias, G.: Wafer-scale integration of GaAs optoelectronic devices with standard Si integrated circuits using a low-temperature bonding procedure. Appl. Phys. Lett. **81**, 5099–5101 (2002)

Geuzebroek, D.: Flexible optical network components based on densely integrated microring resonators. Ph.D. Thesis, University of Twente, ISBN 90-365-2258-7 (2005)

Gheorma, I.L., Osgood, R.M.: Fundamental limitations of optical resonator based high-speed EO modulators. IEEE Photon. Technol. Lett. **14**, 795–797 (2002)

Gottesman, Y., Rao, E.V.K., Rabus, D.G.: New methodology to evaluate the performance of ring resonators using optical low-coherence reflectometry. IEEE J. Lightwave Technol. **6**, 1566–1572 (2004)

Griffel, G.: Synthesis of optical filters using ring resonator arrays. IEEE Photon. Technol. Lett. **12**, 810–812 (2000a)

Griffel, G.: Vernier effect in asymmetrical ring resonator arrays. IEEE Photon. Technol. Lett. **12**, 1642–1644 (2000b)

Griffel, G., Abeles, J.H., Menna, R.J., Braun, A.M., Connolly, J.C., King. M.: Low-threshold InGaAsP ring lasers fabricated using bi-level dry etching. IEEE Photon. Technol. Lett. **12**, 146–148 (2000)

Grover, R.: Indium phosphide based optical micro-ring resonators. Ph.D. Thesis, University of Maryland, College Park (2003)

Grover, R., Absil, P.P., Van, V., Hryniewicz, J., Little, B.E., King, O., Calhoun, L.C., Johnson, F.G., Ho, P.T.: Vertically coupled GaInAsP–InP microring resonators. Opt. Lett. **26**, 506–508 (2001a)

Grover, R., Absil, P.P., Van, V., Hryniewicz, J.V., Little, B.E., King, O., Johnson, F.G., Calhoun, L.C., Ho, P.T.: Vertically coupled GaAs–AlGaAs and GaInAsP–InP microring resonators. Proc. OFC Paper WK2-1 (2001b)

Grover, R., Hryniewicz, J.V., King, O.S., Van, V.: Process development of methane–hydrogen–argon-based deep dry etching of InP for high aspect-ratio structures with vertical facet-quality sidewalls. J. Vac Sci. Technol. B **19**, 1694–1698 (2001c)

Grover, R., Van, V., Ibrahim, T.A., Absil, P.P., Calhoun, L.C., Johnson, F.G., Hryniewicz, J.V., Ho, P.T.: Parallel-cascaded semiconductor microring resonators for high-order and wide-FSR filters. IEEE J. Lightwave Technol. **20**, 900–905 (2002)

Grover, R., Ibrahim, T.A., Ding, T.N., Leng, Y., Kuo, L.C., Kanakaraju, S., Amarnath, K., Calhoun, L.C., Ho, P.T.: Laterally coupled InP-based single-mode microracetrack notch filter. IEEE Photon. Technol. Lett. **15**, 1082–1084 (2003)

Grover, R., Ibrahim, T.A., Kanakaraju, S., Lucas, L., Calhoun, L.C., Ho, P.T.: A Tunable GaInAsP–InP Optical Microring Notch Filter. IEEE Photon. Technol. Lett. **16**, 467–469 (2004)

Haavisto, J., Pajer, G.A.: Resonance effects in low-loss ring waveguides. Opt. Lett. **5**, 510–512 (1980)

Haeiwa, H., Naganawa, T., Kokubun, Y.: Wide range center wavelength trimming of vertically coupled microring resonator filter by direct UV irradiation to SiN ring core. IEEE Photon. Technol. Lett. **16**, 135–137 (2004)

Hagness, S.: FDTD computational electromagnetics modeling of microcavity lasers and resonant optical structures. Ph.D. Thesis, Northwestern University (1998)

Hagness, S.C., Rafizadeh, D., Ho, S.T., Taflove, A.: FDTD Microcavity simulations: Design and experimental realization of waveguide-coupled single-mode ring and whispering-gallery-mode disk resonators. IEEE J. Lightwave Technol. **15**, 2154–2165 (1997)

Hakki, B.W., Paoli, T.L.: Gain spectra in GaAs double-heterostructure injection lasers. J. Appl. Phys **46**, 1299–1306 (1975)

Hamacher, M., Kaiser, R., Heidrich, H., Albrecht, P., Borchert, B., Janiak, K., Löffler, R., Malchow, S., Rehbein, W., Schroeter-Janßen, H.: Monolithic integration of lasers, photodiodes, waveguides and spot size converters on GaInAsP/InP for photonic IC applications. Proc. IPRM 21–24 (2000)

Hamacher, M., Troppenz, U., Heidrich, H., Rabus, D.G.: Active ring resonators based on GaInAsP/InP. Proc. of SPIE **4947**, 212–222 (2003)

Hammer, M.: Resonant coupling of dielectric optical waveguides via rectangular microcavities: The coupled guided mode perspective. Opt. Commun. **214**, 155–170 (2002)

Hammer, M., Yudistira, D., Stoffer, R.: Modeling of grating assisted standing wave microresonators for filter applications in integrated optics. Opt. Quantum Electron. **36**, 25–42 (2004)

Hansen, P.B., Raybon, G., Chien, M.D., Koren, U., Miller, B.I., Young, M.G., Verdiell, J.M., Burrus, C.A.: A 1.54 µm monolithic semiconductor ring laser: CW and mode-locked operation. IEEE Photon. Technol. Lett. **4**, 411–413 (1992)

Haruna, M., Segawa, Y., Nishihara, H.: Nondestructive and simple method of optical-waveguide loss measurement with optimization of end-fire coupling. Electron. Lett. **28**, 1612–1613 (1992)

Hatakeyama, Y., Hanai, T., Suzuki, S., Kokubun, Y.: Loss-Less multilevel crossing of busline waveguide in vertically coupled microring resonator filter. IEEE Photon. Technol. Lett. **16**, 473–475 (2004)

Hauffe, R.: Integrated optical switching matrices constructed from digital optical switches based on polymeric rib waveguides. Ph.D. Thesis, Technical University Berlin (2002)

Haxha, S., Ladely, E.O., Mjeku, M., AbdelMalek, F., Rahman, B.M.A.: Optimization of compact lateral, vertical, and combined tapered spot size converters by use of the beam-propagation method. Appl. Opt. **45**, 288–296 (2006)

Headley, W.R., Reed, G.T., Howe, S., Liu, A., Paniccia, M.: Polarization-independent optical racetrack resonators using rib waveguides on silicon-on-insulator. Appl. Phys. Lett. **85**, 5523–5525 (2004)

Heebner, J.E., Boyd, R.W., Park, Q.H.: SCISSOR solitons and other novel propagation effects in microresonator-modified waveguides. J. Opt. Soc. Am. B **19**, 722–731 (2002)

Heebner, J.E., Lepeshkin, N.N., Schweinsberg, A., Wicks, G.W., Boyd, R.W., Grover, R., Ho, P.T.: Enhanced linear and nonlinear optical phase response of AlGaAs microring resonators. Opt. Lett. **29**, 769–771 (2004)

Heiblum, M., Harris, J.: Analysis of curved optical waveguides by conformal transformation. IEEE J. Quantum Electron. **11**, 75–83 (1975)

Heimala, P., Katila, P., Aarnio, J., Heinämäki, A.: Thermally tunable integrated optical ring resonator with poly-Si thermistor. IEEE J. Lightwave Technol. **14**, 2260–2267 (1996)

Hibino, Y., Terui, H., Sugita, A., Ohmori, Y.: Silica-based optical waveguide ring laser integrated with semiconductor laser amplifier on Si substrate. Electron. Lett. **28**, 1932–1933 (1992)

Hida, Y., Imamura, S., Izawa, T.: Ring resonator composed of low loss polymer waveguides at 1.3 μm. Electron. Lett. **28**, 1314–1316 (1992)

Hidayat, I.S., Toyota, Y., Torigoe, O., Wada, O., Koga, R.: Multipath structure for FSR expansion in waveguide-based optical ring resonator. Electron. Lett. **39** (2003)

Hill, T.M., Dorren, H.J.S., de Vries, T., Leijtens, X.J.M., den Besten, J.H., Smalbrugge, B., Oei, J.S., Binsma, H., Khoe, G.D., Smit, M.K.: A fast low-power optical memory based on coupled micro-ring lasers. Nature **432**, 206–209 (2004)

Hiremath, K.R.: Coupled mode theory based modelling and analysis of circular optical microresonators. Ph.D. Thesis, University of Twente, ISBN 90-365-2267-6 (2005)

Hohimer, J.P., Vawter, G.A.: Unidirectional semiconductor ring lasers with racetrack cavities. Appl. Phys. Lett. **63**, 2457–2459 (1993)

Hohimer, J.P., Craft, D.C., Hadley, G.R., Vawter, G.A., Warren, M.E.: Single-frequency continuous-wave operation of ring resonator diode lasers. Appl. Phys. Lett. **59**, 3360–3362 (1991)

Hohimer, J.P., Vawter, G.A., Craft, D.C., Hadley, G.R.: Improving the performance of semiconductor ring lasers by controlled reflection feedback. Appl. Phys. Lett. **61**, 1013–1015 (1992)

Horst, F., Salemink, H.W.M., Germann, R., Offrein, B.J., Bona, G.L.: High quality ring resonators in high refractive index contrast SiON waveguides. Proc. 1998 IEEE/LEOS Symp. Benelux Chapter:33–36 (1998)

Horst, F., Berendsen, C., Beyeler, R., Bona, G.L., Germann, R., Salemink, H.W.M., Wiesmann, D.: Tunable ring resonator dispersion compensators realized in high-refractive-index contrast SiON technology. Proc. ECOC'2000, Post Deadline Paper PD 2.2 (2000)

Hryniewicz, J.V., Absil, P.P., Little, B.E., Wilson, R.A., Ho, P.T.: Higher order filter response in coupled microring resonators. IEEE Photon. Technol. Lett. **12**, 320–322 (2000)

Huang, Y., Paloczi, G.T., Scheuer, J., Yariv, A.: Soft lithography replication of polymeric microring optical resonators. Opt. Express **11**, 2452–2458 (2003)
Huang, Y., Paloczi, G.T., Poon, J.K.S., Yariv, A.: Demonstration of flexible freestanding all-polymer integrated optical ring resonator devices. Adv. Mater. **16**, 44–48 (2004)
Ibrahim, T.A.: Nonlinear optical semiconductor micro ring resoantors. Ph.D. Thesis, University of Maryland, College Park (2003)
Ibrahim, T.A., Van, V., Ho, P.T.: All-optical time-division demultiplexing and spatial pulse routing with a GaAs/AlGaAs microring resonator. Opt. Lett. **27**, 803–805 (2002)
Ibrahim, T.A., Cao, W., Kim, Y., Li, J., Goldhar, J., Ho, P.T., Lee, C.H.: All-optical switching in a laterally coupled microring resonator by carrier injection. IEEE Photon. Technol. Lett. **15**, 36–38 (2003a)
Ibrahim, T.A., Grover, R., Kuo, L.C., Kanakaraju, S., Calhoun, L.C., Ho, P.T.: All-optical AND/NAND logic gates using semiconductor microresonators. IEEE Photon. Technol. Lett. **15**, 1422–1424 (2003b)
Ibrahim, T.A., Cao, W., Kim, Y., Li, J., Goldhar, J., Ho, P.T., Lee, C.H.: Lightwave switching in semiconductor microring devices by free carrier injection. IEEE J. Lightwave Technol. **21**, 2997–3003 (2003c)
Ji, C., Leary, M.H., Ballantyne, J.M.: Long-wavelength triangular ring laser. IEEE Photon. Technol. Lett. **9**, 1469–1471 (1997)
Jiang, X., Li, X., Zhou, H., Yang, J., Wang, M., Wu, Y., Ishikawa, S.: Compact variable optical attenuator based on multimode interference coupler. IEEE Photon. Technol. Lett. **17**, 2361–2363 (2005)
Kaalund, C.J., Peng, G.D.: Pole-zero diagram approach to the design of ring resonator-based filters for photonic applications. IEEE J. Lightwave Technol. **22**, 1548–1559 (2004)
Kaiser, R., Heidrich, H.: Optoelectronic/Photonic integrated circuits on InP between technological feasibility and commercial success. IEICE Transactions on Electronics E85-C, 970–981 (2002)
Kaiser, R., Trommer, D., Heidrich, H., Fidorra, F., Hamacher, M.: Heterodyne receiver Pies as the first monolithically integrated tunable receivers for OFDM system applications. Opt. Quantum Electron. **28**, 565–573 (1996)
Kaminow, I.P., Stulz, L.W.: Loss in cleaved Ti-diffused LiNbO3 waveguides. Appl. Phys. Lett. **33**, 62–64 (1978)
Kaplan, A.: Modeling of ring resonators with tunable couplers. IEEE J. Select. Top. Quantum Electron. **12**, 86–95 (2006)
Kasaya, K., Mitomi, O., Naganuma, M., Kondo, Y., Noguchi, Y.: A simple laterally tapered waveguide for low-loss coupling to single-mode fibers. IEEE Photon. Technol. Lett. **5**, 345–347 (1993)
Katila, P., Heimala, P., Aarnio, J.: Thermo-optically controlled ring resonator on silicon. Electron. Lett. **32**, 1005–1006 (1996)
Keil, N., Yao, H.H., Zawadzki, C., Bauer, J., Bauer, M., Dreyer, C., Schneider, J.: Athermal all-polymer arrayed-waveguide grating multiplexer. Electron. Lett. **37**, 579–580 (2001)

Kim, M.J., Carpenter, R.W.: Heterogeneous silicon integration by ultra-high vacuum wafer bonding. J. Electron. Mater. **32**, 849–854 (2003)

Kim, S.H., Ryu, H.Y., Park, H.G., Kim, G.H., Choi, Y.S., Lee, Y.H., Kim, J.S.: Two-dimensional photonic crystal hexagonal waveguide ring laser. Appl. Phys. Lett. **81**, 2499–2501 (2002)

Kim, D.H., Im, J.G., Lee, S.S., Ahn, S.W., Lee, K.D.: Polymeric microring resonator using nanoimprint technique based on a stamp incorporating a smoothing buffer layer. IEEE Photon. Technol. Lett. **17**, 2352–2354 (2005a)

Kim, D.G., Shin, J.H., Ozturk, C., Yi, J.C., Chung, Y., Dagli, N.: Total internal reflection mirror-based InGaAsP ring resonators integrated with optical amplifiers. IEEE Photon. Technol. Lett. **17**, 1899–1901 (2005b)

Kim, H.S., Kwon, Y.S., Hong, S.: Square ring laser diode with MMI coupler cavity. IEEE Photon. Technol. Lett. **9**, 584–586 (1997)

Kiyat, I., Kocabas, C., Aydinli, A.: Integrated micro ring resonator displacement sensor for scanning probe microscopies. J. Micromechanics Microengineering **14**, 374–381 (2004)

Kiyat, I., Aydinli, A., Dagli, N.: Polarization characteristics of compact SOI rib waveguide racetrack resonators. IEEE Photon. Technol. Lett. **17**, 2098–2100 (2005)

Kiyat, I., Aydinli, A., Dagli, N.: Low-power thermooptical tuning of SOI resonator switch. IEEE Photon. Technol. Lett. **18**, 364–366 (2006)

Klunder, D.J.W., Krioukov, E., Tan, F.S., Van der Veen, T., Bulthuis, H.F., Sengo, G., Otto, C., Hoekstra, H.J.W.M., Driessen, A.: Vertically and laterally waveguide-coupled cylindrical microresonators in Si_3N_4 on SiO_2 technology. Appl. Phys. B: Laser Opt. **73**, 603–608 (2001)

Klunder, D.J.W., Balistreri, M.L.M., Blom, F.C., Hoekstra, H.J.W.M., Driessen, A., Kuipers, L., van Hulst, N.F.: Detailed analysis of the intracavity phenomena inside a cylindrical microresonator. IEEE J. Lightwave Technol. **20**, 519–529 (2002a)

Klunder, D.J.W., Roeloffzen, C.G.H., Driessen, A.: A novel polarization-independent wavelength-division-multiplexing filter based on cylindrical microresonators. IEEE J. Select. Top. Quantum Electron. **8**, 1294–1299 (2002b)

Klunder, D.J.W., Hoekstra, H.J.W.M., Driessen, A.: A normalized approach for designing cylindrical microresonators. IEEE J. Lightwave Technol. **21**, 1405–1410 (2003a)

Klunder, D.J.W., Tan, F.S., van der Veen, T., Bulthuis, H.F., Sengo, G., Docter, B., Hoekstra, H.J.W.M., Driessen, A.: Experimental and numerical study of SiON microresonators with air and polymer cladding. IEEE J. Lightwave Technol. **21**, 1099–1110 (2003b)

Kohtoku, M., Oku, S., Kadota, Y., Shibata, Y., Yoshikuni, Y.: 200-GHz FSR Periodic multi/demultiplexer with flattened transmission and rejection band by using a Mach–Zehnder interferometer with a ring resonator. IEEE Photon. Technol. Lett. **12**, 1174–1176 (2000)

Kokubun, Y.: Vertically coupled microring resonator filter for integrated add/drop node. IEICE Trans. Electron. **3**, 349–362 (2005)

Kokubun, Y., Funato, N., Takizawa, M.: Athermal waveguides for temperature-independent lightwave devices. IEEE Photon. Technol. Lett. **5**, 1297–1300 (1993)

Kokubun, Y., Yoneda, S., Tanaka, H.: Temperature-independent narrow-band optical filter by an athermal waveguide. IEICE Trans. Electron. E80-C, 632–639 (1997)

Kokubun, Y., Kubota, S., Chu, S.T.: Polarization-independent vertically coupled microring resonator filter. Electron. Lett. **37**, 90–92 (2001)

Kokubun, Y., Kato, T., Chu, S.T.: Box-like response of microring filter by stacked double-ring geometry. IEICE Trans. Electron. E85-C, 1018–1024 (2002)

Kokubun, Y., Hatakeyama, Y., Ogata, M., Suzuki, S., Zaizen, N.: Fabrication technologies for vertically coupled microring resonator with multilevel crossing busline and ultracompact-ring radius. J. Select. Top. Quantum Electron. **11**, 4–10 (2005)

Koonath, P., Kishima, K., Indukuri, T., Jalali, B.: Sculpting of three-dimensional nano-optical structures in silicon. Appl. Phys. Lett. **83**, 4909–4911 (2003)

Koonath, P., Indukuri, T., Jalali, B.: Vertically-coupled micro-resonators realized using three-dimensional sculpting in silicon. Appl. Phys. Lett. **85**, 1018–1020 (2004)

Koonath, P., Indukuri, T., Jalalib, B.: Add–drop filters utilizing vertically coupled microdisk resonators in silicon. Appl. Phys. Lett. **86**, 091102 (2005)

Krauss, T.F., Laybourn, P.J.R., Roberts, J.: CW operation of semiconductor ring lasers. Electron. Lett. **26**, 2095–2097 (1990)

Krauss, T., DeLaRue, R.M., Gontijo, I., Laybourn, P.J.R.: Strip-loaded semiconductor ring lasers employing multimode interference output couplers. Appl. Phys. Lett. **64**, 2788–2790 (1994)

Krauss, T.F., De La Rue, R.M., Laybourn, P.J.R.: Impact of output coupler configuration on operating characteristics of semiconductor ring lasers. IEEE J. Lightwave Technol. **13**, 1500–1507 (1995a)

Krauss, T.F., De La Rue, R.M., Laybourn, P.J.R., Vögele, B., Stanley, C.R.: Efficient semiconductor ring lasers made by a simple self-aligned fabrication process. IEEE J. Select. Top. Quantum Electron. **1**, 757–761 (1995b)

Krioukov, E., Klunder, D.J.W., Driessen, A., Greve, J., Otto, C.: Sensor based on an integrated optical microcavity. Opt. Lett. **27**, 512–514 (2002)

Ksendzov, A., Homer, M.L., Manfreda, A.M.: Integrated optics ring-resonator chemical sensor with polymer transduction layer. Electron. Lett. **40**, 63–65 (2004)

Lee, H.S., Choi, C.H., Beom-Hoan, O., Park, D.G., Kang, B.G., Kim, S.H., Lee, S.G., Lee, E.H.: A nonunitary transfer matrix method for practical analysis of racetrack microresonator waveguide. IEEE Photon. Technol. Lett. **16**, 1086–1088 (2004)

Lee, M.C.M., Wu, M.C.: MEMS-actuated microdisk resonators with variable power coupling ratios. IEEE Photon. Technol. Lett. **17**, 1034–1036 (2005)
Leinse, A.: Polymeric microring resonator based electro optic modulator. Ph.D. Thesis, University of Twente, ISBN 90-365-2168-8 (2005)
Lenz, G., Madsen, C.K.: General optical all-pass filter structures for dispersion control in WDM systems. IEEE J. Lightwave Technol. **17**, 1248–1254 (1999)
Lenz, G., Eggleton, B.J., Madsen, C.K., Slusher, R.E.: Optical delay lines based on optical filters. IEEE J. Quantum Electron. **37**, 525–532 (2001)
Leuthold, J., Joyner, C.H.: Multimode interference couplers with tuneable splitting ratios. Proc. ECOC **3**, 177–178 (2000)
Leuthold, J., Joyner, C.H.: Multimode interference couplers with tunable power splitting ratios. IEEE J. Lightwave Technol. **19**, 700–707 (2001)
Levi, A.F.J.: Microdisk lasers. Solid-State Electron. **37**, 1297–1302 (1994)
Liao, A.S.H., Wang, S.: Semiconductor injection lasers with a circular resonator. Appl. Phys. Lett. **36**, 801–803 (1980)
Little, B.E., Chu, S.T.: Estimating surface-roughness loss and output coupling in microdisk resonators. Opt. Lett. **21**, 1390–1392 (1996)
Little, B.E., Murphy, T.: Design rules for maximally flat wavelength-insensitive optical power dividers using Mach–Zehnder structures. IEEE Photon. Technol. Lett. **9**, 1607–1609 (1997)
Little, B.E., Laine, J.P., Chu, S.T.: Surface-roughness-induced contradirectional coupling in ring and disk resonators. Opt. Lett. **22**, 4–6 (1997a)
Little, B.E., Chu, S.T., Haus, H.A., Foresi, J., Laine, J.P.: Microring resonator channel dropping filters. IEEE J. Lightwave Technol. **15**, 998–1005 (1997b)
Little, B.E., Foresi, J.S., Steinmeyer, G., Thoen, E.R., Chu, S.T., Haus, H.A., Ippen, E.P., Kimerling, L.C., Greene, W.: Ultra-compact Si–SiO microring resonator optical channel dropping filters. IEEE Photon. Technol. Lett. **10**, 549–551 (1998a)
Little, B.E., Haus, H.A., Foresi, J.S., Kimerling, L.C., Ippen, E.P., Ripin, D.J.: Wavelength switching and routing using absorption and resonance. IEEE Photon. Technol. Lett. **10**, 816–818 (1998b)
Little, B.E., Chu, S.T., Pan, W., Ripin, D., Kaneko, T., Kokubun, Y., Ippen, E.: Vertically coupled glass microring resonator channel dropping filters. IEEE Photon. Technol. Lett. **11**, 215–217 (1999)
Little, B.E., Chu, S.T.: Theory of loss and gain trimming of resonator-type filters. IEEE Photon. Technol. Lett. **12**, 636–638 (2000)
Little, B.E., Chu, S.T., Hryniewicz, J.V., Absil, P.P.: Filter synthesis for periodically coupled microring resonators. Opt. Lett. **25**, 344–346 (2000a)
Little, B.E., Chu, S.T., Pan, W., Kokubun, Y.: Microring resonator arrays for VLSI photonics. IEEE Photon. Technol. Lett. **12**, 323–325 (2000b)
Little, B.E., Chu, S.T., Absil, P.P., Hryniewicz, J.V., Johnson, F.G., Seiferth, F., Gill, D., Van, V., King, O., Trakalo, M.: Very high-order microring resonator filters for WDM applications. IEEE Photon. Technol. Lett. **16**, 2263–2265 (2004)

Liu, B., Shakouri, A., Bowers, J.E.: Passive microring-resonator-coupled lasers. Appl. Phys. Lett. **79**, 3561–3563 (2001)

Liu, B., Shakouri, A., Bowers, J.E.: Wide tunable double ring resonator coupled lasers. IEEE Photon. Technol. Lett. **14**, 600–602 (2002a)

Liu, B., Shakouri, A., Rabus, D.G.: Passive microring resonator coupled lasers. Proc. IEEE LEOS Annual Meeting, 742–743 (2002b)

Lui, W.W., Hirono, T., Yokoyama, K., Huang, W.P.: Polarization rotation in semiconductor bending waveguides: A coupled-mode theory formulation. IEEE J. Lightwave Technol. **16**, 929–936 (1998)

Ma, Y., Chang, G., Chang, S., Ho, S.T.: Optical filter responses of InGaAsP microdisk resonators fabricated by polymer wafer bonding. Proc. OFC Paper WY4 (2000a)

Ma, Y., Park, S., Wang, L., Ho, S.T.: Ultracompact multimode interference 3 dB coupler with strong lateral confinement by deep dry etching. IEEE Photon. Technol. Lett. **12**, 492–494 (2000b)

Ma, Y., Chang, G., Park, S., Wang, L., Ho, S.T.: InGaAsP thin-film microdisk resonators fabricated by polymer wafer bonding for wavelength add–drop filters. IEEE Photon. Technol. Lett. **12**, 1495–1497 (2000c)

Ma, Y., Chang, S.H., Chang, S.S., Ho, S.T.: Improved optical filter responses in cascaded InGaAsP/InP microdisk resonators. Electron. Lett. **37**, 564–565 (2001)

Ma, H., Jen, A.K.Y., Dalton, L.R.: Polymer-based optical waveguides: Materials, processing, and devices. Adv. Mater. **14**, 1339–1365 (2002)

Ma, C., Xu, Y., Yan, X., Qin, Z., Wang, X.: Effect of ring spacing on spectral response of parallel-cascaded microring resonator arrays. Opt. Quantum Electron. **37**, 561–574 (2005)

Madsen, C.K., Zhao, J.H.: A general planar waveguide autoregressive optical filter. IEEE J. Lightwave Technol. **14**, 437–447 (1996)

Madsen, C.K., Zhao, J.H.: Postfabrication optimization of an autoregressive planar waveguide lattice filter. Appl. Opt. **36**, 642–647 (1997)

Madsen, C.K., Zhao, J.H.: Optical filter design and analysis, Wiley, New York (1999)

Madsen, C.K., Lenz, G., Bruce, A.J., Capuzzo, M.A., Gomez, L.T., Nielsen, T.N., Brener, I.: Multistage dispersion compensator using ring resonators. Opt. Lett. **24**, 1555–1557 (1999a)

Madsen, C.K., Lenz, G., Bruce, A.J., Cappuzzo, M.A., Gomez, L.T., Scotti, R.E.: Integrated all-pass filters for tunable dispersion and dispersion slope compensation. IEEE Photon. Technol. Lett. **11**, 1623–1625 (1999b)

Madsen, C.K., Cappuzzo, M., Laskowski, E.J., Chen, E., Gomez, L., Griffin, A., Wong-Foy, A., Chandrasekhar, S., Stulz, L., Buhl, L.: Versatile integrated PMD emulation and compensation elements. IEEE J. Lightwave Technol. **22**, 1041–1050 (2004)

Maolatou, C., Khan, M.J., Fan, S., Villeneuve, P.R., Haus, H.A., Joannopolous, J.D.: Coupling of modes analysis of resonant channel add-drop filters. IEEE J. Quantum Electron. **35**, 1322–1331 (1999)

Marcatili, E.A.J.: Bends in optical dielectric guides. Bell Syst. Techn. J. **48**, 2103–2132 (1969a)

Marcatili, E.A.J.: Dielectric rectangular waveguide and directional coupler for integrated optics. Bell Syst. Techn. Journal **48**, 2071–2101 (1969b)

Matsko, A.B., Ilchenko, V.S.: Optical resonators with whispering gallery Modes – Part I: Basics. IEEE J. Select. Top. Quantum Electron. **12**, 3–14 (2006a)

Matsko, A.B., Ilchenko, V.S.: Optical resonators with whispering gallery Modes – Part II: Applications. IEEE J. Select. Top. Quantum Electron. **12**, 15–32 (2006b)

McCall, S.L., Levi, A.F.J., Slusher, R.E., Pearton, S.J., Logan, R.A.: Whispering-gallery mode microdisk lasers. Appl. Phys. Lett. **60**, 289–291 (1992)

Melloni, A.: Synthesis of a parallel-coupled ring-resonator filter. Opt. Lett. **26**, 917–919 (2001)

Melloni, A., Carniel, F., Costa, R., Martinelli, M.: Determination of bend mode characteristics in dielectric waveguides. IEEE J. Lightwave Technol. **19**, 571–577 (2001)

Melloni, A., Martinelli, M.: Synthesis of direct-coupled-resonators bandpass filters for WDM systems. IEEE J. Lightwave Technol. **20**, 296–303 (2002)

Melloni, A., Costa, R., Monguzzi, P., Martinelli, M.: Ring-resonator filters in silicon oxynitride technology for dense wavelength-division multiplexing systems. Opt. Lett. **28**, 1567–1569 (2003a)

Melloni, A., Morichetti, F., Martinelli, M.: Linear and nonlinear pulse propagation in coupled resonator slow-wave optical structures. Opt. Quantum Electron. **35**, 365–379 (2003b)

Menon, V.M., Tong, W., Forrest, S.R.: Control of quality factor and critical coupling in microring resonators through integration of a semiconductor optical amplifier. IEEE Photon. Technol. Lett. **16**, 1343–1345 (2004)

Michelotti, F., Driessen, A., Bertolotti, M. (eds.): Microresonators as building blocks for VLSI photonics. AIP Conf. Proc. 709, Melville, New York (2004)

Mikroulis, S., Bogris, A., Roditi, E., Syvridis, D.: Investigation of an all-optical wavelength converter with reshaping properties based on four-wave mixing in passive microring resonators. IEEE J. Lightwave Technol. **22**, 2743–2746 (2004)

Mikroulis, S., Simos, H., Roditi, E., Syvridis, D.: Ultrafast all-optical and logic operation based on four-wave mixing in a passive InGaAsP–InP microring resonator. IEEE Photon. Technol. Lett. **17**, 1878–1880 (2005)

Morichetti, F., Melloni, A.: Polarization converters based on ring resonator phase shifters. IEEE Photon. Technol. Lett. **18**, 923–925 (2006)

Moslehi, B., Goodman, J.W., Tur, M., Shaw, H.J.: Fiber-optic lattice signal processing. Proc. IEEE 72, 909–930 (1984)

Mule', A.V., Villalaz, R., Gaylord, T.K., Meindl, J.D.: Photopolymer-based diffractive and MMI waveguide couplers. IEEE Photon. Technol. Lett. **16**, 2490–2492 (2004)

Murphy, T.E., Little, B.E., Smith, H.I.: Wavelength- and polarization-insensitive integrated directional couplers using Mach-Zehnder structures. Proc. IPR Paper RTuA5 (1999)

Nabiev, R.F., Francis, D., Chang-Hasnain, C.J.: Lateral and longitudinal mode discrimination in index-guided circular ring semiconductor lasers. IEEE Photon. Technol. Lett. **5**, 975–978 (1993)

Nagai, S., Morishima, G., Yagi, M., Utaka, K.: InGaAsP/InP Multi-mode interference photonic switches for monolithic photonic integrated circuits. Japan. J. Appl. Phys. **38**, 1269–1272 (1999)

Neumann, E.G.: Curved dielectric optical waveguides with reduced transition losses. IEEE Proc. H: Microwaves Opt. Antennas **129**, 278–279 (1982a)

Neumann, E.G.: Low loss dielectric optical waveguide bends. Fiber Integrated Opt. **4**, 203–211 (1982b)

Neumann, E.G., Richter, W.: Sharp bends with low losses in dielectric optical waveguides. Appl. Opt. **22**, 1016–1022 (1983)

Nielson, G.N., Seneviratne, D., Lopez-Royo, F., Rakich, P.T., Giacometti, F., Tuller, H.L., Barbastathis, G.: MEMS based wavelength selective optical switching for integrated photonic circuits. Proc. CLEO (2004)

Numai, T.: Analysis of photon recycling in semiconductor ring lasers. Jpn. J. Appl. Phys. **39**, 6535–6538 (2000)

Obayya, S.S.A., Rahman, B.M.A., Grattan, K.T.V., El-Mikati, H.A.: Beam propagation modeling of polarization rotation in deeply etched semiconductor bent waveguides. IEEE Photon. Technol. Lett. **13**, 681–683 (2001)

Oda, K., Takato, N., Toba, H.: A wide-FSR waveguide double-ring resonator for optical FDM transmission systems. IEEE J. Lightwave Technol. **9**, 728–736 (1991)

Oda, K., Suzuki, S., Takahashi, H., Toba, H.: An optical FDM distribution experiment using a high finesse waveguide-type double ring resonator. IEEE Photon. Technol. Lett. **6**, 1031–1034 (1994)

Ohno, T., Ishii, H., Matsuo, S., Okamoto, H., Kawaguchi, Y., Kondo, Y., Furuta, T., Ito, H., Yoshikuni, Y.: Hybrid modelocking of semiconductor ring lasers incorporating passive deep-ridge waveguides. Electron. Lett. **38**, 884–886 (2002)

Okamoto, H., Haraguchi, M., Fukui, M., Okamoto, T.: Optical filtering by microring resonators. Jpn. J. Appl. Phys. **42**, 2692–2698 (2003)

Orta, R., Savi, P., Tascone, R., Trinchero, D.: Synthesis of multiple-ring-resonator filters for optical systems. IEEE Photon. Technol. Lett. **7**, 1447–1449 (1995)

Painter, O.J., Husain, A., Scherer, A., O'Brien, J.D., Kim, I., Dapkus, P.D.: Room temperature photonic crystal defect lasers at near-infrared wavelengths in InGaAsP. IEEE J. Lightwave Technol. **17**, 2082–2088 (1999)

Paloczi, G.T., Huang, Y., Yariv, A.: Free-standing all-polymer microring resonator optical filter. Electron. Lett. **39**, 1650–1651 (2003a)

Paloczi, G.T., Huang, Y., Yariv, A., Mookherjea, S.: Polymeric Mach–Zehnder interferometer using serially coupled microring resonators. Opt. Express **11**, 2666–2671 (2003b)

Park, H.G., Hwang, J.K., Huh, J., Ryu, H.J., Kim, S.H., Kim, J.S., Lee, Y.H.: Characteristics of modified single-defect two-dimensional photonic crystal lasers. IEEE J. Quantum Electron. **38**, 1353–1365 (2002)

Park, K.H., Kim, M.W., Byun, Y.T., Woo, D., Kim, S.H., Choi, S.S., Chung, Y., Cho, W.R., Park, S.H., Kim, U.: Nondestructive propagation loss and facet reflectance measurements of GaAs/AlGaAs strip-loaded waveguides. J. Appl. Phys. **78**, 6318–6320 (1995)

Park, S., Kim, S.S., Wang, L., Ho, S.T.: Single-mode lasing operation using a microring resonator as a wavelength selector. IEEE J. Quantum Electron. **38**, 270–273 (2002)

Pennings, E.C.M., Deri, R.J., Hawkins, R.J.: Simple method for estimating usable bend radii of deeply etched optical rib waveguides. Electron. Lett. **27**, 1532–1534 (1991)

Pennings, E.C.M., van Roijen, R., van Stralen, M.J.N., Verbeek, B.H., van der Heijden, J.M.M., van Dongen, T.: Spectral behaviour of InP-based ring lasers employing multimode interference devices. Proc. IEEE LEOS Annual Meeting, 617–618 (1993)

Pennings, E.C.M., van Roijen, R., van Stralen, M.J.N., de Waard, P.J., Koumans, R.G.M.P., Verbeek, B.H.: Reflection properties of multimode interference devices. IEEE Photon. Technol. Lett. **6**, 715–718 (1994)

Pereira, S., Sipe, J.E., Heebner, J.E., Boyd, R.W.: Gap solitons in a two-channel microresonator structure. Opt. Lett. **27**, 536–538 (2002)

Poon, J.K.S., Huang, Y., Paloczi, G.T., Yariv, A.: Soft lithography replica molding of critically coupled polymer microring resonators. IEEE Photon. Technol. Lett. **16**, 2496–2498 (2004a)

Poon, J.K.S., Huang, Y., Paloczi, G.T., Yariv, A., Zhang, C., Dalton, L.R.: Wide-range tuning of polymer microring resonators by the photobleaching of CLD-1 chromophores. Opt. Lett. **29**, 2584–2586 (2004b)

Poon, J.K.S., Scheuer, J., Mookherjea, S., Paloczi, G.T., Huang, Y., Yariv, A.: Matrix analysis of microring coupled-resonator optical waveguides. Opt. Express **12**, 90–103 (2004c)

Poon, J.K.S., Scheuer, J., Xu, Y., Yariv, A.: Designing coupled-resonator optical waveguide delay lines. J. Opt. Soc. Am. B **21**, 1665–1673 (2004d)

Poon, J.K.S. Scheuer, J., Yariv, A.: Wavelength-selective reflector based on a circular array of coupled microring resonators. IEEE Photon. Technol. Lett. **16**, 1331–1333 (2004e)

Pradhan, S., Schmidt, B., Martinez, L., Xu, Q., Almeida, V.R., Barrios, C., Lipson, M.: Electro-optic modulator on silicon-on-insulator substrates using ring resonators. Proc. CLEO **1**, 107–109 (2005)

Quidant, R., Weeber, J.C., Dereux, A., Leveque, G., Weiner, J., Girard, C.: Addressing and imaging microring resonators with optical evanescent light. Phys. Rev. B **69**, 081402(R) (2004)

Rabiei, P., Steier, W.H., Zhang, C., Dalton, L.R.: Polymer Micro-ring filters and modulators. IEEE J. Lightwave Technol. **20**, 1968–1975 (2002a)
Rabiei, P., Steier, W.H., Zhang, C., Wang, C.G., Lee, H.J.: Polymer micro-ring modulator with 1 THz FSR. Proc. CLEO Post Deadline Paper (2002b)
Rabiei, P.: Electro-optic and thermo-optic polymer micro-ring resonators and their applications. Ph.D. Thesis, University of Southern California (2003)
Rabiei, P., Steier, W.H.: Tunable polymer double micro-ring filters. IEEE Photon. Technol. Lett. **15**, 1255–1257 (2003)
Rabiei, P.: Calculation of losses in micro-ring resonators with arbitrary refractive index or shape profile and its applications. IEEE J. Lightwave Technol. **23**, 1295–1301 (2005)
Raburn, M., Liu, B., Abraham, P., Bowers, J.E.: Double-bonded InP–InGaAsP vertical coupler 1:8 beam splitter. IEEE Photon. Technol. Lett. **12**, 1639–1641 (2000)
Rabus, D.G.: Realization of optical filters using ring resonators with integrated semiconductor optical amplifiers in GaInAsP/InP. Der Andere Verlag (2002)
Rabus, D.G., Hamacher, M.: MMI-coupled ring resonators in GaInAsP–InP, IEEE Photon. Technol. Lett. **8**, 812–814 (2001)
Rabus, D.G., Hamacher, M., Heidrich, H.: Resonance frequency tuning of a double ring resonator on GaInAsP/InP: Experiment and simulation. Japan. J. Appl. Phys. **41**, 1186–1189 (2002a)
Rabus, D.G., Hamacher, M., Heidrich, H., Troppenz, U.: High Q channel dropping filters using ring resonators with integrated SOAs. IEEE Photon. Technol. Lett. 10, 1442–1444 (2002b)
Rabus, D.G., Hamacher, M., Troppenz, U., Heidrich, H.: Optical filters based on ring resonators with integrated semiconductor optical amplifiers in GaInAsP/InP. IEEE J. Select. Topics Quantum Electron. **6**, 1405–1411 (2002c)
Rabus, D.G., Bian, Z., Shakouri, A.: A GaInAsP/InP double ring resonator coupled laser. IEEE Photon. Technol. Lett. **9**, 1770–1772 (2005a)
Rabus, D.G., Henzi, P., Mohr, J.: Photonic integrated circuits by DUV-induced modification of polymers. IEEE Photon. Technol. Lett. **3**, 591–593 (2005b)
Rafizadeh, D.: Experimental realization of nanofabricated semiconductor waveguide-coupled microcavity ring and disk optical resources. Ph.D. Thesis, Northwestern University (1997)
Rafizadeh, D., Zhang, J.P., Hagness, S.C., Taflove, A., Stair, K.A., Ho, S.T.: Temperature tuning of microcavity ring and disk resonators at 1.5 μm. Proc. IEEE LEOS Ann. Meet. 162–163 (1997a)
Rafizadeh, R., Zhang, J.P., Hagness, S.C., Taflove, A., Stair, K.A., Ho, S.T., Tiberio, R.C.: Waveguide-coupled AlGaAs/GaAs microcavity ring and disk resonators with high finesse and 21.6 nm free spectral range. Opt. Lett. **22**, 1244–1246 (1997b)

Rafizadeh, D., Zhang, J.P., Tiberio, R.C., Ho, S.T.: Propagation loss measurements in semiconductor microcavity ring and disk resonators. IEEE J. Lightwave Technol. **16**, 1308–1314 (1998)

Rayleigh: The problem of the whispering gallery. Cambridge University Scientific Papers **5**, 617–620 (1912). Also published in the Philos. Mag. **20**, 1001–1004, (1910)

Regener, R., Sohler, W.: Loss in low finesse Ti : $LiNbO_3$ optical waveguide resonators. Appl. Phys. B **36**, 143–147 (1985)

Rezzonico, D., Guarino, A., Herzog, C., Jazbinsek, M., Gunter, P.: High-finesse laterally coupled organic–inorganic hybrid polymer microring resonators for VLSI photonics. IEEE Photon. Technol. Lett. **18**, 865–867 (2006)

Rommel, S.L., Jang, J.H., Lu, W., Cueva, G., Zhou, L., Adesida, I., Pajer, G., Whaley, R., Lepore, A., Schellanbarger, Z., Abeles, J.H.: Effect of H_2 on the etch profile of InP/InGaAsP alloys in $Cl_2/Ar/H_2$ inductively coupled plasma reactive ion etching chemistriesfor photonic device fabrication. J. Vac. Sci. Technol. B **20**, 1327–1330 (2002)

Sadagopan, T., Choi, S.J., Choi, S.J., Dapkus, P.D., Bond, A.E.: Optical modulators based on depletion width translation in semiconductor microdisk resonators. IEEE Photon. Technol. Lett. **17**, 567–569 (2005)

Sakamoto, S.R., Ozturk, C., Byun, Y.T., Ko, J., Dagli, N.: Low-loss substrate-removed (SURE) optical waveguides in GaAs–AlGaAs epitaxial layers embedded in organic polymers. IEEE Photon. Technol. Lett. **10**, 985–987 (1998)

Savchenkov, A.A., Ilchenko, V.S., Matsko, A.B., Maleki, L.: Tunable filter based on whispering gallery modes. Electron. Lett. **39**, 389–391 (2003)

Schwelb, O.: Transmission, group delay, and dispersion in single-ring optical resonators and add/drop filters – a tutorial overview. IEEE J. Lightwave Technol. **22**, 1380–1394 (2004)

Schwelb, O., Frigyes, I.: All-optical tunable filters built with discontinuity-assisted ring resonators. IEEE J. Lightwave Technol. **19**, 380–386 (2001)

Seo, C., Chen, J.C.: Low transition losses in bent rib waveguides. IEEE J. Lightwave Technol. **14**, 2255–2259 (1996)

Slusher, R.E., Levi, A.F.J., Mohideen, U., McCall, S.L., Pearton, S.J., Logan, R.A.: Threshold characteristics of semiconductor microdisk lasers. Appl. Phys. Lett. **63**, 1310–1312 (1993)

Smit, M.K., Pennings, E.C.M., Blok, H.: A normalized approach to the design of low-loss optical waveguide bends. IEEE J. Lightwave Technol. **11**, 1737–1742 (1993)

Soldano, L.B., Pennings, E.C.M.: Optical multi-mode interference devices based on self-imaging: Principles and applications. IEEE J. Lightwave Technol. **13**, 615–627 (1995)

Song, D.S., Hwang, J.K., Kim, C.K., Han, I.Y., Jang, D.H., Lee, Y.H.: InGaAsP microdisk lasers on AlxOy. IEEE Photon. Technol. Lett. **12**, 954–956 (2000)

Song, J.H., Park, J.W., Sim, E.D., Baek, Y.: Measurements of coupling and reflection characteristics of butt-joints in passive waveguide integrated laser diodes. IEEE Photon. Technol. Lett. **17**, 1791–1793 (2005)

Sorel, M., Gluck, S., Laybourn, P.J.R.: Semiconductor double ring waveguide resonators. Electron. Lett. **35**, 1551–1552 (1999)

Sorel, M., Laybourn, P.J.R., Giuliani, G., Donati, S.: Unidirectional bistability in semiconductor waveguide ring lasers. Appl. Phys. Lett. **80**, 3051–3053 (2002)

Sorel, M., Giuliani, G., Scirè, A., Miglierina, R., Donati, S., Laybourn, P.J.R.: Operating regimes of GaAs–AlGaAs semiconductor ring lasers: Experiment and model. IEEE J. Quantum Electron. **39**, 1187–1195 (2003)

Sparacin, D.K., Lock, J.P., Hong, C.Y., Gleason, K.K., Kimerling, L.C., Michel, J.: Trimming of silicon nitride microring resonators with a polysilane top cladding. Proc. Group IV Photonics, 117–119 (2005)

Spiekman, L.H., Oei, Y.S., Metaal, E.G., Groen, F.H., Moerman, I., Smit, M.K.: Extremely small multimode interference couplers and ultrashort bends on InP by deep etching. IEEE Photon. Technol. Lett. **6**, 1008–1010 (1994)

Subramaniam, V., De Brabander, G.N., Naghski, D.H., Boyd, J.T.: Measurement of mode field profiles and bending and transition losses in curved optical channel waveguides. IEEE J. Lightwave Technol. **15**, 990–997 (1997)

Sumetsky, M.: Vertically-stacked multi-ring resonator. Opt. Express **13**, 6354–6375 (2005)

Suzuki, S., Shuto, K., Hibino, Y.: Integrated-optic ring resonators with two stacked layers of silica waveguide on Si. IEEE Photon. Technol. Lett. **4**, 1256–1258 (1992)

Suzuki, S., Yanagisawa, M., Hibino, Y., Oda, K.: High-density integrated planar lightwave circuits using SiO_2–GeO_2 waveguides with a high refractive index difference. IEEE J. Lightwave Technol. **12**, 790–796 (1994)

Suzuki, S., Oda, K., Hibino, Y.: Integrated-optic double-ring resonators with a wide free spectral range of 100 GHz. IEEE J. Lightwave Technol. **13**, 1766–1771 (1995)

Suzuki, S., Kokubun, Y., Nakazawa, M., Yamamoto, T., Chu, S.T.: Ultrashort optical pulse transmission characteristics of vertically coupled microring resonator add/drop filter. IEEE Photon. Technol. Lett. **19**, 266–271 (2001)

Suzuki, S., Hatakeyama, Y., Kokubun, Y., Chu, S.T.: Precise control of wavelength channel spacing of microring resonator add–drop filter array. IEEE J. Lightwave Technol. **20**, 745–750 (2002)

Tan, F.: Integrated optical filters based on microring resonators. Ph.D. Thesis, University of Twente, ISBN 90-365-2023-1 (2004)

Tazawa, H., Steier, W.H.: Bandwidth of linearized ring resonator assisted Mach–Zehnder modulator. IEEE Photon. Technol. Lett. **17**, 1851–1853 (2005)

Tazawa, H., Steier, W.H.: Analysis of ring resonator-based traveling-wave modulators. IEEE Photon. Technol. Lett. **18**, 211–213 (2006)

Tee, C.W., Williams, K.A., Penty, R.V., White, I.H.: Fabrication-tolerant active–passive integration scheme for vertically coupled microring resonator. IEEE J. Select. Topics Quantum Electron. **12**, 108–116 (2006)

Tishinin, D.V., Dapkus, P.D., Bond, A.E., Kim, I., Lin, C.K., O'Brien, J.: Vertical resonant couplers with precise coupling efficiency control fabricated by wafer bonding. IEEE Photon. Technol. Lett. **11**, 1003–1005 (1999)

Tredicucci, A., Gmachl, C., Capasso, F., Sivco, D.L., Chu, S.N.G., Hutchinson, A.L., Cho, A.Y.: Very long wavelength ($\lambda = 16\,\mu$m) whispering gallery mode microdisk lasers. Electron. Lett. **36**, 328–330 (2000)

Tsai, C.H., Lee, J.H., Chiang, H.J., Yang, C.C., Shih, H.C., Chen, B.C., Chuang, T.J., Chang. Y.: Semiconductor circular ring lasers fabricated with the cryo-etching technique. IEEE Photon. Technol. Lett. **10**, 751–753 (1998)

Vahala, K.J.: Optical microcavities. Nature **424**, 839–846 (2003)

Vahala, K.J.: Optical microcavities (advanced series in applied physics). World Scientific Publishing (2004)

van Damy Spiekman, L.H., van Ham, F.P.G.M., Groen, F.H., van der Tol. J.J.G.M., Moerman, I., Pascher, W.W., Hamacher, M., Heidrich, H., Weinert, C.M., Smit, M.K.: Novel compact polarization converters based on ultra short bends. IEEE Photon. Technol. Lett. **8**, 1346–1348 (1996)

van Roijen, R., Pennings, E.C.M., van Stalen, M.J.N., van Dongen, T., Verbeek, B.H., van der Heijden, J.M.M.: Compact InP-based ring lasers employing multimode interference couplers and combiners. Appl. Phys. Lett. **64**, 1753–1755 (1994)

Van, V., Absil, P.P., Hryniewicz, J.V., Ho, P.T.: Propagation loss in single-mode GaAs–AlGaAs microring resonators: Measurement and model. IEEE J. Lightwave Technol. **19**, 1734–1739 (2001)

Van, V., Ibrahim, T.A., Absil, P.P., Johnson, F.G., Grover, R., Ho, P.T.: Optical signal processing using nonlinear semiconductor microring resonators. IEEE J. Select. Topics Quantum Electron. **8**, 705–713 (2002a)

Van, V., Ibrahim, T.A., Ritter, K., Absil, P.P., Johnson, F.G., Grover, R., Goldhar, J., Ho, P.T.: All-optical nonlinear switching in GaAs–AlGaAs microring resonators. IEEE Photon. Technol. Lett. **14**, 74–76 (2002b)

Van, V., Little, B.E., Chu, S.T., Hryniewicz, J.V.: Micro ring resonator filters. Proc. LEOS Ann. Meet. **2**, 571–572 (2004)

Vander Rhodes, G.H., Goldberg, B.B., Ünlü, M.S., Chu, S.T., Little, B.E.: Internal spatial modes in glass microring resonators. IEEE J. Select. Topics Quantum Electron. **6**, 46–53 (2000)

Vanderhaegen, B., Van Thourhout, D., De Merlier, J., Sarlet, G., Vanwassenhove, L., Moerman, I., Van Daele, P., Baets, R.: High Q InGaAsP ring resonator filters. Proc. 9th Eur. Conf. Integrated Opt. Tech. Exhibition (ECIO 99), Italy, 381–384 (1999)

Vawter, G.A., Mar, A., Hietala, V., Zolper, J., Hohimer, J.: All optical millimeter-wave electrical signal generation using an integrated mode-locked semiconductor ring laser and photodiode. IEEE Photon. Technol. Lett. **9**, 1634–1636 (1997)

Vörckel, A., Mönster, M., Henschel, W., Bolivar, P.H., Kurz, H.: Asymmetrically coupled silicon-on-insulator microring resonators for compact add–drop multiplexers. IEEE Photon. Technol. Lett. **15**, 921–923 (2003)

Wang, R.P., Dumitrescu, M.M.: Optical Modes in Semiconductor Microdisk Lasers. IEEE J. Quantum Electron. **34**, 1933–1937 (1998)

Wang, T.J., Huang, Y.H., Chen, H.L.: Resonant-wavelength tuning of microring filters by oxygen plasma treatment. IEEE Photon. Technol. Lett. **17**, 582–584 (2005)

Watts, M.R., Qi, M., Barwicz, T., Popovic, M., Rakich, P., Socci, L., Ippen, E.P., Kaertner, F., Smith, H.I.: Towards polarization independent high-index contrast microphotonics. Proc. 28th URSI General Assembly (2005)

Weber, H.P., Ulrich, R.: A thin film ring laser. Appl. Phys. Lett. **19**, 38–40 (1971)

Weiershausen, W., Zengerle, R.: Photonic highway switches based on ring resonators used as frequency-selective components. Appl. Opt. **35**, 5967–5978 (1996)

Weinert, C.M., Agrawal, N.: Three-dimensional finite difference simulation of coupling behavior and loss in multimode interference devices. IEEE Photon. Technol. Lett. **7**, 529–531 (1995)

West, B.R., Honkanen, S.: MMI devices with weak guiding designed in three dimensions using a genetic algorithm. Opt. Express **12**, 2716–2722 (2005)

Xu, Q., Schmidt, B., Pradhan, S., Lipson, M.: Micrometre-scale silicon electro-optic modulator. Nature **435**, 325–327 (2005)

Yalçin, A., Popat, K.C., Aldridge, J.C., Desai, T.A., Hryniewicz, J, Chbouki, N., Little, B.E., King, O., Van, V., Chu, S.T., Gill, D., Anthes-Washburn, M., Ünlü, M.S., Goldberg, B.B.: Optical sensing of biomolecules using microring resonators. IEEE J. Select. Topics Quantum Electron. **12**, 148–155 (2006)

Yan, X., Masanovic, M.L., Skogen, E.J., Hu, Z., Blumenthal, D.J., Coldren, L.A.: Optical mode converter integration with InP-InGaAsP active and passive waveguides using a single regrowth process. IEEE Photon. Technol. Lett. **14**, 1249–1251 (2002)

Yanagase, Y., Suzuki, S., Kokubun, Y., Chu, S.T.: Box-likefilter response and expansion of FSR by a vertically triple coupled microring resonator filter. IEEE J. Lightwave Technol. **20**, 1525–1529 (2002a)

Yanagase, Y., Suzuki, S., Kokubun, Y., Chu, S.T.: Vertical triple series-coupled microring resonator filter for passband flattening and expansion of free spectral range. Japan. J. Appl. Phys. **41**, L141–L143 (2002b)

Yariv, A.: Critical coupling and its control in optical waveguide-ring resonator systems. IEEE Photon. Technol. Lett. **14**, 483–485 (2002a)

Yariv, A.: Universal relations for coupling of optical power between microresonators and dielectric waveguides. Electron. Lett. **36**, 321–322 (2002b)

Yu, S., Krauss, T.F., Laybourn, P.J.R.: Mode locking in large monolithic semiconductor ring lasers. SPIE Opt. Eng. **37**, 1164–1168 (1998)

Zeng, K.C., Dai, L., Lin, J.Y., Jiang, H.X.: Optical resonance modes in InGaN/GaN multiple-quantum-well microring cavities. Appl. Phys. Lett. **75**, 2563–2565 (1999)

Index

Springer Series in

OPTICAL SCIENCES

Volume 1

1 **Solid-State Laser Engineering**
By W. Koechner, 5th revised and updated ed. 1999, 472 figs., 55 tabs., XII, 746 pages

Published titles since volume 90

100 **Quantum Interference and Coherence**
Theory and Experiments
By Z. Ficek and S. Swain, 2005, 178 figs., XV, 418 pages

101 **Polarization Optics in Telecommunications**
By J. Damask, 2005, 110 figs., XVI, 528 pages

102 **Lidar**
Range-Resolved Optical Remote Sensing of the Atmosphere
By C. Weitkamp (Ed.), 161 figs., XX, 416 pages

103 **Optical Fiber Fusion Splicing**
By A.D. Yablon, 2005, 137 figs., XIII, 306 pages

104 **Optoelectronics of Molecules and Polymers**
By A. Moliton, 2005, 229 figs., 592 pages

105 **Solid-State Random Lasers**
By M. Noginov, 2005, 131 figs., XII, 238 pages

106 **Coherent Sources of XUV Radiation**
Soft X-Ray Lasers and High-Order Harmonic Generation
By P. Jaeglé, 2006, 332 figs., XIII, 416 pages

107 **Optical Frequency-Modulated Continuous-Wave (FMCW) Interferometry**
By J. Zheng, 2005, 137 figs., XVIII, 254 pages

108 **Laser Resonators and Beam Propagation**
Fundamentals, Advanced Concepts and Applications
By N. Hodgson and H. Weber, 2005, 587 figs., XXVI, 794 pages

109 **Progress in Nano-Electro Optics IV**
Characterization of Nano-Optical Materials and Optical Near-Field Interactions
By M. Ohtsu (Ed.), 2005, 123 figs., XIV, 206 pages

110 **Kramers–Kronig Relations in Optical Materials Research**
By V. Lucarini, J.J. Saarinen, K.-E. Peiponen, E.M. Vartiainen, 2005,
37 figs., X, 162 pages

111 **Semiconductor Lasers**
Stability, Instability and Chaos
By J. Ohtsubo, 2005, 169 figs., XII, 438 pages

112 **Photovoltaic Solar Energy Generation**
By A. Goetzberger and V.U. Hoffmann, 2005, 139 figs., XII, 234 pages

113 **Photorefractive Materials and Their Applications 1**
Basic Effects
By P. Günter and J.P. Huignard, 2006, 169 figs., XIV, 421 pages

114 **Photorefractive Materials and Their Applications 2**
Materials
By P. Günter and J.P. Huignard, 2005, 100 figs., approx. XII, 300 pages

115 **Photorefractive Materials and Their Applications 3**
Applications
By P. Günter and J.P. Huignard, 2005, 100 figs., approx. XII, 300 pages

Springer Series in

OPTICAL SCIENCES

116 **Spatial Filtering Velocimetry**
Fundamentals and Applications
By Y. Aizu and T. Asakura, 2006, 112 figs., XII, 212 pages

117 **Progress in Nano-Electro-Optics V**
Nanophotonic Fabrications, Devices, Systems, and Their Theoretical Bases
By M. Ohtsu (Ed.), 2006, 122 figs., XIV, 188 pages

118 **Mid-infrared Semiconductor Optoelectronics**
By A. Krier (Ed.), 2006, 443 figs., XVIII, 751 pages

119 **Optical Interconnects**
The Silicon Approach
By L. Pavesi and G. Guillot (Eds.), 2006, 265 figs., XXII, 389 pages

120 **Relativistic Nonlinear Electrodynamics**
Interaction of Charged Particles with Strong and Super Strong Laser Fields
By H.K. Avetissian, 2006, 23 figs., XIII, 333 pages

121 **Thermal Processes Using Attosecond Laser Pulses**
When Time Matters
By M. Kozlowski and J. Marciak-Kozlowska, 2006, approx. 46 figs., XII, 232 pages

122 **Modeling and Analysis of Transient Processes in Open Resonant Structures**
New Methods and Techniques
By Y.K. Sirenko, N.P. Yashina, and S. Ström, 2007, approx. 110 figs., XIV, 346 pages

123 **Wavelength Filters in Fibre Optics**
By H. Venghaus (Ed.), 2007, approx. 210 figs., XXIV, 451 pages

124 **Light Scattering by Systems of Particles**
Null-Field Method with Discrete Sources: Theory and Programs
By A. Doicu, T. Wriedt, and Y.A. Eremin, 2006, 123 figs., XIII, 318 pages

125 **Electromagnetic and Optical Pulse Propagation 1**
Spectral Representations in Temporally Dispersive Media
By K.E. Oughstun, 2007, approx 74 figs., 452 pages

126 **Quantum Well Infrared Photodetectors**
Physics and Applications
By H. Schneider and H.C. Liu, 2006, 153 figs., XVI, 254 pages

127 **Integrated Ring Resonators**
The Compendium
By D.G. Rabus, 2007, approx. 243 figs., XVII, 302 pages

128 **High Power Diode Lasers**
Technology and Applications
By R. Poprawe, P. Loosen, and F. Bachmann (Eds.) 2007, approx. 535 figs., VI, 546 pages

129 **Laser Ablation and its Applications**
By C.R. Phipps (Ed.) 2007, approx. 300 figs., XX, 588 pages

130 **Concentrator Photovoltaics**
By A. Luque and V. Andreev (Eds.) 2007, approx. 242 figs., XV, 298 pages